The Strength and Deformation Properties of Melange

by

Eric Stuart Lindquist

B.S. (University of California at Berkeley) 1990
M.S. (University of California at Berkeley) 1991

A dissertation submitted in partial satisfaction of the

requirements for the degree of

Doctor of Philosophy

in

Engineering-Civil Engineering

in the

GRADUATE DIVISION

of the

UNIVERSITY of CALIFORNIA at BERKELEY

Committee in charge:

Professor Richard E. Goodman, Chair
Professor Richard E. Barlow
Professor Paulo J. Monteiro

1994

The dissertation of Eric Stuart Lindquist is approved:

Richard E Goodman, April 26, 1994
Chair Date

R. E. Barlow April 21, 1994
Date

April 25, 1994
Date

University of California at Berkeley

1994

The Strength and Deformation Properties of Melange

by

Eric Stuart Lindquist

Abstract

The Strength and Deformation Properties of Melange

by

Eric Stuart Lindquist

Doctor of Philosophy in Civil Engineering

University of California at Berkeley

Professor Richard E. Goodman, Chair

Physical model melanges made up of stronger and stiffer blocks in a weaker and softer matrix were tested in triaxial compression to study the effect block proportion and orientation have on melange strength and stiffness. The results of these tests showed that increasing the block proportion generally decreased the cohesion, increased the angle of internal friction and increased the modulus of deformation of the models. The highest block proportion specimens (approximately 70% blocks by volume) had a cohesion as low as half of that of the matrix and an angle of internal friction as much as 16.5° higher than that of the matrix. Block orientation also affected the strength, most notably the cohesion. The specimens with the most adversely oriented blocks (i.e. blocks at an angle of 30° relative to the axial loading direction) had the lowest cohesion. The modulus of deformation was also affected by block orientation. The modulus increased with increasing block proportion, and this increase was most pronounced for the models with blocks oriented parallel to the axial loading direction and least pronounced for those with blocks oriented perpendicular to the axial loading direction.

These results were compared with some limited triaxial compression test data from actual melange specimens. The strength and deformation behavior exhibited by the actual melange specimens compared favorably with that shown by the physical models (i.e. the

angle of internal friction and stiffness of the actual melange specimens increased with increasing block proportion).

Based on the physical model and actual melange test data some design recommendations are given regarding the strength and deformation properties of melange.

Approved: Richard E. Goodman
Professor Richard E. Goodman, Chair

To my parents and Lisa

TABLE OF CONTENTS

LIST OF FIGURES

List of Figures

List of Figures

List of Figures

List of Figures

LIST OF TABLES

ACKNOWLEDGMENTS

I would like to acknowledge my mentor and thesis advisor Professor Richard Goodman for giving me the chance to tackle this challenging project. From being my first undergraduate advisor at Berkeley, to introducing me to intricacies of rock mechanics, he has always been a guiding light I wished to follow. I would also like to thank Professors Paulo Monteiro and Richard Barlow for their interest in my research. Professor Monteiro helped me better understand portland cement concrete; likewise, the logic behind probability models, that all too many of us take for granted, has been revealed to me by Professor Barlow.

Model fabrication and lab testing were carried out with the aid of graduate student Dimitrios Protogirou and undergraduate Jason Choi. I thank them for providing, not only their muscle, but also their ideas to this project. Jon Asselanis deserves thanks for always being able to find the equipment I needed during model fabrication. Fellow students Te-Chih Ke and Bhaskar Thapa were always willing to listen to my latest research findings, as well as my latest complaints. Thanks also go to my colleague Ed Medley for all of his thought provoking comments and ideas and, most importantly, for his friendship.

Funding for this research was provided by the Pacific Gas and Electric Company, San Francisco. I am grateful for their interest and support. Finally, I would like to acknowledge the National Science Foundation and the University of California at Berkeley for providing graduate fellowships that allowed me to live quite comfortably over the last four years.

CHAPTER 1

INTRODUCTION

1.1 Melange Description

Melange is the French word for "mixture". Over the years the word melange has been used to describe a wide variety of rock formations each with its own individual characteristics. Because of this extensive usage, creating a single all encompassing definition has been a daunting task. The most satisfactory definition I have found is that given in the Dictionary of Geological Terms (Bates and Jackson, 1984).

> Melange - A mappable body of rock that includes fragments and blocks of all sizes, both exotic and native, embedded in a fragmented and generally sheared matrix.

In essence, therefore, a melange is a rock body made up of blocks in a matrix (i.e. a block-in-matrix rock or *bimrock* (Medley, 1994)). Other examples of bimrocks are conglomerate, sheared serpentinite and breccia.

Melange formation is a highly controversial topic. It has been postulated that melanges form by one of two general processes. The first is sedimentary mixing. In this process initially bedded unconsolidated sediments are mixed by submarine gravity sliding and later lithified. Melanges formed by this process are called *olistostromes.* The second explanation of melange genesis is tectonic mixing. Tectonic mixing theories explain that a melange forms as part of the accretionary wedge during subduction at plate boundaries. Melanges formed by this process are known as *tectonic melanges.* Many melanges may well have formed by a combination of these two processes. More detailed discussions of melange formation can be found in papers by Cowan (1978), Cowan and Silling (1978), Aalto (1982), Cloos (1984) and many others.

Melanges are found in over 60 countries. Figure 1.1 (Medley, 1994) shows the world distribution of melange. Based on this map and some knowledge of plate tectonics, it is quite clear that melanges are indeed formed in subduction environments.

The melange found in California belongs to the Franciscan formation. Figure 1.2 shows an outcrop of Franciscan melange. The blocks in this photograph are greywacke sandstone and the matrix is sheared shale or argillite. At other places, blocks of siltstone, intact shale, tuff, chert and various types of metamorphic rock can be found in the Franciscan. Although universal agreement has never been reached, it is now generally believed that both olistostromes and tectonic melange can be found in the Franciscan, and much of the melange was probably created by a combination of these processes.

Some notable features of Franciscan melange are listed below.

1. It consists of stronger blocks embedded in a weaker matrix.

2. It has a sheared matrix that ranges from being weakly fissile to markedly scaly. This shearing creates an anisotropic rock fabric. In detail the shears curve around the block margins, the result being that the block-matrix contacts are often sheared.

3. Blocks range in shape from round to elongate and lenticular to tabular. Some blocks show pinch-swell features.

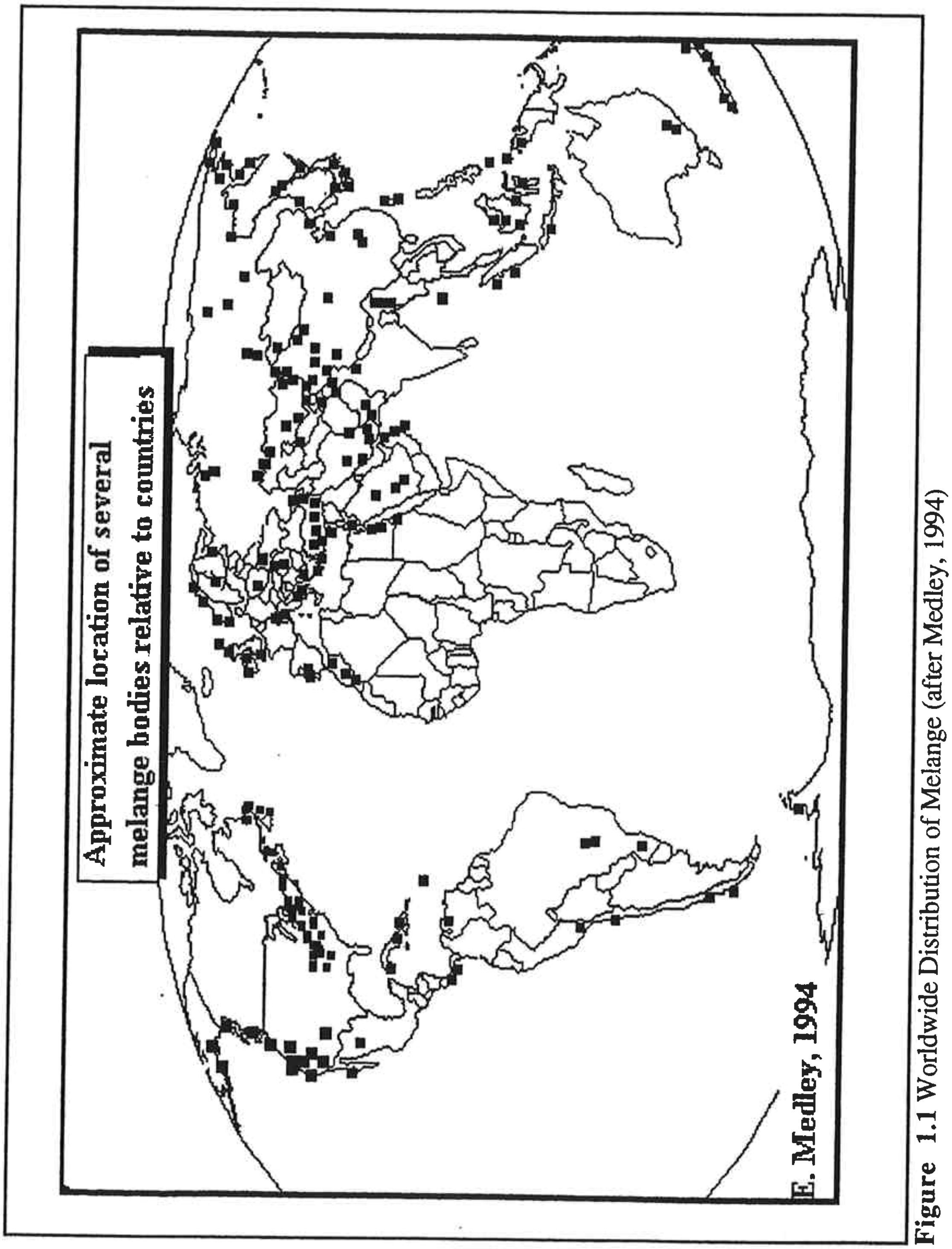

Figure 1.1 Worldwide Distribution of Melange (after Medley, 1994)

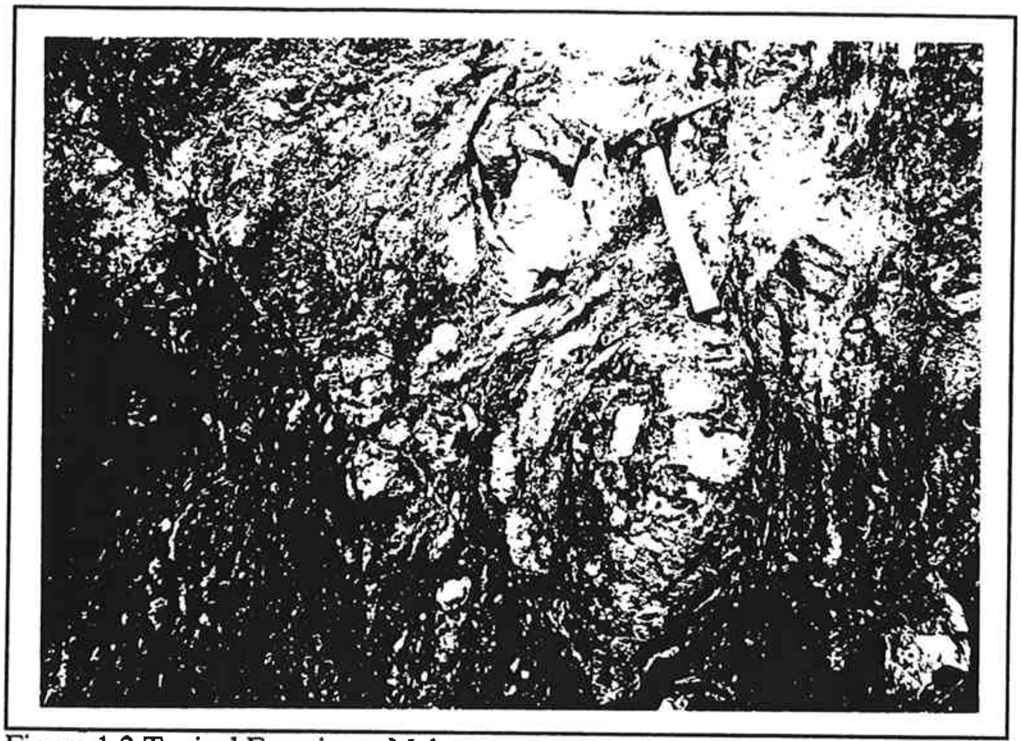

Figure 1.2 Typical Franciscan Melange

4. Each block's longest axis tends to be generally aligned with the shear fabric found in the matrix; hence, smaller blocks tend to align themselves with the margins of larger blocks.

5. Blocks range in size from fragments too small for the eye to see, to slabs thousands of meters long.

The aforementioned characteristics of Franciscan melange have been described by Cowan (1978 and 1985) and other authors. They were substantiated by personal observations made along the California coast.

These characteristics of Franciscan melanges, are found in other melanges as well; thus the results of this research have a wide applicability. Similar melanges, found through a literature search, include the melange in the Shimanto Belt of Japan (Kano et al., 1991), the Lichi melange of Taiwan (Page, 1978), the *Argille Scagliose* (melange) of Italy (Page, 1978), the Uyak (Moore and Wheeler, 1978), Ghost Rocks (Byrne, 1984) and other melanges of Alaska (Cowan, 1985), the Humber Arm Slice Assemblage of Western Newfoundland (Waldron et al., 1988), and the Oyo Complex melange of Nias Island, Indonesia (Moore and Karig, 1980). Sheared serpentinites, which Cowan (1985) described as, "a weakly to strongly foliated, scaly matrix of generally friable serpentinite containing rounded to lenticular blocks of partly to wholly serpentinized ultramafic rocks, mafic igneous rock, and, in some cases, a wide variety of sedimentary-rock types," may be another bimrock to which these research findings can be applied.

1.2 Difficulty Assessing Mechanical Properties

Due to their complex nature, melanges are difficult engineering materials. D'Elia et al. (1984) stated the following regarding the Argille Scagliose, "Given the lithologic and structural characters of the Argille Scagliose it was not possible to carry out laboratory or in-situ tests capable of providing data on the mechanical properties of the mass formation." The mass was simply too heterogeneous to be captured in a small sample. This fact has been realized by many engineers and geologists working with melanges all over the world. The reasons for this difficulty include:

1. Obtaining "undisturbed" samples of a mixture of harder blocks in weaker matrix is quite difficult by coring since the drilling resistance of the harder and softer materials are significantly different. This difference in drilling resistance can cause the harder materials to gouge into the weaker materials resulting in significant sample disturbance, or even a complete loss of the weaker material.

2. Even if one were able to recover an undisturbed sample, it is improbable that the sample would be representative of the melange mass of interest. Large in-situ test samples are perhaps the most promising approach to finding and testing a representative sample, but even this possibility seems remote.

For these reasons, a different approach is needed for determining the mechanical properties of a melange.

It has been found possible to recover and test samples of pure matrix and pure block. Realistically the mechanical properties of the block and matrix components at any site can therefore be determined independently. With these data, one approach might be to design based on the properties of the weaker matrix; however this approach neglects the possibility that the blocks strengthen and stiffen a melange mass, therefore it may be overconservative. A less conservative alternative approach was proposed by Volpe et al. (1991). They suggested that the strength of a melange mass could be represented by the weighted average of the strengths of the weaker matrix and stronger blocks based on their volumetric proportions. Unfortunately, no theoretical basis was provided for this strength model except the intuitive belief that the two components must share in the strength of the whole.

1.3 Research Goals and Dissertation Outline

This research was prompted by an effort to investigate strength models such as that proposed by Volpe et al. (1991). The goals of this research were therefore to determine how the Mohr-Coulomb strength parameters (i.e. cohesion and angle of internal friction) and the stress-strain behavior of melanges are affected by block proportion and block orientation. The aim was to create practical rules that could be used to predict the strength and deformation properties of complex melanges given reasonably accessible information.

As a means to this end, an extensive literature review was completed in an attempt to locate information on the mechanical properties of melange and other block-in-matrix materials (Chapter 2). In addition to this literature review, physical model melanges were fabricated and tested in triaxial compression to study how the block and matrix mechanical properties, their volumetric proportions and block orientation were related to the mechanical properties of the model melange mass. Model fabrication and test procedures are discussed in Chapter 3. Chapter 4 summarizes the test results. A discussion and interpretation of these results are found in Chapter 5. In this discussion I have attempted to explain the deformation and strength behavior exhibited by the models. Specimens of Franciscan melange that were tested in triaxial compression in 1982 and 1983 have been re-examined. The results of these tests on actual melange were compared to the physical model results in an attempt to substantiate the physical model findings (Chapter 6). Chapter 7 presents my recommendations for predicting the mechanical properties of melanges.

CHAPTER 2

REVIEW OF PREVIOUS WORK

As discussed in the Introduction, we are interested in melanges made up of stronger, stiffer blocks in a weaker, softer matrix. This section reviews previous studies that attempted to relate the volumetric proportion of blocks to the shear strength (cohesion and angle of internal friction) and stiffness (modulus of deformation) of a variety of block-in-matrix materials.

2.1 Melanges

Very few studies of the mechanical properties of melanges have been found. Most commonly the strength and deformation characteristics of the melange matrix are assumed to be representative of the melange mass. This section discusses the small number of investigations that attempted to quantify melange strength and deformation properties.

Bedrosian (1978 and 1980) examined slope stability of the Franciscan melange in the Geysers Geothermal Resources Area in northern California. Her investigations led her to suggest that, "Clearly the matrix, being the weakest component, controls the overall stability of slopes underlain by the melange." In Italy, this assumption has been consistently applied by engineers working with the complex Argille Scagliose (melange). For example, in two reports by the Italian Geotechnical Association only the properties of the matrix were reported because it was believed that the matrix controlled the overall mechanical behaviour of the rock mass (AGI, 1979 and 1985). This supposition makes sense when the matrix component makes up the vast majority of the melange mass. It seems intuitive, however, that in areas where rock blocks are more abundant this assumption might be overly conservative.

Evidence provided by both natural and constructed slopes indicates that assuming the mechanical properties of a melange to be completely controlled by the matrix is indeed overconservative. For example, earthflows tend to occur in Franciscan melange in areas where the ratio of blocks to matrix is relatively low but not in areas where the block to matrix ratio is high (Savina, 1978). This strongly suggests that the blocks increase slope stability (i.e. increase the mass strength). D'Elia et al. (1984) provided evidence that the presence of stronger blocks influenced the mass behavior of a melange. During their study of a high cut made in the Argille Scagliose they discovered that, "For representing the in-situ strength ... the upper limit of the shear strength envelopes of the material tested in the laboratory was assumed as being more significant." The only "material tested" in this case was the matrix, a clay shale. Considering the fact that only approximately 15% of the formation in which the cut was made was the block component, it appears that stronger blocks did influence the mass mechanical properties of the melange even when they were present at relatively low proportions. D'Elia et al. (1988) attempted to explain this by suggesting, "the rock component may hinder the formation of regular and continuous slip surfaces." Unfortunately, this hypothesized behavior has not previously been observed.

2.2 Other Block-in-Matrix Materials

2.2.1 Other Rock Types

Conglomerate, tillite, sheared serpentinite and breccia are other examples of block-in-matrix rock. In cases where recovering a representative core sample is not possible, the mechanical properties of these materials are most often determined by large-scale in-situ tests. However it may not always be feasible to test representative samples in-situ, most notably when the block sizes are too large to be reasonably included even in large scale tests. In such cases, the strength and deformation properties of the matrix are most commonly assumed to be representative of the mass. The only study I located which considered the effect of larger blocks on shear strength was done by Savely (1990). Savely (1990) suggested that the cohesion of a boulder conglomerate mass should be assumed to be the same as that of the matrix material, and that the angle of internal friction would be higher than that of the matrix due not only to block-to-block contacts, but also to cobbles and boulders (blocks) increasing the tortuousity of the failure surface. In other words, Savely hypothesized that the cohesion for a boulder conglomerate would be independent of block proportion and the angle of internal friction would increase with increasing block proportion. As with melange, the magnitude of this increase has not previously been quantified.

2.2.2 Portland Cement Concrete

Portland cement concrete can be viewed as an "artificial melange". As in a melange, normal-weight concrete is a mixture of stronger blocks (aggregate) in a weaker matrix (cement paste). The effect of aggregate proportion on the elastic modulus and the uniaxial compressive strength ("shear strength" is not of great interest in concrete) has been discussed by many authors. A brief review of a few representative papers is given below.

Stock et al. (1979) collected data from many sources to create plots of uniaxial compressive strength versus aggregate proportion. Figure 2.1 shows some representative results from various authors as reported by Stock et al. (1979). I have also included some unpublished data provided to me by University of California at Berkeley Civil Engineering Professor Paulo Monteiro. The data in Figure 2.1 indicate that the uniaxial compressive strength of concrete drops, at least initially, as the aggregate volume is increased. Some of these data suggest that this trend reverses itself at higher aggregate proportions. A possible explanation for why concrete strength drops as the aggregate proportion is increased is that the volume of cement paste immediately surrounding a piece of aggregate is a zone of higher porosity and therefore weakness. This volume of weak material is known as the "transition zone" (Mehta and Monteiro, 1993). Adding aggregate, therefore, introduces multiple weak links in a concrete mass. This quite conceivably explains why concrete becomes weaker as aggregate proportion is increased.

A significant number of experimental and theoretical studies considered the relationship between aggregate proportion and elastic modulus. In many of these studies various theoretical and empirical formulae were used to predict the elastic modulus of concrete given the elastic properties (elastic moduli and sometimes Poisson's ratios) of the cement paste and aggregate and the volumetric proportions of these two concrete components. Hirsch (1962), Counto (1964), Hansen (1965), Stock et al. (1979), Benveniste (1987) and Mehta and Monteiro (1993) are just a few of the authors who either proposed and/or discussed predictive models for the modulus. A discussion of some of the simplest theoretical formulae for predicting the elastic modulus of multiphase materials is reserved until Section 5.1. Experimental results for concrete from a few different sources are presented in Figure 2.2. These results show that the elastic modulus of concrete increases with increasing aggregate proportion (as long as the aggregate has a higher elastic modulus than the cement paste). It has been shown that this increase is generally not as great as is predicted by the strict Hashin-Shtrikman bounds (Hashin and Shtrikman (1963) used variational principles in the theory of elasticity to set upper and lower bounds on the elastic modulus of multiphase materials) due to the presence of the more porous and therefore "softer" transition zone (Nilsen and Monteiro, 1993). This transition zone is a "third component" of concrete that has not been accounted for in any analytical models to date.

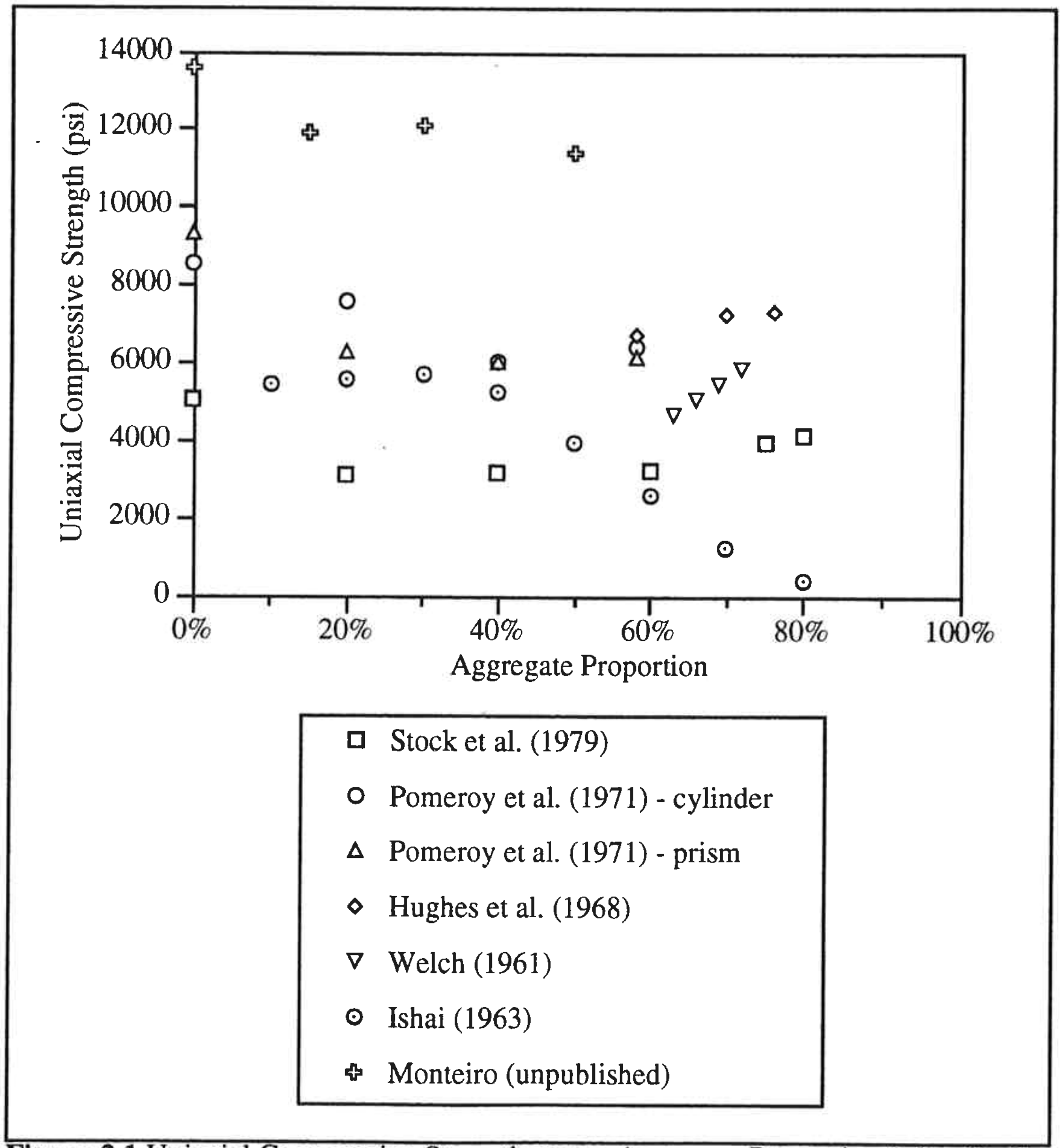

Figure 2.1 Uniaxial Compressive Strength versus Aggregate Proportion (after Stock et al., 1979)

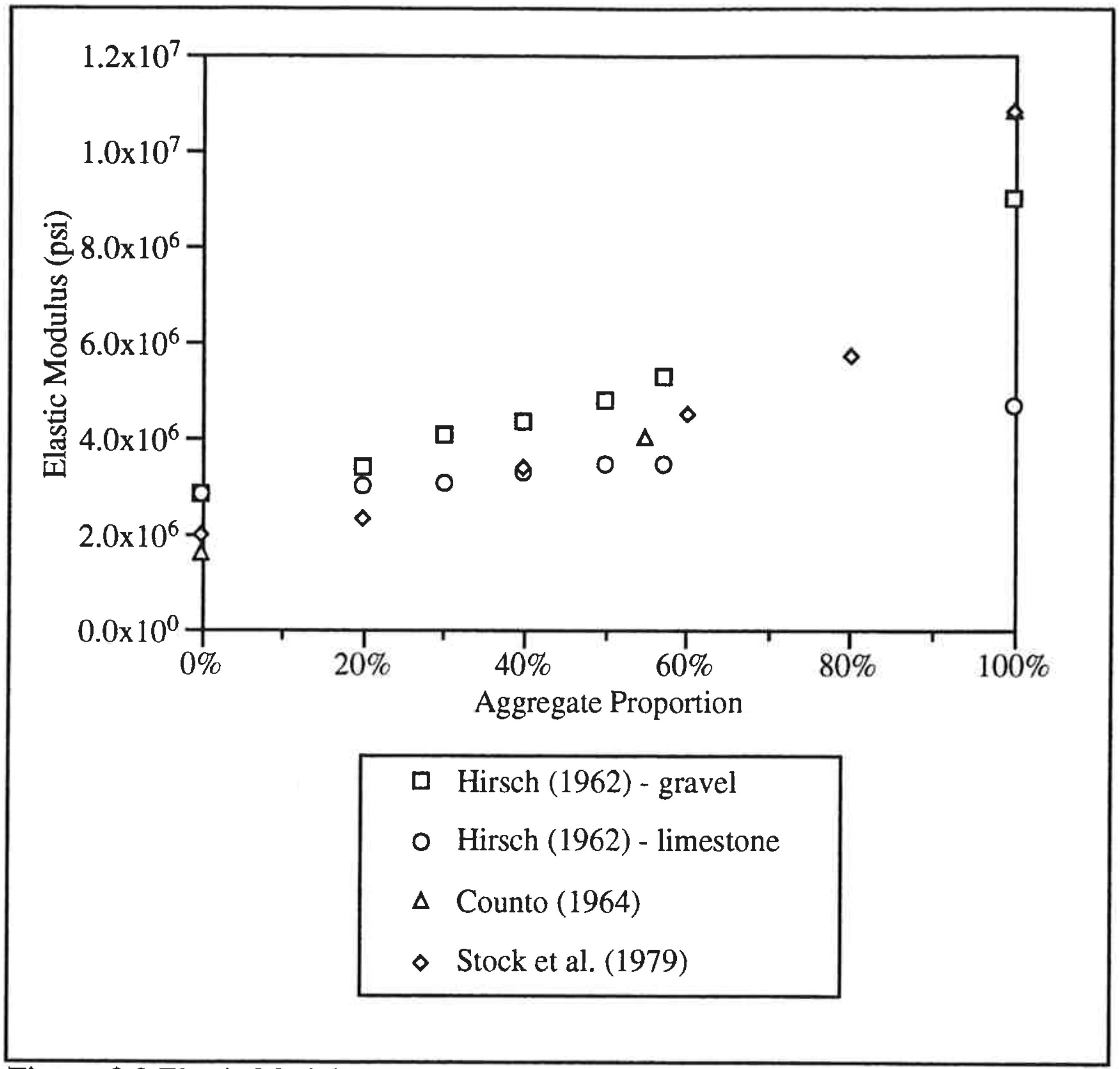

Figure 2.2 Elastic Modulus versus Aggregate Proportion

2.2.3 Heterogeneous Soils

Heterogeneous soil mixtures consisting of coarser particles in a finer matrix can also be viewed as a sort of "melange". Heterogeneous soils result from both natural and artificial processes. Tills, alluvium, colluvium and fault gouge are all examples of naturally formed heterogeneous soils. Artificially formed heterogeneous soils include earth-rock fill and mine waste. As discussed previously, the best way of assessing the strength of a block-in-matrix material is to test a sample large enough to include the full range of particle sizes. For example, it has been suggested that large samples are required to determine the strength of tills (McGown and Derbyshire, 1977 and McKinlay et al., 1974). As for other block-in-matrix materials, it will not always be feasible to test samples large enough to be representative of the mass. In these cases, a relationship between a soil's coarse particle proportion and its mechanical properties will be required.

Many melanges have matrixes that are "rock-like" (i.e. they are stronger and more brittle than soil and they tend to fail by fracturing). The differences in strength as well as stiffness of the matrix material and the individual coarse particles in a heterogeneous soil is most often many orders of magnitude. This is not typically the case for a melange. In certain cases however, a melange matrix may be sheared to such an extent that it is essentially a soil. For this reason, it is believed that the results of experimental studies that addressed the effect of coarse particle (block) proportion on a soil's mechanical properties will be relevant to at least "soil matrix" melanges. It is unclear if these results will be applicable to melanges with "rock" matrixes.

The studies I have located that relate coarse particle proportion to the strength and deformation properties of heterogeneous soils are listed in Table 2.1. Table 2.1 identifies the test type, matrix material and coarse particles used in each case. Most of this previous experimental work examined the effect of coarse particle proportion on a soil's Mohr-Coulomb shear strength parameters (i.e. either the total and/or effective stress peak and/or residual cohesion and angle of internal friction), and some studied how the deformation properties (e.g. material stiffness and dilatancy) were affected by coarse particle proportion. A discussion of the results of these studies follows. I have broken down the

Table 2.1 Summary of Previous Experimental Work On Heterogeneous Soils

Reference	Test Type	Matrix Material	Coarse Particles	Notes
Holtz and Gibbs (1956)	triaxial (CD)	medium to coarse sand	subrounded to angular gravel	samples compacted to 50% and 70% relative density
Miller and Sowers (1957)	triaxial (UU) no ppm*	silty clay	sand and fine gravel	samples compacted to maximum dry density (standard Proctor)
Kurata and Fujishita (1960)	direct shear (CU)	silt and clay	sand	loose samples consolidated under the same normal stress
Holtz and Ellis (1961)	triaxial (UU) with ppm*	sandy clay (SC-CL)	subrounded to subangular gravel	samples compacted to 95% maximum dry density (standard Proctor)
Borowicka (1965)	direct shear (CD)	clay	silt	
Doddiah et al. (1969)	triaxial (UU) no ppm*	silty sand (2% clay)	gravel	samples compacted to maximum dry density (standard Proctor)
Patwardhan et al. (1970)	direct shear	clay (ML)	subangular cobbles	samples prepared with similar matrix densities
Kawakami and Abe (1970)	triaxial (CU) with ppm*	clay (CH)	coarse sand	samples compacted to maximum dry density (standard Proctor)
Fedorov and Sergevnina (1973)	direct shear (CU)	clay	sand and gravel	compaction not specified
Kenney (1977)	direct shear (CD)	various clays	various bulky minerals	
Rathee (1981)	direct shear (CD)	fine to medium sand	rounded to subrounded gravel	samples compacted to 25% and 75% relative density
Lupini et al. (1981)	ring shear	clay	silt and sand	
Donaghe and Torrey (1985)	triaxial (CU and UU) with ppm*	sand (SP) mixed with clay (CL)	gravel	samples compacted to 95% maximum dry density (standard Proctor)
Shakoor and Cook (1990)	unconfined compression	silty clay (CL)	gravel	samples compacted to maximum dry density (standard Proctor)
West (1992)	direct shear (CU)	bentonite grease mix	steel rods	samples not compacted
Fragazzy et al. (1992)	triaxial (CD)	sand	subrounded to rounded gravel	samples prepared to the same far-field matrix density
Irfan and Tang (1993)	triaxial (CU) with ppm* and direct shear (CD)	silty sand (<2% clay)	gravel	samples prepared with similar matrix densities

*ppm = pore pressure measurement

studies into two categories based on whether or not the matrix material used contained clay. The reason for this breakdown will become apparent later.

Clay matrix studies

The researchers who employed matrix materials containing significant amounts of clay are Miller and Sowers (1957), Kurata and Fujishita (1960), Holtz and Ellis (1961), Borowicka (1965), Patwardhan et al. (1970), Kawakami and Abe (1970), Fedorov and Sergevnina (1973), Kenney (1977), Lupini et al. (1981), Donaghe and Torrey (1985), Shakoor and Cook (1990) and West (1992).

First, I will discuss those references reporting the effect of coarse particle proportion on the total stress peak angle of internal friction and cohesion. Figures 2.3(a) and (b) present results of unconsolidated undrained triaxial tests by Miller and Sowers (1957), direct shear tests by Kurata and Fujishita (1960) and consolidated undrained triaxial tests by Kawakami and Abe (1970). Figure 2.3(a) illustrates that the total stress angle of internal friction for each of the tested soils seemed to be unaffected by the presence of coarse particles until the coarse particle proportion (by weight) reached a threshold. Beyond this threshold, the angle of internal friction began to increase rapidly. The data indicate a threshold of about 70 percent coarse particles for the soil used by Miller and Sowers (1957), about 60 percent for the soil used by Kurata and Fujishita (1960) soil and about 50 percent for the soil used by Kawakami and Abe (1970). Additional evidence for this type of behavior was presented by Fedorov and Sergevnina (1973). Their results displayed a threshold at a coarse particle proportion of about 40 percent. Figure 2.3(b) indicates that the total stress cohesion of the soil used by Miller and Sowers (1957) began to decrease slowly at first, and then underwent a sudden drop at a coarse particle proportion

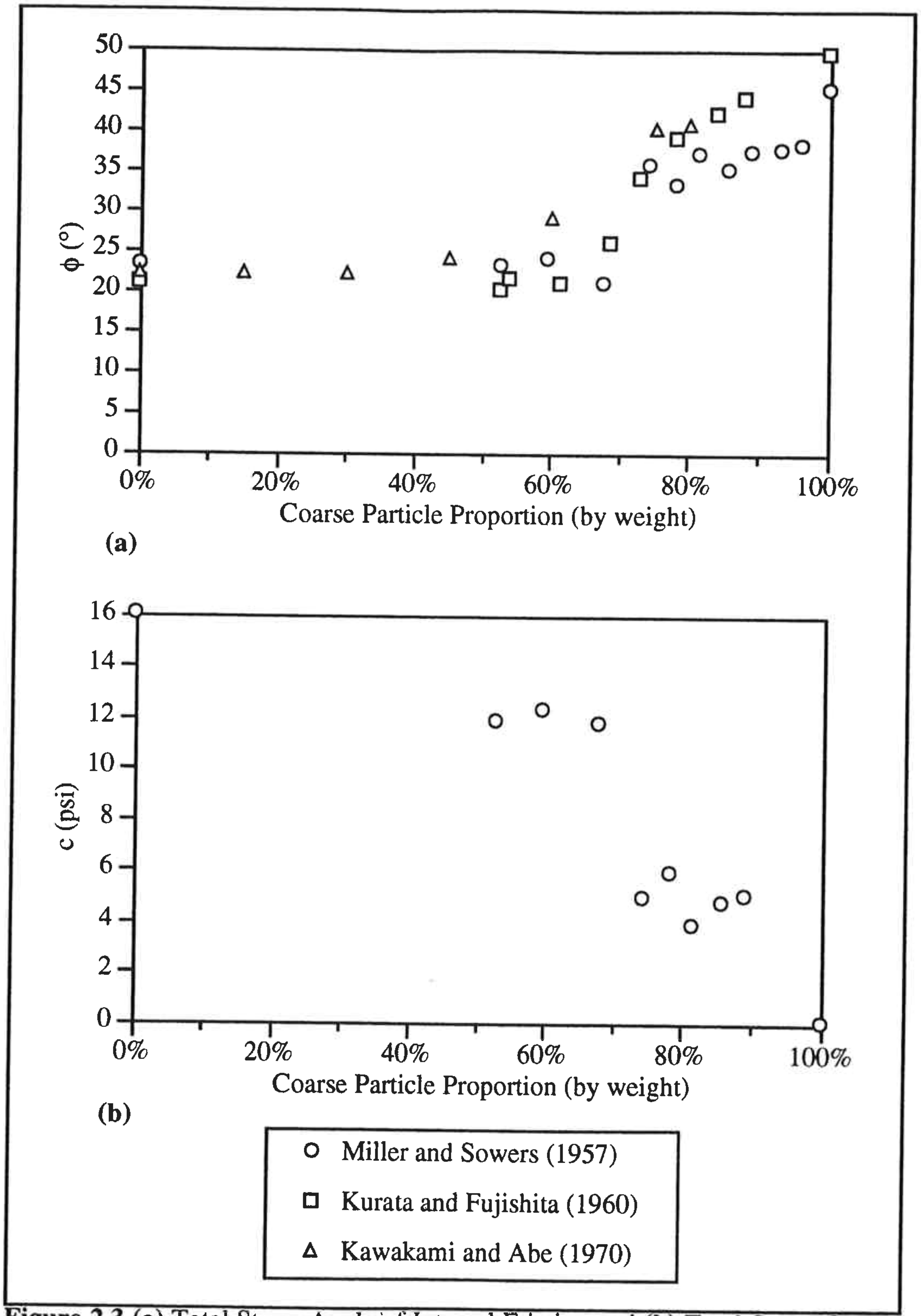

Figure 2.3 **(a)** Total Stress Angle of Internal Friction and **(b)** Total Stress Cohesion versus Coarse Particle Proportion (Clay Matrix)

of around 70 percent (the same threshold indicated by the angle of internal friction data). Miller and Sowers (1957) postulated that this strong behavioral change was the result of sand grain interaction. In other words, at an aggregate content of about 70 percent (by weight) the sand formed a granular skeleton which dominated the strength behavior of the soil. The same hypothesis was used by Rodine and Johnson (1976) to explain why the mechanical behavior of debris flow materials are dominated by the matrix phase even at significant coarse particle proportions.

A physical model consisting of steel rods embedded in a matrix of bentonite grease (a mixture of three parts dry bentonite with one part industrial grease) was used by West (1992) to study the shear behavior of heterogeneous soils. Figures 2.4(a) and (b) show the effect that the volumetric rod proportion had on the total stress peak angle of internal friction and cohesion. These physical models demonstrated strength behavior similar to that illustrated by the aforementioned studies (i.e. when the rod proportion reached a threshold value of about 50 percent, the angle of internal friction increased and the cohesion decreased).

Effective stress peak strength parameters were reported by Holtz and Ellis (1961) and Kawakami and Abe (1970). Graphs of effective stress angle of internal friction and cohesion versus coarse particle proportion are given in Figures 2.5(a) and (b). Figure 2.5(a) indicates that the angle of internal friction began to increase when the coarse particle proportion (by weight) exceeded about 40 percent in both the Holtz and Ellis (1961) study and the Kawakami and Abe (1970) study. The increases in the effective stress angle of internal friction with increase in coarse particle proportion were not nearly as great as the increases in the total stress angle of internal friction (Figure 2.3(a)) simply because the effective stress angles of internal friction for the clay matrixes were much higher than that

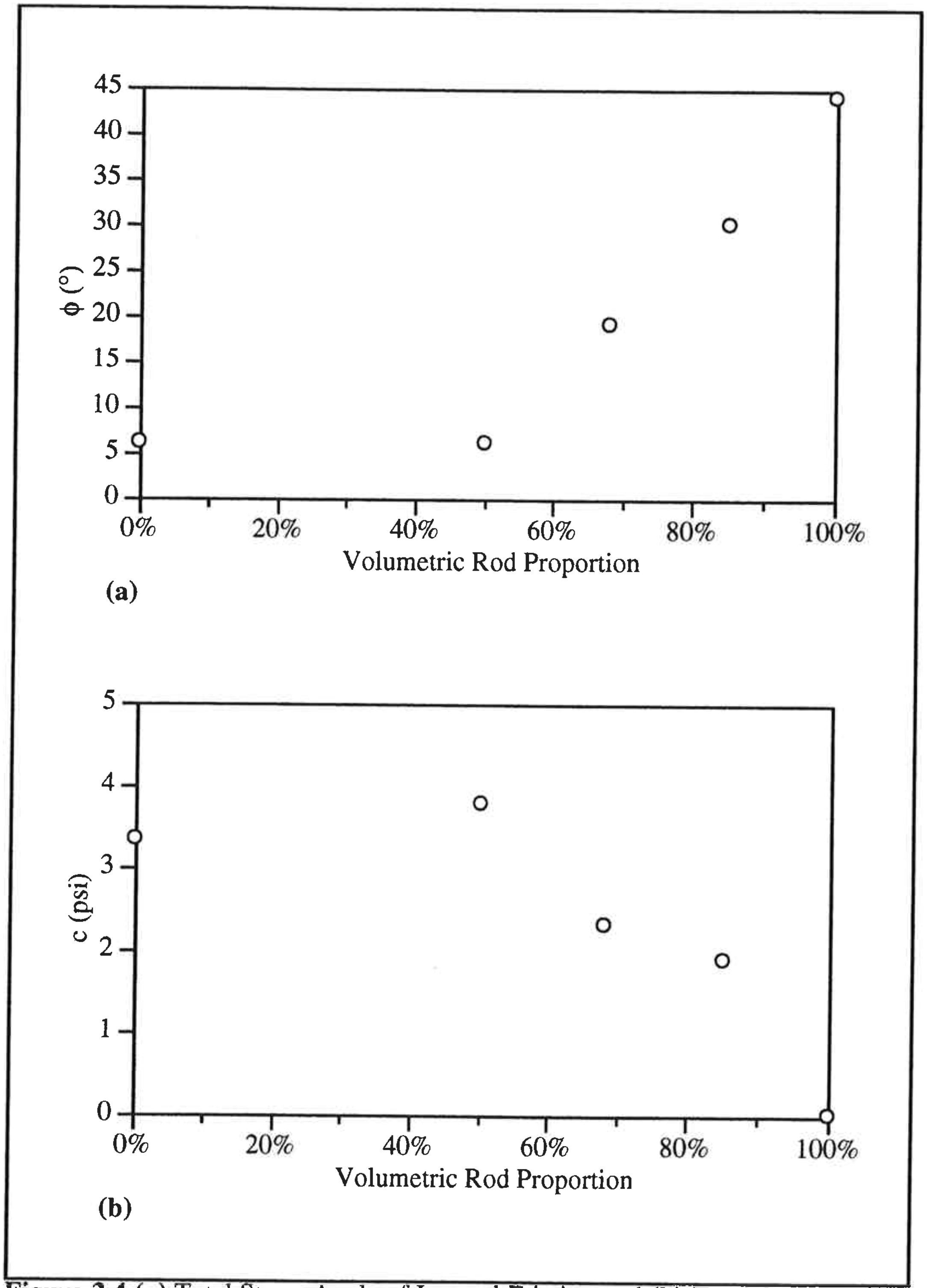

Figure 2.4 **(a)** Total Stress Angle of Internal Friction and **(b)** Total Stress Cohesion versus Volumetric Rod Proportion (after West, 1992)

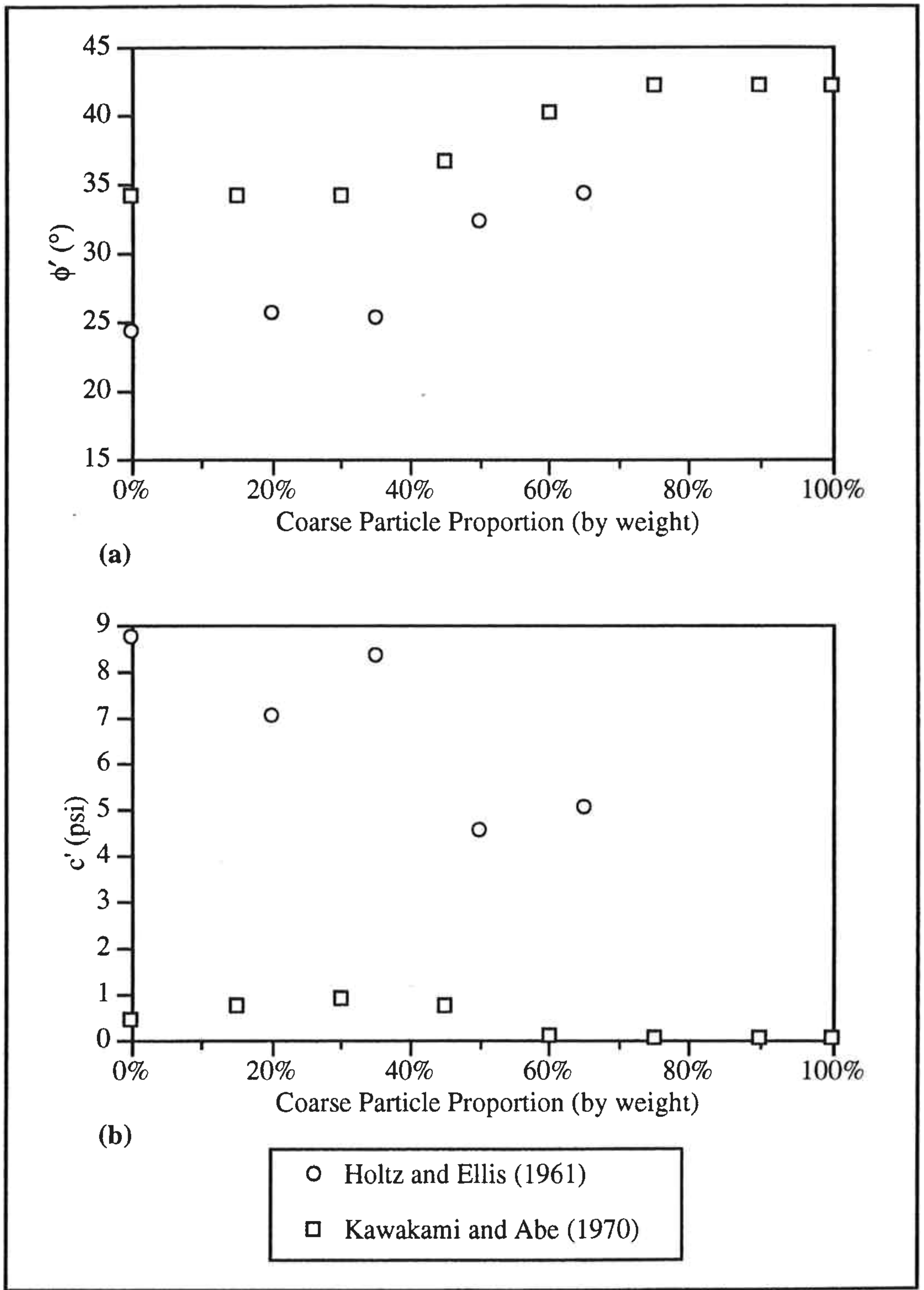

Figure 2.5 **(a)** Effective Stress Angle of Internal Friction and **(b)** Effective Stress Cohesion versus Coarse Particle Proportion (Clay Matrix)

of the total stress angles of internal friction. Figure 2.5(b) shows that in both studies the effective stress cohesion generally decreased with increasing coarse particle proportion.

Borowicka (1965), Kenney (1977) and Lupini et al. (1981) investigated how granular particles affected the residual angle of internal friction for clays. All three studies found that the residual angle of internal friction increased only above a threshold coarse particle proportion, as was the case for the peak strength parameters discussed above. Lupini et al. (1981) suggested that an increase in angle of internal friction actually occurred before the coarse particle proportion was high enough to result in particle to particle contact. They hypothesized that the increased shear resistance was the result of the coarse particles preventing the clay particles from aligning to form thin shear zones.

Different measures of strength were reported by Patwardhan et al. (1970) and Shakoor and Cook (1990). Patwardhan et al. (1970) employed a large direct shear apparatus to test mixtures of cobbles and clay. Figure 2.6 shows that the shear resistance of the cobble-clay mixtures (a combination of cohesion and friction) increased slowly at first and then more rapidly at higher cobble proportions. Once again, the data indicate that there was a threshold coarse particle proportion at which the more rapid increase began. Shakoor and Cook (1990) studied the effect of gravel content on the unconfined compressive strength of mixtures of clay and gravel. Figure 2.7 shows that the unconfined compressive strength decreased with increasing gravel content. This drop in unconfined compressive strength is somewhat similar to that exhibited by concrete as discussed in the previous section.

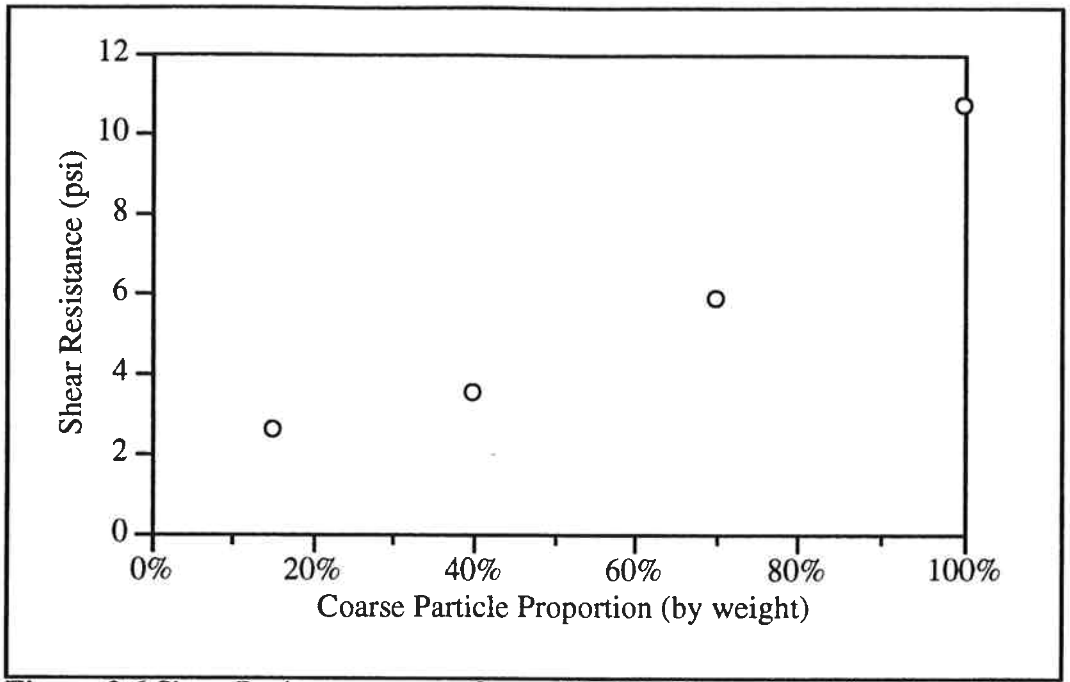

Figure 2.6 Shear Resistance versus Coarse Particle Proportion (after Patwardhan et al., 1970)

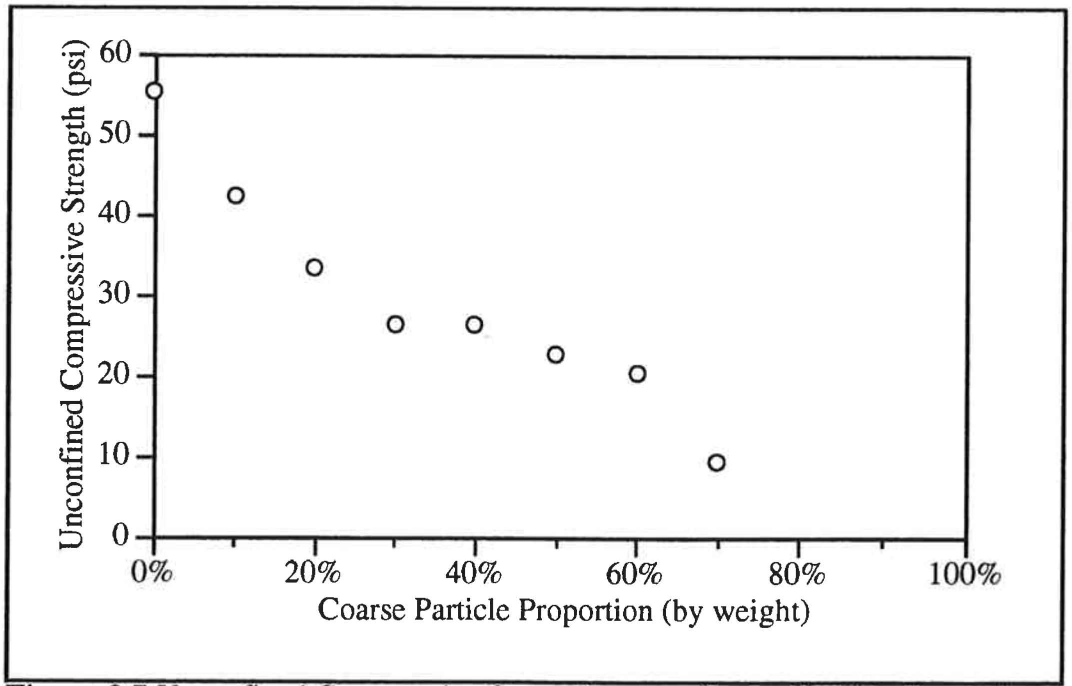

Figure 2.7 Unconfined Compressive Strength versus Coarse Particle Proportion (after Shakoor and Cook, 1990)

Many of the authors reported that the soils they tested became stiffer and more dilatant at higher coarse particle proportions. Just as for the strength behavior, increased stiffness and dilatancy were realized only at coarse particle proportions above some threshold value.

In general, the type and amount of clay in the matrix will affect the threshold at which the strength and deformation changes of a heterogeneous soil initiate. In addition, the gradation and shape of the coarse particles will also play an important role. If, for instance, the coarse particles in a heterogeneous soil are well graded, a very high coarse particle proportion can be achieved before particle to particle contact will occur. These factors were discussed in significant detail by West (1992).

Clayless matrix studies

Those studies which fall into this category are Holtz and Gibbs (1956), Doddiah et al. (1969), Rathee (1981), Fragazzy et al. (1992) and Irfan and Tang (1993).

Selected representative results from Holtz and Gibbs (1956), Rathee (1981) and Irfan and Tang (1993) are plotted in Figure 2.8. These results show that the effective stress angle of internal friction increased with increasing proportions of coarse particles. This increase was rather small for all the soils except for those tested by Irfan and Tang (1993). The reason why the results from Irfan and Tang (1993) were so different is not clear. Unlike the results for a heterogeneous soil having a clay matrix, with a sand matrix there does not appear to be a threshold coarse particle proportion that must be reached before the angle of internal friction increases. The results (not graphed) reported by Doddiah et al. (1969) further support this type of increase. Irfan and Tang (1993) provided

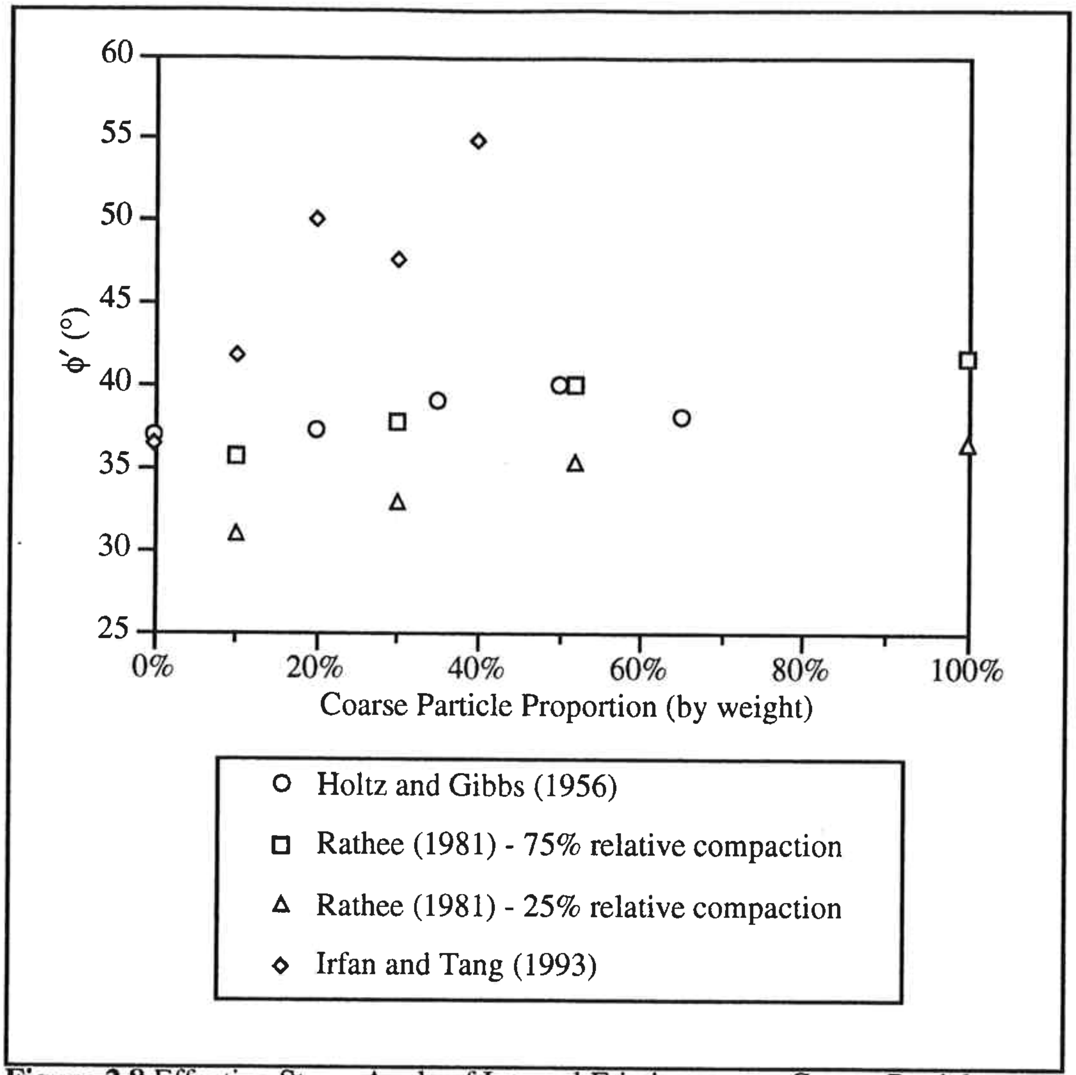

Figure 2.8 Effective Stress Angle of Internal Friction versus Coarse Particle Proportion (Clayless Matrix)

further evidence for increased angles of internal friction with increasing coarse particle content through back-calculations of cut slopes in colluvium and some simple numerical modeling of block-in-matrix slopes. Irfan and Tang (1993) also reported that the shear modulus of their soil increased with increasing coarse particle content.

These results are directly contradicted by the findings of Fragazzy et al. (1992). Fragazzy et al. (1992) ran consolidated drained triaxial tests on mixtures of subrounded-to-rounded gravel floating in a finer grained sand matrix. They found that the gravel had no effect on the strength and deformation properties of the soil as long as the far-field matrix densities (i.e. the density of the matrix away from the coarse particles) were the same in both the pure sand and gravel-sand mixtures. An explanation for why the mixtures were unaffected may be that the angle of internal friction of the gravel used was very close to that of the sand matrix. Whether this was the case is unclear because Fragazzy et al. (1992) never tested mixtures with large gravel proportions.

In almost all of the studies reported, samples were prepared to some standard relative compaction or relative density. One result of this sample preparation method was that increasing the coarse particle proportion generally decreased the average matrix density. The mechanical properties of the matrix were therefore not constant for different coarse particle proportions; in particular, the matrix strength and stiffness most likely decreased at higher coarse particle proportions due to the decreased matrix densities. Only Patwardhan et al. (1970), West (1992), Fragazzy et al. (1992) and Irfan and Tang (1993) prepared samples with similar matrix densities. Despite this point, the following conclusions regarding the strength and deformation properties of heterogeneous soils can be drawn from the previous discussion:

1. The total and effective stress angles of internal friction increase with increasing coarse particle proportion. For materials with clay matrixes this increase is only realized beyond some threshold proportion of coarse particles. Below this threshold a heterogeneous soil behaves essentially as its clay matrix. These increases most likely reflect the observation that the presence of coarse particles increases the tortuousity or thickness of shear surfaces. Direct coarse particle contact will definitely result in an increase at very high coarse particle

proportions. On the other hand, an increase appears to occur immediately in heterogeneous soils with clayless matrixes.

The only specific recommendation as to the magnitude of this increase, found in the literature, was made by Irfan and Tang (1993). They recommended that for colluvium the effective stress angle of internal friction can be assumed to: (1) increase 4° for every 10 percent increase in coarse particle proportion for coarse particle proportions between 25 and 60 percent; (2) be the same as the angle of internal friction of the matrix for coarse particle proportions less than 25 percent; and (3) undergo no further increase above a coarse particle proportion of 60 percent.

2. Cohesion generally decreases with increasing coarse particle proportion. Once again, this decrease only begins above some threshold coarse particle proportion.

3. Data suggest that the stiffness of a heterogeneous soils increases with increasing coarse particle proportion.

2.2.4 Others

Many composites consist of stronger inclusions in a weaker matrix. No studies relating the shear strength of composites and inclusion proportion have been located. Many of the same theoretical models that can be used to predict the elastic modulus of concrete can and have been used to predict the elastic moduli of various composites.

2.3 Conclusions

Based on the aforementioned studies, some predictions regarding the effect of block proportion on the stiffness and shear strength of a melange are:

1. An increase in the block proportion will result in a higher angle of internal friction. At lower block proportions it is postulated that this increase will be due to the blocks increasing the tortuousity or thickness of the shear failure surface, and at high block proportions there will be an increase once block to block contact is realized.

2. There is conflicting evidence as to how the cohesion will be affected by block proportion. As stated previously, Savely (1990) suggested that the cohesion of a conglomerate matrix should be assumed to be that of the mass. On the other hand, the literature on heterogeneous soils supports a cohesion decrease. The advice offered by the literature is therefore inconsistent with respect to how cohesion will be affected by block proportion.

3. An increase in the block proportion will result in greater mass stiffness. The literature on portland cement concrete provides the best evidence for increased stiffness.

The physical model study discussed in the following chapters was used to confirm these hypotheses and provide practical guidance for predicting the properties of a melange.

CHAPTER 3

PHYSICAL MODEL FABRICATION AND TESTING

3.1 Introduction

Six-inch diameter cylindrical specimens of model melange were fabricated and tested in triaxial compression to determine their Mohr-Coulomb strength parameters and stress-strain behavior. This section outlines all of the facets of this test program, from the decision on appropriate model materials to a description of the triaxial testing equipment.

3.2 General Model Characteristics

An attempt was made to retain sufficient characteristics of Franciscan melange so the principles gained from the model test results could be applied with some confidence to the Franciscan, but at the same time to keep the model general enough so that these same concepts could be applied to other melanges around the world. The variables considered were limited to those which are reasonably obtainable in the field. In this light, the pertinent melange features that were preserved in the physical models are discussed below.

As mentioned in Chapter 1, Franciscan melange has a fabric due to both block alignment and prevalent shearing around the blocks. This is an important structural characteristic because anisotropic rock has particularly strong directionalism with respect to strength (Jaeger, 1960 and Donath, 1964). For instance, Gostelow and Loucaides (1988) found that their shear strength test results on a scaly foliated clay were widely scattered due to an anisotropic rock fabric. A.G.I. (1985) also reported that strength tests on a sheared shale matrix material resulted in widely scattered results due to the presence of shears oriented in different directions in different samples. The physical models used in this research therefore needed to incorporate oriented blocks and mock shearing.

The block shapes in the models needed to be similar to those in the field. Model block shape therefore ranged from lenticular to tabular and round to elongate. The ratio of maximum axial dimension to minimum axial dimension for all block sizes was 2 to 3.

In order to find a proper block size distribution for the model melange, I made block measurements at a number of Franciscan melange outcrops along the California coast. I found very roughly that for every 1 block with maximum dimension x to 2x there were 4 blocks with maximum dimension 1/2x to x and so on. This basic block size distribution was applied to the models. For example, if there were 5 blocks in the 3 to 6-inch range in the model, there were 20 in the 1 1/2 to 3-inch range and 80 in the 3/4 to 1 1/2-inch range.

As mentioned in the Introduction, there are blocks of a wide range of sizes in melange. The largest blocks in a melange mass are often of quite significant size relative to the volume of interest. For this reason, the maximum block size in the model was not limited to one sixth the specimen diameter, which is the guideline typically followed in soils testing. Particles with maximum dimensions as large as about 3/4 the specimen diameter (i.e. about 4 1/2 inches) were incorporated in the models. The smallest block size was approximately 1/4 inch. The fact that the largest block's size was quite significant in comparison to the specimen size could have resulted in what West (1992) referred to as "small scale behavior." The large blocks could potentially dominate the strength and deformability of a mass depending on their exact location. "Small scale behavior" would be indicated if test results were nonrepeatable (i.e. there was a wide variability in the stress-strain behavior and strength results for supposedly similar models). If the test results were nonrepeatable, interpretation of the results would have been difficult. It was determined early in the test program that, although the maximum block size was quite significant relative to the specimen size, the test results were repeatable and therefore "small scale behavior" was not indicated.

The strength of Franciscan melange matrix is variable depending particularly on the degree to which it is sheared. In general, though, it is considered a weak rock. The matrix material was therefore designed to have properties typical of a weak rock. Blocks, on the other hand, can range from being highly fractured, relatively weak rock to extremely strong competent rock. In order to keep the test results as tractable as possible, the blocks used in the model melange were only of one strength. The ratio of block to matrix strength was made significant yet not overwhelming. This was done so that it could be checked whether or not a failure surface would pass through the blocks or skirt the edges of the blocks. If the strength ratio was made too large, the latter would have been the only possibility.

3.3 Modeling Materials

Cemented soils were chosen as the materials to model both the block and matrix components. A sand-cement mixture was used for the blocks and a clay-cement mixture for the matrix. Plaster and portland cement mixed with soils have been used extensively to simulate rock in physical models, therefore these were the two cementing agents considered for use. It was discovered early in this research that many plasters harden quite quickly (some even in a matter of minutes) allowing insufficient time to form the blocks, as described in the next section. On the other hand, the setting time for portland cement is much longer. Accordingly, portland cement was chosen as the cementing agent. The soils used were Monterey #60 sand for the blocks and western-grade bentonite for the matrix. Monterey #60 is a fine, uniformly graded sand often used for sand-blasting. Western-grade bentonite is commonly used for slurry walls and a variety of industrial applications.

To meet the strength criteria set out in the previous section, a number of trial batches of block and matrix material were prepared. It proved to be quite difficult to produce blocks of desirable strength that retained sufficient brittleness. This problem was overcome by replacing a very large proportion of the portland cement in a mix with Class C (ASTM C 618) fly ash. The fly ash produced a weaker yet still brittle material. A second difficulty was preventing an inordinate number of shrinkage cracks from forming in the matrix material upon drying. To overcome this problem the proportion of portland cement to bentonite had to be quite high. The final material proportions are given in the table below.

Table 3.1 Material Proportions for Model Components

Matrix		Block	
Material	Parts by Weight	Material	Parts by Weight
cement	20	sand	70
bentonite	4	fly ash	35
water	17	cement	7
		water	15

In order to model matrix shearing, various procedures were considered. Initial trials were made at physically shearing the matrix as the portland cement paste was beginning to set. This method was quickly found to be both excessively difficult and ineffective at producing shears. Focus was next placed on creating planes of weakness in the model by introducing thin layers of a weaker material into the matrix. An attempt was made using flakes of bentonite as these planes of weakness. These flakes were created by drying a thin layer of bentonite slurry in a baking pan. This approach was also quickly abandoned when it was found that the flakes were so flimsy that they tended to completely break down when incorporated into the matrix. Also, creating the large number of layers needed for the models simply would have taken too long due to the limited oven space available for drying. Thin layers of wax were next considered and quickly became the material of choice. Layers of wax could be created in large numbers relatively quickly (this process is discussed in the next section), and they were strong enough to be placed in the models without breaking down. In trial tests it was found that these layers served their purpose as planes of weakness quite well. During additional trials one further problem was discovered; the friction between the wax and the bentonite-portland cement matrix was too high. To reduce this friction, the wax layers were coated with talcum powder as they cooled.

Although not sheared, the bond at the contact between the block and matrix in the model was expected to be weak because portland cement was used as the bonding agent. This weakness zone was anticipated due to the presence of a "transition zone" as discussed in the previous chapter's section on concrete.

The relevant mechanical properties of these materials are presented in Chapter 4.

3.4 Types and Numbers of Specimens

Using the aforementioned modeling materials, cylindrical specimens with different block proportions and block orientations were created. The variety of specimen types are illustrated schematically in Figure 3.1. Specimens with four different block orientations, each with three block proportions, were fabricated, in addition to the pure matrix and pure block specimens. The arrows in the diagram indicate the axial loading direction. A group of specimens with similar block proportions and the same block orientation are identified as x-#, where x is l, m or h depending on whether the specimens were of low (l - 27 to 36 percent), medium (m - 49 to 61 percent) or high (h - 70 to 76 percent) block proportion and the # is the angle between the axial loading direction and the orientation in which the blocks were aligned (either 0, 30, 60 or 90 degrees). Individual specimens have an additional identifying number (i.e. they are identified as x-#-#). The additional # is the confining stress (in psi) at which the specimen was tested. Matrix specimens are identified as matrix-# and block specimens are identified as block-# where the # is the confining stress (in psi).

Five specimens of each type, along with seven pure matrix and ten pure block specimens were created. This means a total of 67 six-inch diameter (matrix and block-in-matrix) specimens and 10 two-inch diameter (block) specimens were tested for this study. These numbers do not include all of the trial mixes required to finalize the model materials and specimen preparation methods. In total, over 100 six-inch diameter and 80 two-inch diameter specimens were tested.

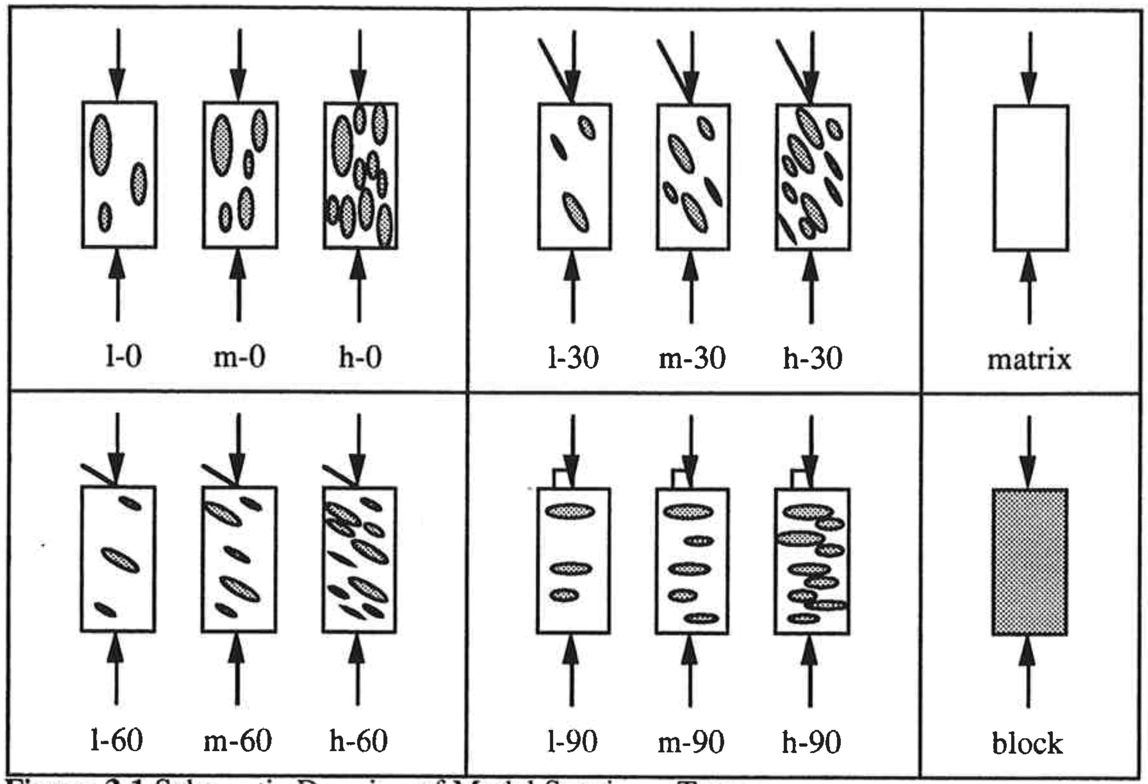

Figure 3.1 Schematic Drawing of Model Specimen Types

3.5 Specimen Fabrication

The method by which the model melange specimens were fabricated is outlined in this section. The steps in the fabrication process were:

1. Creating thin layers of wax coated with talc -

The wax was melted in a small beaker placed on a heating element. A steel plate was then warmed on the heating element. Melted wax was poured on the steel plate to uniform thickness of about 0.03 inches. Heating the steel plate in a uniform manner was very important for achieving this uniform thickness. The wax was allowed to cool (two to three minutes) until it was semi-solid. The plate was then placed back on the heating element for five to ten seconds so that an extremely thin layer of melted wax would form at the wax-steel interface. This allowed the semi-solid wax to be peeled off the plate. The warm wax was placed in a baking dish filled with talcum powder and coated on both sides. Two steel plates were employed concurrently. Figure 3.2 shows a resultant layer and a broken layer (see step 4).

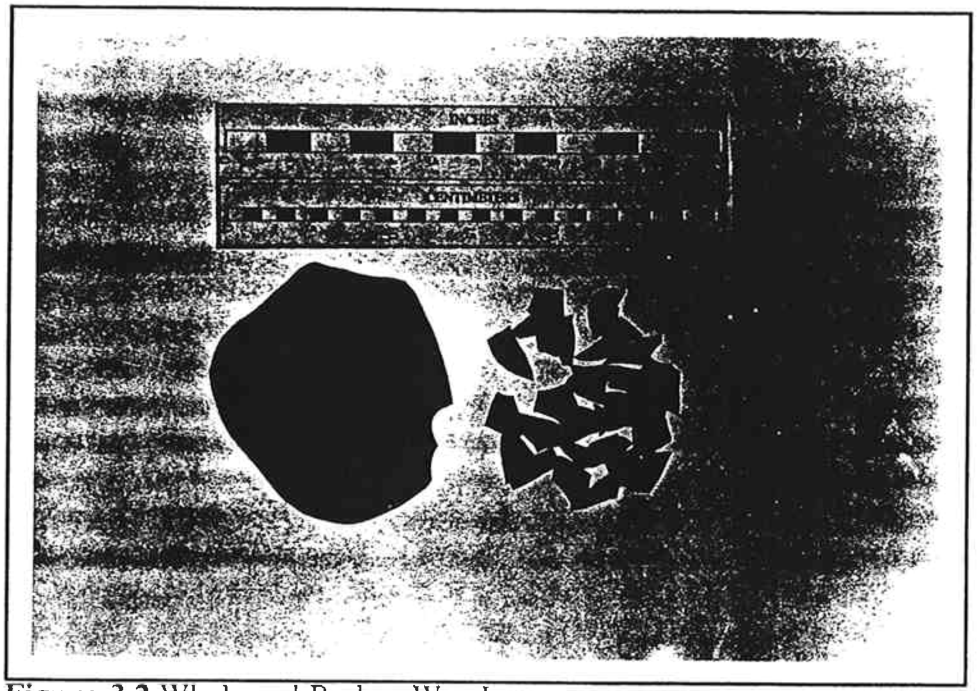

Figure 3.2 Whole and Broken Wax Layers

2. Molding the blocks-

The sand, fly ash, portland cement and water mixture was well combined using an electric rotary mixer. The larger blocks (those larger than one inch in maximum dimension) were formed using styrofoam molds (Figure 3.3). These molds were lined with plastic wrap to ease block removal. The forms were filled with enough of the sand mixture to create a rounded top to each block. Blocks smaller than one inch were formed by hand and placed on pieces of plywood covered with plastic wrap. Before being transferred to a fog room (73° F, 100% relative humidity) for curing, the blocks were covered with another piece of plastic wrap. Some blocks of various sizes and shapes are shown in Figure 3.4.

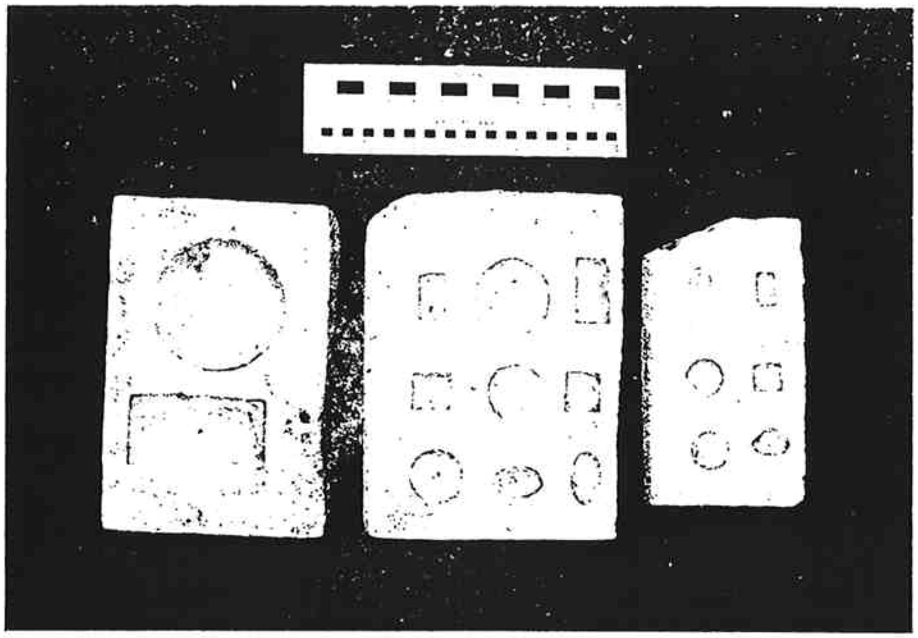

Figure 3.3 Styrofoam Block Molds

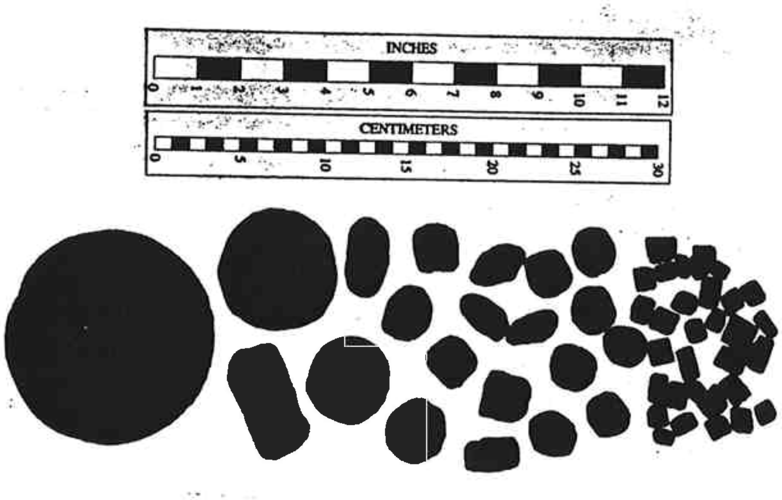

Figure 3.4 Various Blocks

3. Preparing the blocks for inclusion in the model melange-

After curing the blocks for about 24 hours they were unmolded. The proper weight of blocks was then grouped for either a low, medium or high block proportion specimen. These blocks were then placed in a bucket of water to remove any loose sand and to saturate the blocks. Typically the blocks would remain in the water for about one hour. The blocks were removed from the water and their surfaces patted dry so that they were in approximately saturated surface dry (SSD) condition. The blocks were prepared to this condition so they would not tend to add or remove water from the freshly mixed matrix material.

4. Preparing the wax for inclusion in the model melange-

The proper amount of wax for either a low, medium or high block proportion specimen was weighed. These layers were then broken down to much smaller flakes (approximately one inch in maximum dimension for the most part - see Figure 3.2).

5. Fabricating a block of model melange-

The matrix materials (bentonite, portland cement and water) were well combined in an electric rotary mixer. The wooden form (Figure 3.5), in which two blocks of physical model melange were fabricated, was coated with oil to ease block removal. Each block was about 13 inches long by 7 inches wide by 7 inches deep. The matrix, blocks and wax were combined as follows: some of the matrix was added to the form followed by some of the wax layers and some of the blocks. The largest blocks (those with maximum dimensions of greater than 1 1/2 inches) were aligned to create the fabric discussed previously. The smaller blocks and the wax layers naturally tended to align themselves with the edges of the larger blocks. This process continued until the form was filled and all the wax and blocks were incorporated. Because the blocks were denser than the matrix, moving the form would have caused the blocks to sink to the bottom of the block. Due to this problem, the fabrication was done in the fog room so that the specimen would not have to be moved until the matrix material had set.

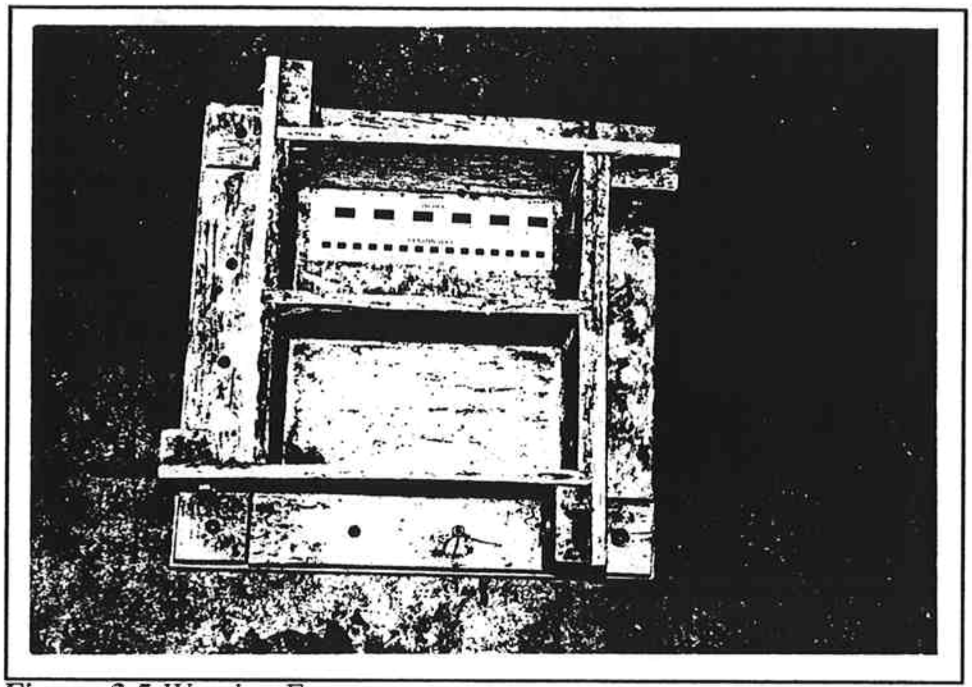

Figure 3.5 Wooden Form

6. Unmolding the melange block-

The formwork was removed from the melange block approximately 24 hours after the block was poured. The block was then returned to the fog room for an additional 6 days.

7. Preparing the test specimen (coring, cutting, surfacing)-

After the 7 day moist cure the block was cored using a hydraulically driven drill press (Figure 3.6) with a six-inch core barrel. The ends of the specimen were then rough cut with a diamond saw (Figure 3.7). Next the ends of the specimen were ground smooth and perpendicular to the specimen's longitudinal axis using a milling machine equipped with a diamond cutting wheel (Figure 3.8).

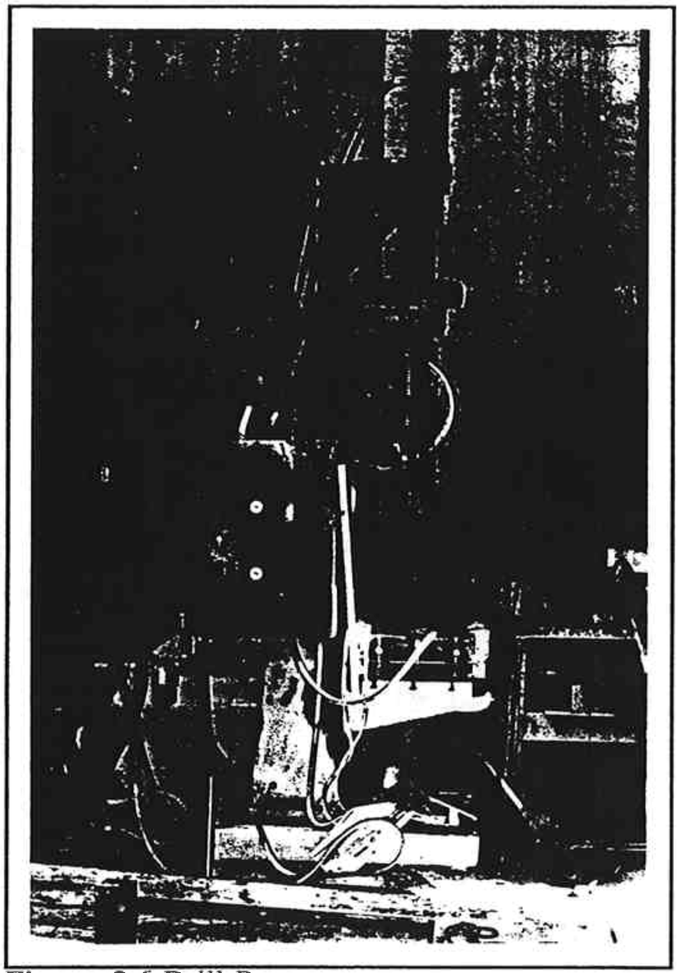

Figure 3.6 Drill Press

8. Drying the specimen-

The specimen was then placed in another room to dry. The room was maintained at a constant 75° F and a relative humidity of 50±10%. The specimen remained in this room for 6 days. On the seventh day of drying the specimen was moved to a room maintained at 100° F and a relative humidity of less than 30%. The specimen was tested the following day after being allowed to cool to room temperature.

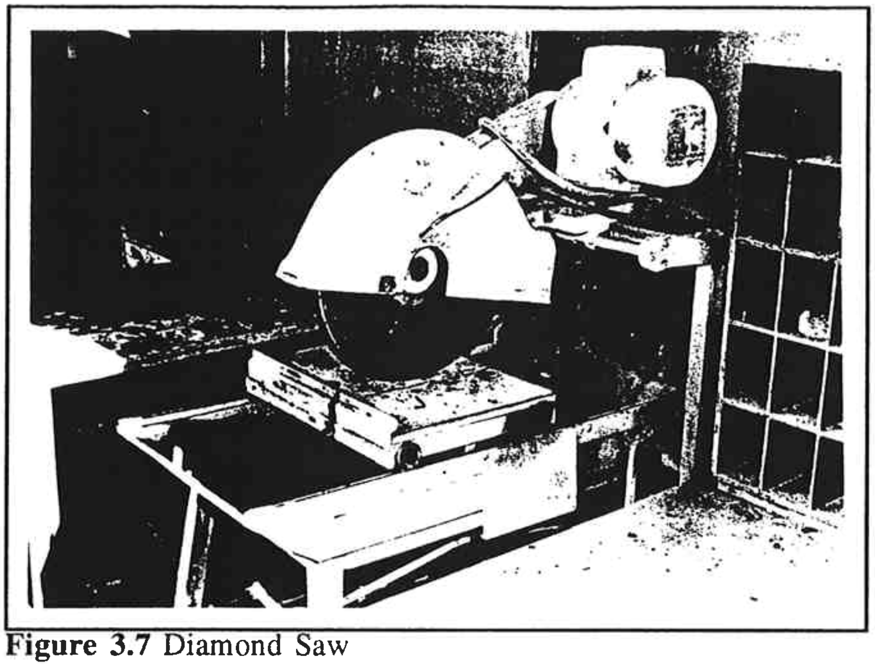

Figure 3.7 Diamond Saw

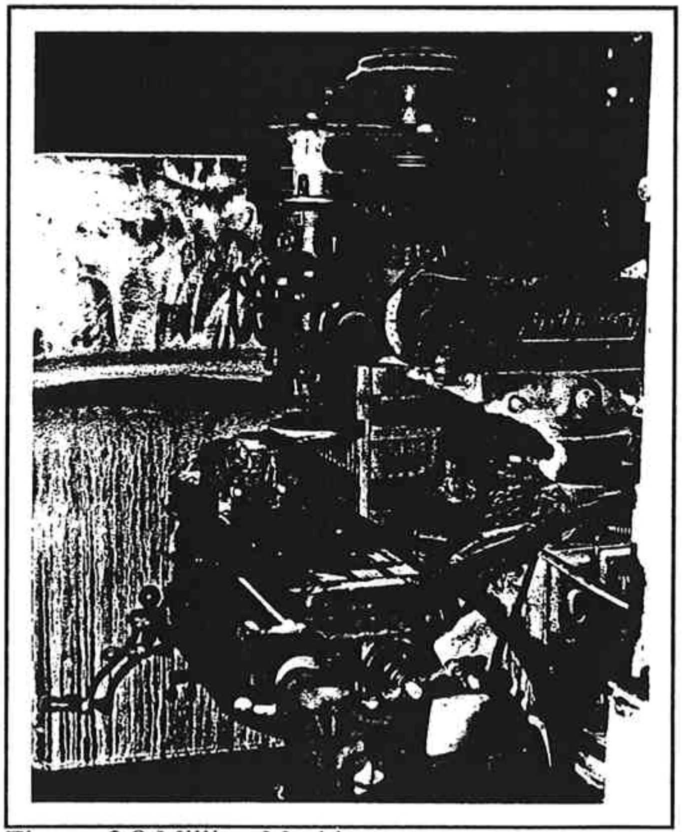

Figure 3.8 Milling Machine

The pure matrix specimens were prepared by the same steps except no blocks were added as the matrix was poured. The pure block specimens were cast as a block from which two-inch diameter specimens were cored.

3.6 Fabrication and Testing Schedule

A typical week of specimen preparation and testing is outlined below.

Monday

1. mixed the block material and molded the blocks for the two model melange specimens that would be poured Tuesday
2. created a sufficient number of wax layers for the week's specimens

Tuesday, Wednesday, Thursday and Friday

1. unmolded the blocks that had been prepared the previous day
2. proportioned the blocks for the two model melange specimens and placed the blocks in buckets of water
3. unmolded the two model melange specimens that had been prepared the previous day (Wednesday, Thursday and Friday)
4. mixed the block material and molded the blocks for the two model melange specimens that would be poured the next day (Tuesday, Wednesday and Thursday)
5. proportioned the wax for the two model melange blocks
6. removed the blocks from the water and dried their surfaces
7. cleaned and oiled the wooden form
8. mixed the matrix material

9. combined the matrix material, blocks and wax layers to create two model melange specimens
10. tested the two model melange specimens that had been prepared two weeks previously in triaxial compression
11. cored, cut and surfaced the two model melange specimens that had been prepared the previous week

Saturday
1. unmolded the two model melange specimens that had been prepared the previous day

In addition to these tasks, specimens were moved to different curing environments on proper days.

Using this schedule 8 specimens could be prepared and tested each week. The specimen preparation and testing of the final models ended up taking 11 weeks of intensive labor.

3.7 Triaxial Testing Procedure

Tests were carried out in accordance with the ISRM "Suggested Methods for Determining the Strength of Rock Materials in Triaxial Compression" (Vogler and Kovari, 1981). Testing involved the following steps:

1. inserting the specimen into the triaxial cell
2. applying a small confining stress to hold the specimen in the cell
3. placing the cell in the loading frame

4. increasing the confining stress and axial stress simultaneously so that the specimen remained under essentially hydrostatic compression until the desired confining stress was reached
5. starting data acquisition
6. increasing the axial load so that failure would occur within 5-15 minutes
7. continuing axial deformation until "residual" strength was reached
8. unloading and removing the failed specimen from the cell

The testing equipment employed is described briefly in the following section.

3.8 Testing Equipment

3.8.1 Hoek Triaxial Cell

One two-inch diameter and one six-inch diameter Hoek cell (Hoek and Franklin, 1968) were used during triaxial testing. Both cells were manufactured by Roctest, Inc. Figure 3.9 is a schematic drawing of a typical Hoek cell and Figure 3.10 is a photograph of the two-inch and six-inch cells. As the schematic shows, the cell itself is essentially made up of two parts - a mild steel body (consisting of a cylinder and two threaded end caps) and a polyurethane rubber sleeve. The hydraulic fluid used to provide confining stress is prevented from contacting the specimen by the rubber sleeve. The hydraulic fluid is maintained between the cell body and the rubber sleeve at all times (except when sleeve replacement is necessary). Unlike other triaxial cells it is therefore not necessary to drain the hydraulic fluid after each test in order to remove a failed specimen and insert a new one. This feature greatly reduces the time required to run a triaxial test.

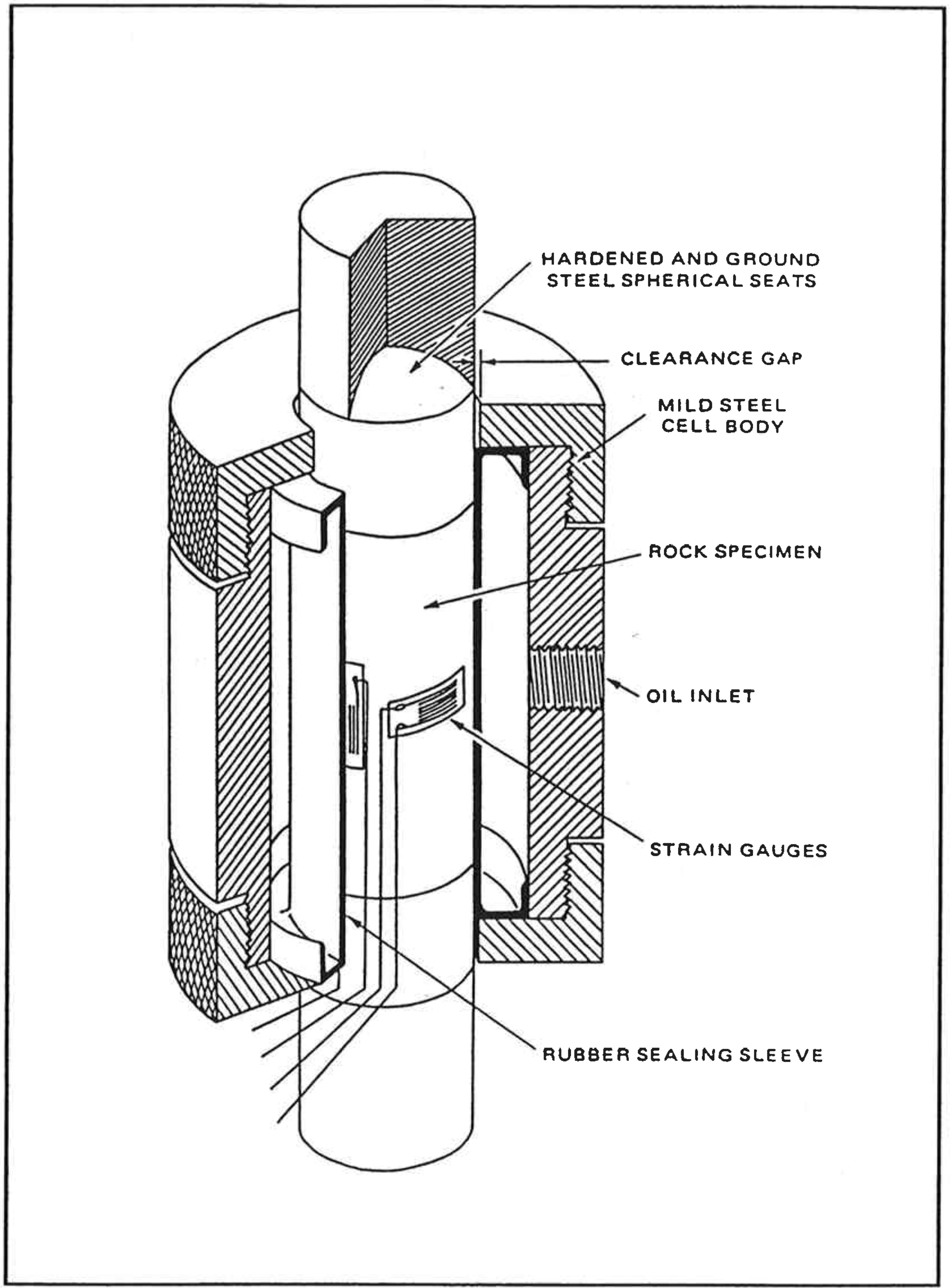

Figure 3.9 Schematic Drawing of a Hoek Triaxial Cell (after Roctest, 1991)

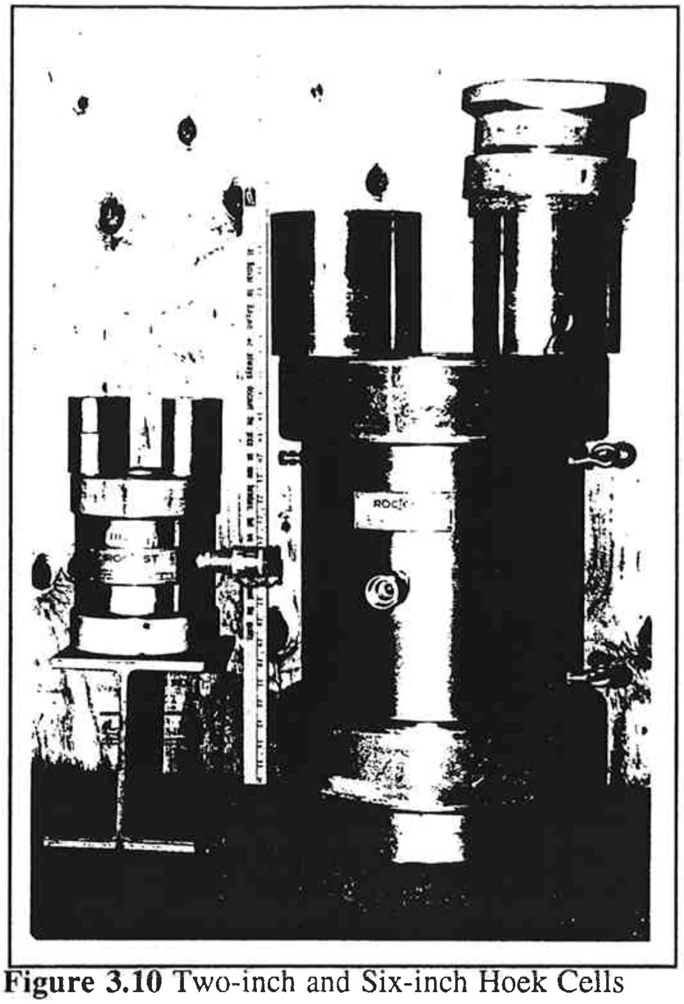

Figure 3.10 Two-inch and Six-inch Hoek Cells

3.8.2 Loading Frame and Testing Machine

Figure 3.11 is the Riehle Model FS-160 screw-powered testing machine that was used to axially load the model specimens. The load capacity of this machine is 160,000 pounds. It is important to note that the stiffness of this reaction frame is greater than the slope of the post-peak portion of the complete stress-strain curve for the specimens tested in this research, therefore post-peak stress-strain behavior could easily be observed.

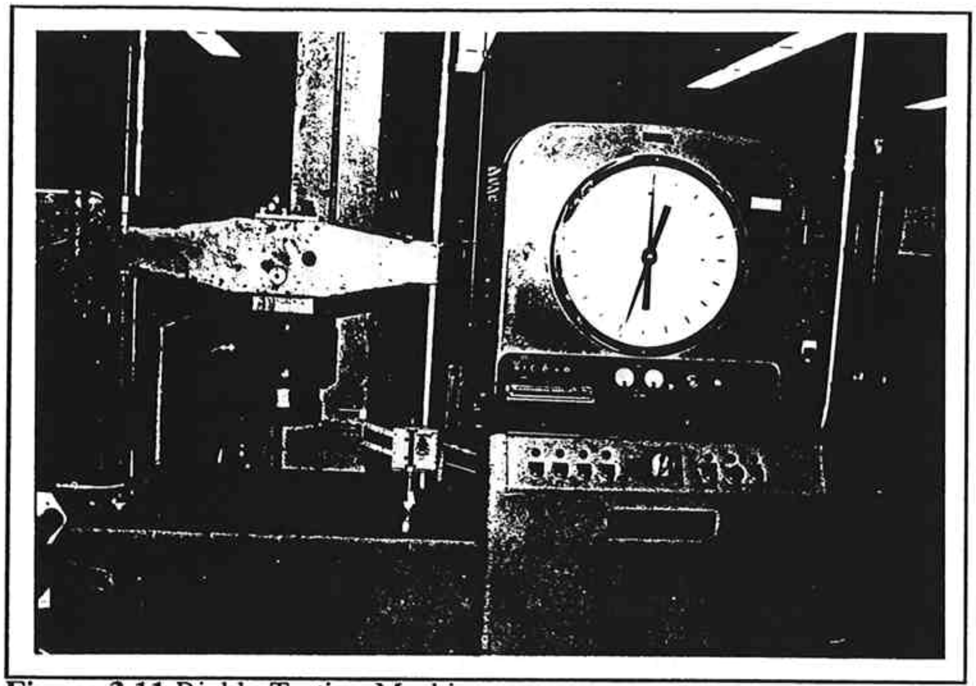

Figure 3.11 Riehle Testing Machine

3.8.3 Hydraulic Equipment

Confining pressures were applied and maintained using an Enerpac P39 hand pump and a High Pressure Equipment Co. screw pump (Figure 3.12). The Enerpac pump was used to make coarse changes in the pressure and fine adjustments were made using the screw pump. This system allowed the confining stress to be maintained within 2% of its desired value throughout each test.

3.8.4 Data Acquisition

Three variables were measured and recorded during testing; the axial load, the confining pressure and the upper loading platen's vertical displacement. The upper platen's

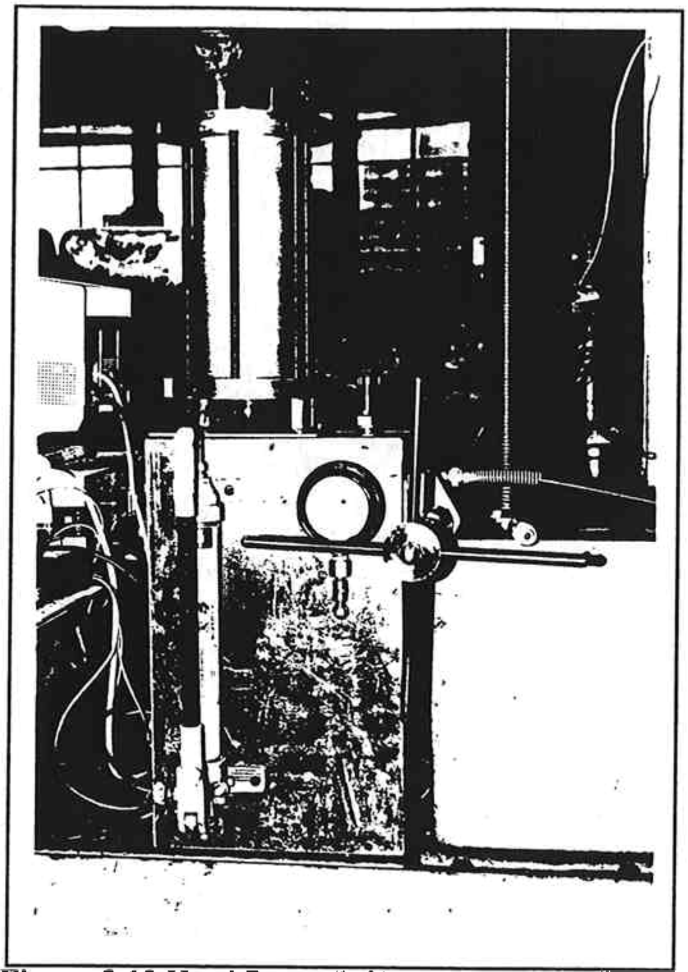

Figure 3.12 Hand Pump (left) and Screw Pump (right)

vertical displacement was a very close approximation of the specimen's axial deformation.

The axial load was measured using an Interface model 1240AF 200,000 pound load cell. A variable reluctance pressure transducer manufactured by Validyne Engineering Corporation (model DP303-64) was used to measure the confining pressure. The vertical displacement of the upper platen was tracked with a Riehle Model DU-5 Universal Measuring Instrument (i.e. essentially a linear variable differential transformer (LVDT) connected to a measuring arm). Figure 3.13 shows the Universal Measuring Instrument in position with its extension arm against the upper platen.

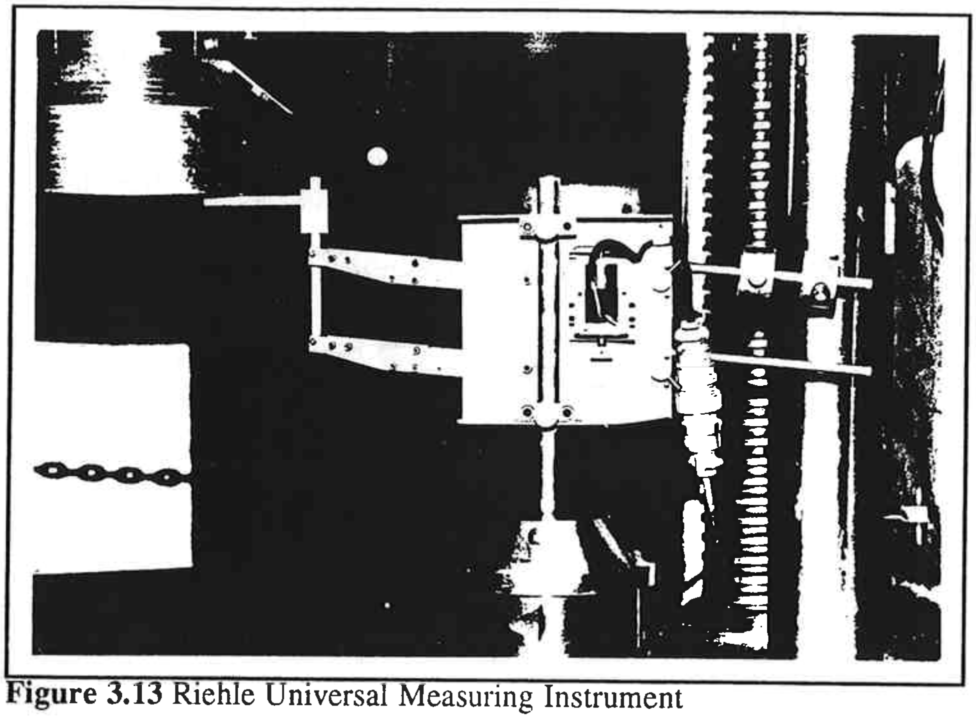

Figure 3.13 Riehle Universal Measuring Instrument

A Validyne CD19A Carrier Demodulator provided transducer excitation and amplified and demodulated the output from the load cell, pressure transducer and Universal Measuring Instrument. A Validyne MC1-10 case accommodated the three CD19A plug-in modules as shown in Photo 3.14. The module shown at the far right in the MC1-10 case is a Validyne PM212-2 Plug-in Digital Panel Meter which could be used to monitor the voltage output of any of the carrier demodulators.

A Computer Boards Incorporated CIO-AD16 expansion board converted the analog (voltage) outputs from the carrier demodulators to digital signals allowing the voltages to be monitored by an Everex 386 25 MHz computer. Data were recorded using Quinn-Curtis Software's Lablog2.

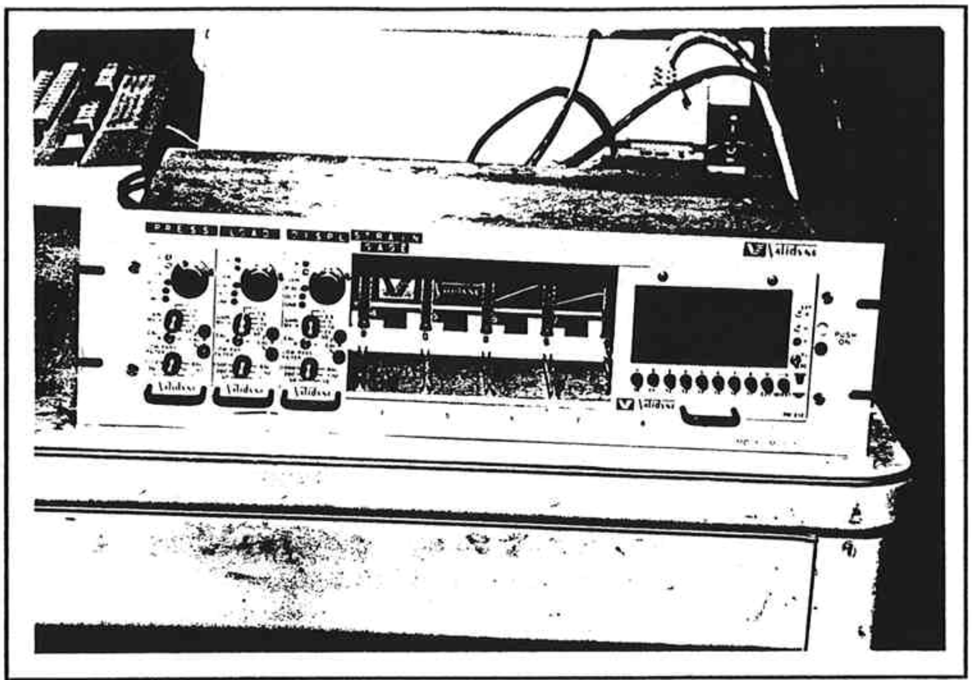

Figure 3.14 Validyne MC1-10 Case Containing Carrier Demodulators and Voltage Meter

CHAPTER 4

PHYSICAL MODEL TEST RESULTS

This section presents the results of the triaxial compression tests on the physical models described in the previous section. More detailed discussion and analysis of these results are reserved until Chapter 5.

As discussed in the previous chapter, it was checked whether the presence of blocks that were large relative to the sample size resulted in "small scale behavior." Tests were reasonably repeatable (stress-strain behavior and strength were fairly consistent); therefore, it is not believed that "small scale behavior" was occurring. Hence, test result interpretation will not be a problem.

4.1 Stress-Strain Behavior

Appendix B contains the complete stress-strain curves for all 77 triaxial tests. Two characteristic values measured from each of these curves, the modulus of deformation and the axial strain at failure are reported in the following sections.

4.1.1 Modulus of Deformation

The modulus of deformation is defined in this study as the slope of a line drawn from the origin of the stress-strain curve to the point on the virgin loading curve corresponding to 40 percent of the maximum stress difference ($(\sigma_1\text{-}\sigma_3)_{max}$). This measure is typically called the secant modulus (Mehta and Monteiro, 1993). The term modulus of deformation is used rather than the modulus of elasticity because during virgin loading the model specimens underwent both recoverable (elastic) and nonrecoverable (plastic) deformations.

Table 4.1 presents the modulus values measured from all the stress-strain curves.

4.1.1.1 Effect of Block Proportion

Figures 4.1 through 4.4 show that increasing the block proportion generally increased the modulus of deformation. Each plot is for a different block orientation as indicated by the schematic specimen sketch next to each plot. Note that the moduli values for the medium (approximately 50 percent) block proportion specimens with 0° and 30° block orientations fall below the trend set by the low and high proportion specimens. Potential explanations for this apparently anomalous behavior are discussed in Chapter 5. Note also that the rate of increase in modulus with block proportion decreased as the blocks were varied from vertical to horizontal. This fact is made clearer by the graphs presented in the next section.

4.1.1.2 Effect of Block Orientation

Figures 4.5 through 4.7 are plots of modulus of deformation versus block orientation. Figure 4.5 presents the results for the specimens with low block proportions, while Figure 4.6 is for medium and Figure 4.7 is for high block proportions. As noted in the previous section, the modulus generally decreased as the block orientation was varied from parallel to the axial loading direction (0°) to perpendicular to the axial loading direction (90°). This decrease was not strongly expressed by the specimens with medium block proportions but was quite pronounced for the high block proportion specimens.

Table 4.1 Modulus of Deformation Values

Specimen	Block Proportion	Modulus (psi)
matrix-50	0%	3.4E+5
matrix-100	0%	3.6E+5
matrix-125	0%	3.4E+5
matrix-150	0%	3.4E+5
matrix-200	0%	3.4E+5
matrix-225	0%	3.6E+5
matrix-250	0%	3.5E+5
block-0	100%	6.2E+5
block-50	100%	7.1E+5
block-75	100%	6.6E+5
block-100	100%	6.8E+5
block-125	100%	6.0E+5
block-150	100%	6.6E+5
block-175	100%	6.5E+5
block-200	100%	6.6E+5
block-225	100%	6.7E+5
block-250	100%	6.3E+5
l-0-50	28%	4.5E+5
l-0-100	30%	3.9E+5
l-0-150	29%	4.3E+5
l-0-200	31%	4.2E+5
l-0-250	28%	4.7E+5
l-30-50	29%	4.3E+5
l-30-100	32%	4.1E+5
l-30-150	34%	4.5E+5
l-30-200	31%	4.4E+5
l-30-250	31%	4.5E+5
l-60-50	31%	3.3E+5
l-60-100	36%	4.2E+5
l-60-150	33%	3.7E+5
l-60-200	33%	3.8E+5
l-60-250	32%	3.8E+5
l-90-50	29%	3.9E+5
l-90-100	29%	4.1E+5
l-90-150	28%	4.5E+5
l-90-200	32%	4.1E+5
l-90-250	27%	4.0E+5
m-0-50	52%	4.4E+5
m-0-100	50%	4.2E+5
m-0-150	50%	3.9E+5
m-0-200	49%	4.6E+5
m-0-250	49%	4.1E+5
m-30-50	54%	4.0E+5
m-30-100	53%	4.1E+5
m-30-150	53%	4.2E+5
m-30-200	53%	4.2E+5
m-30-250	53%	4.2E+5
m-60-50	53%	4.0E+5
m-60-100	56%	4.0E+5
m-60-150	54%	4.8E+5
m-60-200	55%	3.8E+5
m-60-250	53%	3.8E+5
m-90-50	61%	4.2E+5
m-90-100	54%	3.7E+5
m-90-150	57%	4.4E+5
m-90-200	60%	4.3E+5
m-90-250	56%	3.7E+5
h-0-57	71%	5.6E+5
h-0-100	73%	6.0E+5
h-0-150	72%	5.8E+5
h-0-200	72%	5.8E+5
h-0-250	72%	6.0E+5
h-30-50	75%	5.7E+5
h-30-100	74%	5.5E+5
h-30-150	73%	5.2E+5
h-30-200	74%	5.4E+5
h-30-250	76%	5.6E+5
h-60-50	73%	3.8E+5
h-60-100	75%	5.0E+5
h-60-150	71%	4.9E+5
h-60-200	74%	4.3E+5
h-60-250	73%	4.1E+5
h-90-50	70%	3.4E+5
h-90-100	70%	4.3E+5
h-90-150	71%	3.8E+5
h-90-200	71%	5.2E+5
h-90-250	72%	4.0E+5

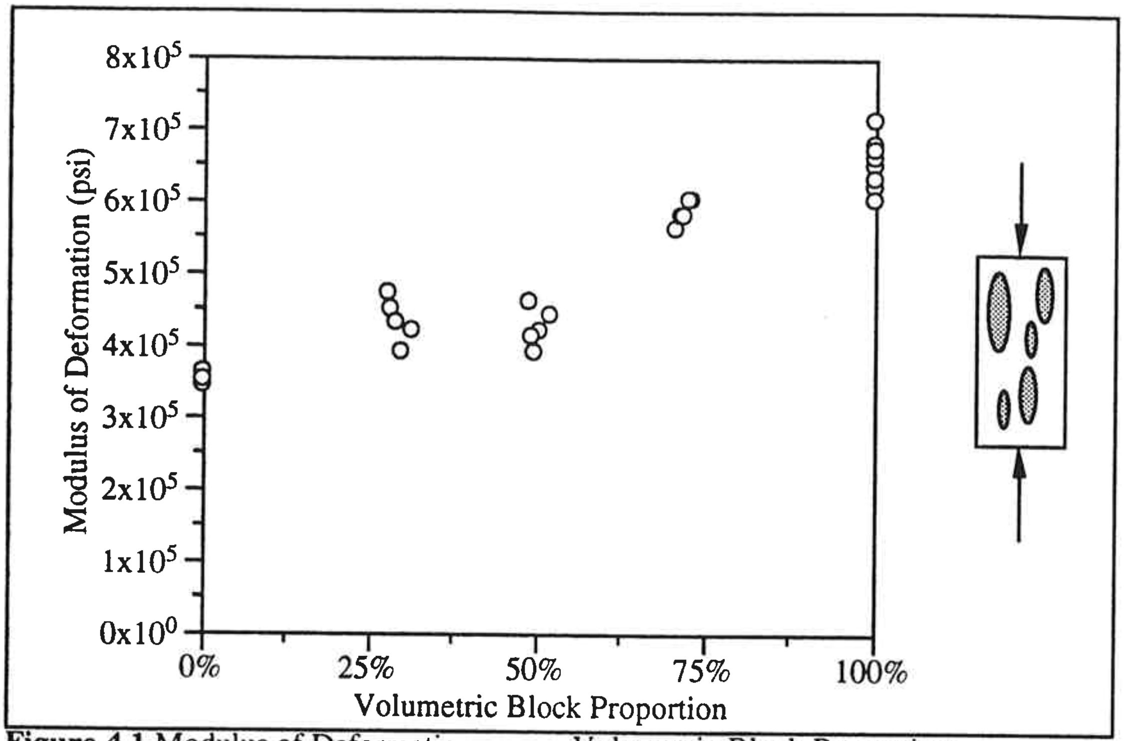

Figure 4.1 Modulus of Deformation versus Volumetric Block Proportion - 0° Orientation

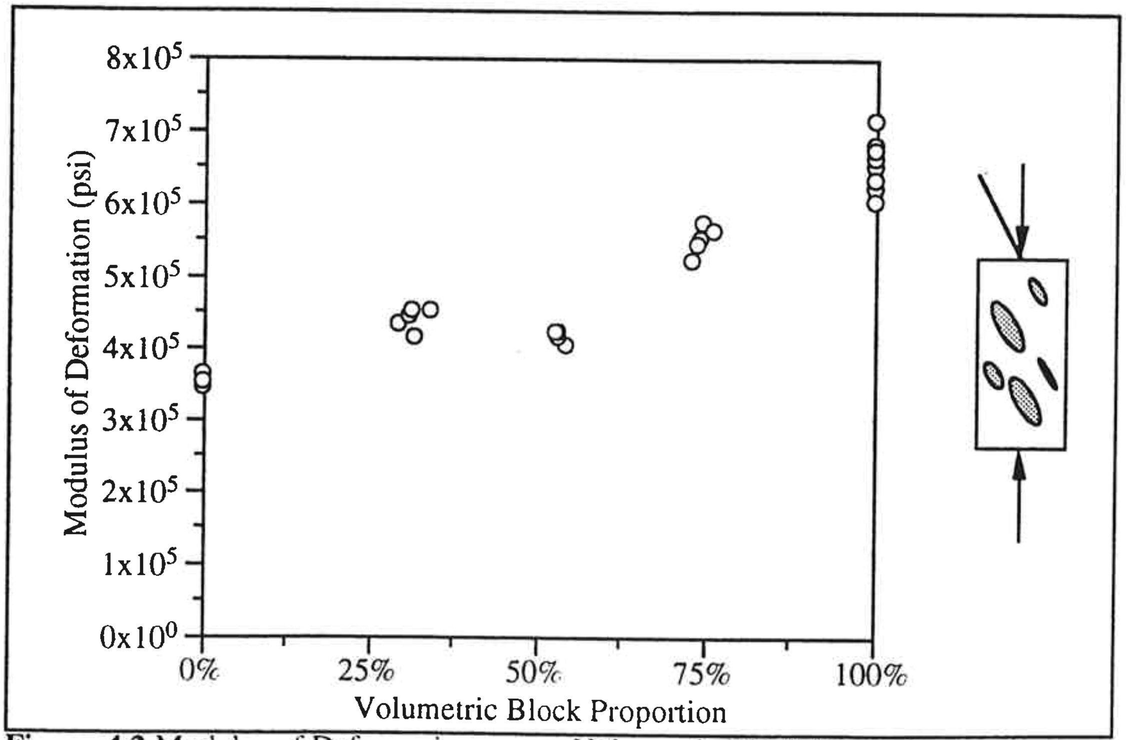

Figure 4.2 Modulus of Deformation versus Volumetric Block Proportion - 30° Orientation

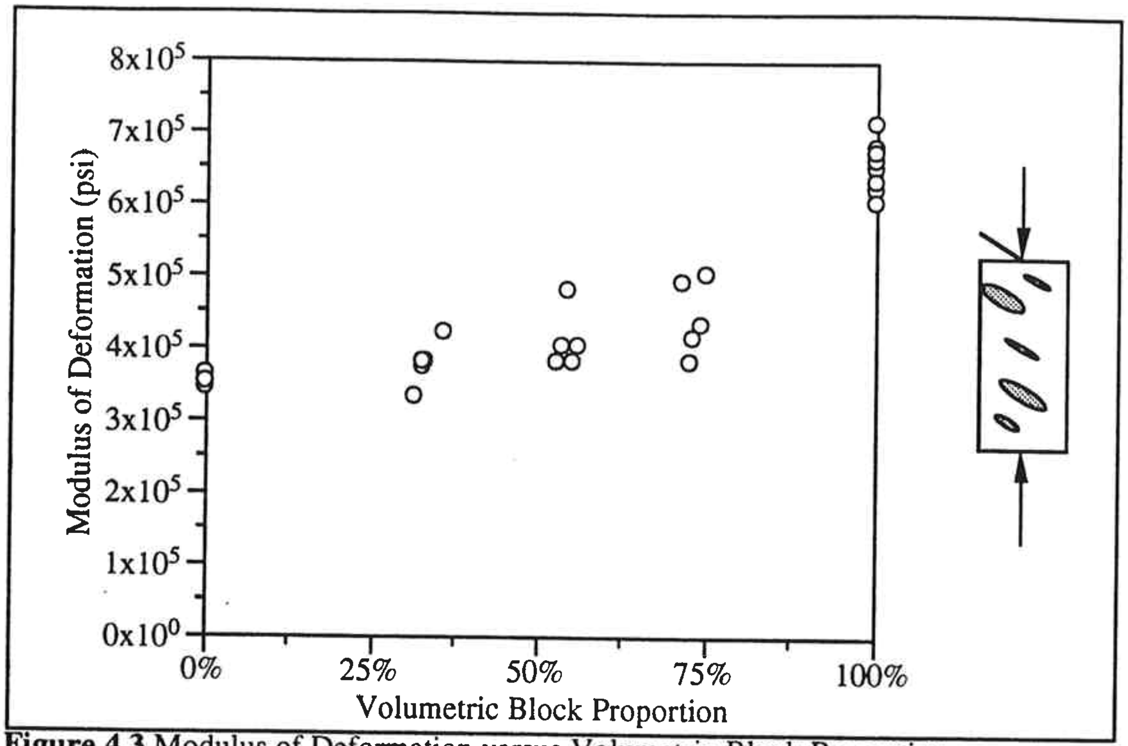

Figure 4.3 Modulus of Deformation versus Volumetric Block Proportion - 60° Orientation

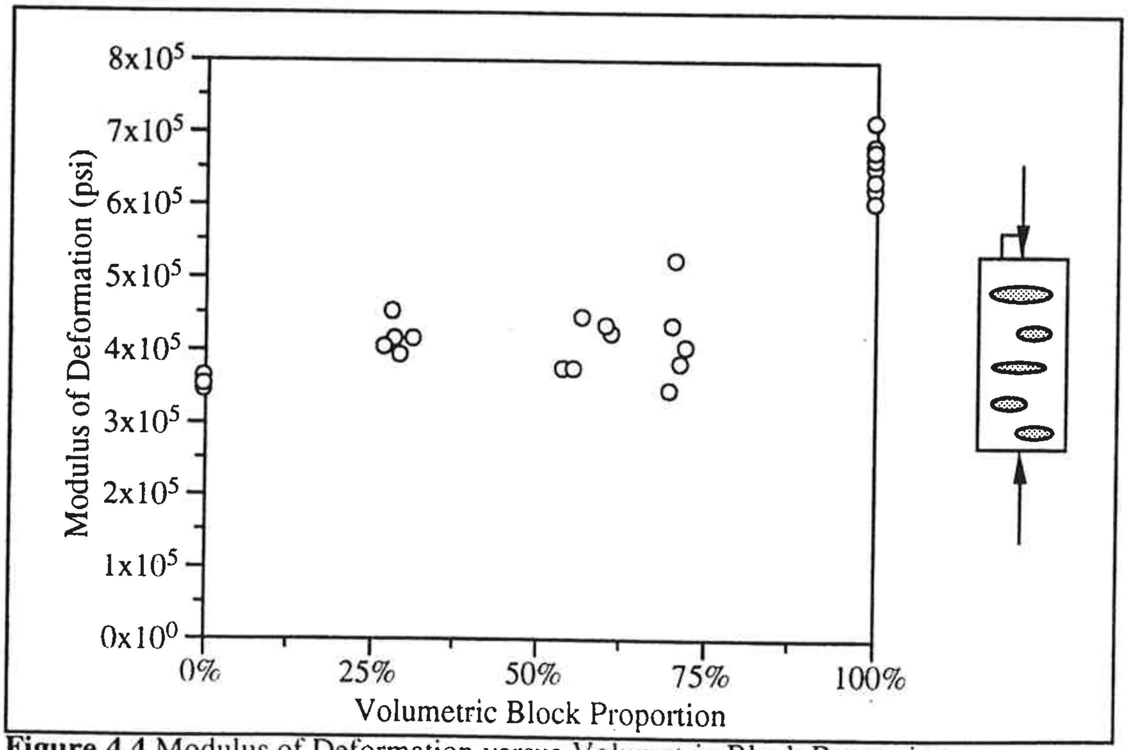

Figure 4.4 Modulus of Deformation versus Volumetric Block Proportion - 90° Orientation

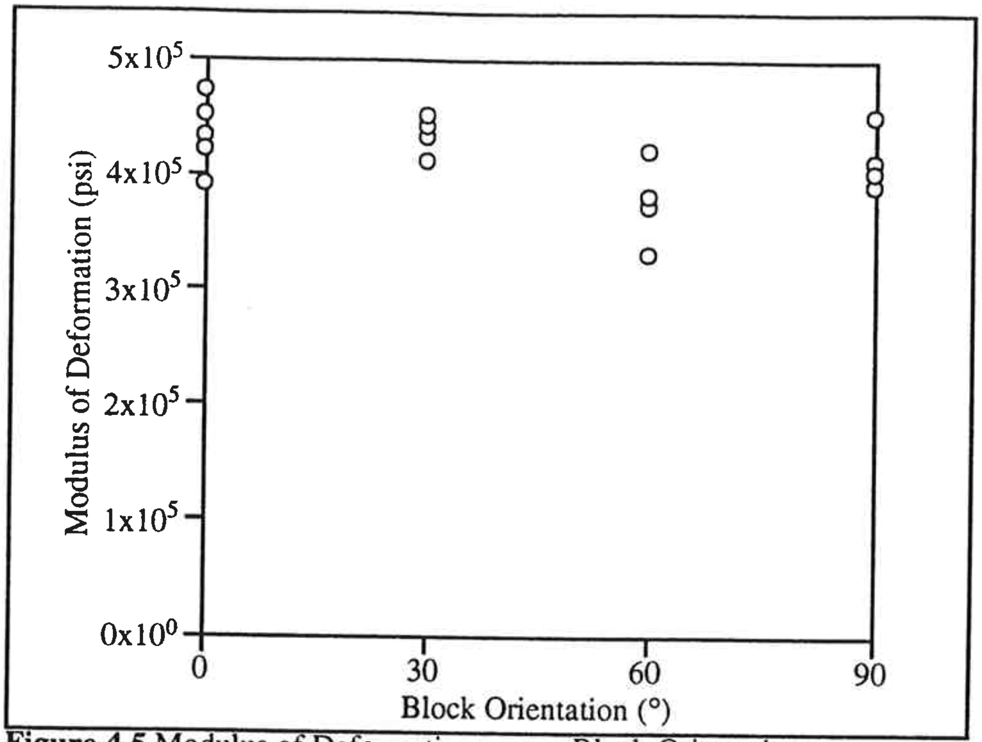

Figure 4.5 Modulus of Deformation versus Block Orientation - Low Block Proportion

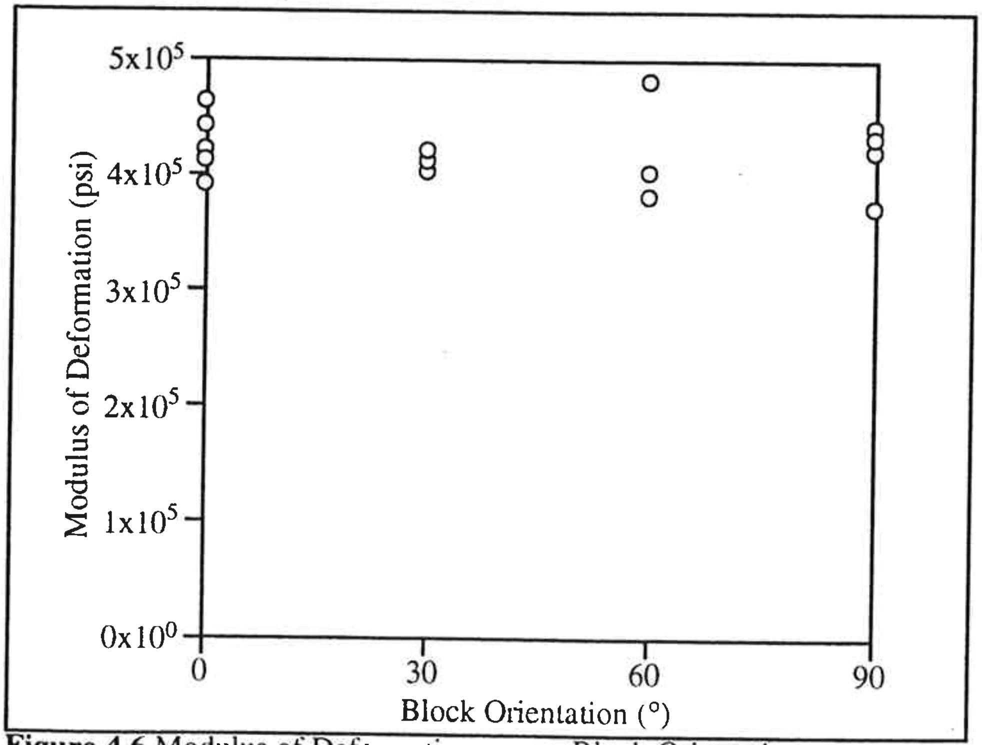

Figure 4.6 Modulus of Deformation versus Block Orientation - Medium Block Proportion

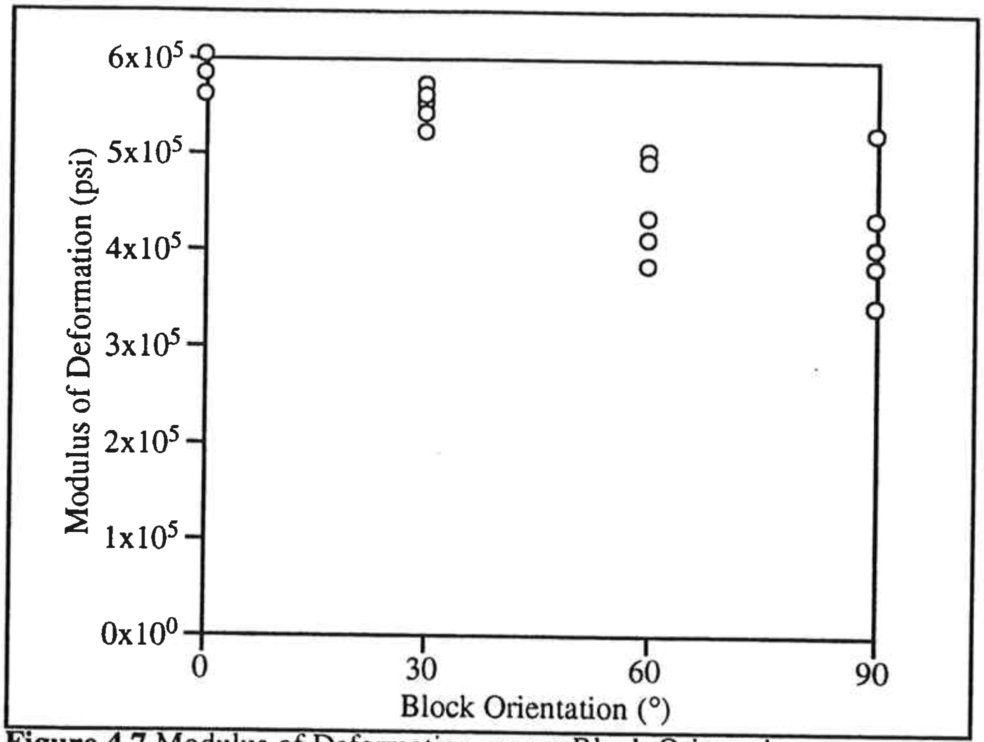

Figure 4.7 Modulus of Deformation versus Block Orientation - High Block Proportion

Some simple analytical models are used in the next chapter to explain the effect blocks had on the stiffness of the physical models.

4.1.2 Strain at Failure

The values of axial strain at failure for all the specimens are listed in Table 4.2. Strain at failure is simply defined as the strain at which the maximum stress difference ($(\sigma_1 - \sigma_3)_{max}$) was realized.

Table 4.2 Strain at Failure Values

Specimen	Block Proportion	Strain at Failure (%)
matrix-50	0%	0.46
matrix-100	0%	0.65
matrix-125	0%	0.61
matrix-150	0%	0.72
matrix-200	0%	0.82
matrix-225	0%	0.96
matrix-250	0%	0.90
block-0	100%	0.54
block-50	100%	0.55
block-75	100%	0.61
block-100	100%	0.61
block-125	100%	0.52
block-150	100%	1.00
block-175	100%	1.00
block-200	100%	1.22
block-225	100%	1.06
block-250	100%	1.15
l-0-50	28%	0.42
l-0-100	30%	0.54
l-0-150	29%	0.49
l-0-200	31%	0.67
l-0-250	28%	0.75
l-30-50	29%	0.45
l-30-100	32%	0.51
l-30-150	34%	0.53
l-30-200	31%	0.58
l-30-250	31%	0.96
l-60-50	31%	0.50
l-60-100	36%	0.51
l-60-150	33%	0.82
l-60-200	33%	0.76
l-60-250	32%	1.03
l-90-50	29%	0.47
l-90-100	29%	0.57
l-90-150	28%	0.52
l-90-200	32%	0.93
l-90-250	27%	1.07
m-0-50	52%	0.40
m-0-100	50%	0.57
m-0-150	50%	0.70
m-0-200	49%	0.63
m-0-250	49%	1.02
m-30-50	54%	0.40
m-30-100	53%	0.52
m-30-150	53%	0.79
m-30-200	53%	0.55
m-30-250	53%	0.93
m-60-50	53%	0.44
m-60-100	56%	0.59
m-60-150	54%	0.69
m-60-200	55%	0.80
m-60-250	53%	0.78
m-90-50	61%	0.47
m-90-100	54%	0.73
m-90-150	57%	0.79
m-90-200	60%	0.86
m-90-250	56%	1.32
h-0-57	71%	0.46
h-0-100	73%	0.56
h-0-150	72%	0.62
h-0-200	72%	1.04
h-0-250	72%	0.87
h-30-50	75%	0.35
h-30-100	74%	0.40
h-30-150	73%	0.44
h-30-200	74%	0.66
h-30-250	76%	0.74
h-60-50	73%	0.41
h-60-100	75%	0.48
h-60-150	71%	0.61
h-60-200	74%	0.98
h-60-250	73%	1.32
h-90-50	70%	0.73
h-90-100	70%	0.72
h-90-150	71%	0.79
h-90-200	71%	0.86
h-90-250	72%	1.52

4.1.2.1 Effect of Block Proportion

Figures 4.8 through 4.12 show strain at failure versus volumetric block proportion. Each graph is for a different confining stress. No consistent change in strain at failure with block proportion is indicated.

4.1.2.2 Effect of Block Orientation

Strain at failure is plotted versus block orientation in Figures 4.13 through 4.15. Each graph is for a particular block proportion range (i.e. low, medium or high). These graphs show that, as expected, the strain at failure generally increased with increasing confining stress. An indication of how block orientation affected the strain at failure is only clear for the high block proportion specimens (Figure 4.15). The high block proportion specimens with the most "adversely" oriented blocks (30°) had the lowest strain at failure and the 90° specimens generally had the highest. In fact, it appears that the data roughly follow a parabolic relationship with a minimum at 30° (for each confining stress). Some slight evidence of this type of relationship between strain at failure and block orientation can be found in Figures 4.13 and 4.14 as well.

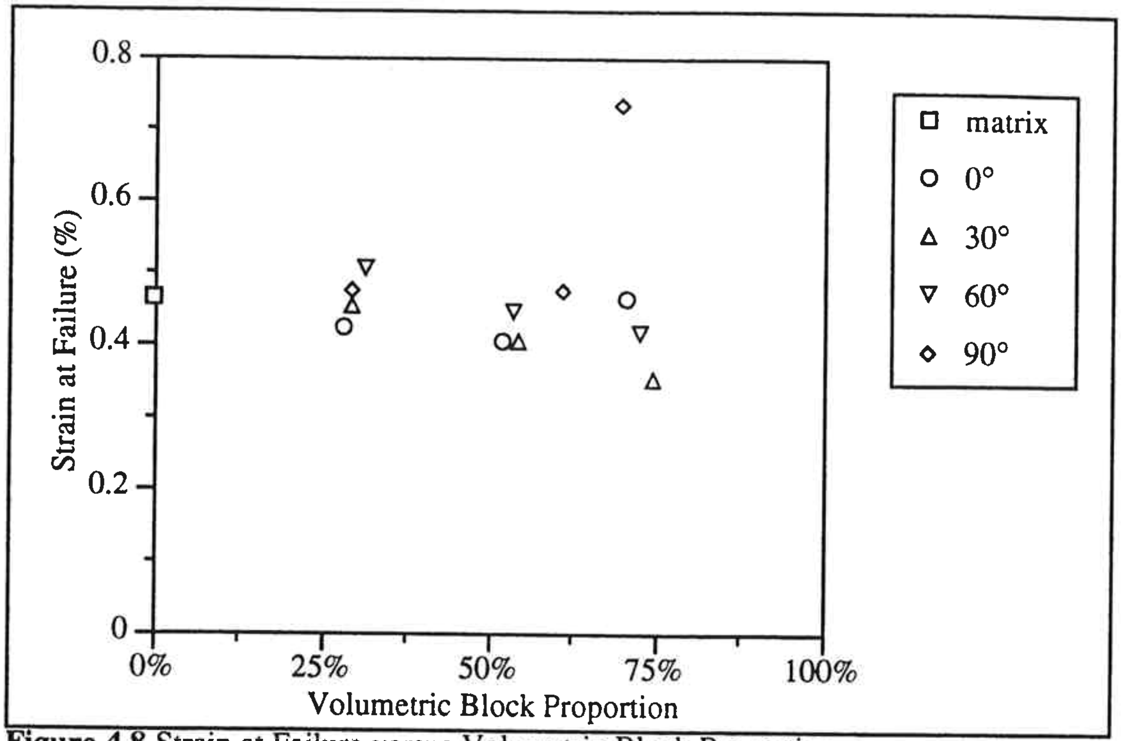

Figure 4.8 Strain at Failure versus Volumetric Block Proportion - Confining = 50 psi

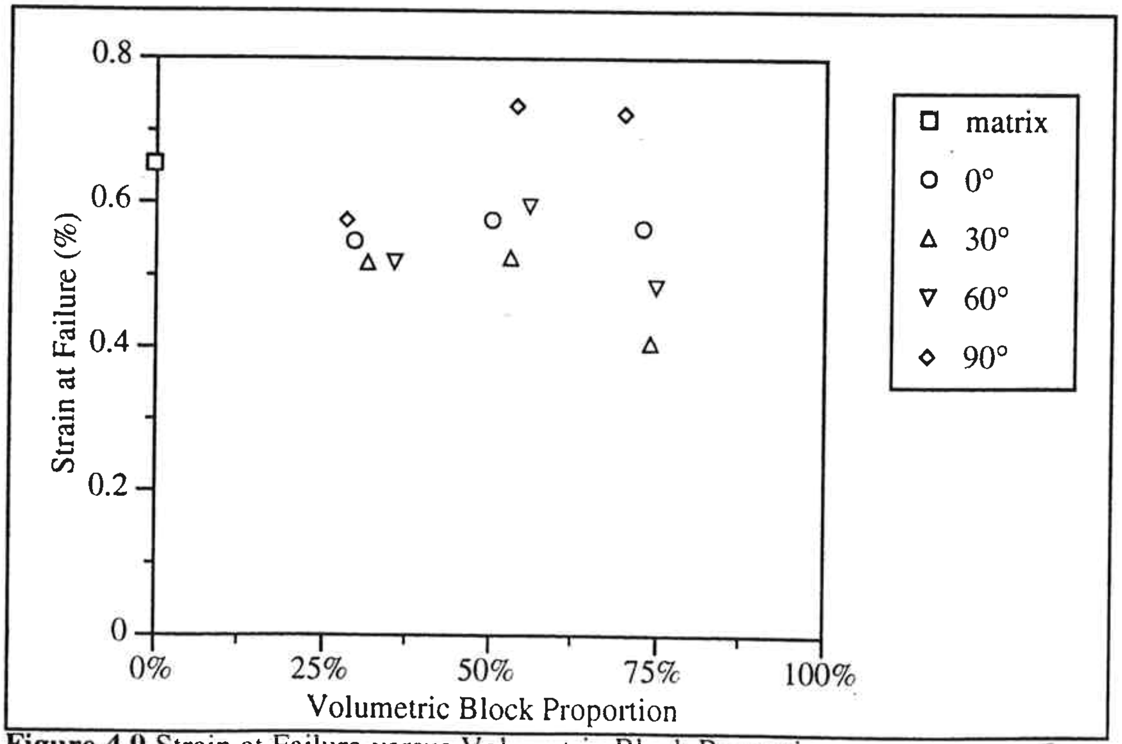

Figure 4.9 Strain at Failure versus Volumetric Block Proportion - Confining = 100 psi

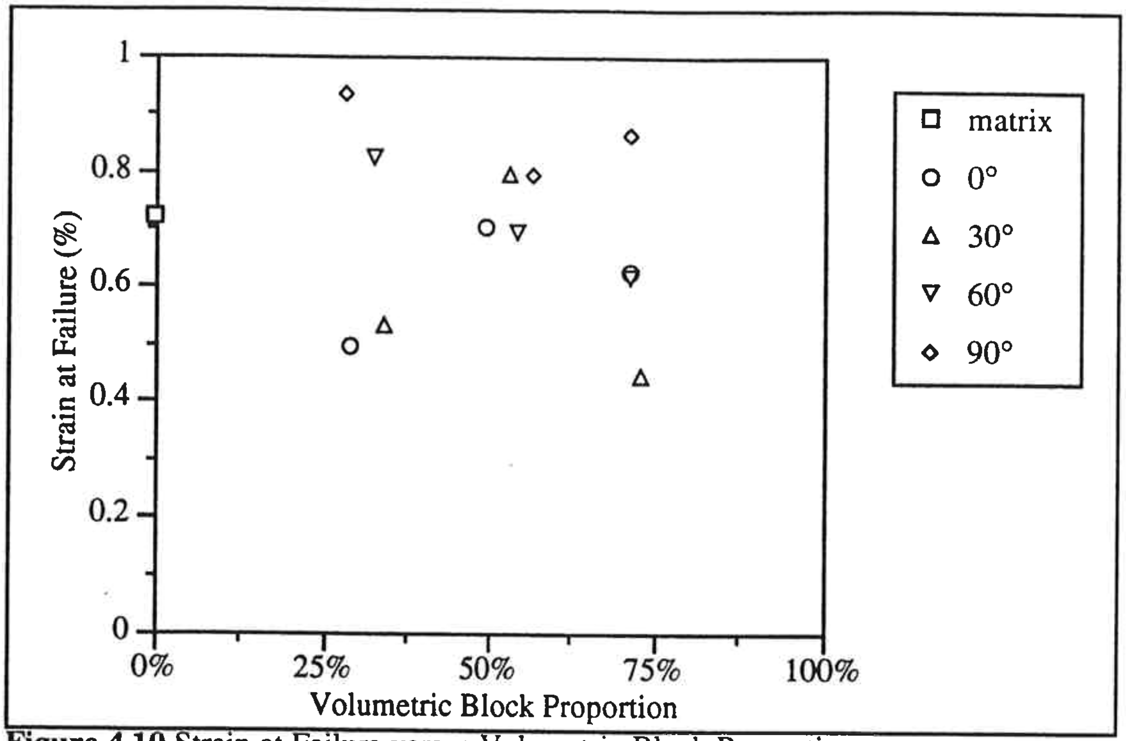

Figure 4.10 Strain at Failure versus Volumetric Block Proportion - Confining = 150 psi

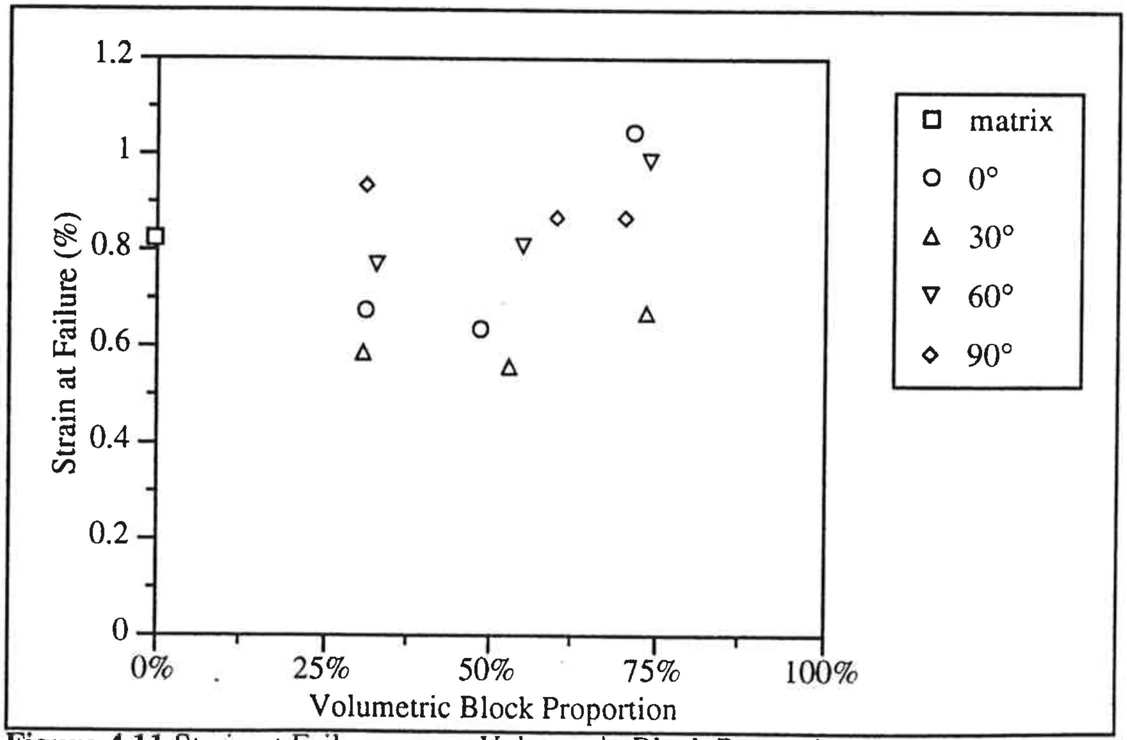

Figure 4.11 Strain at Failure versus Volumetric Block Proportion - Confining = 200 psi

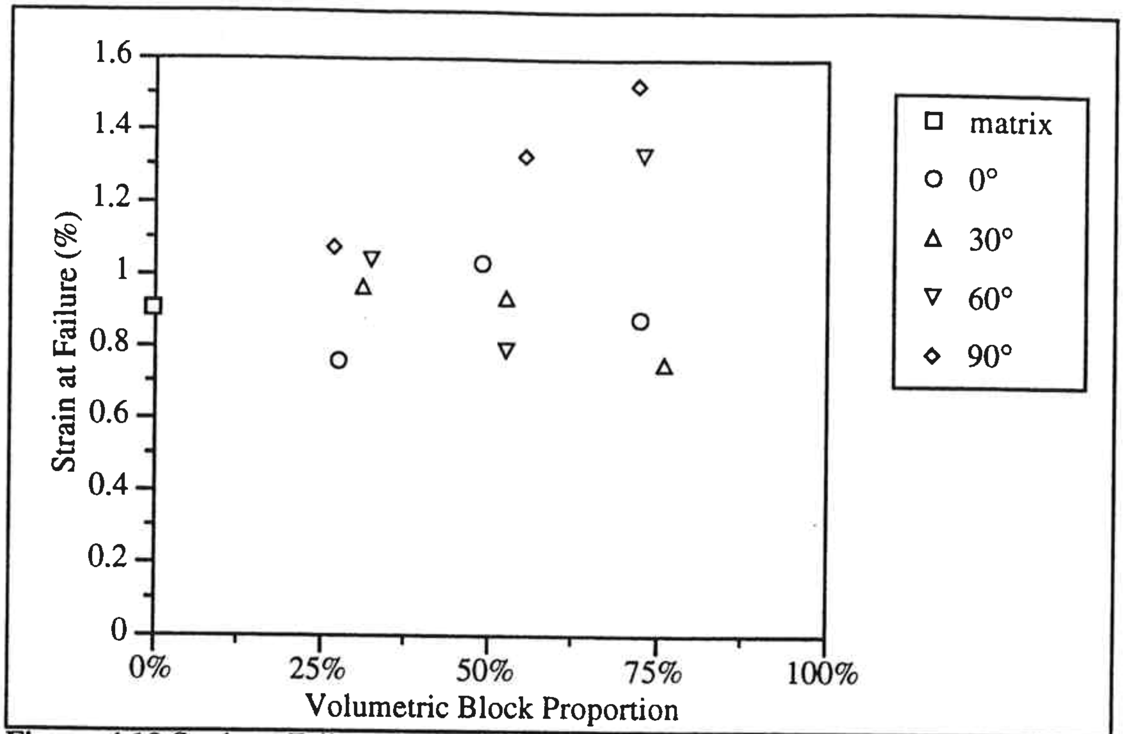

Figure 4.12 Strain at Failure versus Volumetric Block Proportion - Confining = 250 psi

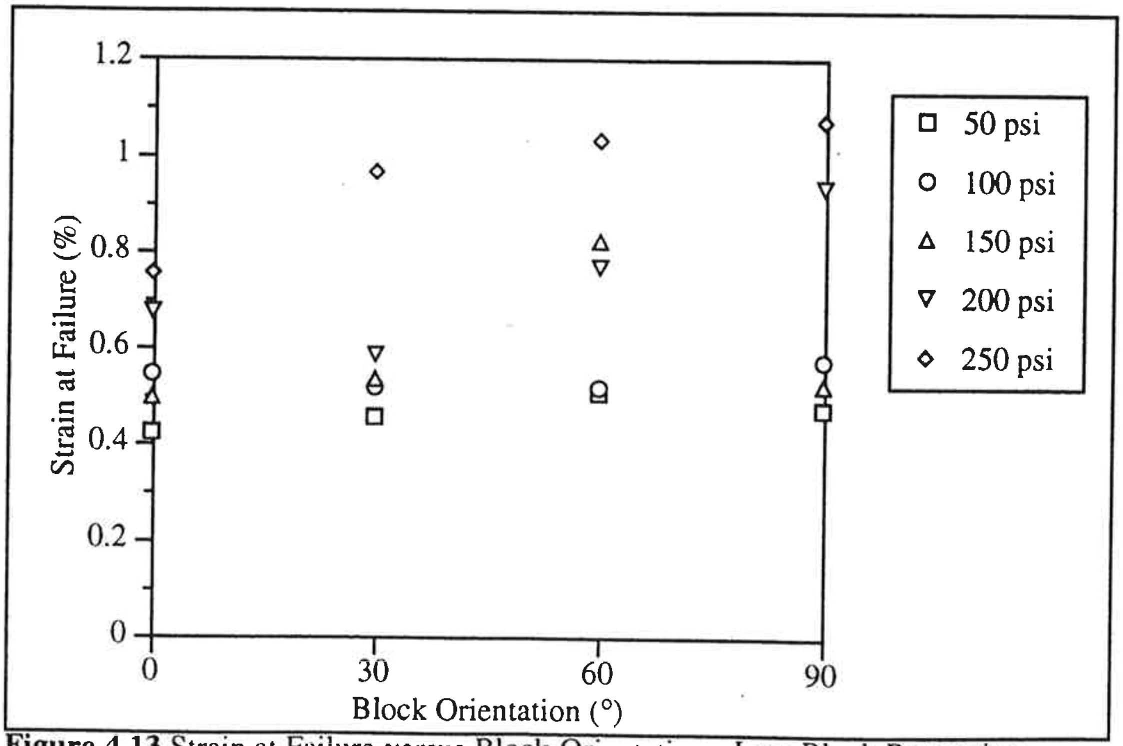

Figure 4.13 Strain at Failure versus Block Orientation - Low Block Proportion

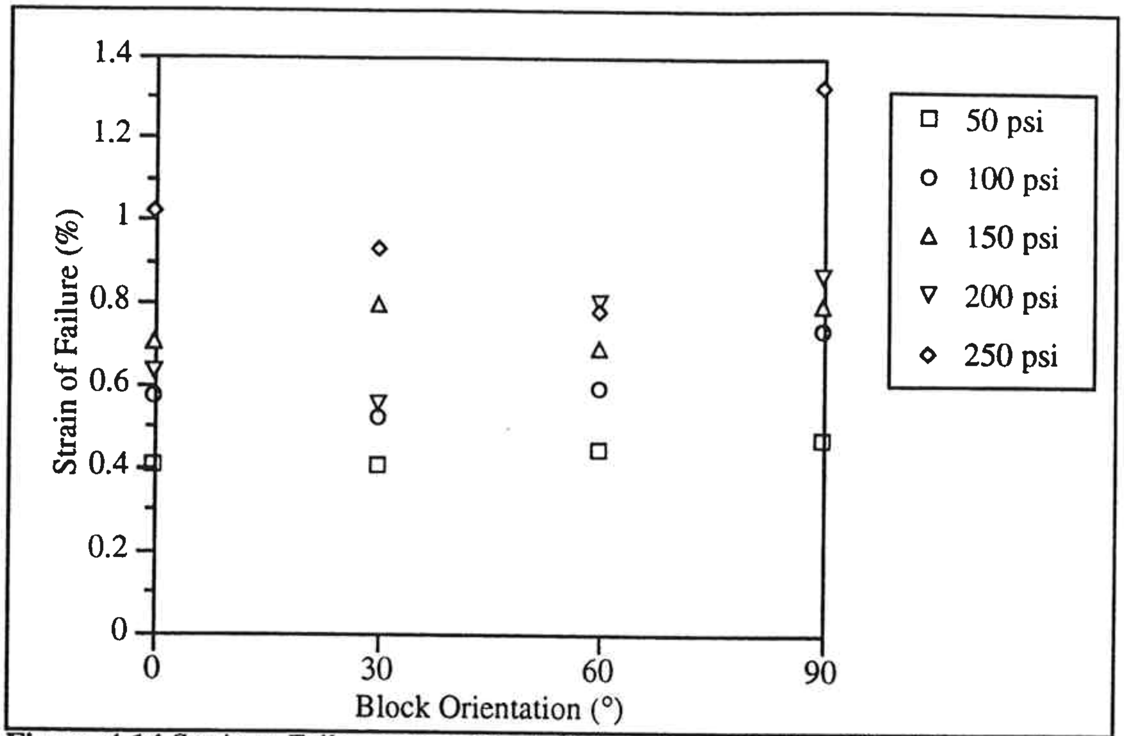

Figure 4.14 Strain at Failure versus Block Orientation - Medium Block Proportion

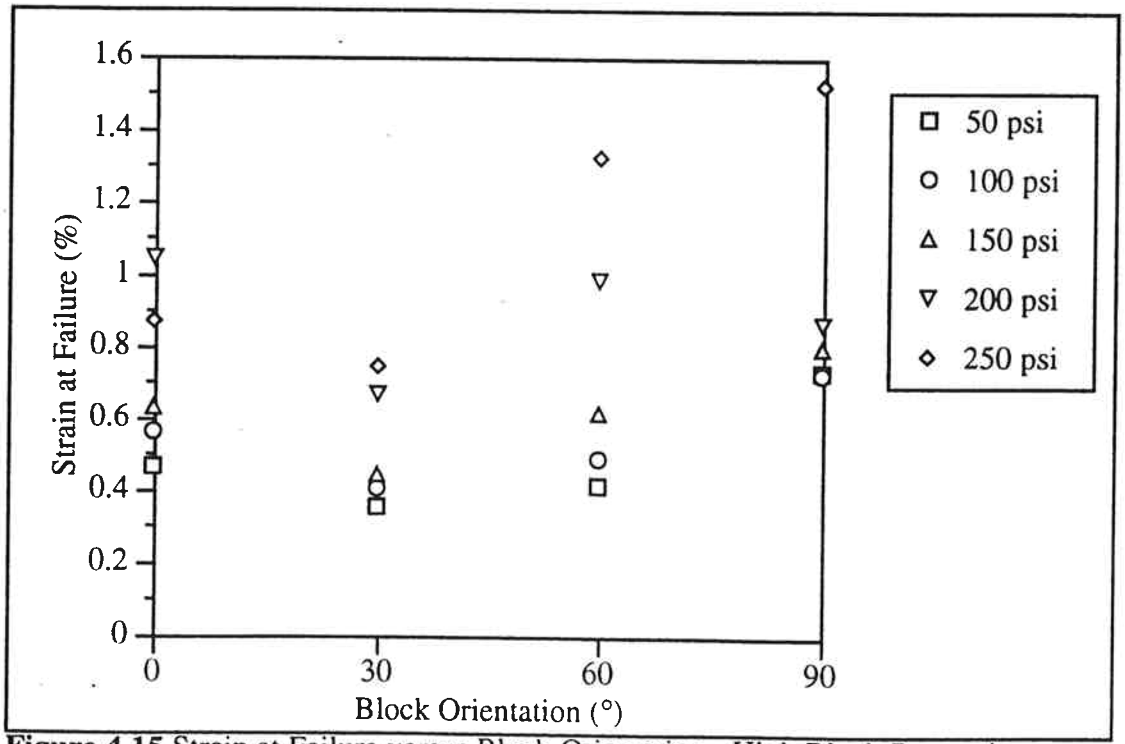

Figure 4.15 Strain at Failure versus Block Orientation - High Block Proportion

4.2 Strength

The Mohr-Coulomb strength parameters, cohesion (c) and angle of internal friction (ϕ), are used to represent the strengths of the physical models. The effects that block proportion and block orientation had on these parameters are reported in the following sections. The methodology used to determine these parameters, and the raw test data from which they were calculated is given in Appendix C. Appendix C also contains Mohr circle plots of the test data.

4.2.1 Cohesion

Table 4.3 lists the values of cohesion for specimens with different block proportions and orientations.

4.2.1.1 Effect of Block Proportion

The effect of block proportion on cohesion is summarized in Figure 4.16. This plot shows that increasing the block proportion generally decreased the cohesion. In fact, the specimens with high block proportions (approximately 70 percent) had a cohesion only about half that of the matrix alone. Note that the cohesions of the 0° and 60° block orientation specimens with lowest block proportions were about the same as the pure matrix. These data suggest that there was a threshold block proportion below which the presence of blocks had little effect on cohesion. The fact that the 30° and 90° low block proportion specimens had a lower cohesion implies this threshold might have been around 25 to 30 percent for these models.

Table 4.3 Cohesion Values

Specimen Type	Average Block Proportion	c (psi)
matrix	0%	330
block	100%	445
l-0	29%	345
l-30	31%	250
l-60	33%	377
l-90	29%	276
m-0	50%	233
m-30	53%	206
m-60	54%	229
m-90	57%	231
h-0	72%	199
h-30	74%	163
h-60	73%	180
h-90	71%	302

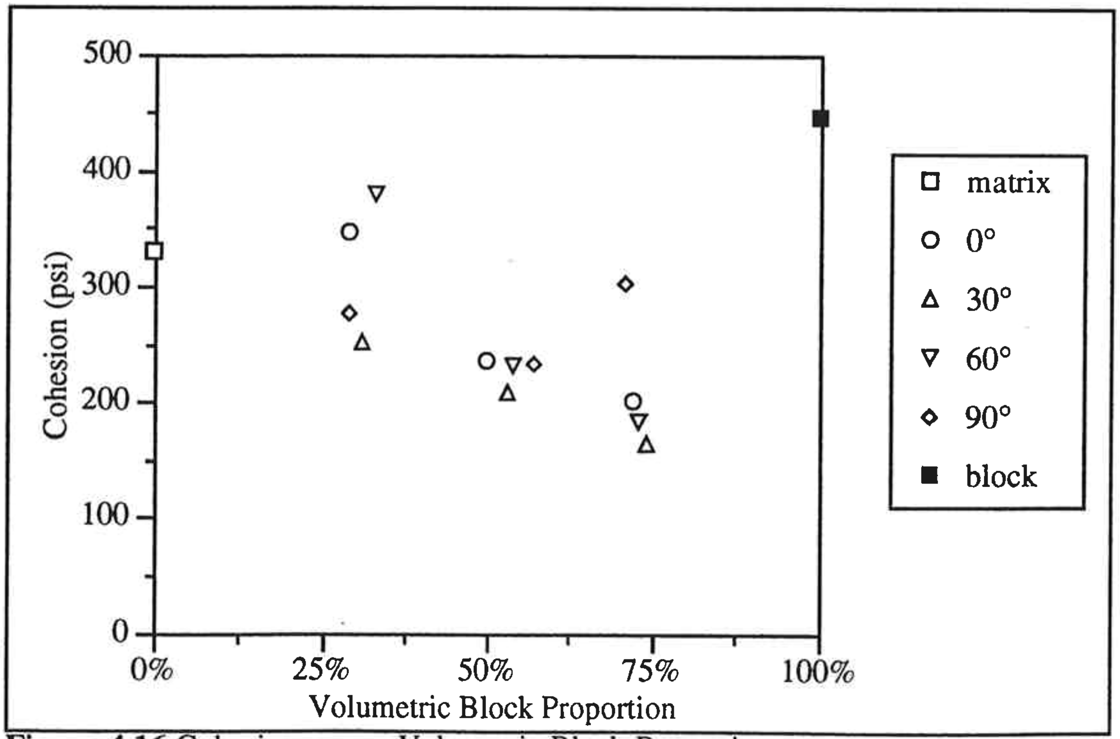

Figure 4.16 Cohesion versus Volumetric Block Proportion

4.2.1.2 Effect of Block Orientation

As discussed in Chapter 3, fabric anisotropy creates strength anisotropy in rocks. When planes of weakness (e.g. cleavage or shears) are oriented "adversely" with respect to the loading, the result is a significantly lower strength. The block-in-matrix models used in this study were anisotropic due to the orientation of the larger blocks in the specimens. Although the fabric created by orienting the blocks was not nearly as strong as that formed, by say, slaty cleavage, it still resulted in some strength anisotropy. Plots of cohesion versus block orientation (Figures 4.17 through 4.19) show this effect. Note that in all cases the specimens with blocks oriented at 30° relative to the axial loading direction had the lowest cohesion, and that the medium and high block proportion specimens with 0° and 90° orientations had higher cohesions than those with 30° and 60° orientations. These trends are similar, although less pronounced, to those found by Jaeger (1960) and Donath (1964).

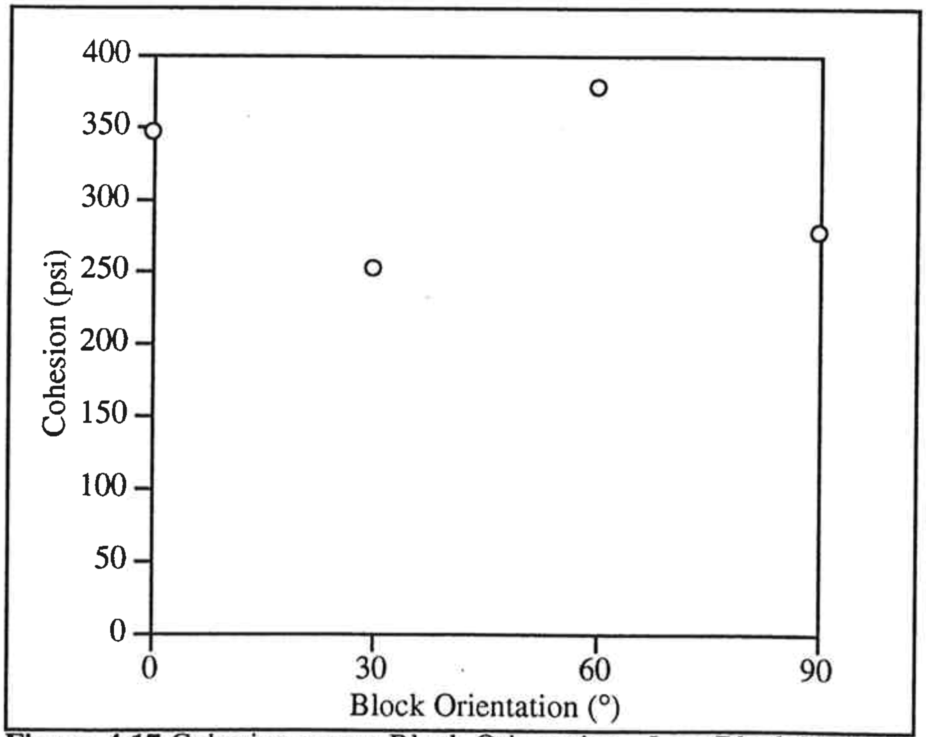

Figure 4.17 Cohesion versus Block Orientation - Low Block Proportion

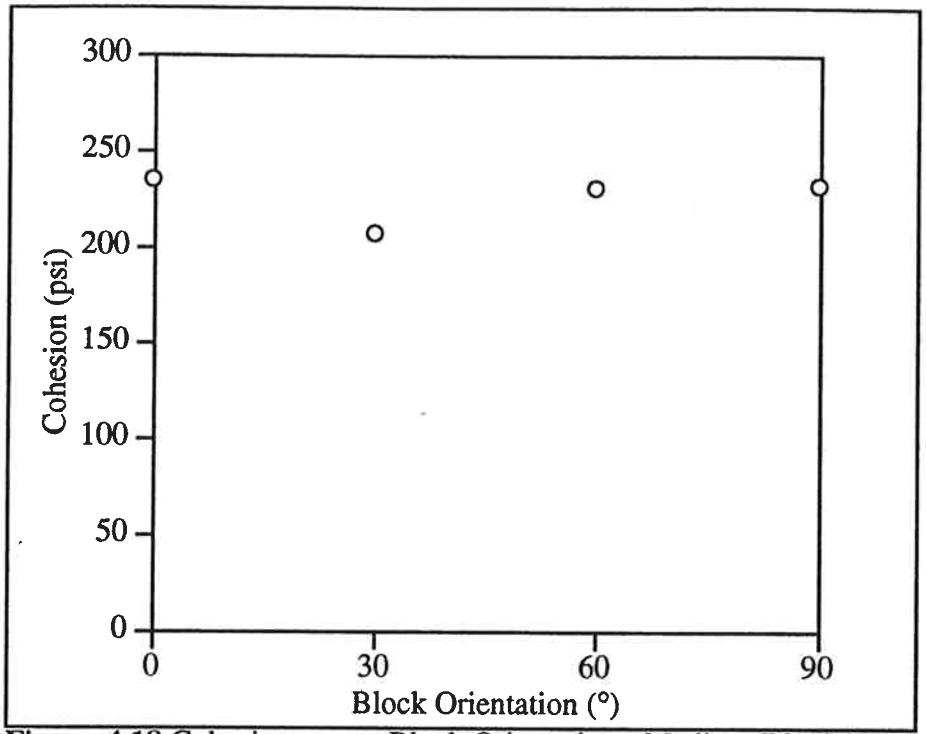

Figure 4.18 Cohesion versus Block Orientation - Medium Block Proportion

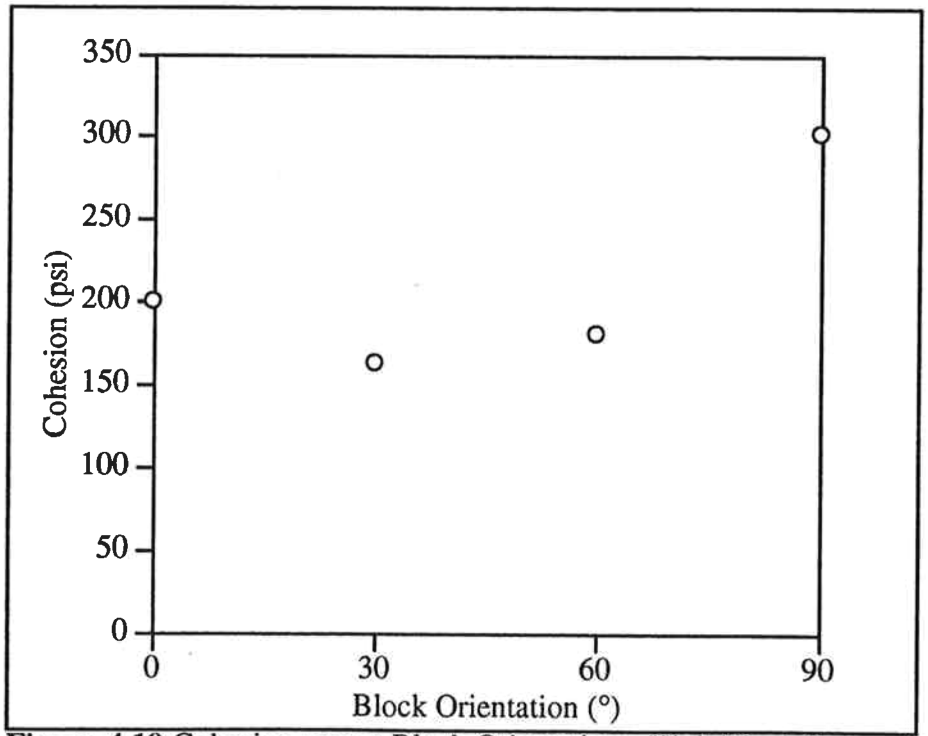

Figure 4.19 Cohesion versus Block Orientation - High Block Proportion

4.2.2 Angle of Internal Friction

Table 4.4 lists the values of angle of internal friction for specimens with different block proportions and orientations.

Table 4.4 Angle of Internal Friction Values

Specimen Type	Average Block Proportion	ϕ (°)
matrix	0%	24.7
block	100%	38.3
l-0	29%	26.2
l-30	31%	32.9
l-60	33%	23.4
l-90	29%	32.8
m-0	50%	33.5
m-30	53%	32.3
m-60	54%	33.3
m-90	57%	37.6
h-0	72%	39.6
h-30	74%	38.2
h-60	73%	41.2
h-90	71%	34.0

4.2.2.1 Effect of Block Proportion

Figure 4.20 shows that the angle of internal friction increased with increasing block proportion. This increase was as much as 16.5° for the 60° orientation high block proportion specimens over the pure matrix specimens. The 0° and 60° low block proportion specimens had an angle of internal friction not significantly different from that of the matrix. On the other hand the 30° and 90° low block proportion specimens had values that were quite a bit higher. As for the cohesion, these data indicate that there was a threshold block proportion (25 to 30 percent) below which the angle of internal friction was little affected by the presence of blocks. This threshold value is similar to the 25 percent threshold suggested by Irfan and Tang (1993) for colluvium (see Chapter 2).

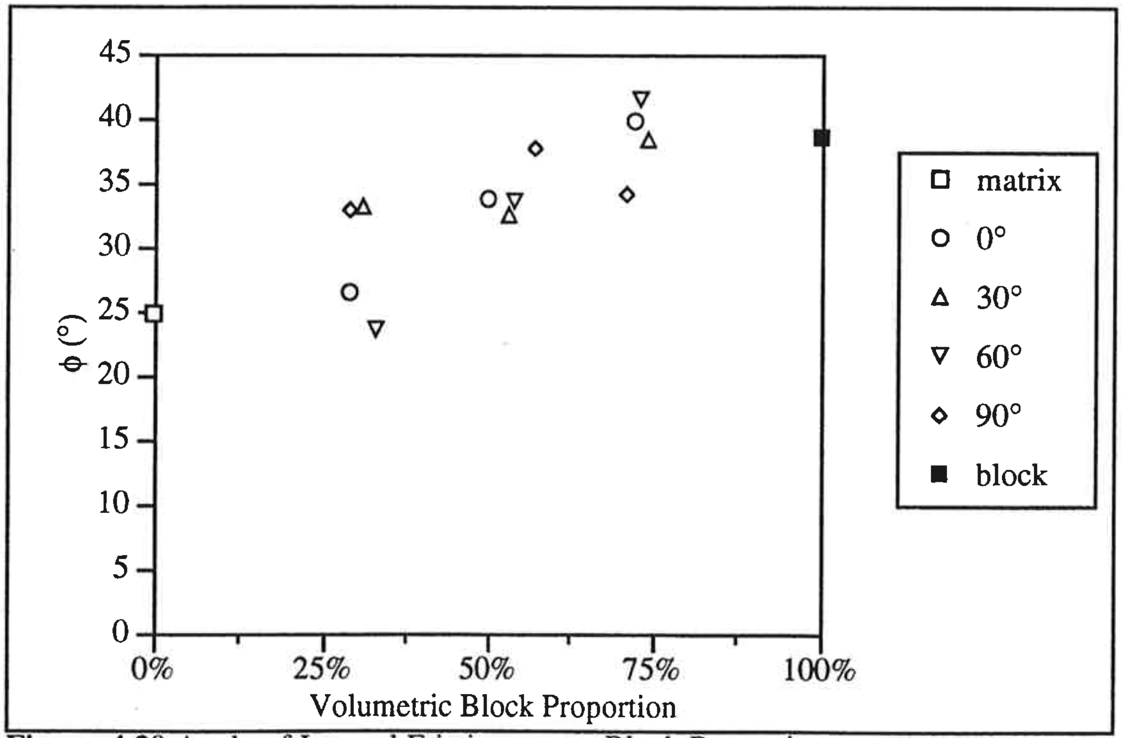

Figure 4.20 Angle of Internal Friction versus Block Proportion

4.2.2.2 Effect of Block Orientation

Anisotropy of the angle of internal friction is considered in Figures 4.21 through 4.23. These plots of angle of internal friction versus block orientation give little indication that there was any consistent effect of anisotropy on the angle of internal friction. The only specimens that showed any apparent strength anisotropy whatsoever were the medium block proportion specimens (Figure 4.22). The medium and high block proportion graphs indicate that angle of internal friction did not vary too significantly with block orientation. The effect of anisotropy on angle of internal friction is known to generally be less severe than the effect on cohesion (Goodman, 1989); therefore, these results were not unexpected.

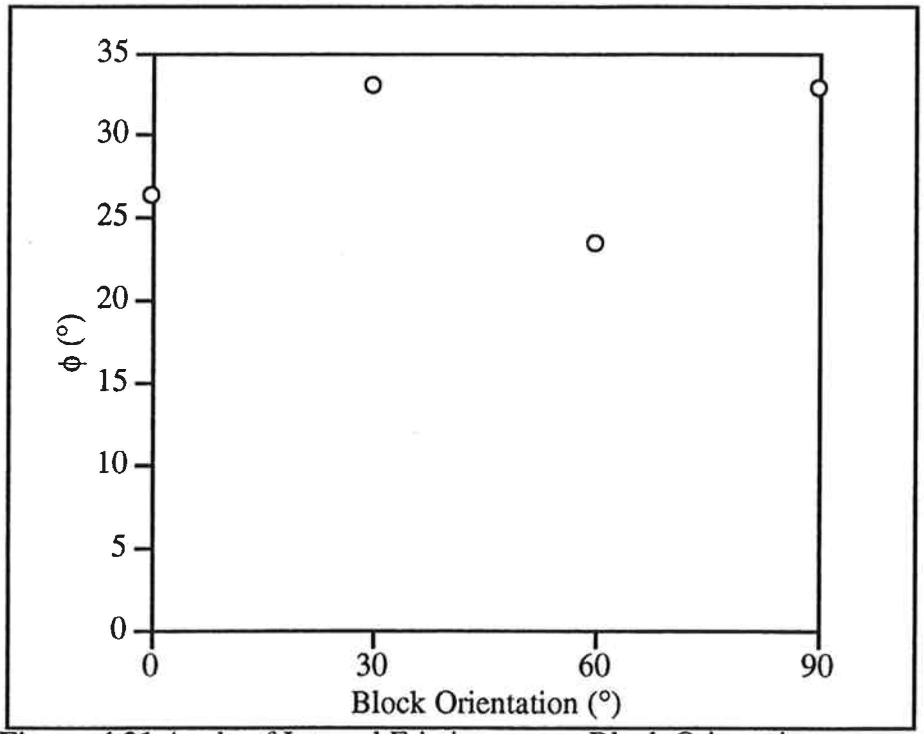

Figure 4.21 Angle of Internal Friction versus Block Orientation - Low Block Proportion

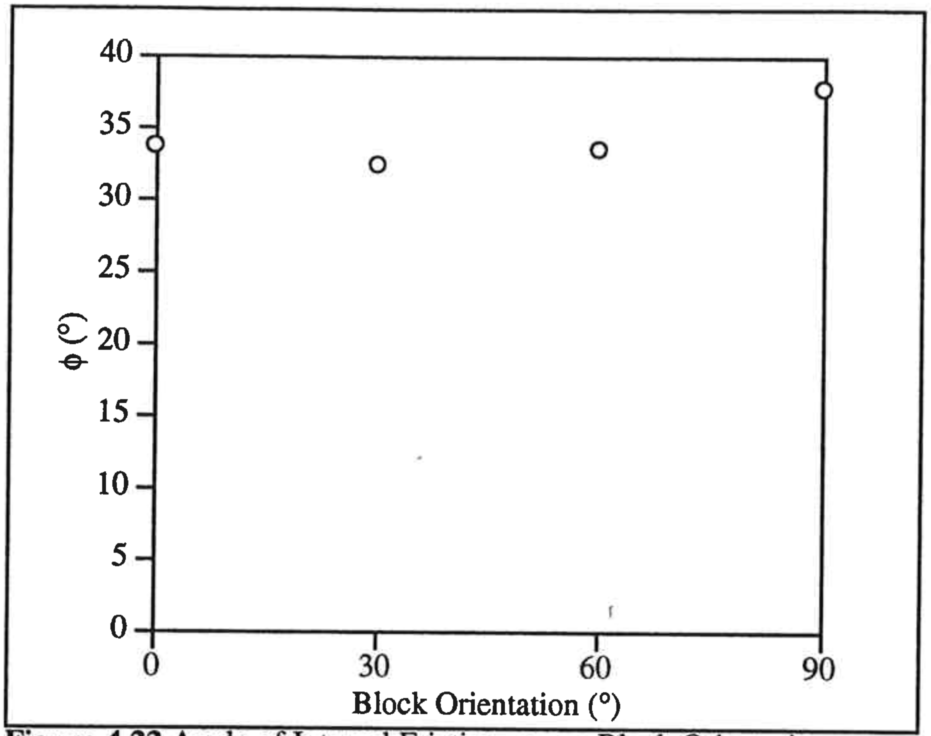

Figure 4.22 Angle of Internal Friction versus Block Orientation - Medium Block Proportion

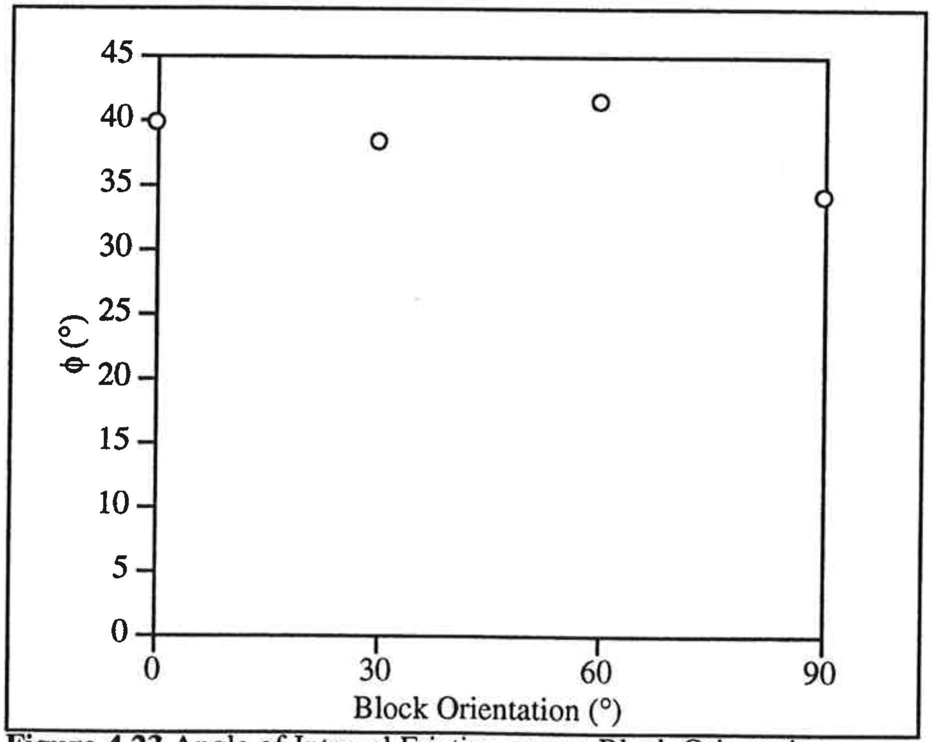

Figure 4.23 Angle of Internal Friction versus Block Orientation - High Block Proportion

4.3 Failure Types Exhibited

A tracing of the cylindrical surface of each failed specimen is presented in Appendix D (unrolled cylinders are shown). Appendix D also contains a photograph of each failed specimen. The block-in-matrix model specimens most commonly failed along inclined shear surfaces. The failures generally followed the block-matrix contacts and wax "shears". Because the failures occurred at the block margins, the orientations of the largest blocks typically controlled the orientation of the failure surface. Figure 4.24 (the tracing of failed specimen h-60-50) shows a good example of the failure surface following the block-matrix contacts.

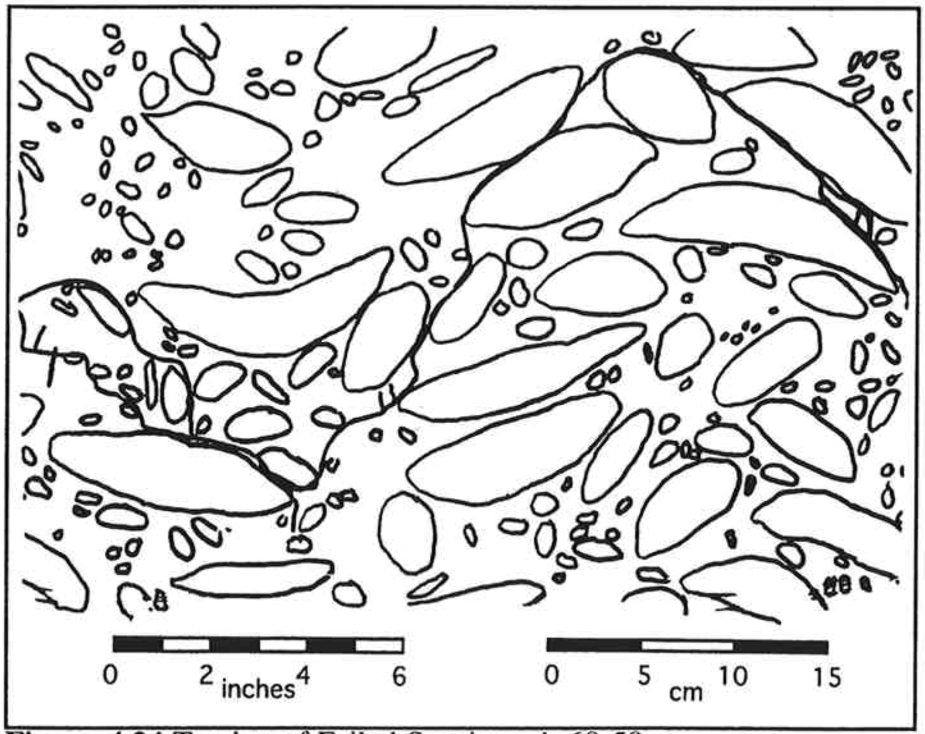

Figure 4.24 Tracing of Failed Specimen h-60-50

Evidence of tensile splitting existed in some specimens, particularly the 0° and 90° specimens that were tested at low confining stresses. It was also evident during testing that these specimens underwent more lateral expansion (more dilation). Most likely these tensile cracks formed to assist the formation of a continuous failure surface through the specimen. This type of cracking is well illustrated in Figure 4.25 (the tracing of failed specimen h-90-50).

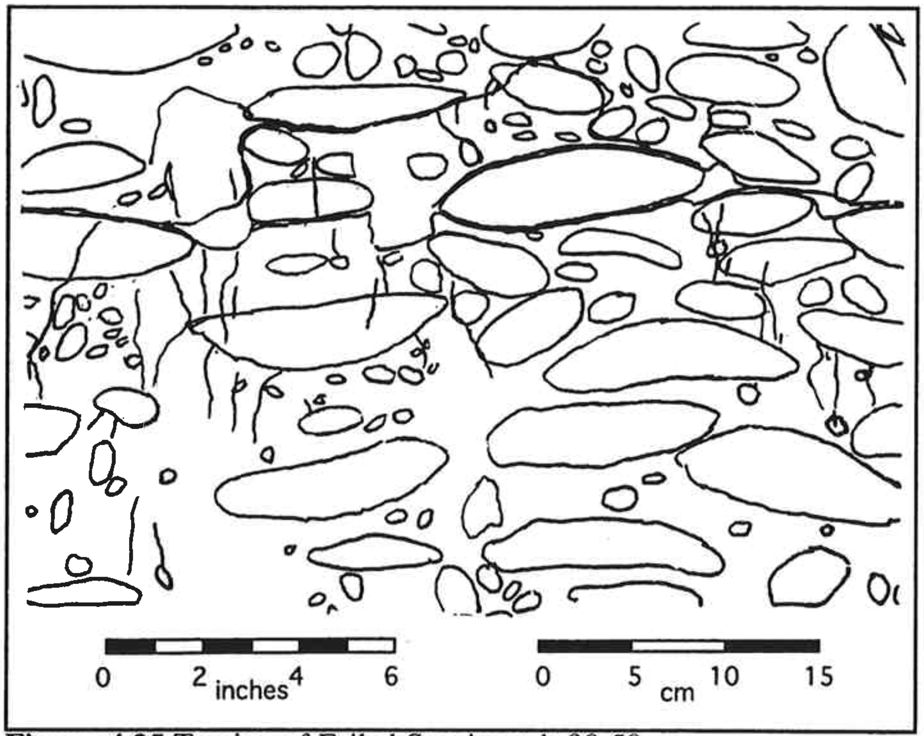

Figure 4.25 Tracing of Failed Specimen h-90-50

CHAPTER 5

DISCUSSION OF PHYSICAL MODEL TEST RESULTS

5.1 Stress-Strain Behavior

The bounding conditions of uniform strain (Voight) and uniform stress (Reuss) for volumes made up of layered components can be used to help explain why the modulus of deformation increased with increasing block proportion and how the block orientation affected this increase. Loading situations under which uniform strain (parallel) and uniform stress (series) would arise in a layered volume are illustrated in Figure 5.1. Equations for predicting the moduli of these models are derived and discussed by Mehta and Monteiro (1993).

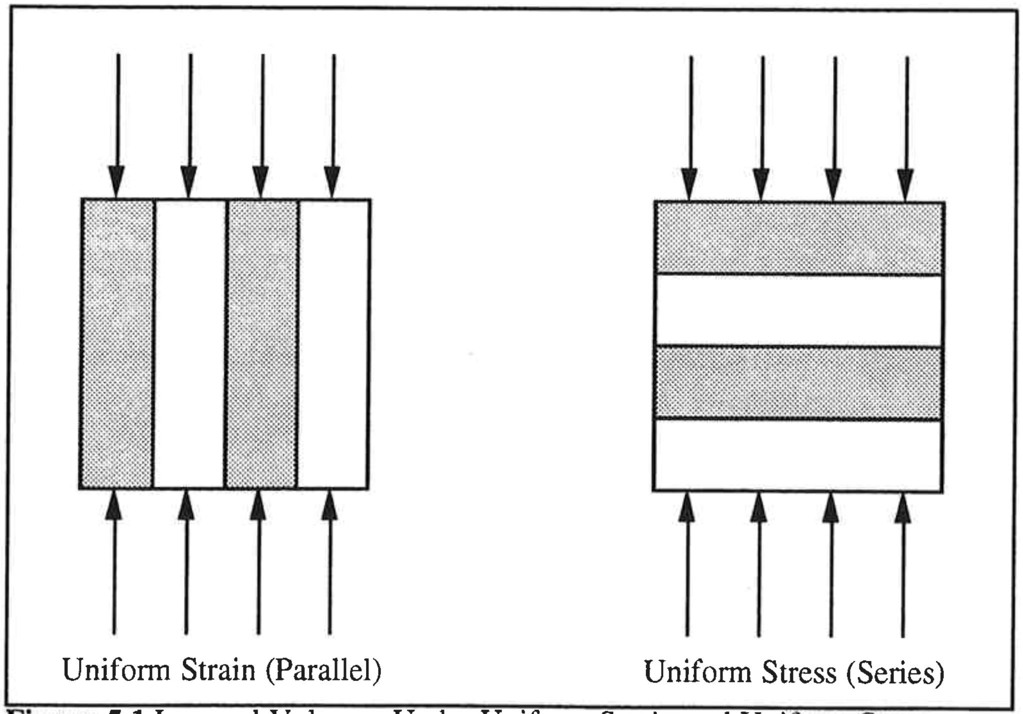

Figure 5.1 Layered Volumes Under Uniform Strain and Uniform Stress Conditions

The modulus for the parallel case is given by the formula

$$E = E_b\theta + E_m(1-\theta), \tag{5.1}$$

where E is the modulus of the mass, E_b is the modulus of the block material, E_m is the modulus of the matrix material and θ is the volumetric proportion of the block material. In other words, the modulus of the mass is simply the weighted average of the moduli of the block and matrix materials based on their volumetric proportions. This equation is a simplification because it does not account for lateral deformations. The complete formula (when lateral deformations are accounted for) is

$$E = E_b\theta + E_m(1-\theta) + \frac{27(1-\theta)(\theta)(G_bK_m - G_mK_b)^2}{(3K_v + G_v)(3K_m + E_m)(3K_b + E_b)}, \tag{5.2}$$

where G_b and G_m are the shear moduli of the block and matrix materials, respectively; K_b and K_m are the bulk moduli of the block and matrix materials, respectively; and $K_v = K_b\theta+K_m(1-\theta)$ and $G_v = G_b\theta+G_m(1-\theta)$. Note that

$$K = \frac{E}{3(1-2v)} \tag{5.3}$$

and

$$G = \frac{E}{2(1+v)}. \tag{5.4}$$

The last term in equation (5.2) vanishes when the Poisson's ratios of the block and matrix materials are equal (i.e. equation (5.2) reduces to equation (5.1)). Even when the

Poisson's ratios of the block and matrix materials are not equal, the last term will tend to be small in relation to the other terms.

The modulus for the series case is given by the formula

$$\frac{1}{E} = \frac{\theta}{E_b} + \frac{(1-\theta)}{E_m}. \tag{5.5}$$

This equation is the same whether or not lateral deformations are considered.

The parallel model provides an upper bound and the series model provides a lower bound between which the modulus values of all mixtures of the two components should fall, regardless of the mixture's geometry. In other words, any two-component block-in-matrix material should fall within these bounds. Stricter (i.e. tighter) bounds on the modulus for mixtures consisting of blocks in a matrix, such as those derived by Hashin and Shtrikman (1963), could also be used to analyze the model melanges. In addition, one could consider the case of layered two-component models with the layers inclined at between 0° to 90° relative to the axial loading direction. Axial deformation of such a model results not only from compression, but also due to shear strain/normal stress coupling or shear stress/normal strain coupling. Despite the potential for analyzing the physical models by more complex methods, it is believed that the parallel and series models can sufficiently explain the modulus results. For the sake of simplicity (and because it is not believed the last term in equation (5.2) will be that significant for these materials), equations (5.1) and (5.5) will be used to define the upper and lower modulus bounds on the graphs in this chapter.

Chapter 5 Discussion of Physical Model Test Results

Based on the geometry of the models used in this study one would expect the moduli values of the specimens with blocks oriented at 0° relative to the axial loading direction to fall closer to the upper (parallel) bound and the 90° oriented specimens to fall closer to the lower (series) bound with the 30° and 60° specimens in between. To check this, Figures 5.2 through 5.5 show the modulus of deformation versus block proportion for the different block orientations along with the parallel and series bounds based on the average modulus of the matrix and average modulus of the blocks. In Figure 5.2 (0° orientation) the data for the lowest and highest block proportion specimens fall close to the upper bound, as was expected. The 30° low and high block proportion data (Figure 5.3) also fall within the bounds. The data for the medium (approximately 50%) block proportion 0° and 30° specimens fall significantly below the lower bound, though. Some possible reasons for this are discussed later in this section. The data in Figures 5.4 (60° orientation) and 5.5 (90° orientation) fall well below the lower bound for the most part. In fact, many of the high block proportion, 90° orientation specimens have moduli lower than those of the 90° low block proportion specimens. The modulus must have been affected by some other factor, most significantly when the blocks were oriented at larger angles (60° and 90°) relative to the axial loading direction.

Wax layer alignment helps explain why the modulus values for the 60° and 90° specimens fall below the lower modulus bound. In the pure matrix specimens the wax layers were randomly oriented, but as more and more blocks were added to the model melanges, the wax layers became more strongly oriented parallel to the block edges as shown in Figure 5.6. Figure 5.6 is a photograph of failed specimen h-0-57. Note that most of the visible wax is oriented nearly parallel to the closest block edge. In the 90° specimens this wax alignment was therefore approximately perpendicular to the axial loading direction. The wax was much less stiff than the cemented soils. In fact, during

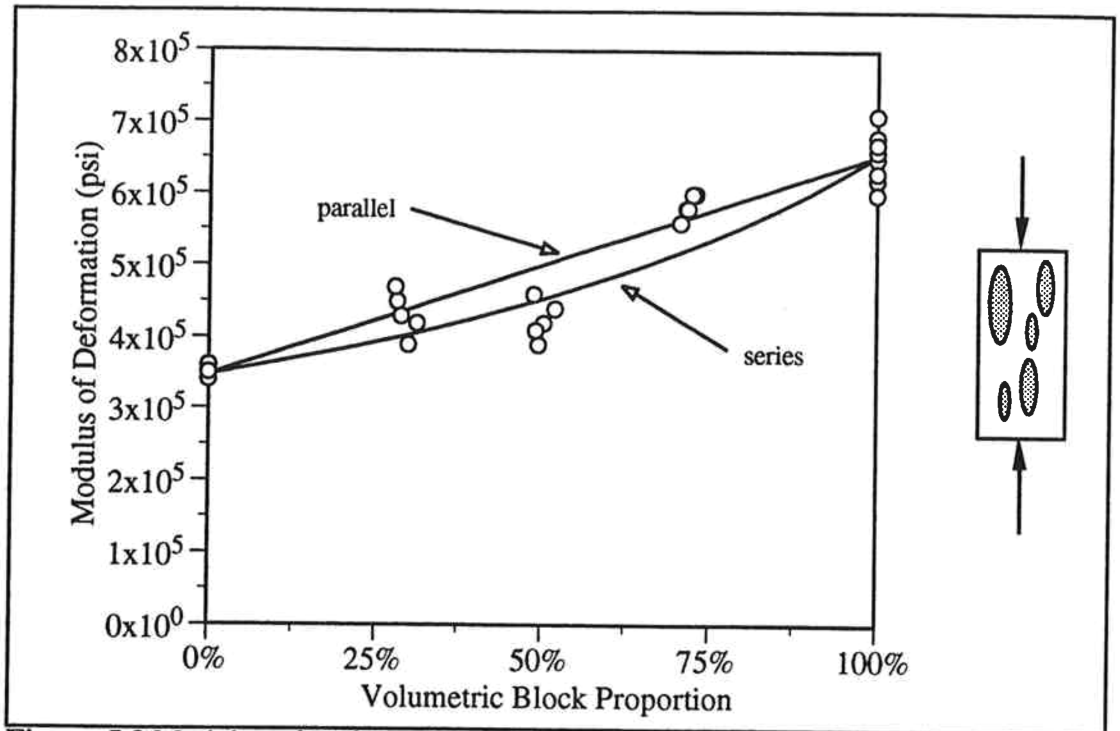

Figure 5.2 Modulus of Deformation versus Volumetric Block Proportion Including Bounds - 0° Orientation

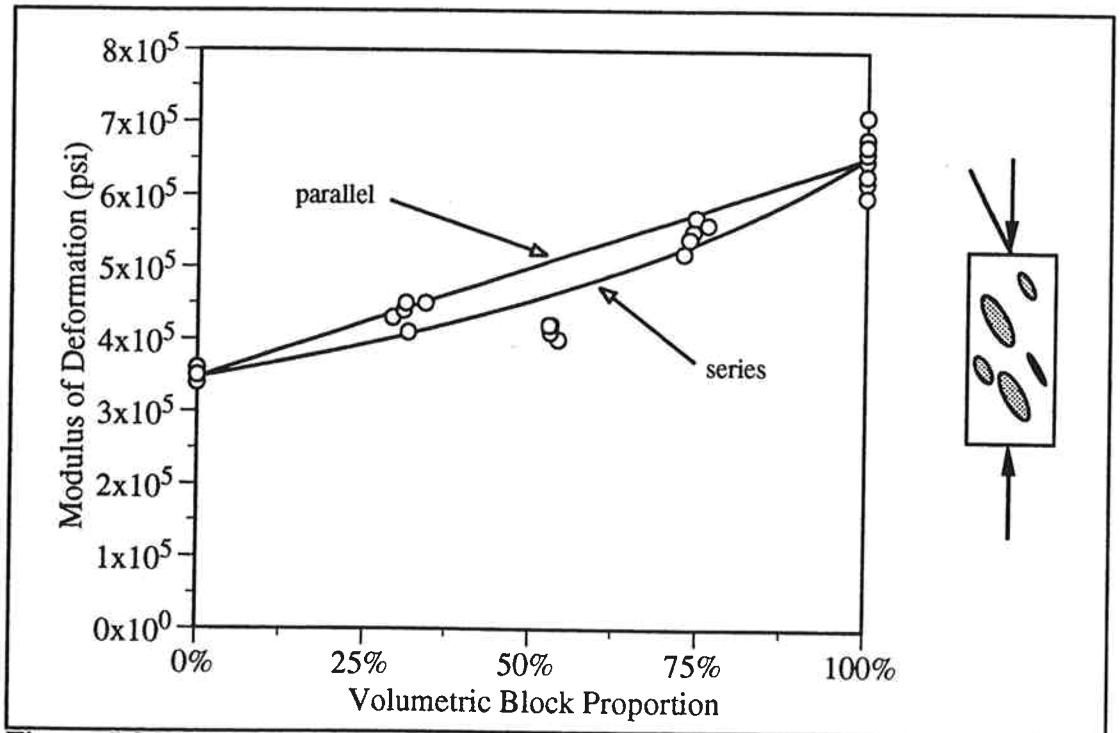

Figure 5.3 Modulus of Deformation versus Volumetric Block Proportion Including Bounds - 30° Orientation

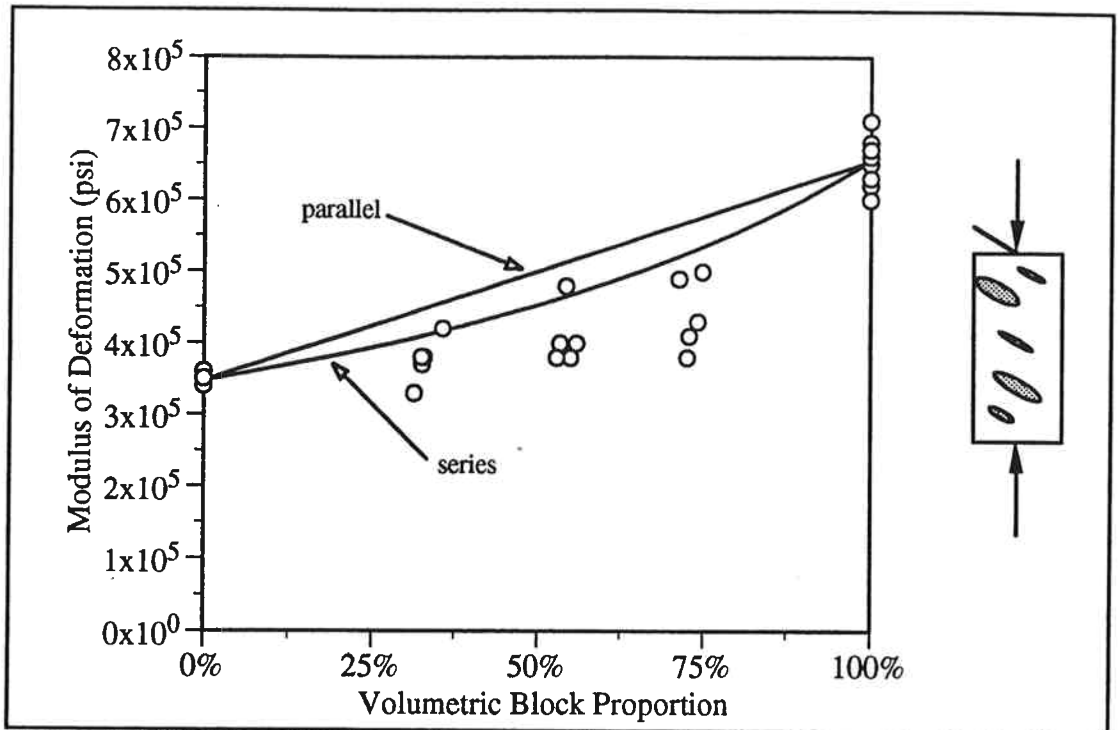

Figure 5.4 Modulus of Deformation versus Volumetric Block Proportion Including Bounds - 60° Orientation

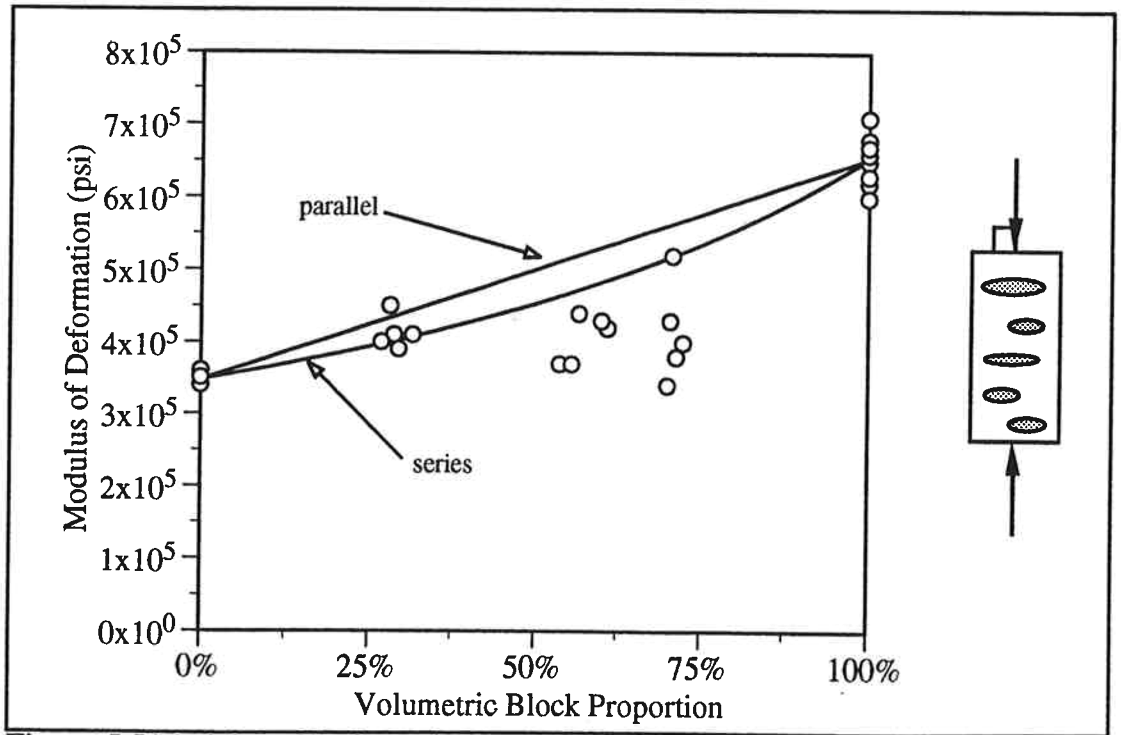

Figure 5.5 Modulus of Deformation versus Volumetric Block Proportion Including Bounds - 90° Orientation

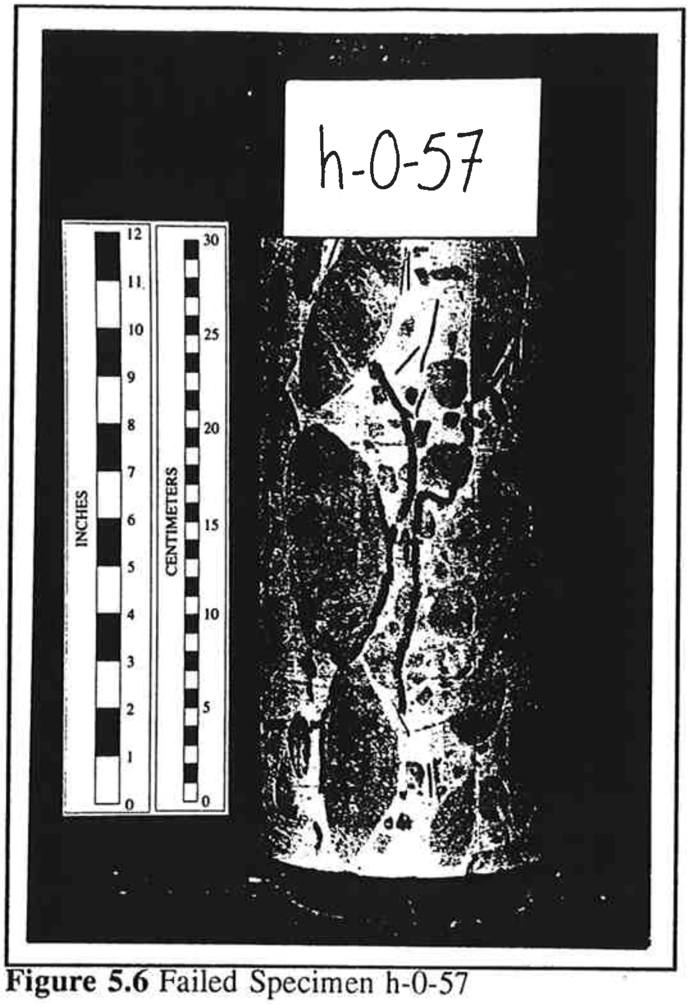

Figure 5.6 Failed Specimen h-0-57

tests run to determine the modulus of the wax, it was found that the wax underwent very rapid stress relaxation (creep); therefore, the wax layers almost behaved like thin tabular voids in the matrix. Tabular voids oriented at large angles relative to the direction of axial loading would, and indeed did, greatly reduce the moduli of the 60° and 90° specimens.

The seemingly anomalous behavior of the 0° and 30° medium block proportion specimens has not proven easy to explain. One possible explanation is that the matrix and block material used in these specimens had moduli lower than the average values found by testing. The 0° and 30° modulus data, along with series and parallel bounds based on the lowest matrix and block modulus values, rather than the average values as shown in Figures 5.2 through 5.5, are plotted in Figure 5.7 and 5.8. These bounds do fall closer to the medium proportion values, but they still are not low enough. Also, there is no clear reason why the lowest matrix and block modulus values would be only applicable to these specimens. One possibility is that the blocks were less dense, and hence less stiff, in the medium block proportion specimens. The blocks were consistently produced by the same process; therefore, there is no reason that this should have occurred. To verify that the blocks were not less dense in the medium block proportion specimens, a sample of blocks were taken and their densities checked. This check showed that there was no significant difference in block density between the medium block proportion specimens and the low and high block proportion specimens.

A more likely solution is based on the alignment of the wax layers in the specimens. Inspections of the 0° and 30° medium block proportion specimens indicated that an unusually large proportion of the wax layers were aligned approximately perpendicular to the axial loading direction, even though the blocks were aligned at much smaller angles to the axial loading direction (Figure 5.9 - specimen m-0-50 is a good example). An unusually large number of wax layers aligned perpendicular to the axial loading direction would explain this anomalous behavior.

It is now believed that during the fabrication process the wax layers were inadvertently aligned this way. During the fabrication of the low block proportion specimens, wax and some smaller blocks were tossed into the matrix material and then mixed in. Some larger (aligned) blocks were then added to the mix. More matrix material was then added. This process was repeated as the form was filled. The wax was therefore relatively randomly incorporated before the larger aligned blocks were added. On the other

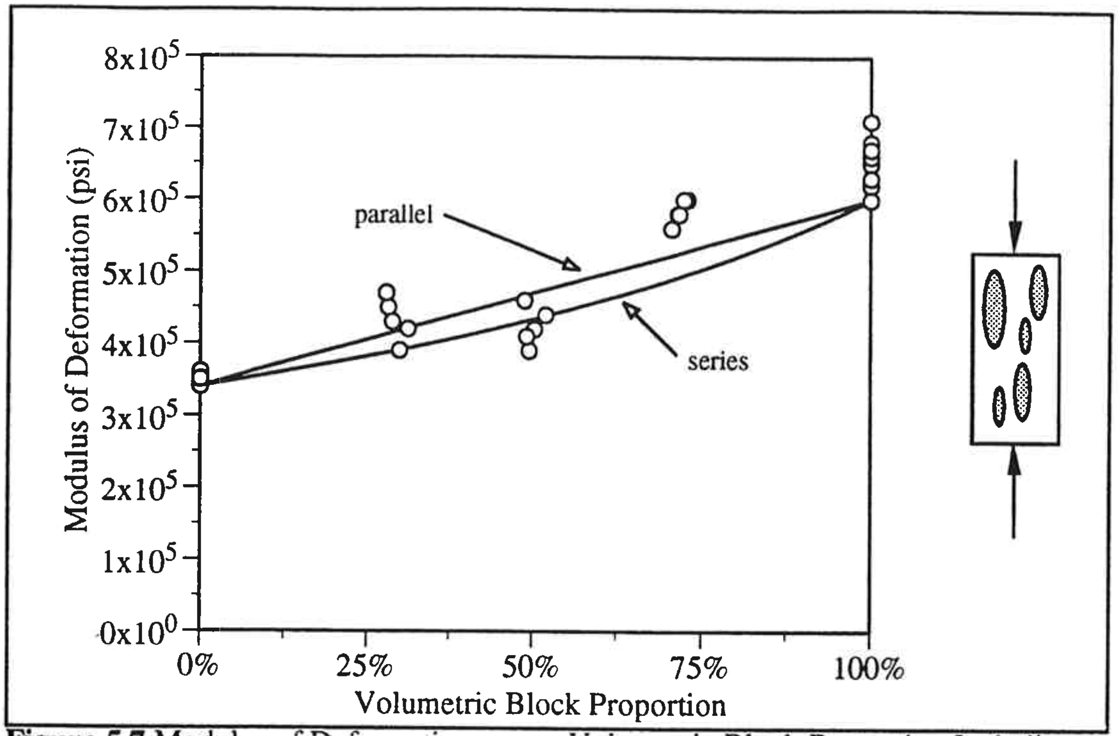

Figure 5.7 Modulus of Deformation versus Volumetric Block Proportion Including Minimum Bounds - 0° Orientation

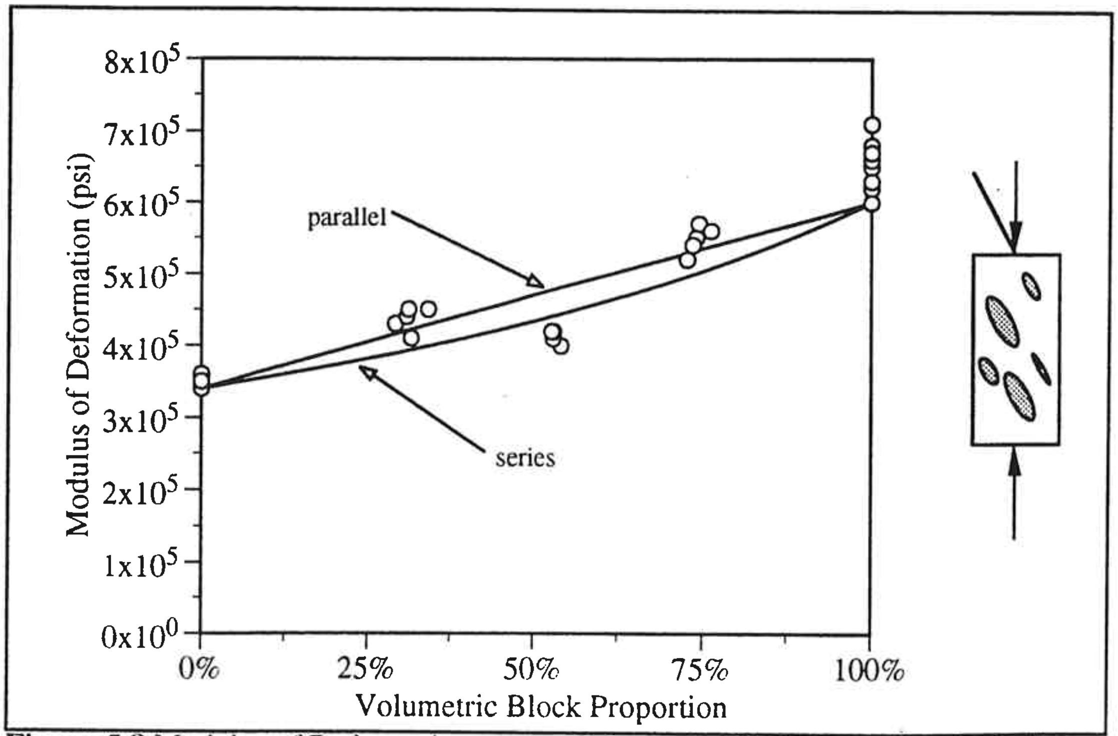

Figure 5.8 Modulus of Deformation versus Volumetric Block Proportion Including Minimum Bounds - 30° Orientation

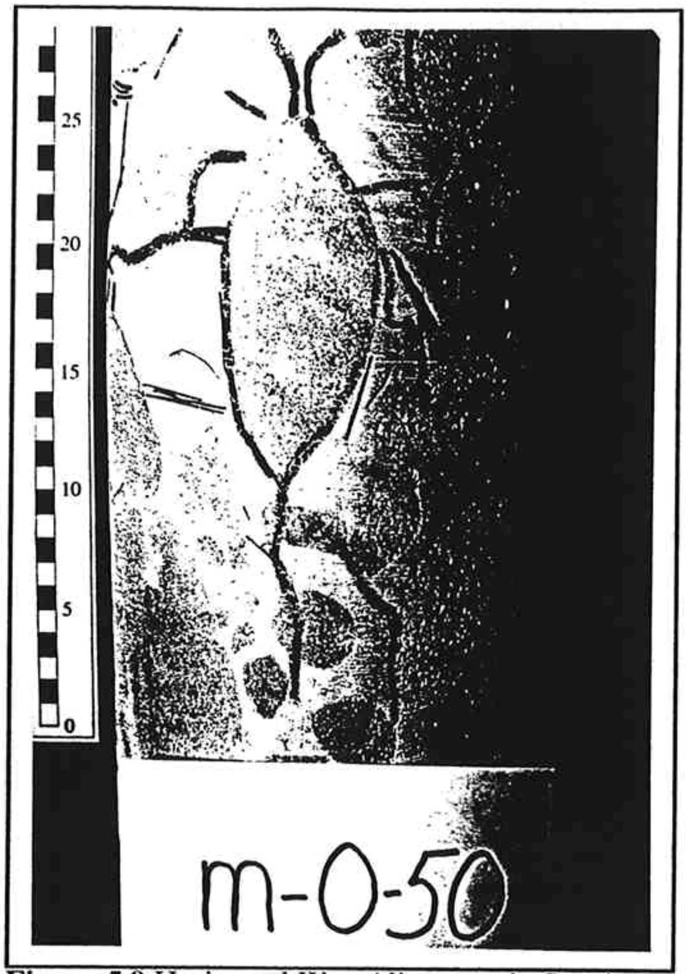

Figure 5.9 Horizontal Wax Alignment in Specimen m-0-50

hand, in the high block proportion specimens the wax and small blocks were also tossed into the mix, but there was not room in the form (because there were so many large blocks) to allow the wax to be randomized. The large proportion of aligned blocks therefore strongly oriented the wax. The medium block proportion specimens were somewhere in between. The wax was tossed into the matrix material, but, as was the case for the high proportion specimens, could not be randomized due to the number of large blocks. Although the block proportion was relatively high, it was not high enough to strongly align all the wax layers; hence, the orientation in which the wax was initially tossed into the form was important. In retrospect, it is believed that the layers were inadvertently preferentially oriented perpendicular to the direction of axial loading due to the manner in which the wax layers were picked up and then dropped into the form.

5.2 Strength Behavior

The failed specimens provided clear evidence as to how and why the blocks affected the cohesion and angle of internal friction of these model melanges. As discussed in Chapter 4, the surfaces along which shear failures occurred generally formed at the block-matrix contacts and along the wax "shears". One reason why the failures occurred at the block-matrix contacts is that this interface was the boundary between materials with dissimilar deformability properties. Because of the difference in deformability properties, the block and matrix material would tend to undergo differential strains (and as a result fail) at their contact (unless the stresses within the block and matrix material were different in exactly such a way that the materials would undergo the same strains at their contact). Contact failure resulted, at least in part, because the block and matrix materials wanted to undergo differential strains and these differential strains induced additional stresses at the contacts.

Another factor is that the contacts were surfaces of weakness. Triaxial compression tests on six specially prepared 2-inch diameter cylindrical specimens with throughgoing planar block-matrix contacts or wax layers were run to illustrate this fact. Figure 5.10 is a sketch showing the two types of specimen tested, and Figure 5.11 is a photograph showing a failed specimen of each type. Test results are presented in Appendix E.

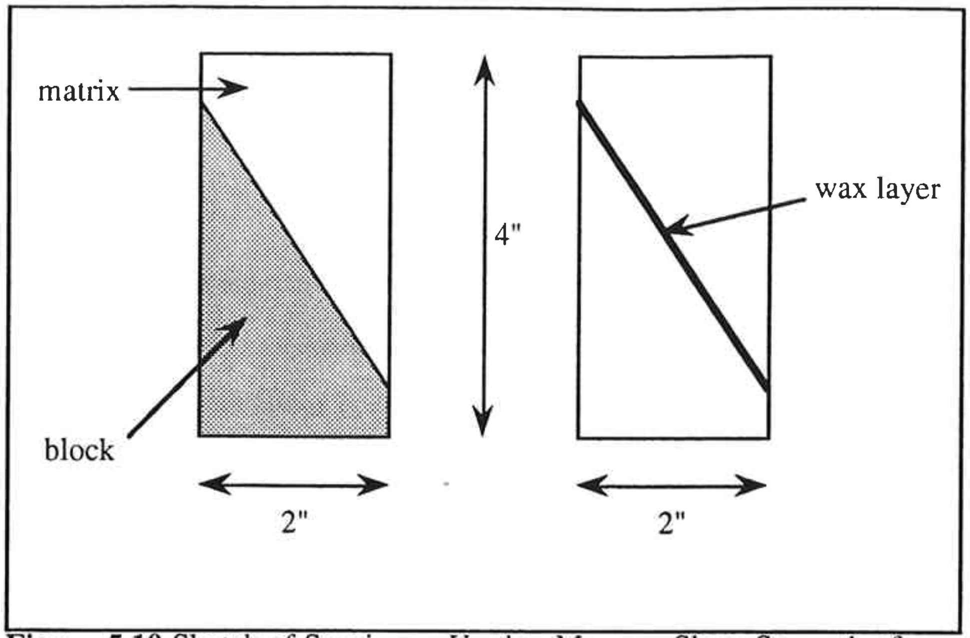

Figure 5.10 Sketch of Specimens Used to Measure Shear Strength of Block-Matrix Contacts and Wax "Shears"

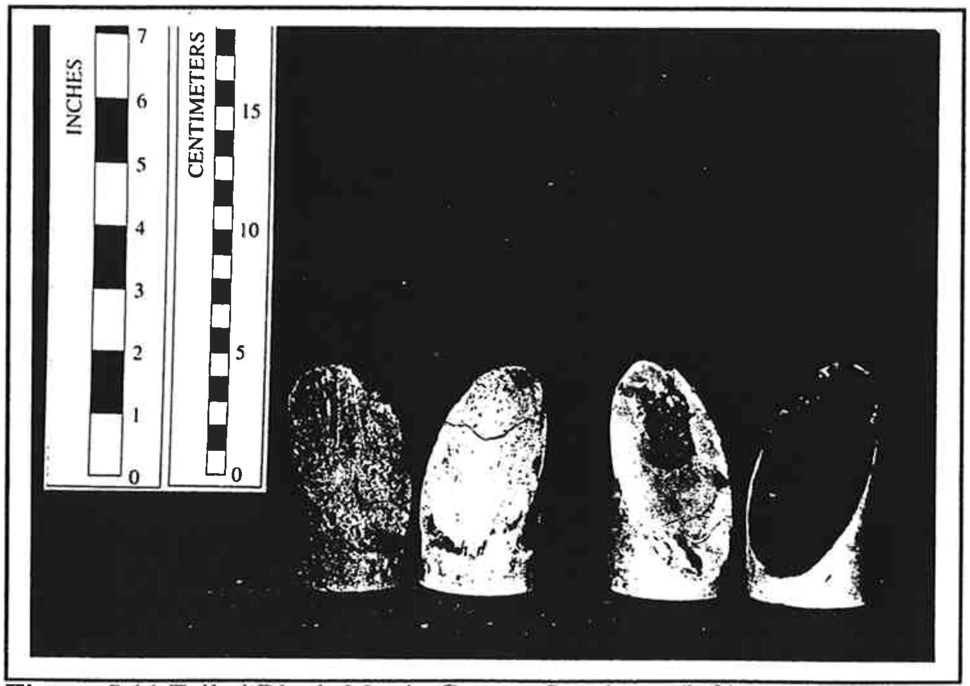

Figure 5.11 Failed Block-Matrix Contact Specimen (left) and Wax "Shear" Specimen (right)

Chapter 5 Discussion of Physical Model Test Results

The Mohr-Coulomb strength parameters determined for the block-matrix contact were a cohesion of 150 psi and a angle of internal friction of 30°. The wax shears had a cohesion of 56 psi and an angle of internal friction of 12°.

Increasing the block proportion increased the number of block-matrix contacts, and, although the total number of wax "shears" in the specimens decreased proportionally with the volume proportion of matrix, the remaining wax layers were more consistently aligned with the large blocks. The higher block proportion specimens therefore had a larger number of more well aligned weakness surfaces, the result being a lower mass cohesion. This being the case, had the surfaces of weakness in the models had lower cohesions, the decrease in mass cohesion with increasing block proportion would have been even more substantial.

The increase in the angle of internal friction can be explained by two factors. First, because the angle of internal friction between the block and matrix materials ($\phi_j = 30°$) was higher than the angle of internal friction for the pure matrix ($\phi = 24.7°$), and because the failure passed predominately along the block-matrix contacts, the angle of internal friction of the block-in-matrix models would be expected to be higher than the pure matrix angle of internal friction. This increase would be somewhat tempered however, because the blocks were often surrounded by many wax "shears" ($\phi_j = 12°$) along which sliding occurred. Figure 5.12 shows the wax "shears" along the failure surface of specimen h-30-150.

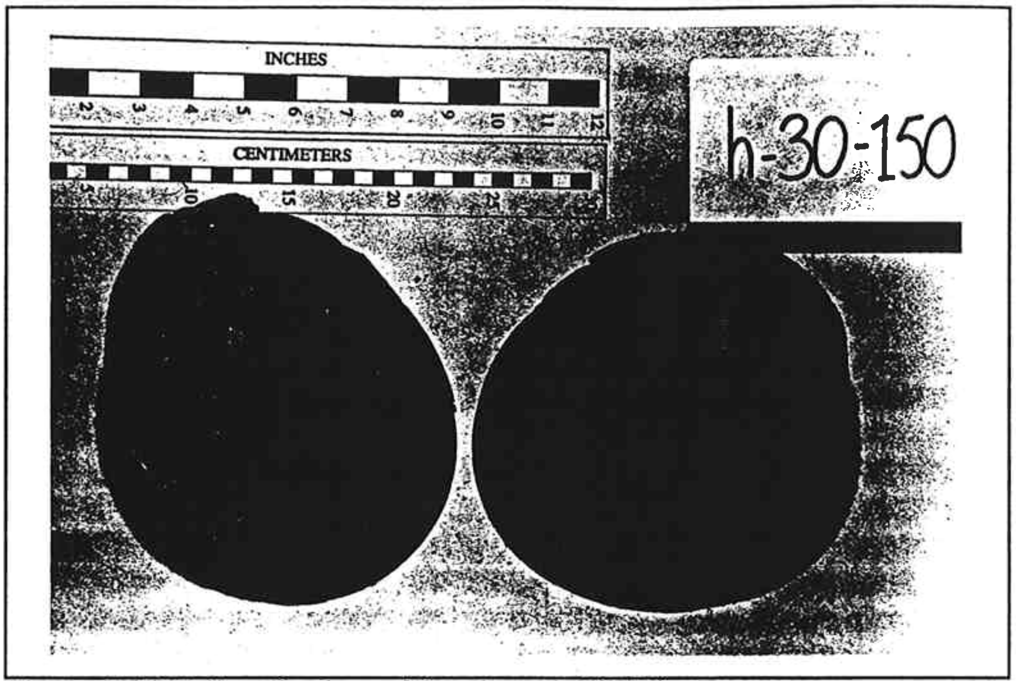

Figure 5.12 Failure Surface of Specimen h-30-150

A second, and more important factor is the effect blocks had on the tortuousity of the failure surface. As mentioned in Chapter 2, an increase in tortuousity of the failure surface due to the presence of blocks in bimrocks has been hypothesized by D'Elia et al. (1988) for melange and Savely (1990) for boulder conglomerate. Figure 5.13 shows a cross-section of failed specimen h-0-150. The blocks essentially created failure surface "roughness". In fact, the failure surface only very rarely passed through the blocks. The result of this roughness is that dilation along the failure surface and/or crushing of the matrix needed to occur to allow sliding. Minor matrix crushing can be seen near the center of the specimen in Figure 5.13. Because failure only rarely passed through the blocks, it does not appear that the strength (cohesion and angle of internal friction) of the blocks in the block-in-matrix models played a role in the strength of the mass. The strength contrast between the blocks and matrix required to prevent failure through the blocks is not known, but these test results indicate that the strength difference need only be modest.

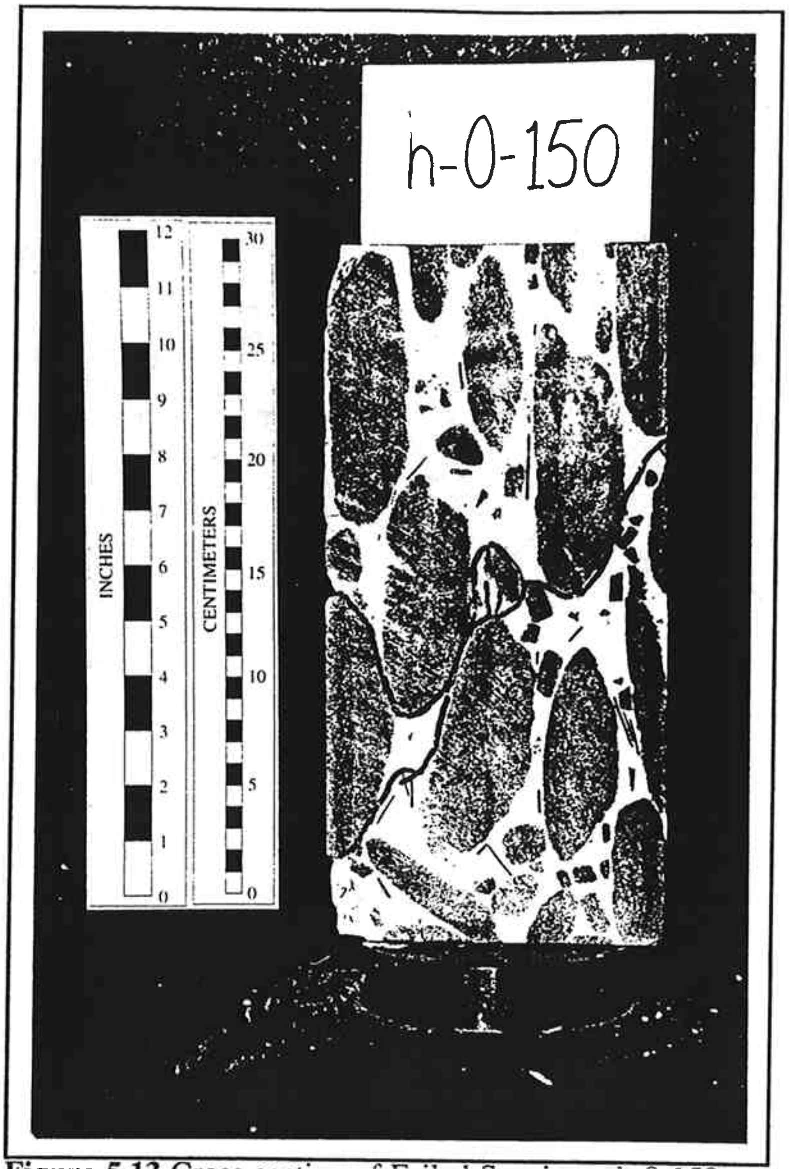

Figure 5.13 Cross-section of Failed Specimen h-0-150

The increased tortuousity of the failure surface readily explains the increased angle of internal friction with block proportion. As the block proportion increased, the greater was the number of blocks to be avoided by the failure surface in the same volume. Interestingly, some of the high block proportion specimens had angles of internal friction higher than the pure block material. Due to the drop in cohesion with block proportion, though, the overall shear strengths of theses specimens were lower.

Block-to-block contacts are another possible factor that could explain part of the increase in angle of internal friction with increasing block proportion, but substantial block-to-block contact was rarely found even in the high block proportion models; therefore, it is unlikely that this factor played any significant role. This is probably the case in actual melange as well. During my observations of Franciscan melange I rarely found block-to-block contact even in volumes with high block proportions.

5.3 The Importance of Block Orientation on Field Behavior

The model failures showed that, although block orientation did not affect the strength of the models too significantly, the orientation of the larger blocks in particular strongly controlled the orientation of the failure. Because these models were tested in triaxial compression, there was significant freedom as to the orientation in which the failure surface could form. On the other hand, if these models had been tested in direct shear, the failure surface orientation would have been much more restricted by the nature of the test. Due to the geometrical restriction of the failure surface inherent in the direct shear test, block orientation most likely would have had a more significant effect on the strength. If, for instance, a horizontal shear was attempted through a model with vertically inclined blocks, assuming the blocks are of significant size relative to the sample size, failure would require that either (1) the failure surface be very "rough" (failure around the vertically aligned blocks), (2) the failure surface be forced through the blocks, or (3) significant crushing and deformation of the matrix take place to allow the blocks to rotate or move horizontally. Any one of these effects would result in a larger strength increase due to block orientation than was found in the triaxial models.

Some of this same thinking can be used to examine a few field situations. It is easy to imagine situations in which geometrical limitations on the orientation of a potential failure are present in the field. In these cases it is believed that block orientation might be a significant factor affecting the stability of the mass.

First, consider the effect of melange block orientation on the stability of a slope. Figures 5.14(a) and (b) show a cross-section of a hillslope with approximately the same block proportions but different block orientations. The blocks are approximately perpendicular to the slope face in Figure 5.14(a) and approximately parallel to the slope face in Figure 5.14(b). A potential failure surface is illustrated for each case. Note that in Figure 5.14(a) the failure surface must deviate to avoid blocks, whereas in Figure 5.14(b) the failure surface can form along the block-matrix contacts. The failure surface is therefore likely to be more tortuous when the blocks are oriented perpendicular to the slope face. In addition, the strength along the failure surface formed is likely to be much lower in the case when the blocks are oriented parallel to the slope face because of the prevalent shearing in a melange at the block-matrix contacts and in the matrix itself approximately parallel to the block edges.

A dam foundation provides another interesting case. Cross-sections of two dam foundations with approximately the same block proportions but different block orientations are shown in Figure 5.15(a) and (b). A potential failure surface (assuming the failure passes around the blocks) is shown in for each case. Intuitively, the foundation with the vertically aligned blocks (Figure 5.15(a)) will be more stable against shear failure then the foundation with horizontally aligned blocks (Figure 5.15(b)) for the same reasons given in the hillslope stability example.

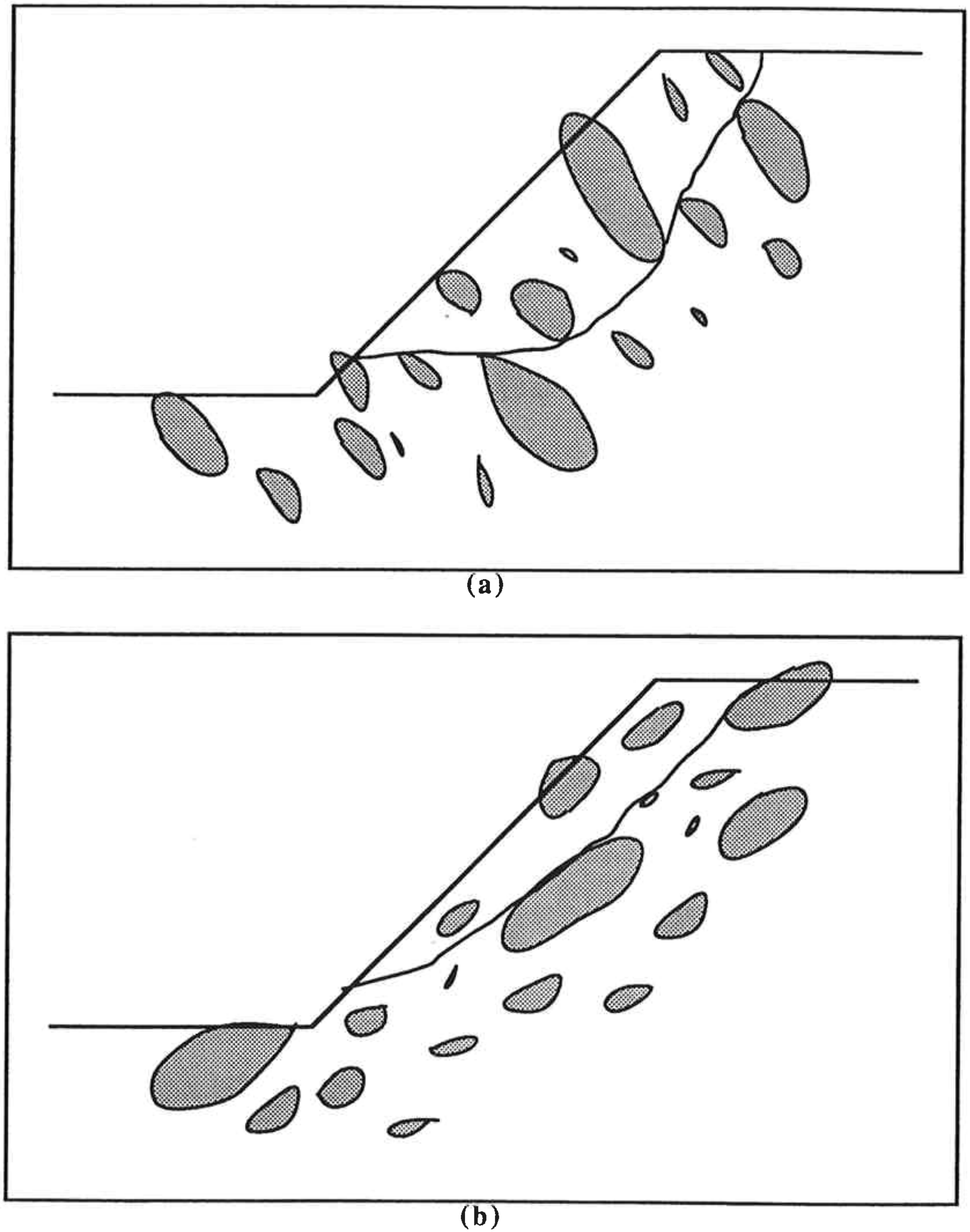

Figure 5.14 Slope with Potential Failure Surface **(a)** Blocks Aligned Perpendicular to Slope **(b)** Blocks Aligned Parallel to Slope

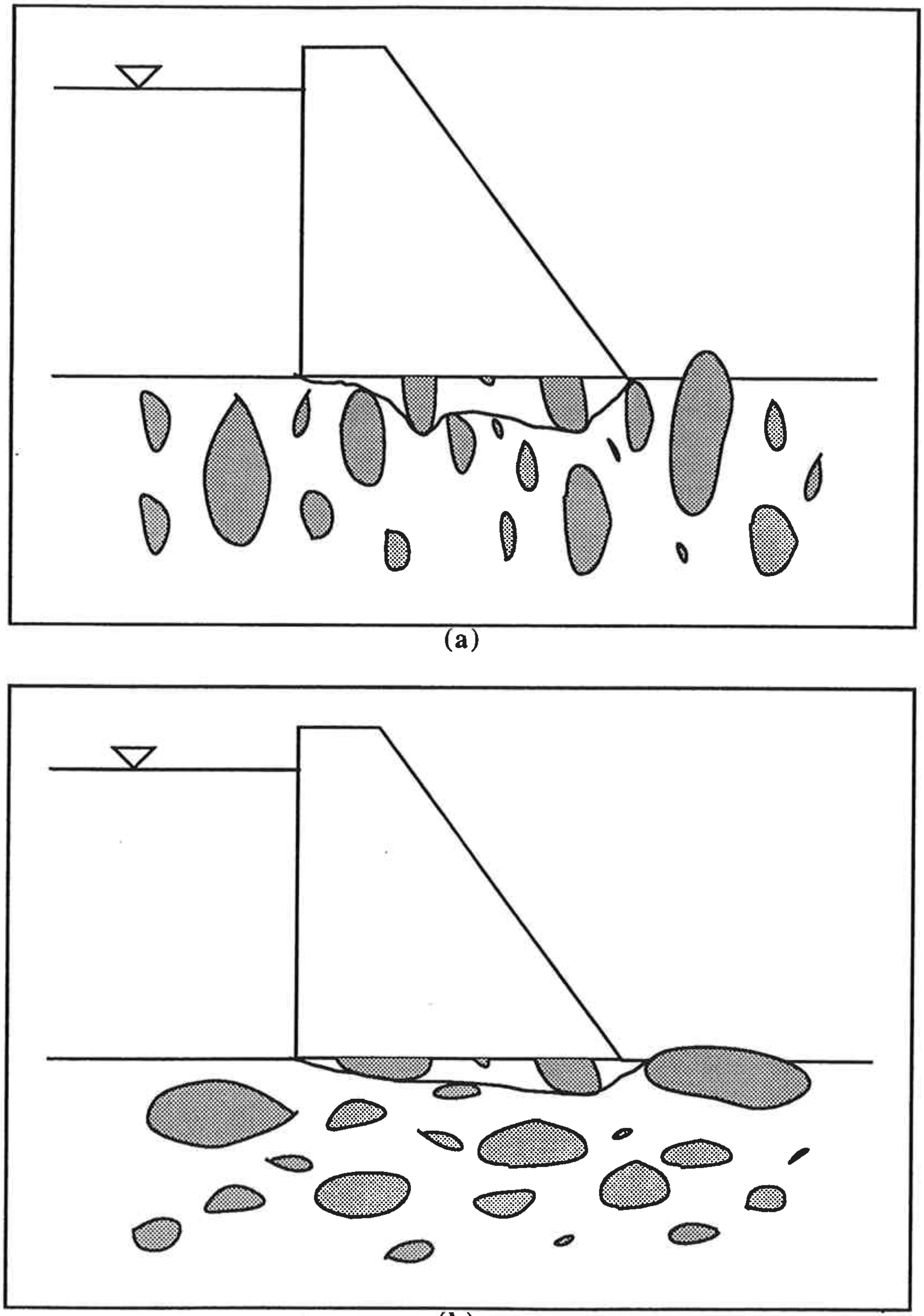

(a)

(b)

Figure 5.15 Dam Foundation with **(a)** Vertically Aligned Blocks **(b)** Horizontally Aligned Blocks

Based on the model tests and these simple schematic examples, it appears that the location and orientation of the largest blocks in a melange mass are particularly important. The largest blocks not only create the greatest deviations in the shear surface (increasing the angle of internal friction), but they also provide the most continuous surfaces of weakness along which the mass might fail (decreasing the cohesion). This is an important consideration that goes beyond block proportion. For instance, it is possible in a low block proportion melange mass that the presence of one large block in an advantageous location (at the toe of a slope for instance) could mean the difference between the mass being stable and unstable. On the other hand, it is conceivable in a high block proportion melange with adversely oriented blocks that the block-matrix contacts could create an almost throughgoing surface of weakness along which the mass could fail.

5.4 Model Test Limitations

Although it is believed that these physical models sufficiently recreated some basic characteristics of melange (and perhaps some other block-in-matrix rocks), they did have some limitations. These limitations are enumerated below.

1. Certain features that may play a very important role in field behavior of a melange were not modeled. For example, large shears are often found in melanges. These zones of weak material may have a significant impact on the field behavior of a melange mass; therefore, it is important that these shears be identified and accounted for in engineering design. Another example is the potential for a single large block to greatly influence the mass behavior as discussed in the previous section.

2. Only one block size distribution and set of block shapes were employed. These two variables might have a significant impact on the mechanical behavior of a melange, although it is believed that the general behavioral trends found in this model study would not have changed even if these variables had been altered.

3. Blocks of only one stiffness and strength were employed. In an actual melange, various rock types are often found as blocks at a single site. These different blocks will have different stiffnesses, therefore the actual problem of determining the mass stiffness is a multi-component rather than a two-component problem. Because the strengths of the blocks do not seem to affect the mass strength, the fact that blocks with a variety of strengths were not used probably did not make a difference in the findings of this model study.

4. Only one matrix material was used. If, for example, a much weaker matrix material had been used, one would expect the failures of the physical models to have involved more matrix crushing. Although it is likely that the failure surface still would have formed at the block-matrix contacts, certain blocks might have rotated and translated as crushing and deformation of the matrix material took place during shearing (more like blocks in a soil matrix). The triaxially tested specimens of actual melange discussed in the following chapter verify this hypothesis.

CHAPTER 6

TRIAXIAL TEST RESULTS FOR ACTUAL MELANGE SPECIMENS

6.1 Source of Specimens

The Franciscan melange specimens discussed in this chapter were collected from beneath Scott Dam. Scott Dam is a concrete gravity structure located northeast of Ukiah, California, about 115 miles north of San Francisco. Figure 6.1 is a map showing the dam location. The dam is owned and operated by the Pacific Gas and Electric Company (PG&E). Concerns over the stability of the dam created the need for multiple exploratory borings into the foundation rock over the years, the last of which were completed in 1982. The samples studied here are some of those collected in the fall of 1982.

Figure 6.2 shows a plan view of the dam. Five borings were completed in 1982. They are identified as 1982-1, 1982-2, 1982-4, 1982-8 and 1982-9. The first three borings were made along the dam crest, and the latter two were made at the base of the spillway. The samples discussed in this chapter were tested in triaxial compression by Harding-Lawson Associates (HLA) in late 1982 and early 1983. A total of 20 tests were run. The failed specimens remained in storage for over ten years and were only recently (February 1994) scavenged from a PG&E storage locker. Many of the specimens became completely disaggregated over the years, but seven of them were still in relatively good shape. Those seven are analyzed in the following sections. The hope was to show that the strength behavior exhibited by these specimens is in concert with that shown by the physical models discussed previously.

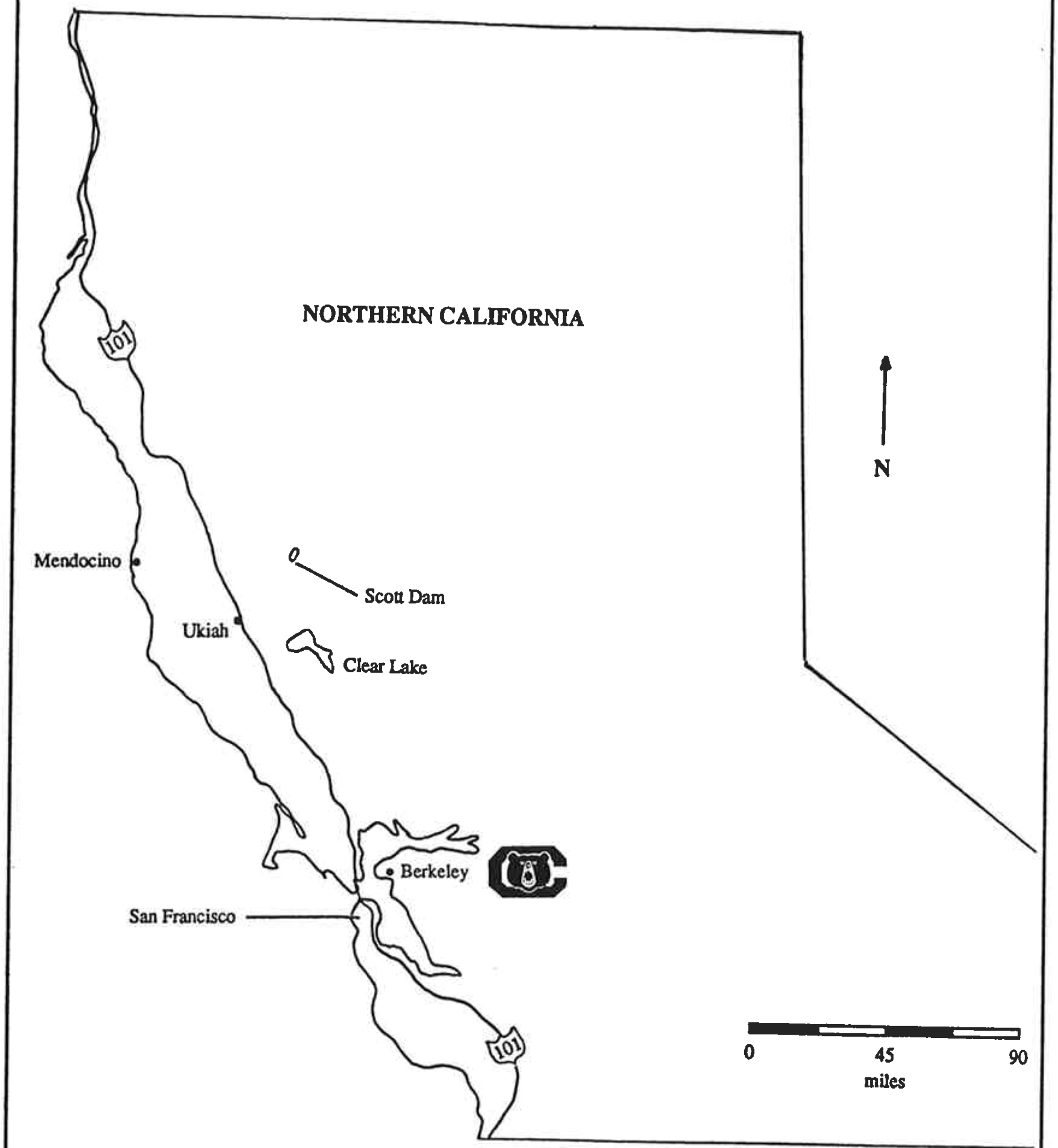

Figure 6.1 Map Showing Location of Scott Dam

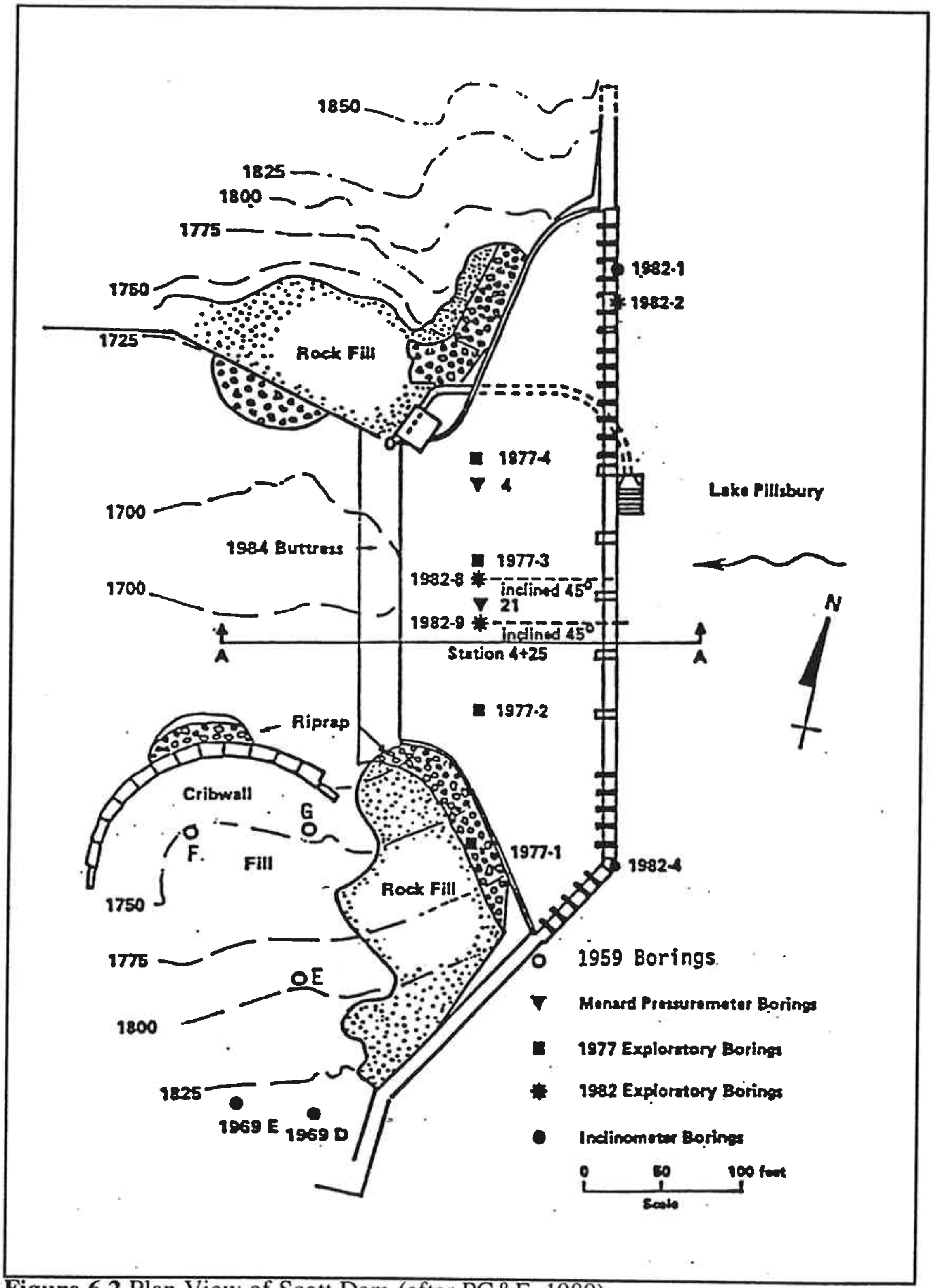

Figure 6.2 Plan View of Scott Dam (after PG&E, 1989)

6.2 Specimen Descriptions

The seven reasonably intact specimens were 82-1@ (a depth of) 125.9', 82.8@39.1', 82-8 @113.0', 82-8@114.0', 82-9@45.4', 82-9@51.5' and 82-9@53.0'. Photographs of what remained of each are given in Figures 6.3 through 6.9. Specimens were reported to be 3.95 to 4.16 inches in diameter with length-to-diameter ratios of 2 to 2.3 before testing (HLA, 1983). Plaster caps were cast on many of the specimen ends to provide flat surfaces for loading. Plaster was also used to patch holes in the specimens when necessary. Some of the remnants of this plaster (the white material) can be seen in the specimen photos.

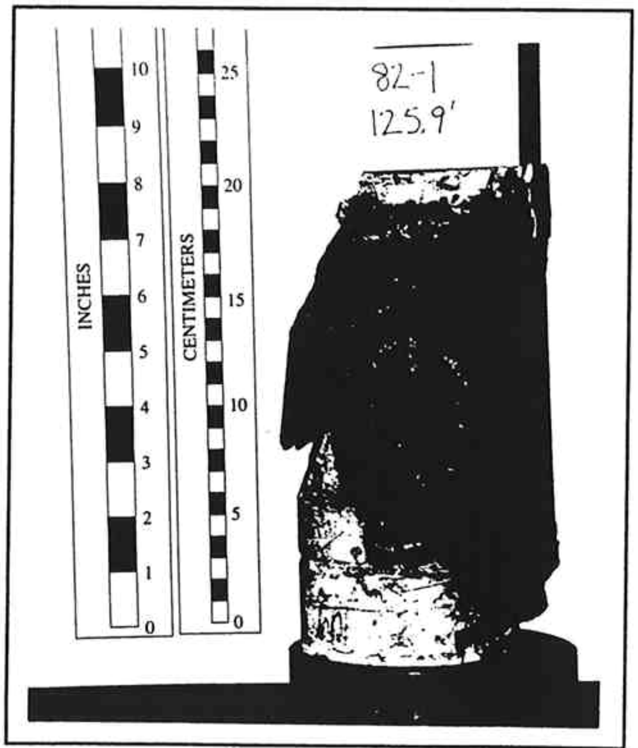

Figure 6.3 Specimen 82-1@125.9'

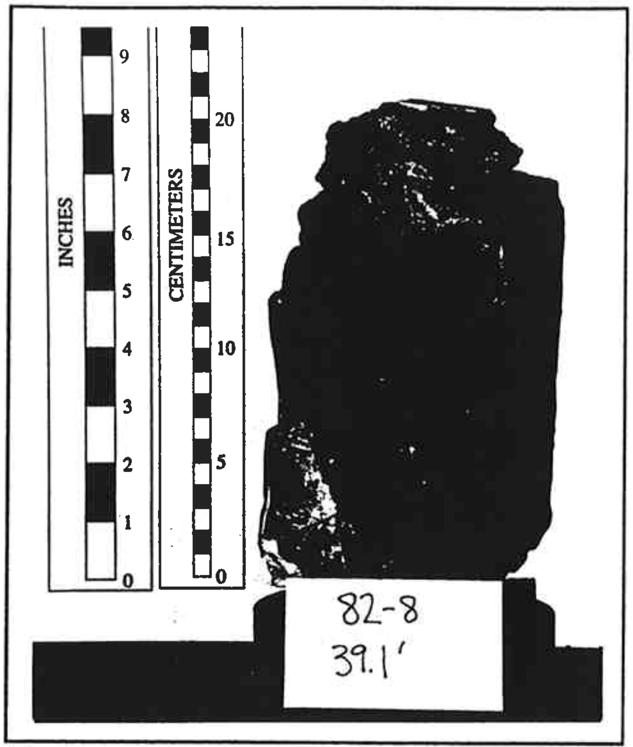

Figure 6.4 Specimen 82-8@39.1'

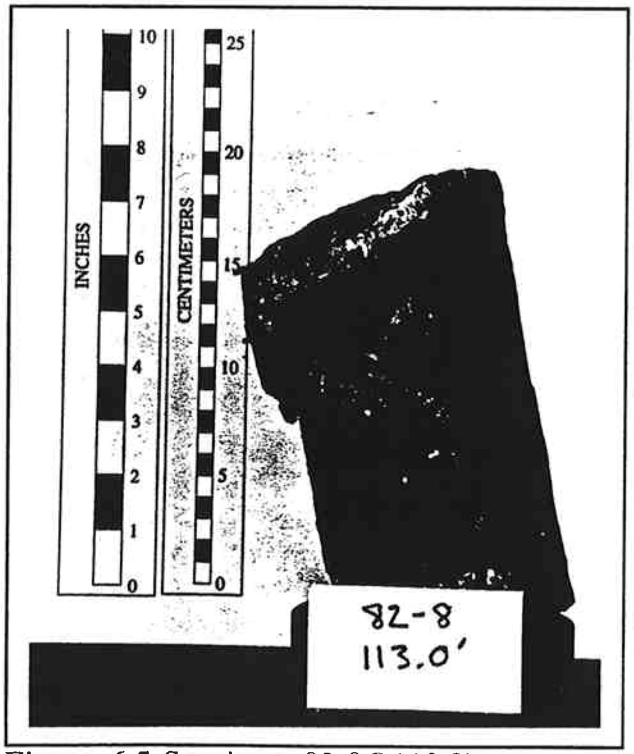

Figure 6.5 Specimen 82-8@113.0'

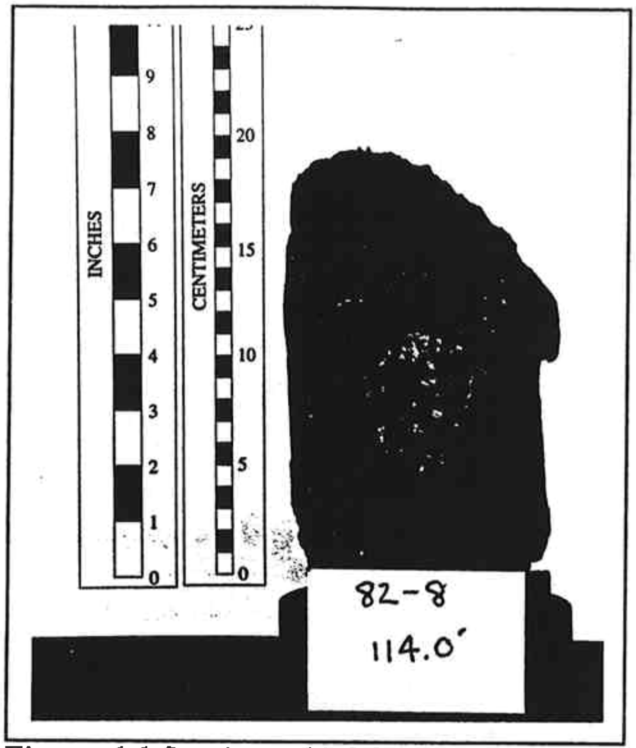

Figure 6.6 Specimen 82-8@114.0'

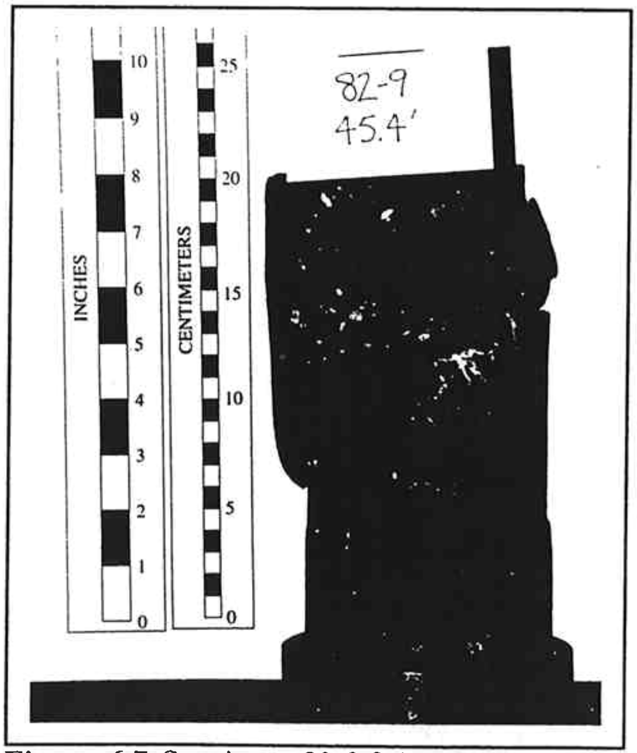

Figure 6.7 Specimen 82-9@45.4'

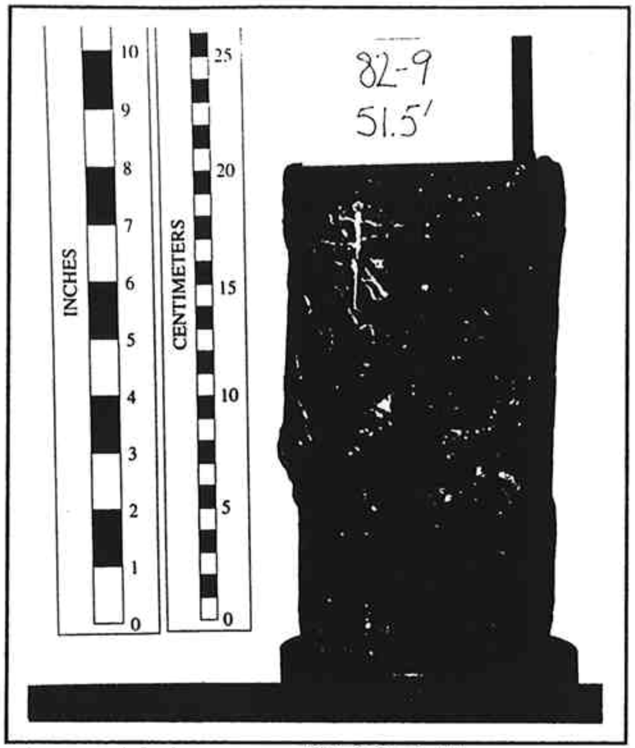

Figure 6.8 Specimen 82-9@51.5'

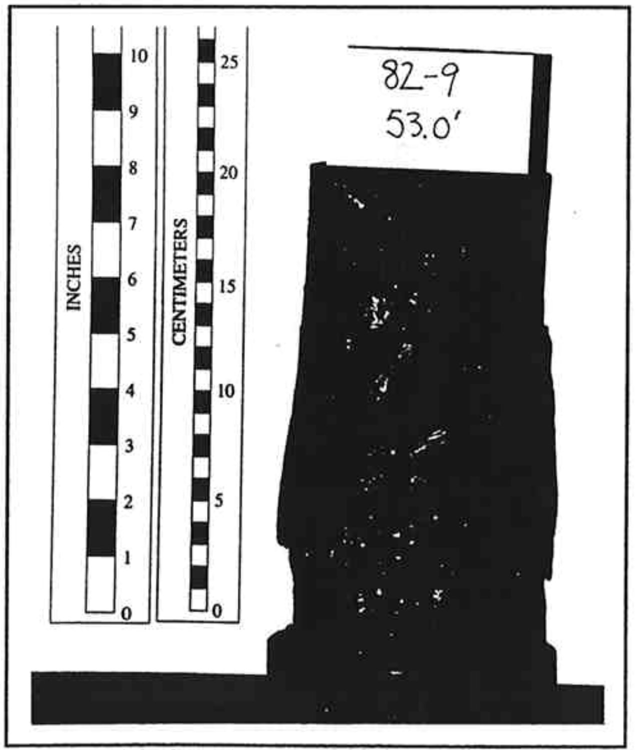

Figure 6.9 Specimen 82-9@53.0'

The specimens were all mixtures of sheared shale and harder blocks of either greywacke sandstone and/or intact shale. The greywacke appears as the lighter component in the photographs. Table 6.1 gives brief descriptions of the specimens and how they failed.

It was immediately evident when studying the failures in these specimens that they were quite similar to the failures exhibited by the physical models. The failures formed around the blocks and generally followed the block-matrix contacts. Figure 6.10 is a closer view of Specimen 82-9@51.5' that shows displacement along a block-matrix contact. The dark line just to the right of the specimen center shows a shadow caused by the sheared shale matrix overhanging the block on the right side of the specimen. This is strong evidence that the physical models properly replicated melange failure behavior. The failures showed more matrix crushing than the physical models. This was most likely due

Figure 6.10 Close-up of Specimen 82-9@51.5'

Table 6.1 Scott Dam Specimen Descriptions

Specimen	General Description	Failure Description
82-1@125.9'	mostly greywacke, but contains a single continuous steeply dipping zone of sheared shale through the specimen	failed along the steeply dipping sheared shale seam, fractured greywacke also spalled off outside of specimen
82.8@39.1'	mixture of greywacke and sheared shale	shear zone formed at greywacke block edges at approximately a 30° angle relative to the axial loading direction
82-8@113.0'	mixture of greywacke, intact shale and sheared shale	shear zone formed around stronger blocks at approximately a 70° angle relative to axial loading direction
82.8@114.0'	mixture of greywacke, intact shale and sheared shale	shear zone formed around stronger blocks at approximately a 55° angle relative to the axial loading direction
82-9@45.4'	sheared shale at the specimen ends with single block of greywacke in the middle	sheared along throughgoing shale-greywacke contact (approximately 50° relative to the axial loading direction)
82-9@51.5'	mostly sheared shale with a few blocks of greywacke	shear zone formed around greywacke blocks at approximately a 45° angle relative to the axial loading direction
82-9@53.0'	sheared shale with very few small greywacke fragments	shear zone formed at approximately a 45° angle relative to the axial loading direction

to the fact that the melange matrix was substantially more sheared and crushed (weaker) than model matrix prior to testing. Also, the melange specimens were tested to much larger axial strains than the models, and it is believed that more matrix crushing would have occurred in the physical models if they had been taken to higher strains as well.

The volumetric proportion of stronger blocks (larger than a No. 4 sieve) in each of the specimens has been estimated. Appendix F gives a detailed description of how these proportions were estimated and Table 6.2 presents the proportions determined.

Table 6.2 Volumetric Block Proportions of Scott Dam Specimens

Specimen	Volumetric Block Proportion
82-1@125.9'	72%
82.8@39.1'	40%
82-8@113.0'	71%
82.8@114.0'	36%
82-9@45.4'	37%
82-9@51.5'	23%
82-9@53.0'	13%

6.3 Strength Results

The test results presented here were taken from the original testing report (HLA, 1983). Specimens 82-1@125.9', 82-8@39.1', 82-9@45.4', 82-9@51.5' and 82-9@53.0' were tested under consolidated undrained conditions with pore pressure measurements and specimens 82-8@113.0' and 82-8@114.0' were tested under consolidated drained conditions. Failure was defined as the point of maximum effective stress ratio, $(\sigma_1'/\sigma_3')_{max}$. It was determined in a later report by PG&E (1989) that the cohesions of these specimens were close to zero. Using the assumption of zero cohesion, it was possible to calculate an effective stress angle of internal friction (ϕ') for each specimen. The values of σ_1' and σ_3' at failure and the method used to calculate the effective stress angle of internal friction are also given in Appendix F. Table 6.3 presents the effective stress angles of internal friction.

Table 6.3 Effective Stress Angles of Internal Friction for Scott Dam Specimens

Specimen	ϕ'
82-1@125.9'	30.4°
82.8@39.1'	48.2°
82-8@113.0'	54.3°
82.8@114.0'	40.1°
82-9@45.4'	27.6°
82-9@51.5'	32.0°
82-9@53.0'	28.4°

Figure 6.11 is a plot of effective stress angle of internal friction versus volumetric block proportion. It appears that the effective stress angle of internal friction generally increased with increasing block proportion.

The strengths of specimen 82-1@125.9' (point 2) and 82-9@45.4' (point 1) fell well below the trend set by the other specimens. An examination of these specimens and their modes of failure indicates why these strengths were so much lower. Specimen 82-1@125.9' had a steeply inclined, throughgoing zone of sheared shale (see Figure 6.3). The failure took place within this weak zone, therefore only the strength of the matrix was actually measured. Note that an effective stress angle of internal friction of 30.4° is close to the value for specimen 82-9@53.0' which was almost pure sheared shale. Specimen 82-9@45.4' also had a prominent weakness plane. In this case it was a throughgoing block-matrix contact (see Figure 6.7). The measured strength was therefore representative of the block-matrix contact strength, and not the strength of the melange.

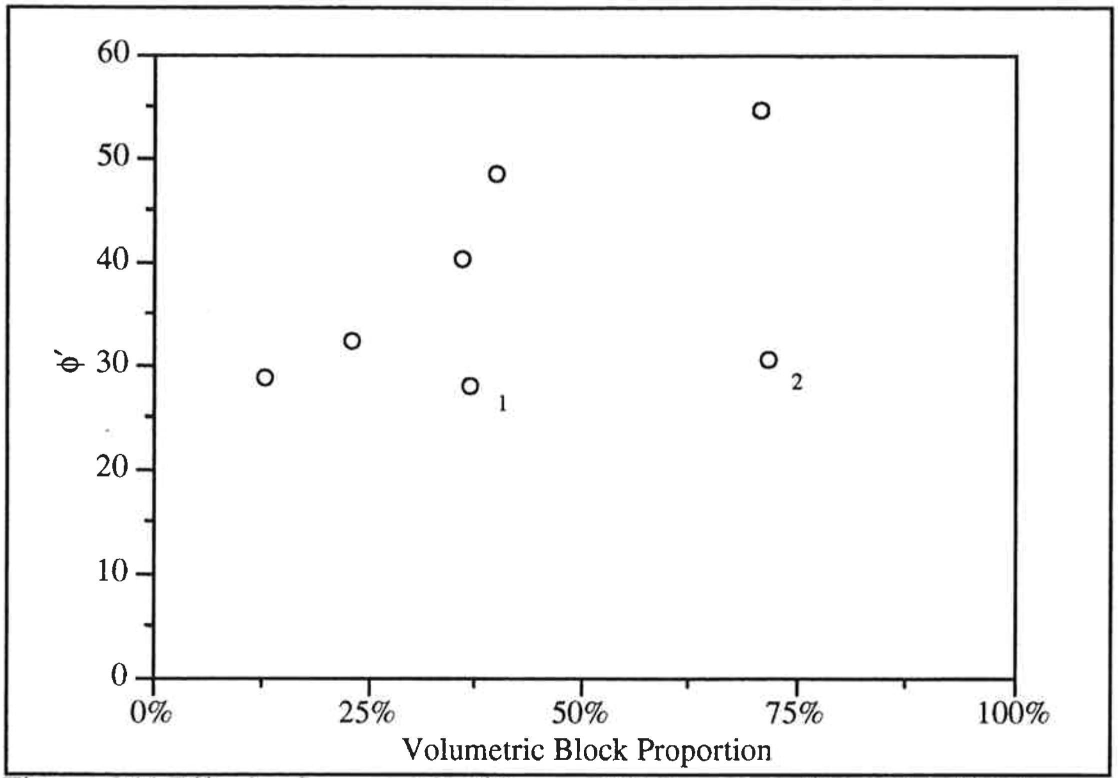

Figure 6.11 Effective Stress Angle of Internal Friction versus Volumetric Block Proportion

The remaining specimens consisted of blocks in a matrix; hence, they were more representative of the melange mass. These specimens showed an increase in effective stress angle of internal friction of about 4.5° per 10 percent increase in block proportion. This increase is similar to, although slightly larger than, the increase found for the physical models. The increase may well have been larger because the blocks in the melange samples were not nearly as well oriented or well distributed as in the physical models. Differences in the block shapes and block size distributions between the actual melange samples and the physical models might also explain why the increase was greater for the actual melange samples.

6.4 Stress-Strain Results

Stress-strain data were infrequently taken by hand during the Harding-Lawson triaxial tests.

The two stress-strain curves for the drained specimens are presented in Figure 6.12. The "stress difference" (vertical axis) is simply the difference between the axial stress and the confining stress (σ_1-σ_3). Specimen 82-8@113.0' had a modulus of deformation of approximately 1800 ksf, while specimen 82-8@114.0' had a modulus of deformation of approximately 1200 ksf. As expected, the specimen with a higher block proportion (82-8@113.0') was stiffer.

Figure 6.13 presents the stress-strain curves for the five undrained tests. Note that these curves have a significantly different shape than those for the drained specimens. This is due to pore pressure changes that take place during an undrained test. The stress difference did not peak (i.e. continued to increase with strain) because the specimens were quite dilatant. This dilatancy caused negative pore pressures to develop as the test progressed, increasing the effective confining stress. Hence, the stress difference continued to increase with increasing strain. Analyzing the mass stiffness in these undrained tests in terms of block proportion has not been found to be possible because of the effects of pore pressure generation. Pore pressure generation is a function of many variables, including the consolidation stress and the initial effective confining stress used in a test. There are insufficient data available to be able to understand the interaction of all the variables. In addition, the relatively linear initial portions of these curves are so short that estimating modulus values for these tests is of questionable value.

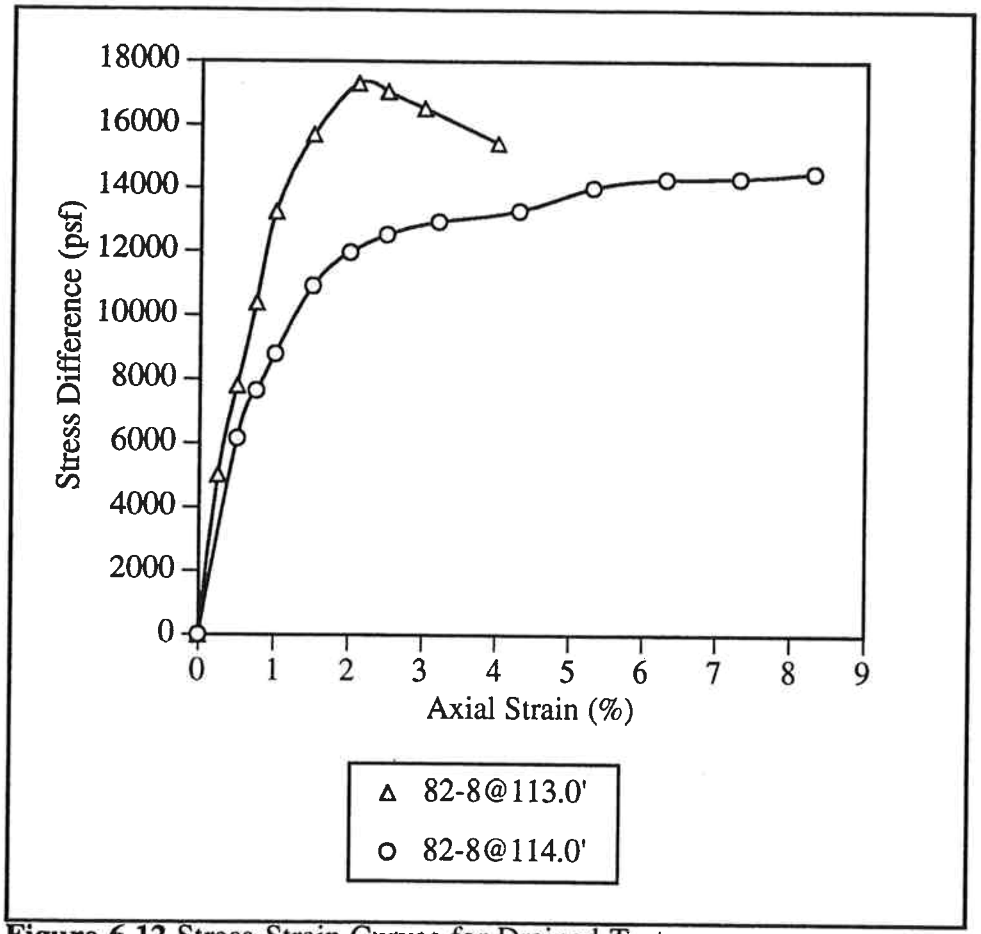

Figure 6.12 Stress-Strain Curves for Drained Tests

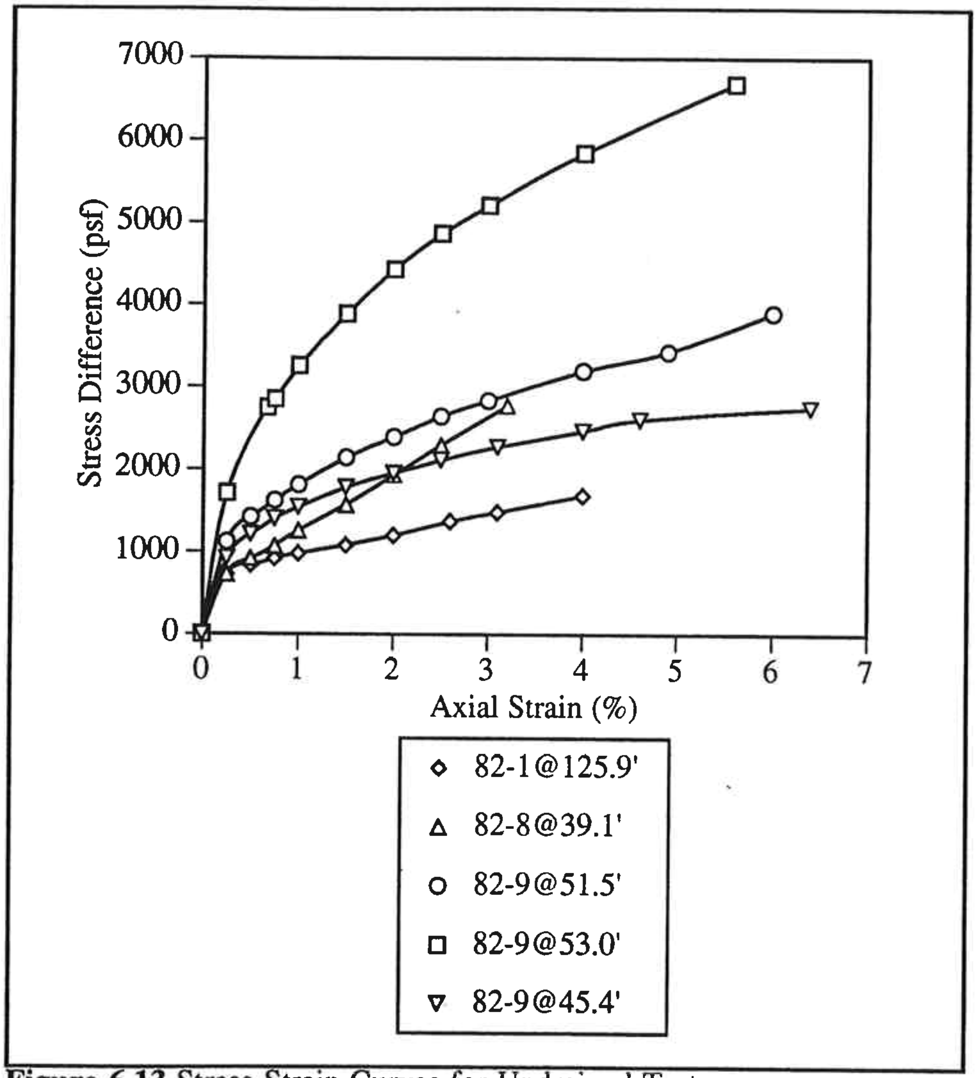

Figure 6.13 Stress-Strain Curves for Undrained Tests

CHAPTER 7

CONCLUSIONS AND RECOMMENDATIONS

The physical model melanges used in this study are believed to have, in general, accurately modeled the expected behavior of an actual melange mass. The data produced in this model study, when combined with the findings of the literature search and the results of the triaxial compression tests on Franciscan melange specimens from the Scott Dam site, allow one to come to the following conclusions and make some recommendations about the effect that block proportion and block orientation have on the stiffness and strength, as well as the mode of failure in a melange.

1. The stiffness of a melange will increase with increasing block proportion. The stiffness increase will be smallest in the direction perpendicular to the block orientation due not only to the orientation of the blocks, but most likely also due to the presence of zones of more deformable material (shears) that run parallel to the block edges. The magnitude of the increase in stiffness is difficult to accurately quantify. Figure 7.1 shows all the modulus versus block proportion data for the models. Almost all the data fall between the average modulus of the matrix (the lower bound shown) and the weighted average of the block and matrix moduli based on their volumetric proportions (the upper bound shown). The upper bound is the "parallel case" discussed previously in Chapter 5. Conservatively, the modulus of a melange mass can be assumed to be the same as the modulus of the matrix, although it will almost certainly be higher.

2. The cohesion of a melange will decrease with increasing block proportion, due to the weak block-matrix contacts in particular. The magnitude of this decrease is believed to be

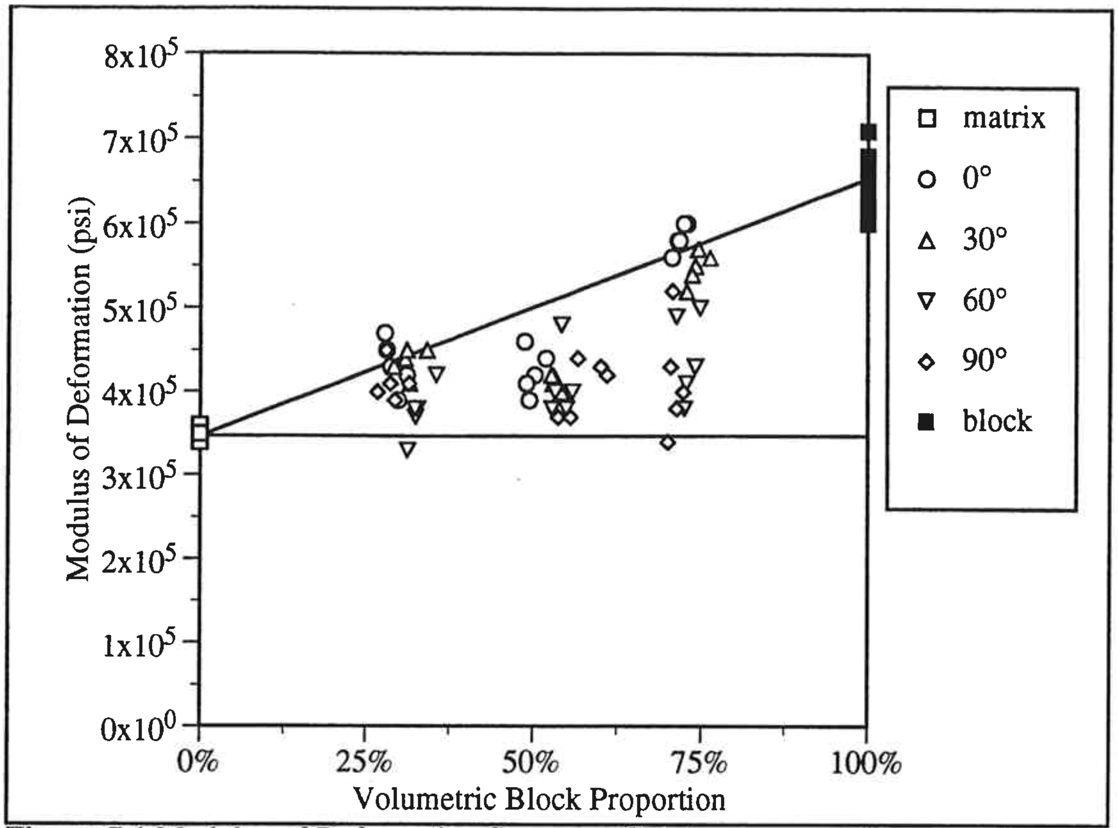

Figure 7.1 Modulus of Deformation Summary Graph

dependent on the cohesion along the weakness surfaces found in a melange (i.e. the block-matrix contacts and shears). A trend line through the model data is shown in Figure 7.2. Note that if the decreasing trend is extrapolated to 100 percent block, the value of cohesion indicated is approximately 120 psi. This value lies between that for the block-matrix contacts and the wax "shears". It is hypothesized that if these weakness surfaces had had lower cohesions, the cohesion of the mass would have decreased with increasing block proportion even more substantially. A logical and conservative suggestion (particularly if little is known about the strength of the weakness surfaces in a melange) is that the cohesion be assumed to decrease linearly toward zero with increasing block proportion. This suggested guideline is also indicated on Figure 7.2.

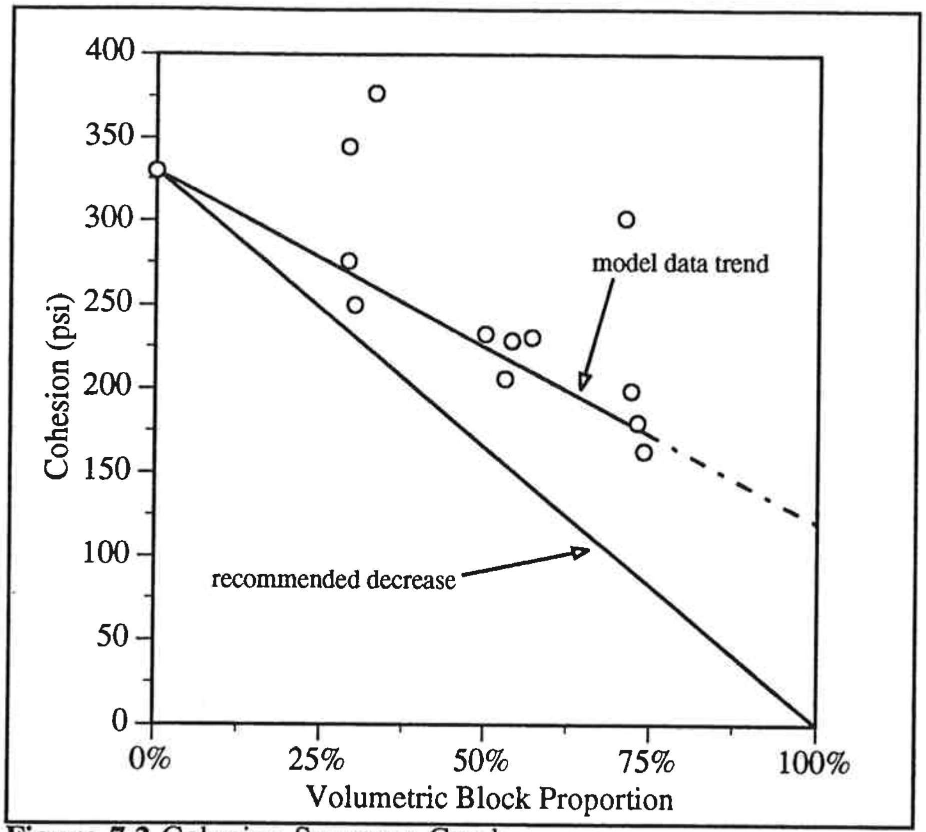

Figure 7.2 Cohesion Summary Graph

3. The angle of internal friction of a melange will increase with increasing block proportion due to an increase in the tortuousity of the failure surface. The values of change in the angle of internal friction versus block proportion for both the models and the Scott Dam Franciscan melange are shown in Figure 7.3. The effective stress angle of internal friction for the Franciscan melange was assumed to be 28°. Also indicated is the recommended increase in angle of internal friction with block proportion proposed for colluvium by Irfan and Tang (1993). The Irfan and Tang (1993) suggestion is a bit unconservative in predicting the angle of internal friction increase for the models used in this study; therefore, a more conservative suggested increase is indicated. The proposed angle of internal friction increase is 3° for every 10 percent increase in block proportion above 25 percent. Note that

this increase is quite conservative in predicting the angle of internal friction increase for the Scott Dam Franciscan melange specimens.

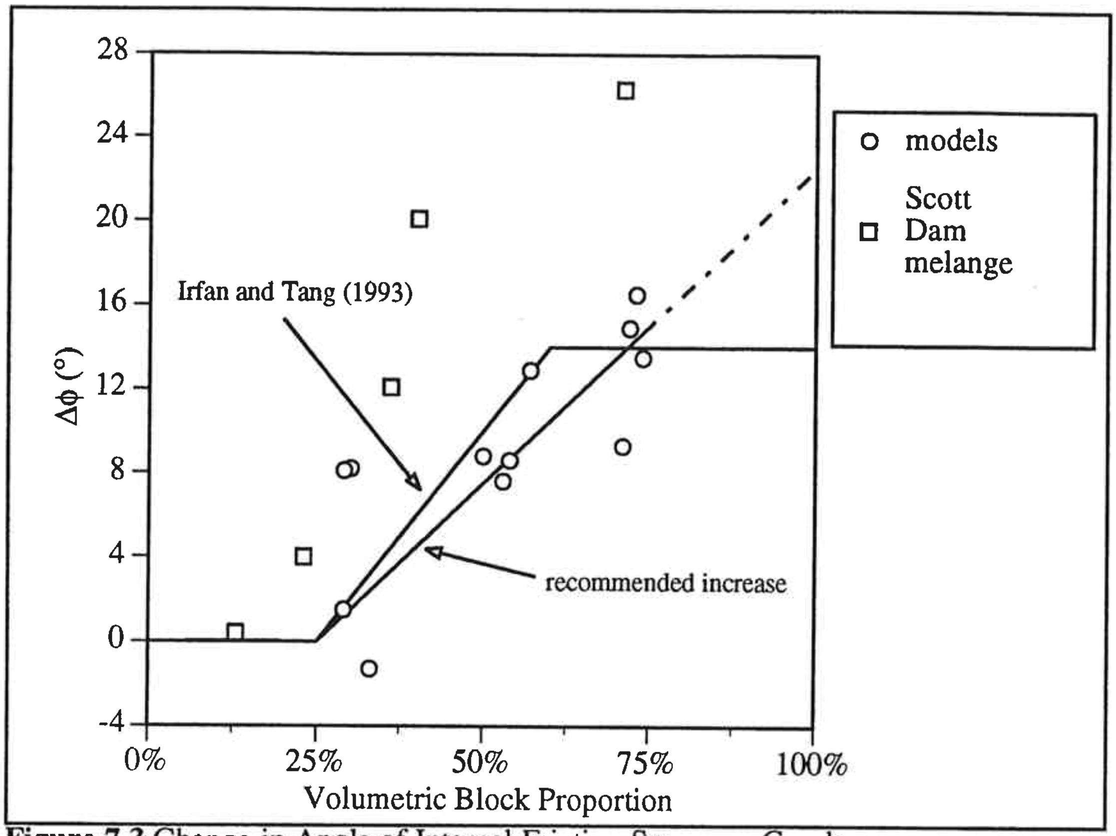

Figure 7.3 Change in Angle of Internal Friction Summary Graph

Combining the guidelines in 2 and 3 results in the following shear strength model

$$\tau_p = c_{matrix}(1-\theta) + \sigma\tan(\phi_{matrix} + \Delta\phi(\theta)), \qquad (7.1)$$

where τ_p is the mass shear strength, c_{matrix} is the cohesion of the matrix, θ is the volumetric block proportion, σ is the normal stress, ϕ_{matrix} is the angle of internal friction for the matrix, and $\Delta\phi(\theta)$ is the suggested angle of internal friction increase for the block proportion of interest (i.e. a 3° increase for every 10 percent increase in block proportion above 25 percent). This is believed to be a conservative model for predicting the shear strength of a melange.

4. Block orientation (of the largest blocks in particular) will strongly influence the failure geometry. Failure surfaces will zigzag around blocks and, because the block-matrix contacts are surfaces of weakness, the failures will form at the block-matrix contacts. In situations where the potential failure orientations are geometrically constrained, the orientation of the largest blocks may, therefore, be critical to the mass stability.

In order to apply these recommendations, the block proportion must be determined in the field. Some ideas on how the block proportion can be estimated are given by Medley (1994).

Two other factors should also be considered when applying these recommendations. First, there is a maximum block proportion above which mixtures of stronger and weaker rock can no longer be classified as block-in-matrix rock simply because there will not be sufficient weaker material to envelop the blocks. Therefore, there is a block proportion above which melange will no longer be found. The shape and size distribution of melange blocks allow this proportion to be quite high (perhaps 85 or 90 percent). Above a strong rock proportion of 85 to 90 percent the mass should really be classified as a highly fractured rock mass and should be analyzed as such. One methodology for analyzing highly fractured rock masses was proposed by Savely (1987). Second, as discussed in the Introduction, these findings may apply to block-in-matrix rocks that are similar to melange. Sheared serpentinite, in particular, shares many characteristics with melange. It is not suggested that these findings be applied to corestone bearing saprolites, however. Although corestone bearing saprolites consist of stronger blocks in a weaker matrix, there is no sharp dividing line between the blocks and matrix as in melange. In saprolites the blocks grade into the matrix, therefore the contact between the two will not be a well defined surface of weakness. The surfaces of weakness will more likely be the relict discontinuities found in a saprolite. Experimental research similar to that done in this study could be expected to reveal a model for stony saprolite shear strength.

The findings of this study could be more firmly established with further research. Some suggested research topics include:

1. the influence of the block shapes and the block size distribution on the mechanical properties of block-in-matrix materials.

2. large in-situ direct shear tests in melange to provide additional evidence of the stress-strain and strength behavior and failure characteristics shown by the models in this study.

3. studies of slopes to see if block proportion and block orientation can be related to their stability

4. detailed studies of existing slope failures to check if the failure surfaces are as hypothesized in this study (i.e. around the blocks and particularly at the block-matrix contacts).

5. the continual development and eventual application of computer codes with sufficient power to numerically model block-in-matrix materials such as melange. Ke (1993) has begun this work by using discontinuous deformation analysis (DDA) to calculate the elastic modulus of a block-in-matrix model under uniaxial compression.

REFERENCES

Aalto, K.R. (1982) The Franciscan Complex of northernmost California: sedimentation and tectonics, in Leggett, J.K., ed., *Trench-Forearc Geology: Sedimentation and Tectonics on Modern and Ancient Active Plate Margins*, Geological Society of London Special Publication 10, pp. 419-432.

A.G.I. (1979) Some Italian experiences on the mechanical characterization of structurally complex formations, *Proceedings, 4th International Congress on Rock Mechanics*, vol. 1, Montreux, pp. 827-846.

A.G.I. (1985) Geotechnical properties and slope stability in structurally complex clay soils, in *Geotechnical Engineering in Italy, An Overview, 1985*, Associazione Geotechnica Italiana, pp. 189-225.

Bates, R.L. and Jackson, J.A. (1984) *Dictionary of Geological Terms*, Doubleday, New York.

Bedrosian, T.L. (1978) Geology and slope stability in The Geysers Geothermal Resource Area, *California Geology*, **31**, pp. 151-159.

Bedrosian, T.L. (1980) *Geology and Slope Stability in Selected Parts of The Geysers Geothermal Resource Area (Sonoma County), California*, California Division of Mines and Geology Special Report 142.

Benveniste, Y. (1987) A new approach to the application of Mori-Tanaka's theory in composite materials, *Mechanics of Materials*, **6**, pp. 147-157.

Borowicka, H. (1965) The influence of colloidal content on the shear strength of clays, *Proceedings of the 6th International Conference on Soil Mechanics and Foundation Engineering*, vol. 1, pp. 175-178.

References

Byrne, T. (1984) Early deformation in melange terranes of the Ghost Rocks Formation, Kodiak Islands, Alaska, in Raymond, L.A., ed., *Melanges: Their Nature, Origin, and Significance*, Geological Society of America Special Paper 198, pp. 21-51.

Cloos, M. (1984) Flow melanges and the structural evolution of accretionary wedges, in Raymond, L.A., ed., *Melanges: Their Nature, Origin, and Significance*, Geological Society of America Special Paper 198, pp. 71-79.

Counto, U.J. (1964) The effect of the elastic modulus of the aggregate on the elastic modulus, creep and creep recovery of concrete, *Magazine of Concrete Research*, **16**, pp. 129-138.

Cowan, D.S. (1978) Origin of blueschist-bearing chaotic rocks in the Franciscan Complex, San Simeon, California, *Geological Society of America Bulletin*, **89**, pp. 1415-1423.

Cowan, D.S. (1985) Structural styles in Mesozoic and Cenozoic melanges in the western Cordillera of North America, *Geological Society of America Bulletin*, **96**, pp. 451-462.

Cowan, D.S. and Silling, R.M. (1978) A dynamic, scaled model of accretion at trenches and its implications for the tectonic evolution of subduction complexes, *Journal of Geophysical Research*, **83**, pp. 5389-5396.

D'Elia, B., Distefano, D., Esu, F. and Federico, G. (1988) Deformations and stability of high cuts in a structurally complex formation: analysis and prediction, *Proceedings of the 5th International Symposium on Landslides*, Lausanne, pp. 599-604.

D'Elia, B., Distefano, D., Federico, G. and Oliva, S. (1984) Full-scale study of a high cut in a structurally complex formation, *Proceedings of the 4th International Symposium on Landslides*, vol. 2, Toronto, pp. 57-62.

Doddiah, D., Bhat, H.S., Somasekhar, P.V., Sosalegowda, H.B. and Ranganath, K.N. (1969) Shear characteristics of soil-gravel mixtures, *Journal of the Indian National Society of Soil Mechanics and Foundation Engineering*, **8**, pp. 57-66.

References

Donaghe, R.T. and Torrey III, V.H. (1985) *Strength and Deformation Properties of Earth-Rock Mixtures*, Technical Report GL-85, US Army Engineer Waterways Experiment Station, Vicksburg, Mississippi.

Donath, F.A. (1964) Strength variation and deformational behavior in anisotropic rock, in Judd, W.R. (ed.) *State of Stress in the Earth's Crust*, American Elsevier Publishing Co., Inc., New York, pp. 281-298.

Fedorov,V.I. and Sergevnina, V.V. (1973) Effect of clay filler on the strength characteristics of rubble-clay soils, *Osnovaniya Fundamenty i Mekhanika Grutov*, **6**, pp. 13-15.

Fragazzy, R.J., Su, J., Siddiqi, F.H. and Ho, C.L. (1992) Modeling strength of sandy gravel, *Journal of Geotechnical Engineering*, **118**, pp. 920-935.

Goodman, R.E. (1989) *Introduction to Rock Mechanics*, John Wiley and Sons, New York.

Gostelow, T.P. and Loucaides, G. (1988) Slope instability in allochthonous sediments: an example form the Moni melange, Cyprus, *Proceedings of the 5th International Symposium on Landslides*, vol. 1, Lausanne, pp. 161-168.

Hansen, T.C. (1965) Theories of multi-phase materials applied to concrete, cement mortar and cement paste, in Brooks, A.E. and Newman, K., eds. *The Structure of Concrete (and Its Behavior Under Load)*, Cement and Concrete Association, London, pp. 16-23.

Harding-Lawson Associates (1983) *Laboratory Testing Scott Dam - Lake County, California*, prepared for the Pacific Gas and Electric Company, HLA Job No. 560,052.01.

Hashin, Z. and Shtrikman, S. (1963) A variational approach to the theory of the elastic behaviour of multiphase materials, *Journal of the Mechanics and Physics of Solids*, **11**, pp. 127-140.

References

Hirsch, T.J. (1962) Modulus of Elasticity of concrete affected by elastic moduli of cement paste matrix and aggregate, *Journal of the American Concrete Institute*, **59**, pp. 427-447.

Hoek, E. and Franklin, J.A. (1968) Simple triaxial cell for field or laboratory testing of rock, *Transactions of the Institute of Mining and Metallurgy (Section A: Mining Industry)*, pp. A22-A26.

Holtz, W.G. and Gibbs, H.J. (1956) Triaxial shear tests on pervious gravelly soils, *Journal of the Soil Mechanics and Foundations Division, American Society of Civil Engineers*, **82**, pp. 867.1-867.22.

Holtz, W.G. and Ellis, W. (1961) Triaxial shear characteristics of clayey gravel soils, *Proceedings of the 5th International Conference of Soil Mechanics and Foundation Engineering*, Paris, vol. 11, pp. 143-149.

Irfan, T.Y. and Tang K.Y. (1993) *Effect of the Coarse Fractions on the Shear Strength of Colluvium*, GEO Report No. 23, Geotechnical Engineering Office, Civil Engineering Department, Hong Kong.

Jaeger, J.C. (1960) Shear failure of anisotropic rocks, *Geological Magazine*, **97**, p. 65-72.

Kano, K., Nakaji, M. and Takecuchi, S. (1991) Asymmetrical melange fabrics as possible indicators of the convergent direction of plates: a case study from the Shimanto Belt of the Akaishi Mountains, central Japan, *Tectonophysics*, **185**, pp. 375-388.

Kawakami, H. and Abe, H. (1970) Shear characteristics of saturated gravelly clays, *Transactions of the Japanese Society of Civil Engineers*, **2**, Part 2, pp. 295-298.

Ke, T.-C. (1993) *Simulated Testing of Two Dimensional Heterogeneous and Discontinuous Rock Masses Using Discontinuous Deformation Analysis*, Ph.D. Thesis, University of California, Berkeley.

References

Kenney, T.C. (1977) Residual strengths of mineral mixtures, *Proceedings of the 9th International Conference on Soil Mechanics and Foundation Engineering*, San Francisco, vol. 1, pp. 155-160.

Kurata, S. and Fujishita, T. (1960) Research on the engineering properties of sand-clay mixtures, *Proceedings of the 1st Asian Regional Conference on Soil and Mechanics and Foundation Engineering*, New Delhi, India, vol. 1, part 4, paper 5, pp. 1-12.

Lupini, J.F., Skinner, A.E. and Vaughn, P.R. (1981) The drained residual strength of cohesive soils, *Geotechnique*, **31**, pp. 181-213.

McGown, A. and Derbyshire, E. (1977) Genetic influences on the properties of tills, *Quarterly Journal of Engineering Geology*, **10**, pp. 389-410.

McKinlay, D.G., Tomlinson, M.J. and Anderson, W.F. (1974) Observations on the undrained strength of glacial till, *Geotechnique*, **24**, pp. 503-516.

Medley, E.W. (1994) *The Engineering Characterization of Melange and Similar Block-in-Matrix Rocks (Bimrocks)*, Ph.D. Thesis, University of California, Berkeley.

Mehta, P.K. and Monteiro, P.J.M. (1993) *Concrete: Structure, Properties, and Materials*, Prentice-Hall, Inc., Englewood Cliffs, New Jersey.

Miller, E.A. and Sowers, G.F. (1957) The strength characteristics of soil-aggregate mixtures, *Highway Research Board Bulletin*, **183**, pp. 16-23.

Moore, G.F. and Karig, D.E. (1980) Structural geology of Nias Island, Indonesia: implications for subduction zone tectonics, *American Journal of Science*, **280**, pp. 193-223.

Moore, J.C. and Wheeler, R.L. (1978) Structural fabric of a melange Kodiak Islands, Alaska, *American Journal of Science*, **278**, pp. 739-765.

Nilsen, A.U. and Monteiro, P.J.M. (1993) Concrete: a three phase material, *Cement and Concrete Research*, **23**, pp. 147-151.

References

Pacific Gas and Electric Company (1989) *Foundation Shear Strengths for Scott Dam*, FERC Project No. 77, State Dam No. 97-101, Lake County, California.

Page, B.M. (1978) Franciscan melanges compared with olistostromes of Taiwan and Italy, *Tectonophysics*, **47**, pp. 223-246.

Patwardhan, A.S., Rao, J.S. and Gaidhane, R.B. (1970) Interlocking effects and shearing resistance of boulders and large size particles in a matrix of fines on the basis of large scale direct shear tests, *Proceedings of the 2nd Southeast Asian Conference on Soil Mechanics*, Singapore, pp. 265-273.

Rathee, R.K. (1981) Shear strength of granular soils and its prediction by modelling techniques, *Journal of the Institution of Engineers*, India, **62**, pp. 64-70.

Roctest (1991) *Hoek Triaxial Cell Instruction Manual*, Plattsburgh, New York.

Rodine, J.D. and Johnson, A.M. (1976) The ability of debris, heavily freighted with coarse clastic materials, to flow on gentle slopes, *Sedimentology*, **23**, p. 213-234.

Savely, J.P. (1987) *Probabilistic Analysis of Fractured Rock Masses*, Ph.D. Thesis, University of Arizona.

Savely, J.P. (1990) Determination of shear strength of conglomerates using a Caterpillar D9 ripper and comparison with alternative methods, *International Journal of Mining and Geological Engineering*, **8**, pp. 203-225.

Savina, M.E. (1978) Occurrence of earthflows and hillslope evolution in Franciscan melanges of northern California, *Geological Society of America, Abstracts with Programs*, **10**, p. 485.

Shakoor, A. and Cook, B.D. (1990) The effect of stone content, size, and shape on the engineering properties of a compacted silty clay, *Bulletin of the Association of Engineering Geologists*, **27**, pp. 245-253.

Stock, A.F., Hannant, D.J. and Williams, R.I.T. (1979) The effect of aggregate concentration upon the strength and modulus of elasticity of concrete, *Magazine of Concrete Research*, **31**, pp. 225-234.

Waldron, J.W.F., Turner, D., Stevens, K.M. (1988) Stratal disruption and development of melange, Western Newfoundland: effect of high fluid pressure in an accretionary terrain during ophiolite emplacement, *Journal of Structural Geology*, **10**, pp. 861-873.

West, L.J. (1992) *The Shear Behaviour of Heterogeneous Soils*, Ph.D. thesis, The University of Leeds.

Vogler, U.W. and Kovari, K. (1981) Suggested methods for determining the strength of rock materials in triaxial compression, in Brown, E.T. ed. *Rock Characterization Testing and Monitoring - ISRM Suggested Methods*, Pergamon Press, Oxford, pp. 123-128.

Volpe, R.L., Ahlgren, C.S. and Goodman, R.E. (1991) Selection of engineering properties for geologically variable foundations, *Proceedings of the 17th International Congress on Large Dams*, Paris, pp. 1087-1101.

APPENDIX A

Physical Model Specimen Dimensions and Block Proportions

This appendix contains the specimen dimensions and volumetric block proportions for all 77 tested physical model melange specimens. Table A.1 gives the lengths, diameters, weights and unit weights for the matrix specimens and Table A.2 provides the same information for the block specimens. The specimen dimensions and block proportions for the block-in-matrix specimens are listed in Table A.3.

Volumetric block proportion was determined using the formula

$$\text{Block Proportion} = \frac{\gamma_s - \gamma_m}{\gamma_b - \gamma_m}, \qquad \text{(A.1)}$$

where γ_s is the specimen unit weight, γ_m is the average matrix unit weight (83.1 pcf) and γ_b is the average block unit weight (116.8 pcf).

Appendix A Physical Model Specimen Dimensions and Block Proportions

Table A.1 Matrix Specimen Dimensions

Specimen	Length (in.)	Diameter (in.)	Weight (lbs.)	Unit Weight (pcf)
matrix-50	12.39	5.90	16.29	83.1
matrix-100	12.11	5.91	15.93	82.9
matrix-125	12.16	5.91	16.04	83.1
matrix-150	12.22	5.91	16.17	83.3
matrix-200	12.19	5.92	16.14	83.1
matrix-225	12.24	5.91	16.16	83.2
matrix-250	12.09	5.92	16.01	83.1

Mean Unit Weight of Matrix = 83.1 pcf

Table A.2 Block Specimen Dimensions

Specimen	Length (in.)	Diameter (in.)	Weight (lbs.)	Unit Weight (pcf)
block-0	4.37	1.986	0.9127	116.5
block-50	4.60	1.985	0.9634	116.9
block-75	4.54	1.988	0.9502	116.5
block-100	4.53	1.980	0.9436	116.9
block-125	4.48	1.980	0.9325	116.8
block-150	4.49	1.985	0.9369	116.5
block-175	4.58	1.984	0.9590	117.0
block-200	4.47	1.983	0.9325	116.7
block-225	4.50	1.984	0.9392	116.7
block-250	4.60	1.984	0.9634	117.1

Mean Unit Weight of Blocks = 116.8 pcf

Table A.3 Block-in-Matrix Specimen Dimensions and Block Proportions

Specimen	Length (in.)	Diameter (in.)	Weight (lbs.)	Unit Weight (pcf)	Block Proportion
1-0-50	12.22	5.91	17.97	92.6	28%
1-0-100	12.25	5.91	18.12	93.2	30%
1-0-150	12.11	5.91	17.84	92.8	29%
1-0-200	12.16	5.91	18.07	93.6	31%
1-0-250	11.88	5.91	17.45	92.5	28%
1-30-50	12.09	5.91	17.84	92.9	29%
1-30-150	12.18	5.91	18.30	94.6	34%
1-30-200	12.00	5.91	17.82	93.5	31%
1-30-250	12.19	5.91	18.12	93.6	31%
1-60-50	12.14	5.91	18.05	93.7	31%
1-60-100	12.16	5.91	18.36	95.1	36%
1-60-150	12.21	5.91	18.23	94.0	32%
1-60-200	11.91	5.91	17.80	94.2	33%
1-60-250	12.17	5.91	18.17	94.0	32%
1-90-50	12.12	5.91	17.90	93.0	29%
1-90-100	12.23	5.91	18.02	92.8	29%
1-90-150	12.08	5.91	17.75	92.6	28%
1-90-200	12.17	5.91	18.10	93.7	31%
1-90-250	12.14	5.91	17.76	92.1	27%
m-0-50	12.25	5.91	19.57	100.6	52%
m-0-100	12.19	5.91	19.36	100.1	50%
m-0-200	12.17	5.91	19.24	99.6	49%
m-0-250	12.28	5.91	19.42	99.6	49%
m-30-50	12.15	5.91	19.55	101.4	54%
m-30-100	12.21	5.91	19.57	101.0	53%
m-30-150	12.16	5.91	19.49	101.0	53%
m-30-200	12.22	5.91	19.59	101.0	53%
m-30-250	12.20	5.91	19.54	100.9	53%

Table A.3 Continued

Specimen	Length (in.)	Diameter (in.)	Weight (lbs.)	Unit Weight (pcf)	Block Proportion
m-60-50	12.10	5.91	19.42	101.1	53%
m-60-100	12.16	5.91	19.68	101.9	56%
m-60-150	12.13	5.91	19.53	101.4	54%
m-60-200	12.21	5.91	19.70	101.7	55%
m-60-250	12.19	5.91	19.53	100.9	53%
m-90-50	12.23	5.91	20.13	103.7	61%
m-90-100	12.19	5.91	19.59	101.2	54%
m-90-150	12.06	5.91	19.57	102.2	57%
m-90-200	12.23	5.91	20.07	103.4	60%
m-90-250	12.10	5.91	19.56	101.8	56%
h-0-57	12.29	5.91	20.85	106.9	71%
h-0-100	12.24	5.91	20.92	107.7	73%
h-0-150	12.10	5.91	20.59	107.2	71%
h-0-200	12.22	5.91	20.81	107.3	72%
h-0-250	12.26	5.91	20.93	107.5	72%
h-30-50	12.02	5.91	20.65	108.2	74%
h-30-100	12.16	5.91	20.87	108.1	74%
h-30-150	12.21	5.91	20.86	107.6	73%
h-30-200	12.06	5.91	20.66	107.9	74%
h-30-250	12.06	5.91	20.83	108.8	76%
h-60-50	12.14	5.91	20.73	107.5	73%
h-60-100	11.88	5.91	20.43	108.3	75%
h-60-150	11.94	5.91	20.30	107.1	71%
h-60-200	11.78	5.91	20.21	108.1	74%
h-60-250	12.19	5.91	20.83	107.6	73%
h-90-50	12.28	5.91	20.80	106.7	70%
h-90-100	12.24	5.91	20.76	106.8	70%
h-90-150	12.01	5.91	20.43	107.1	71%
h-90-200	12.16	5.91	20.64	106.9	71%
h-90-250	12.26	5.91	20.91	107.5	72%

APPENDIX B

Physical Model Stress-Strain Curves

This appendix contains the 77 stress-strain curves for the physical model specimens. The vertical axis, identified as the "stress difference", is the difference between the axial stress and confining stress (σ_1-σ_3). A schematic specimen sketch accompanies each plot to ease identification.

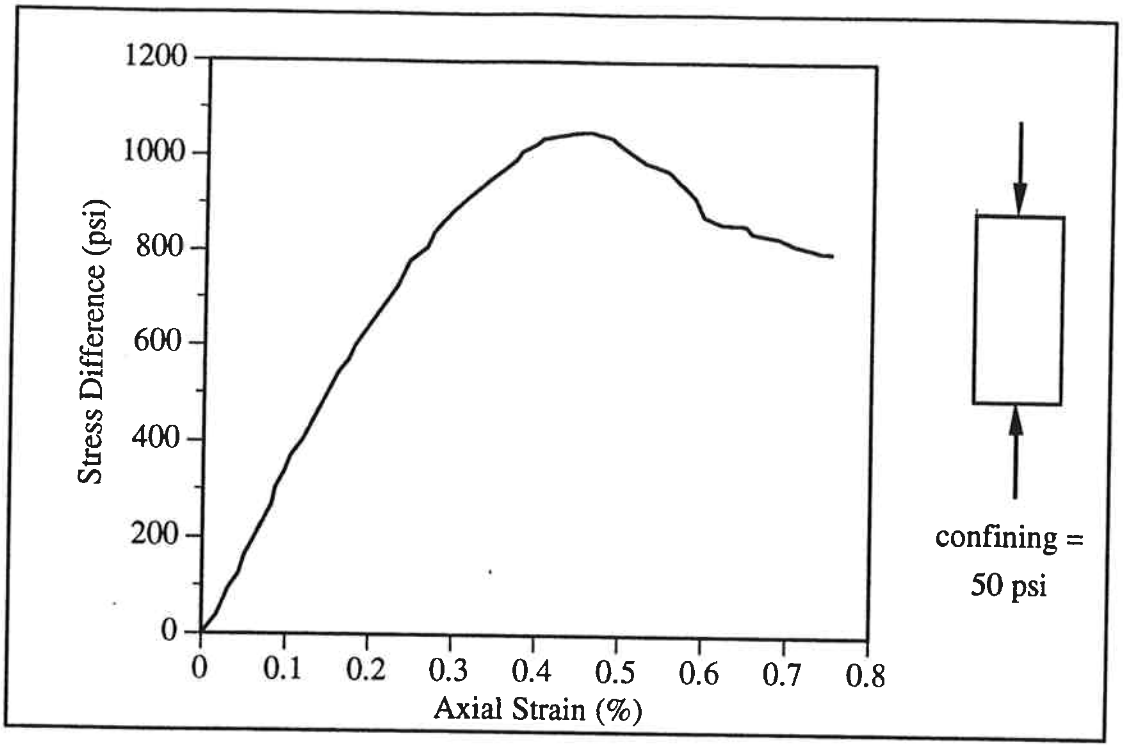

Figure B.1 Stress-Strain Curve for matrix-50

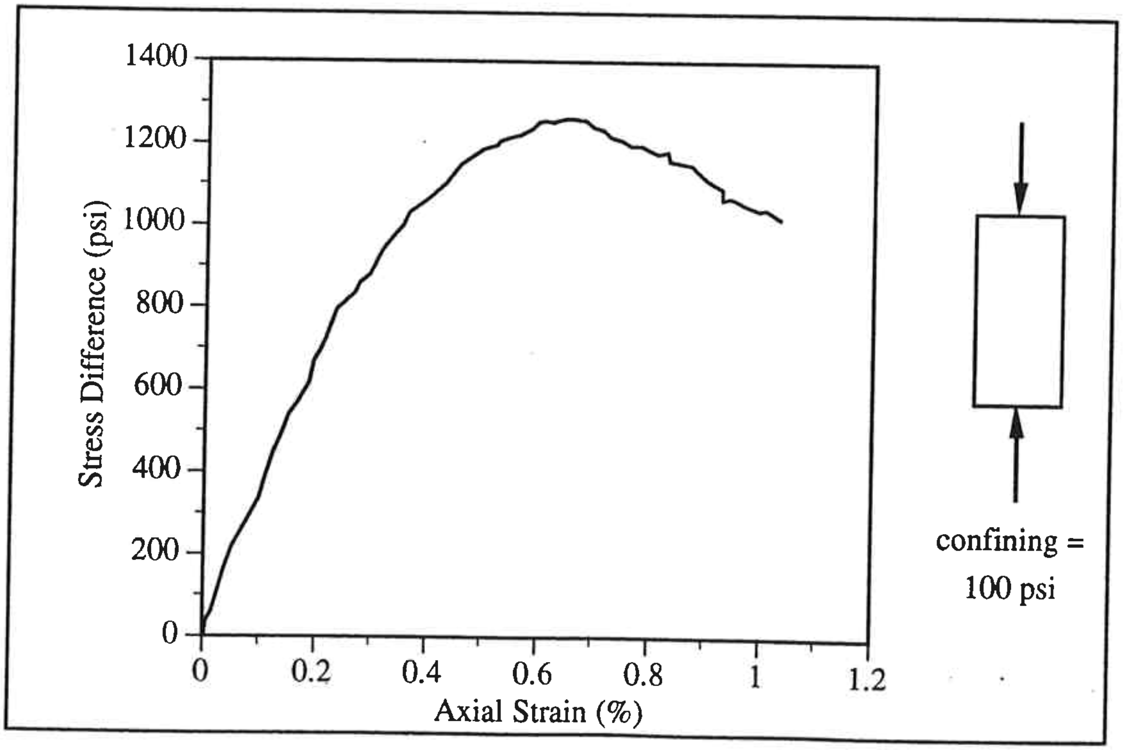

Figure B.2 Stress-Strain Curve for matrix-100

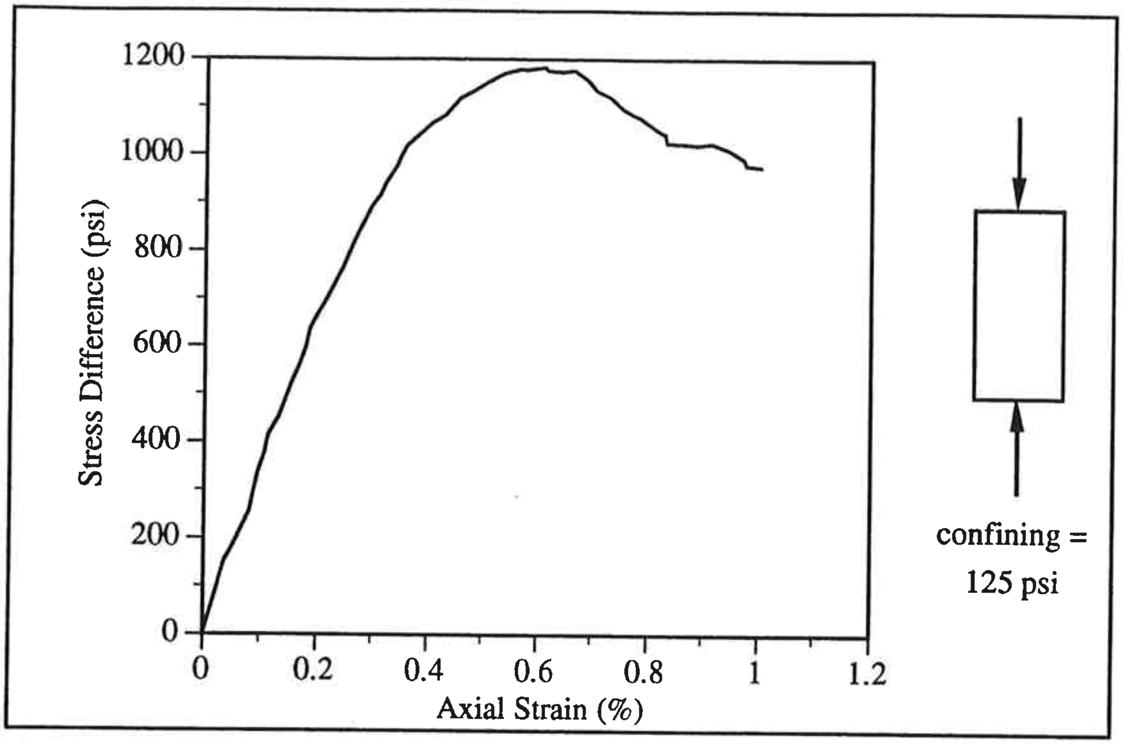

Figure B.3 Stress-Strain Curve for matrix-125

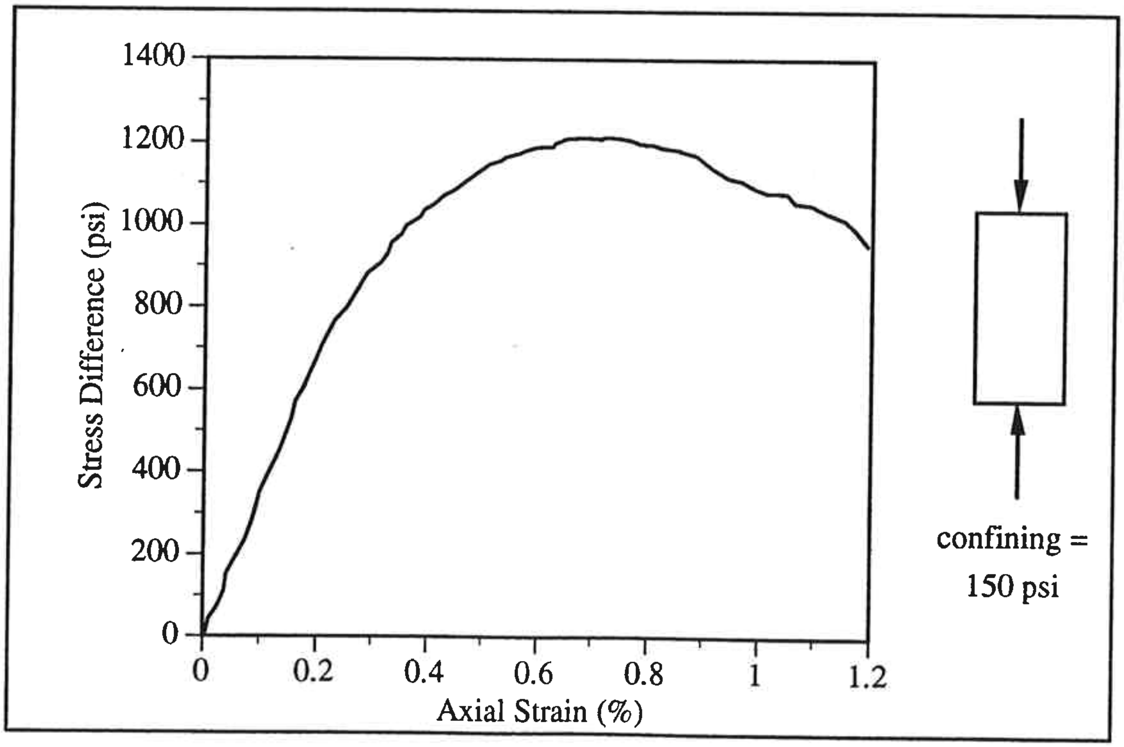

Figure B.4 Stress-Strain Curve for matrix-150

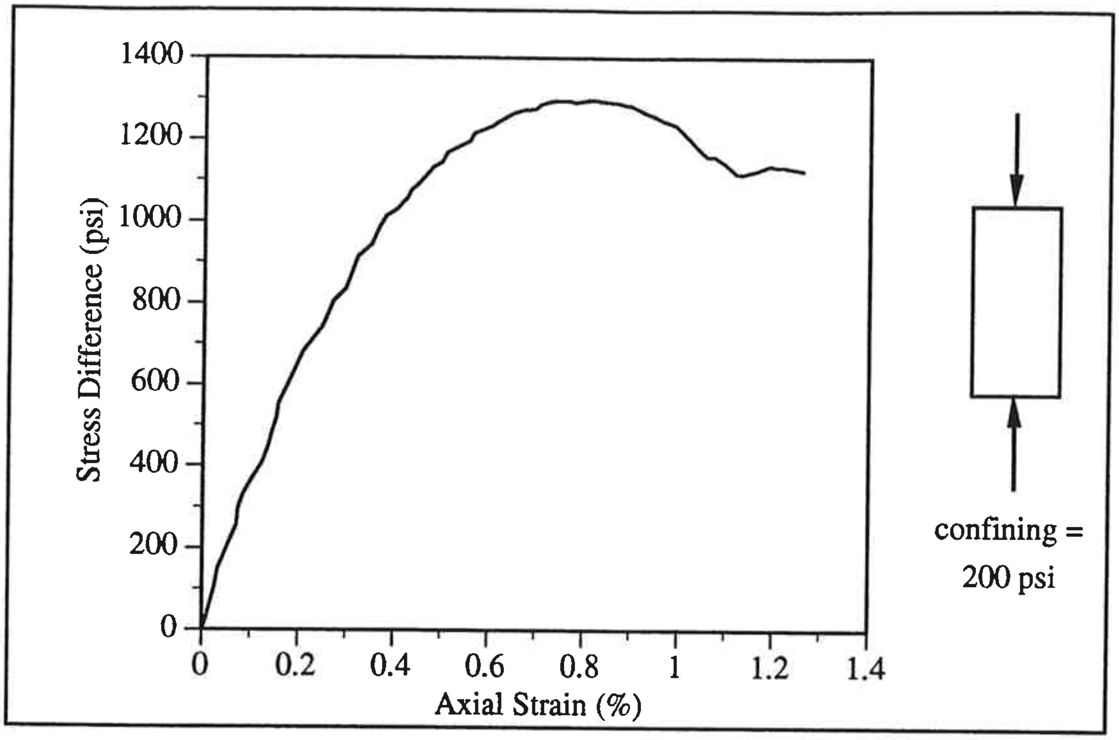

Figure B.5 Stress-Strain Curve for matrix-200

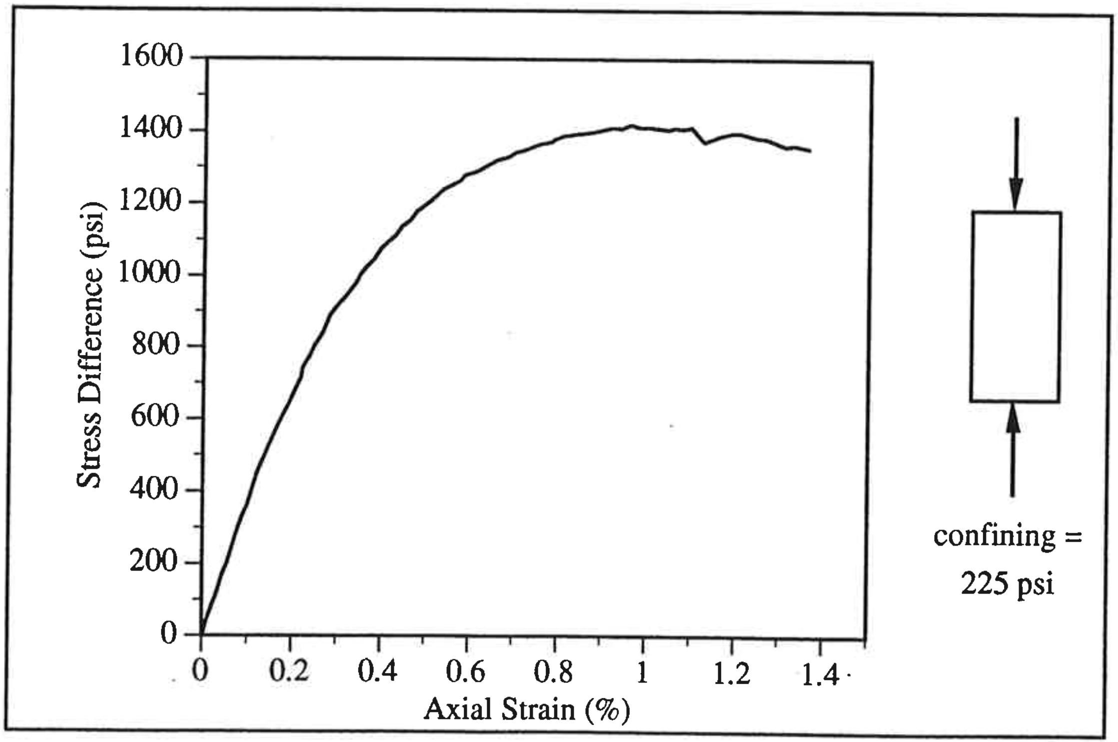

Figure B.6 Stress-Strain Curve for matrix-225

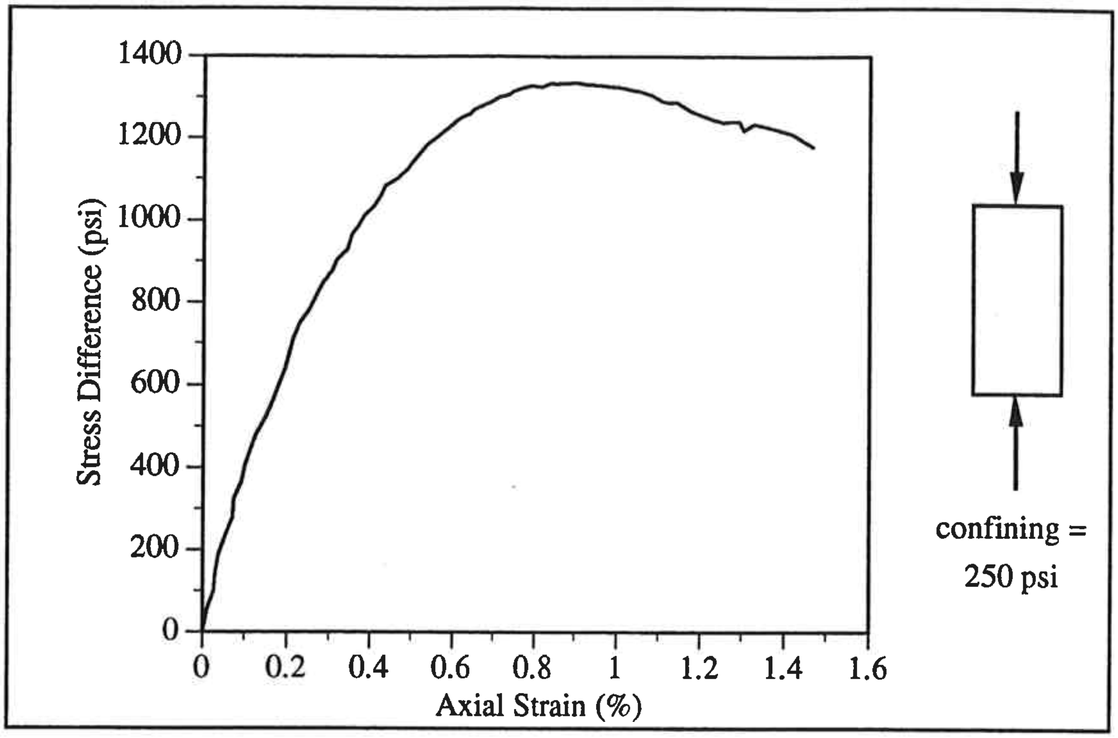

Figure B.7 Stress-Strain Curve for matrix-250

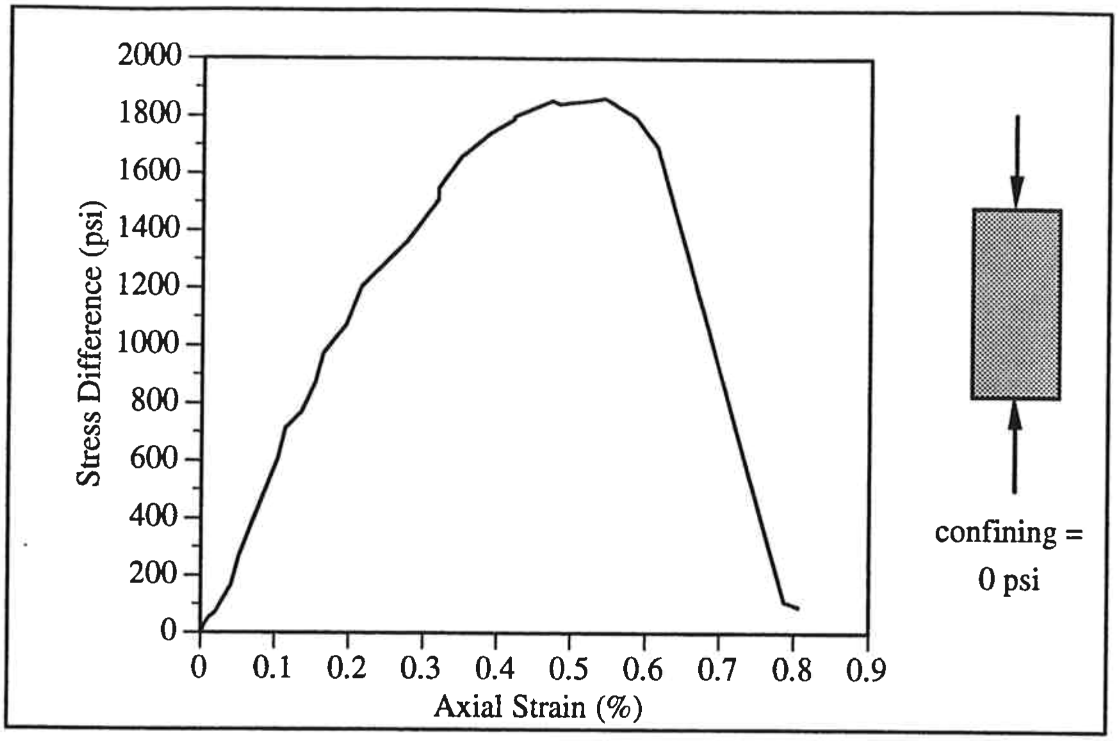

Figure B.8 Stress-Strain Curve for block-0

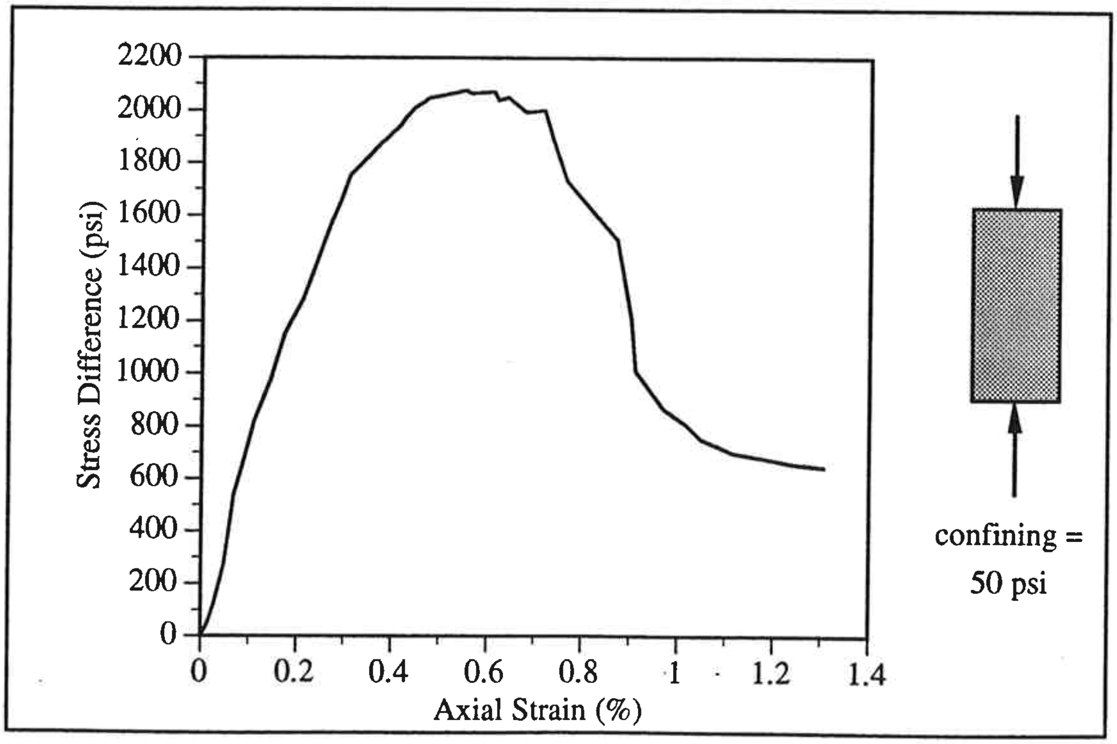

Figure B.9 Stress-Strain Curve for block-50

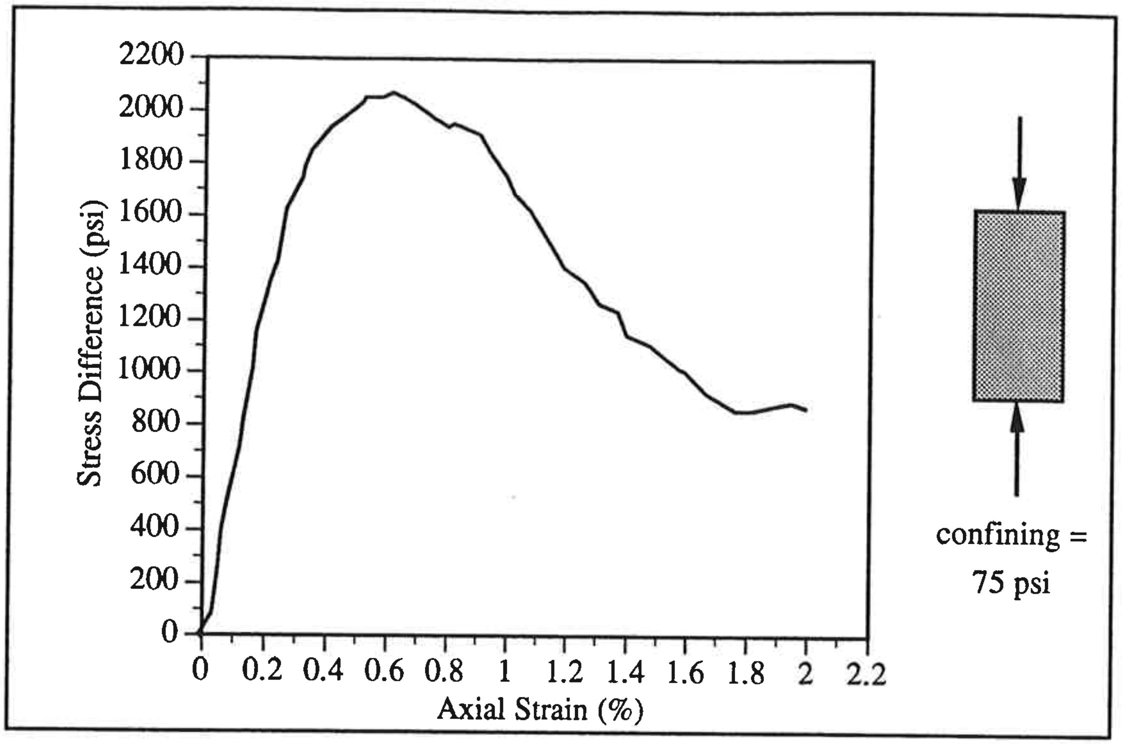

Figure B.10 Stress-Strain Curve for block-75

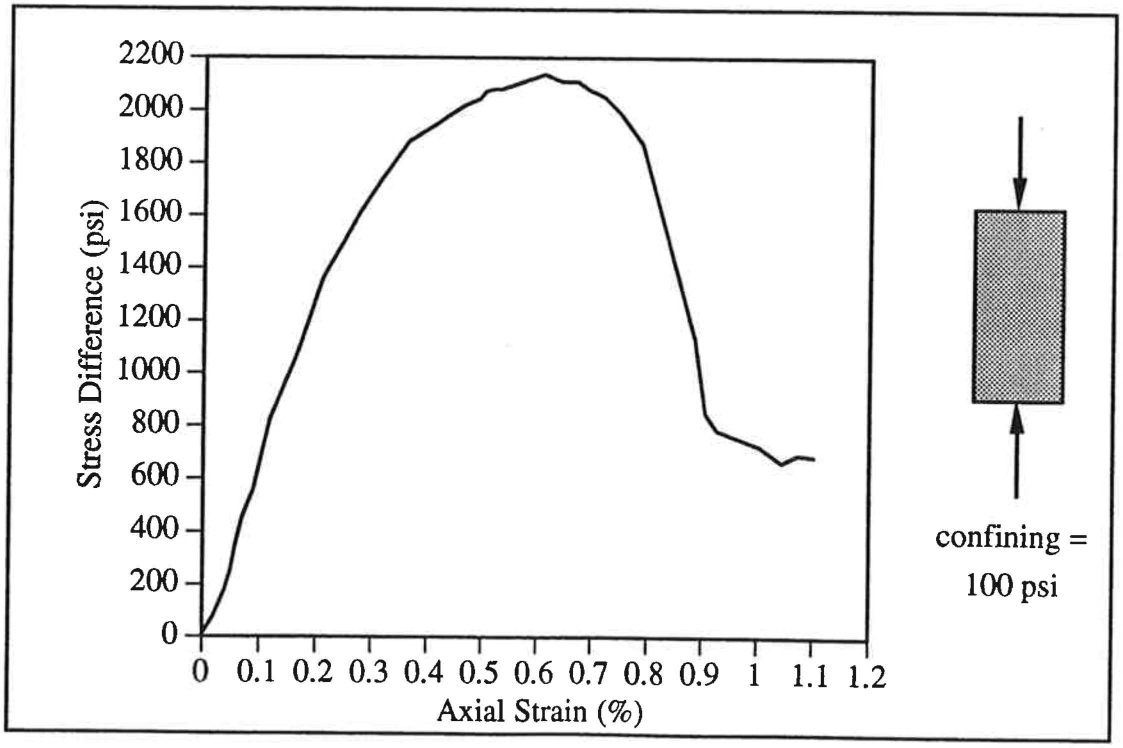

Figure B.11 Stress-Strain Curve for block-100

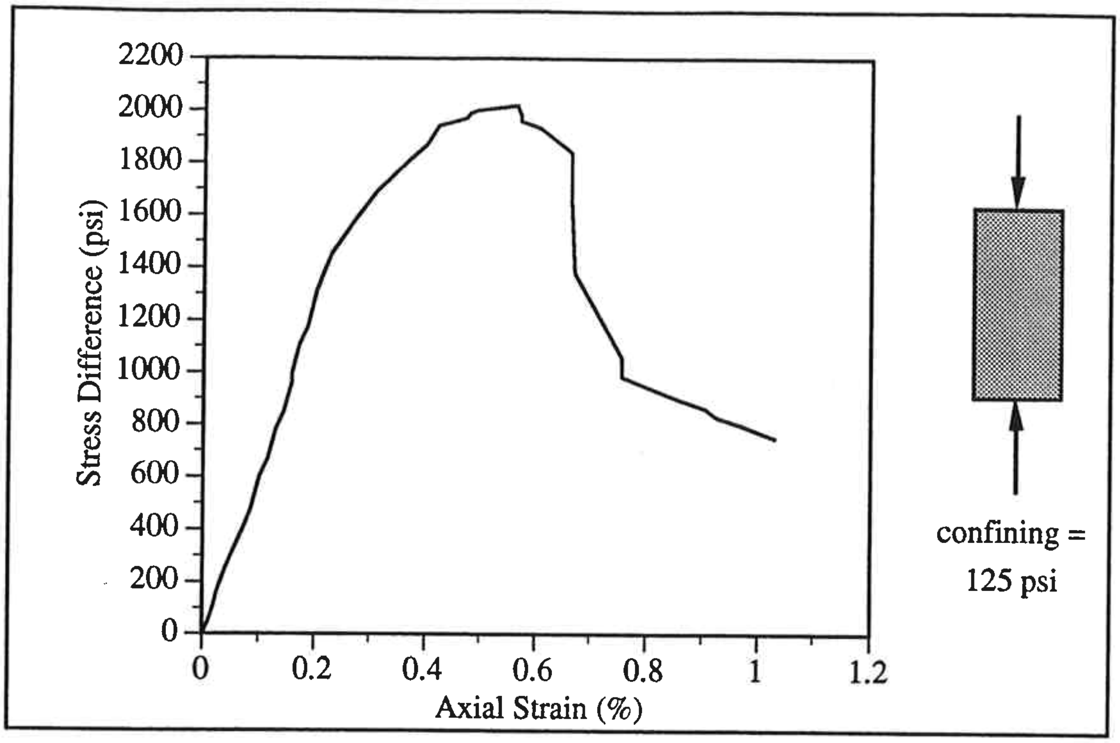

Figure B.12 Stress-Strain Curve for block-125

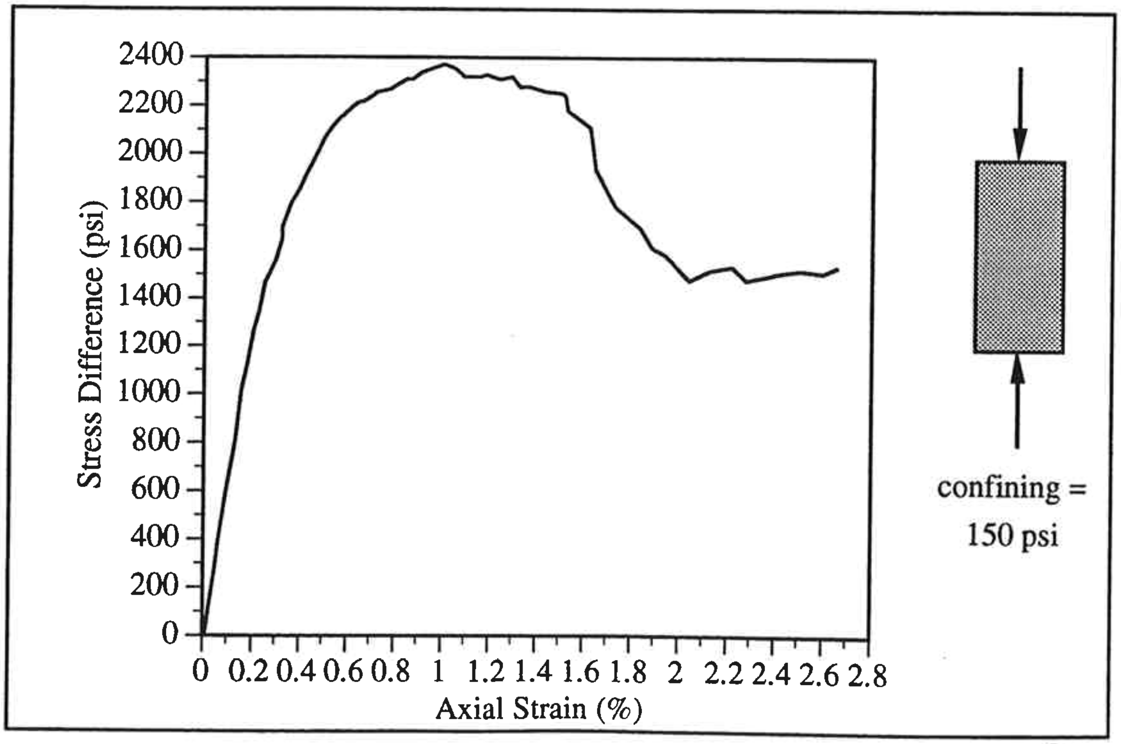

Figure B.13 Stress-Strain Curve for block-150

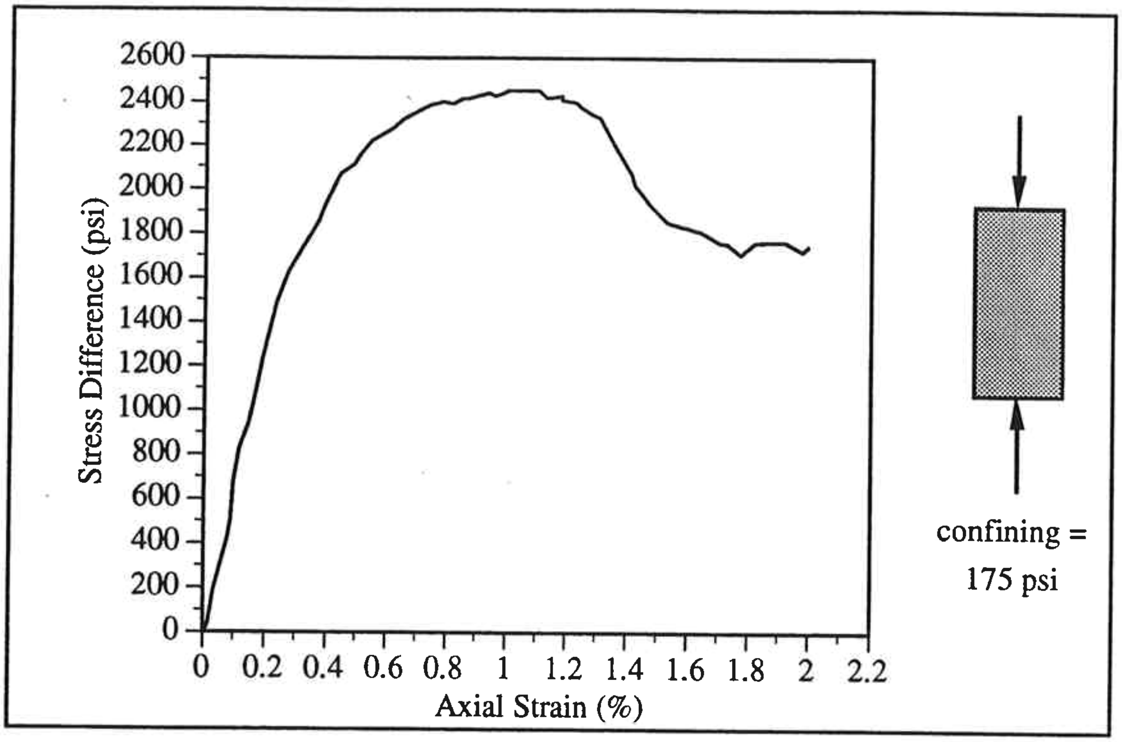

Figure B.14 Stress-Strain Curve for block-175

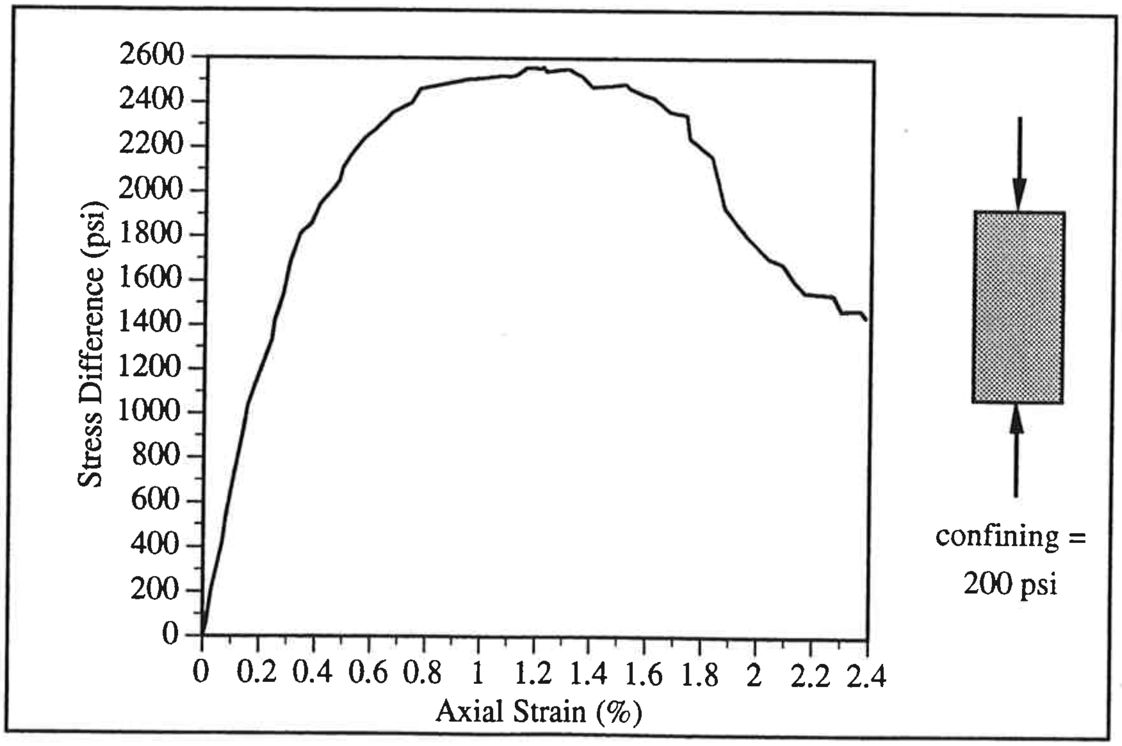

Figure B.15 Stress-Strain Curve for block-200

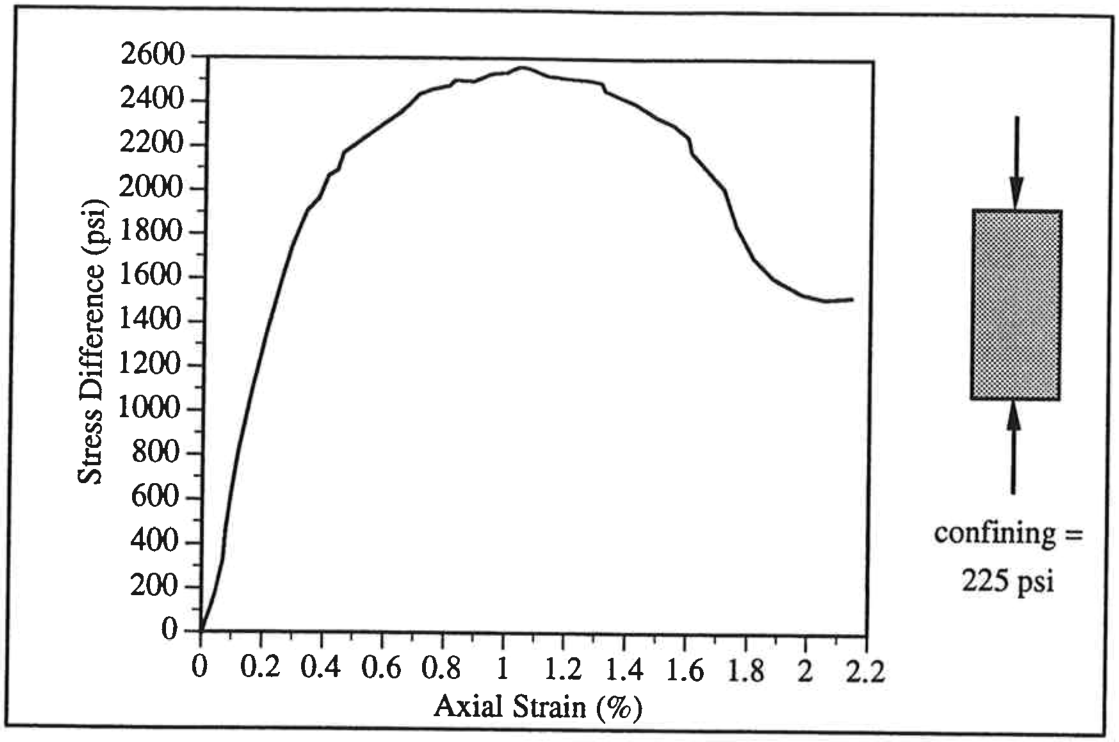

Figure B.16 Stress-Strain Curve for block-225

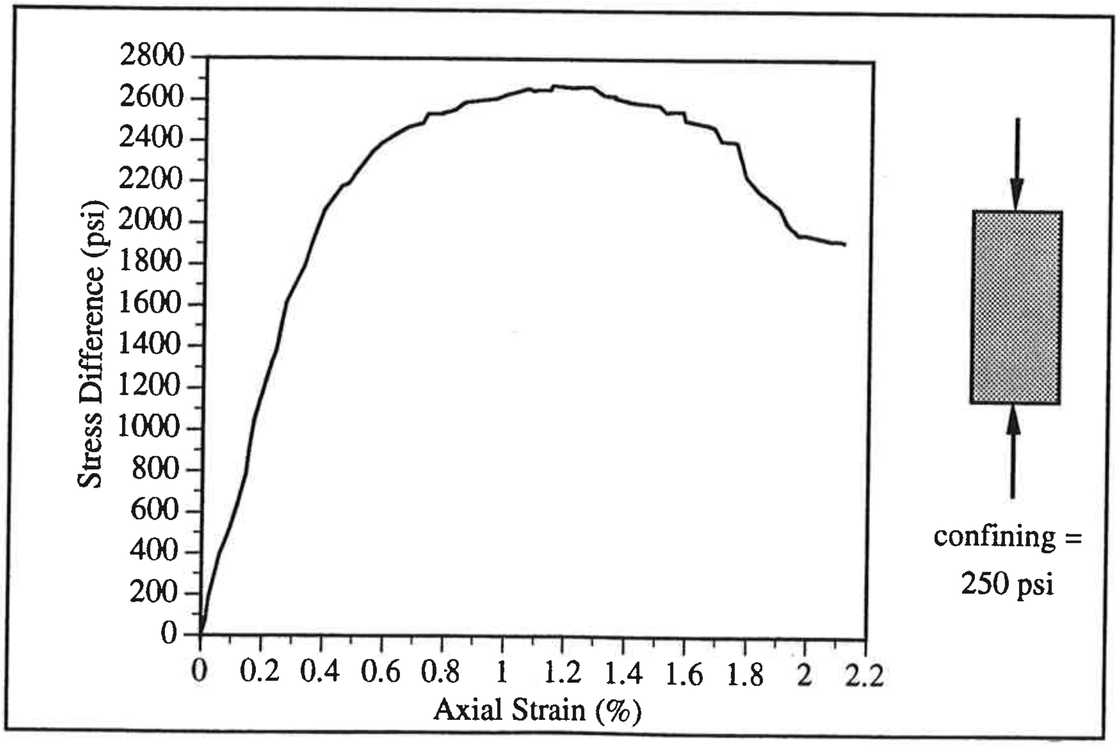

Figure B.17 Stress-Strain Curve for block-250

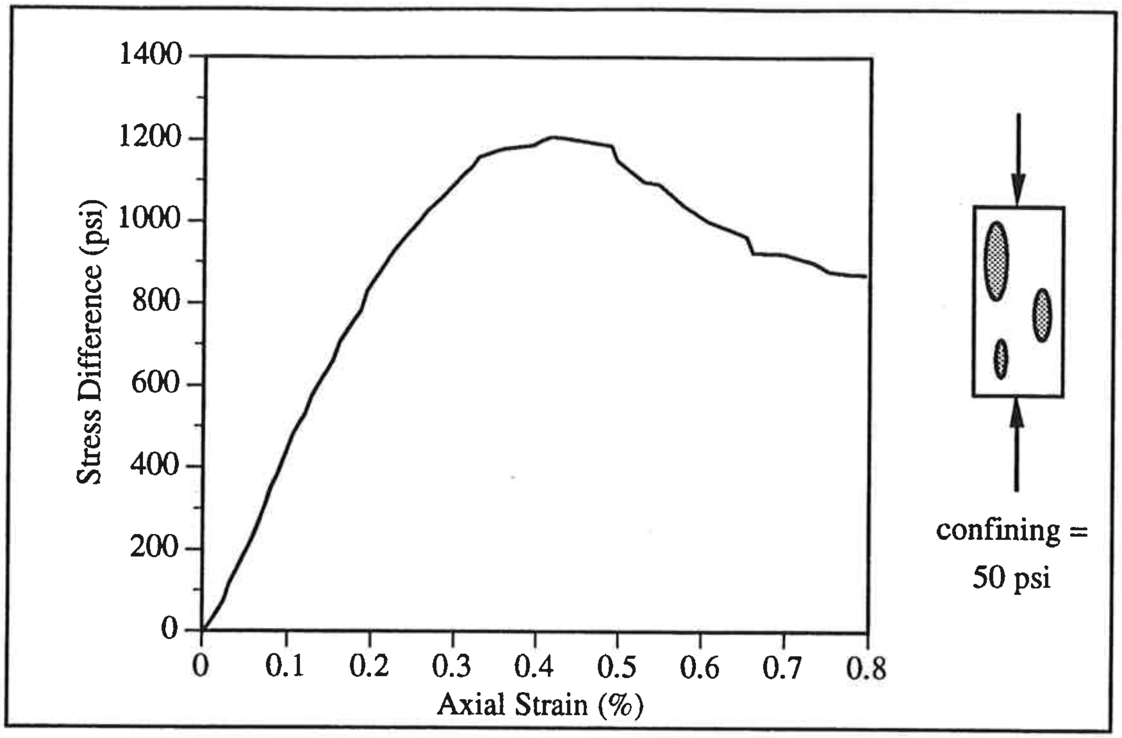

Figure B.18 Stress-Strain Curve for 1-0-50

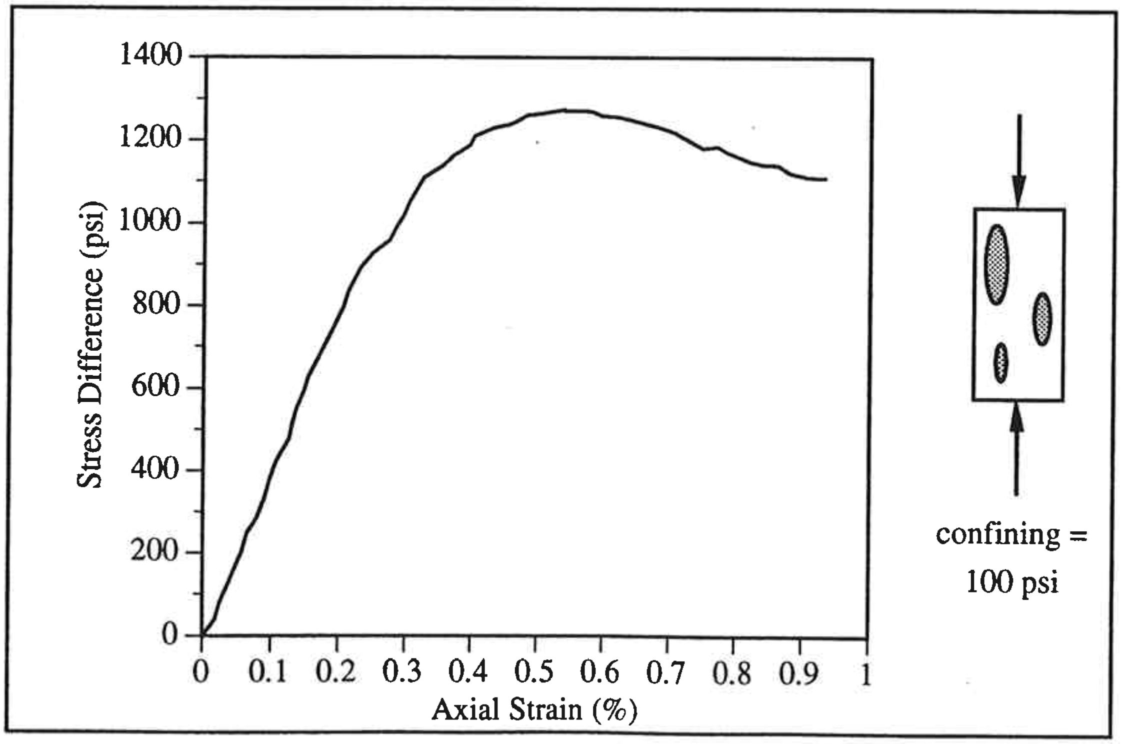

Figure B.19 Stress-Strain Curve for 1-0-100

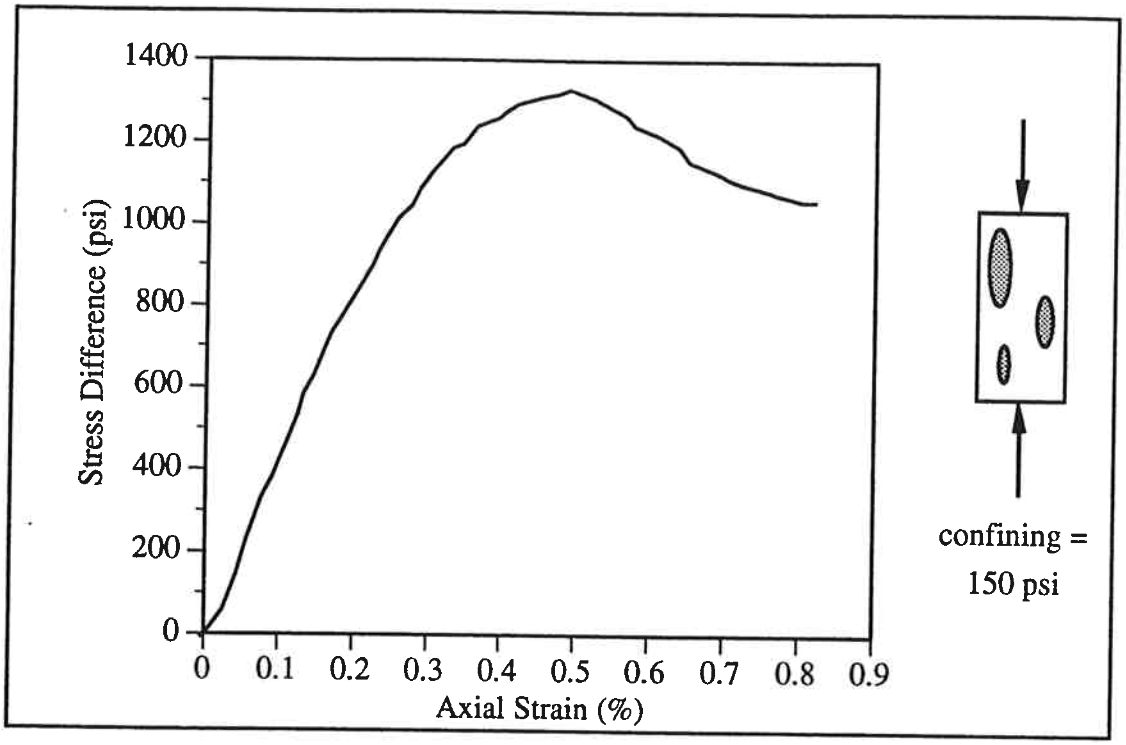

Figure B.20 Stress-Strain Curve for 1-0-150

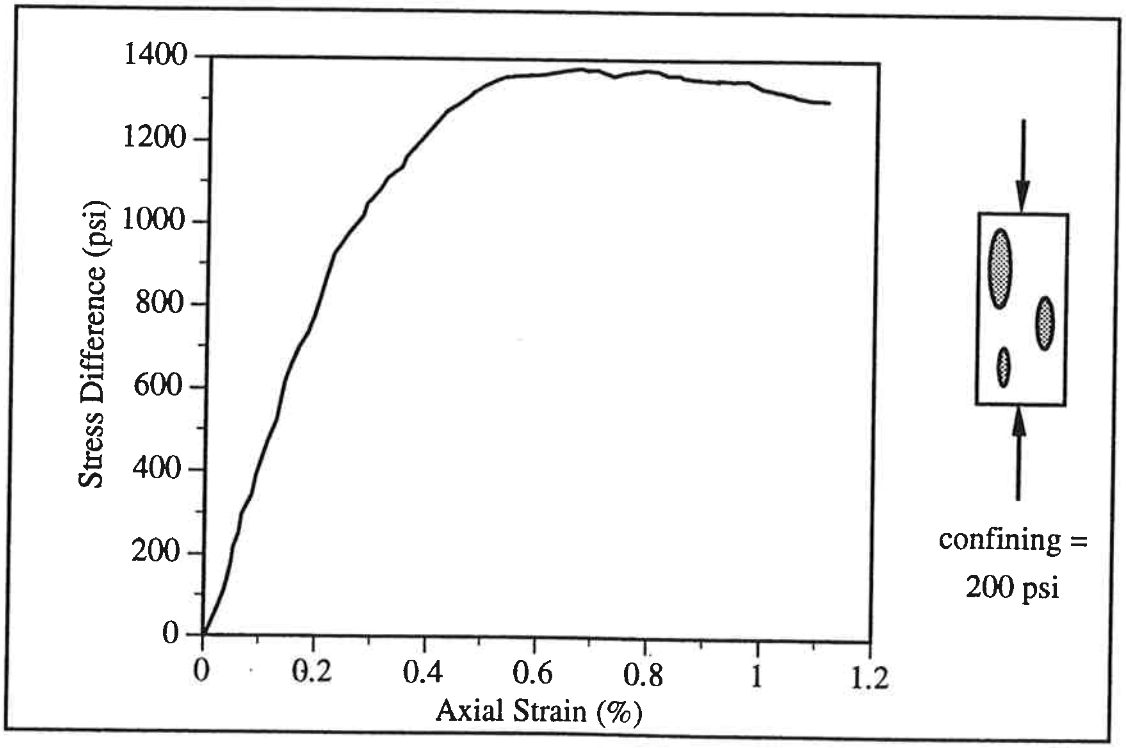

Figure B.21 Stress-Strain Curve for 1-0-200

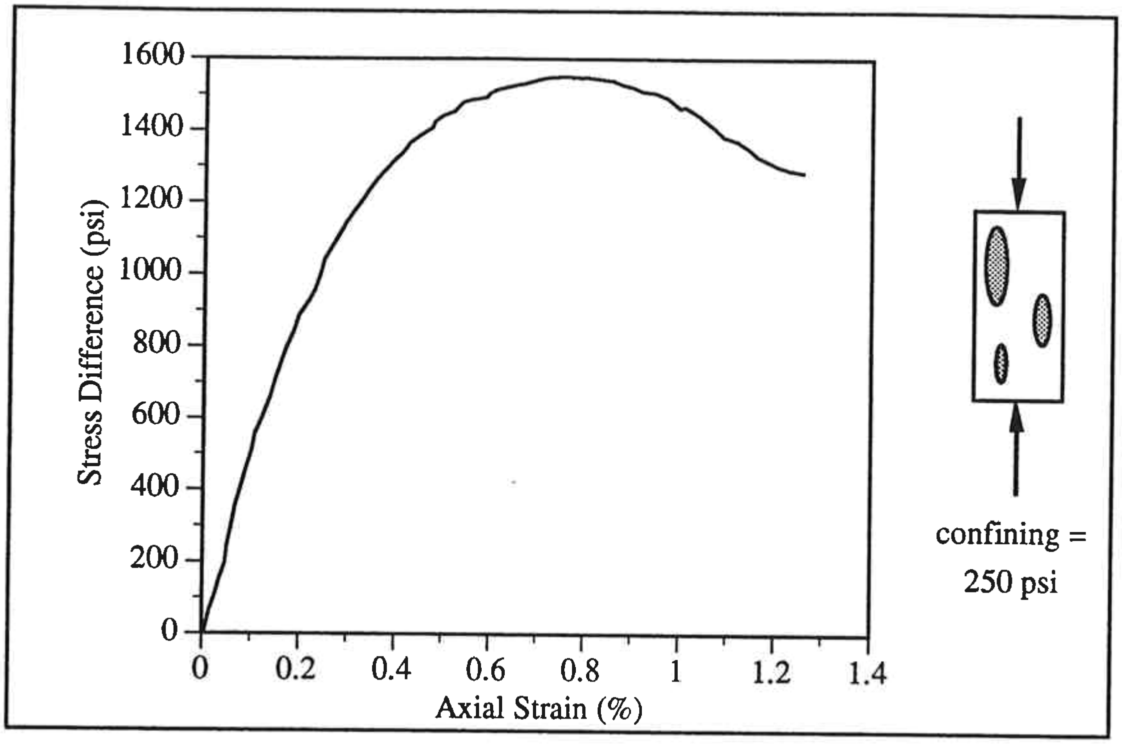

Figure B.22 Stress-Strain Curve for 1-0-250

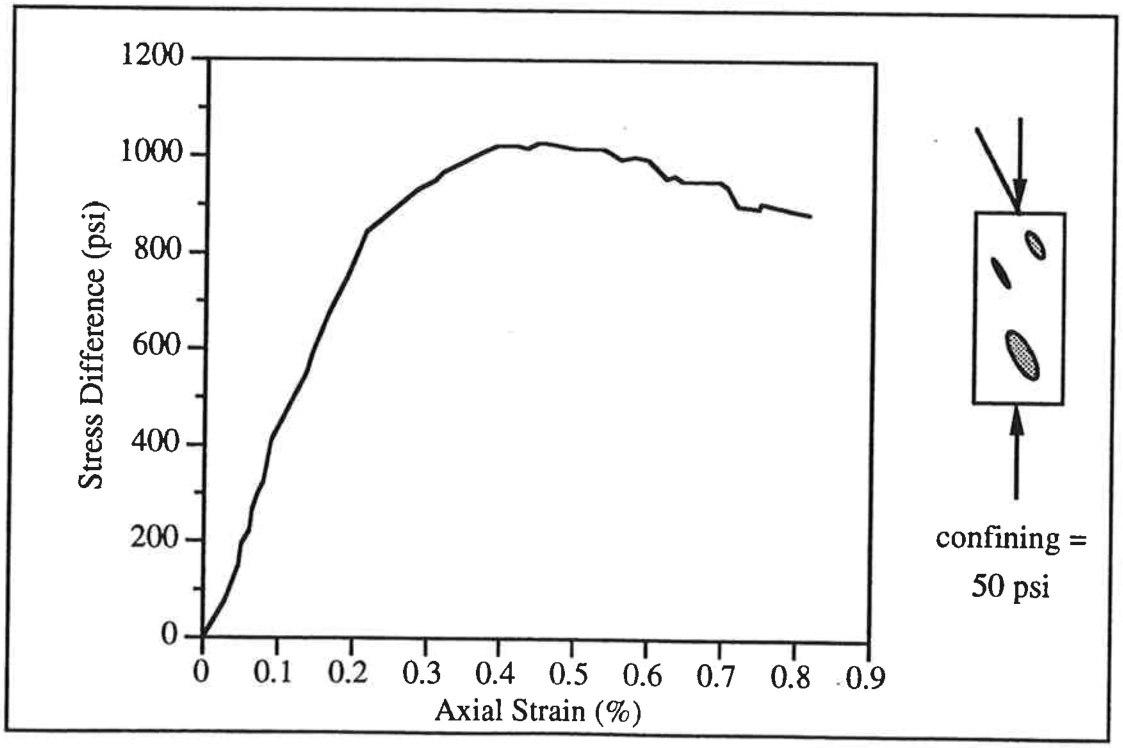

Figure B.23 Stress-Strain Curve for 1-30-50

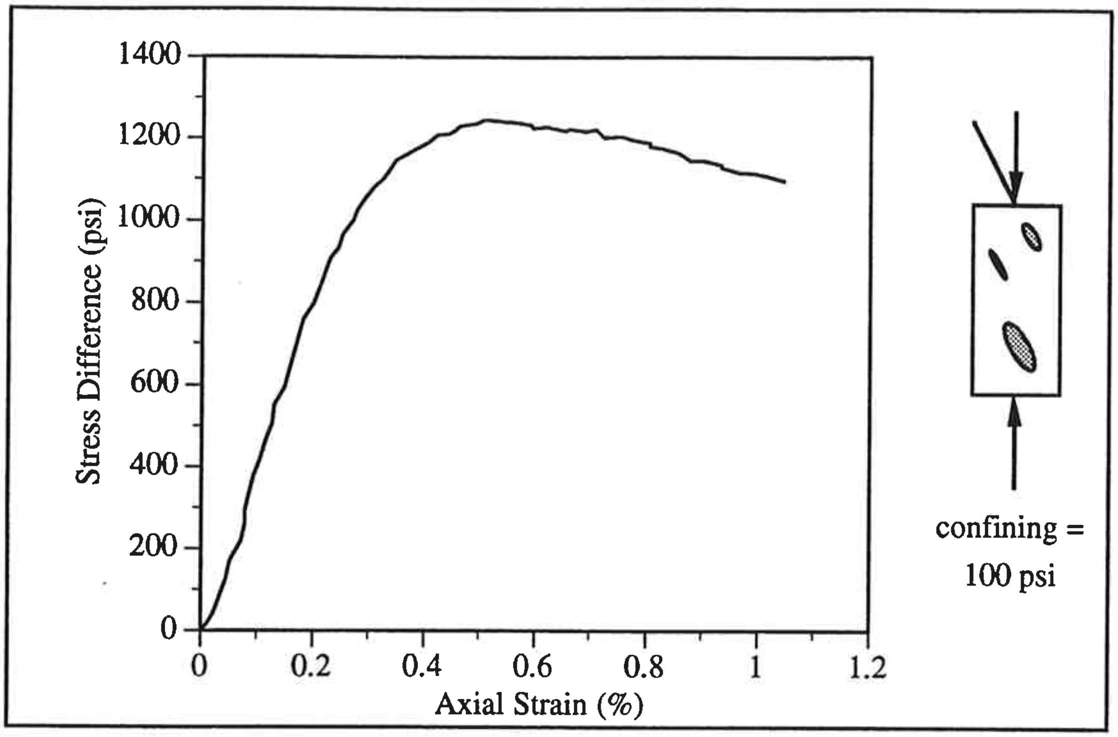

Figure B.24 Stress-Strain Curve for 1-30-100

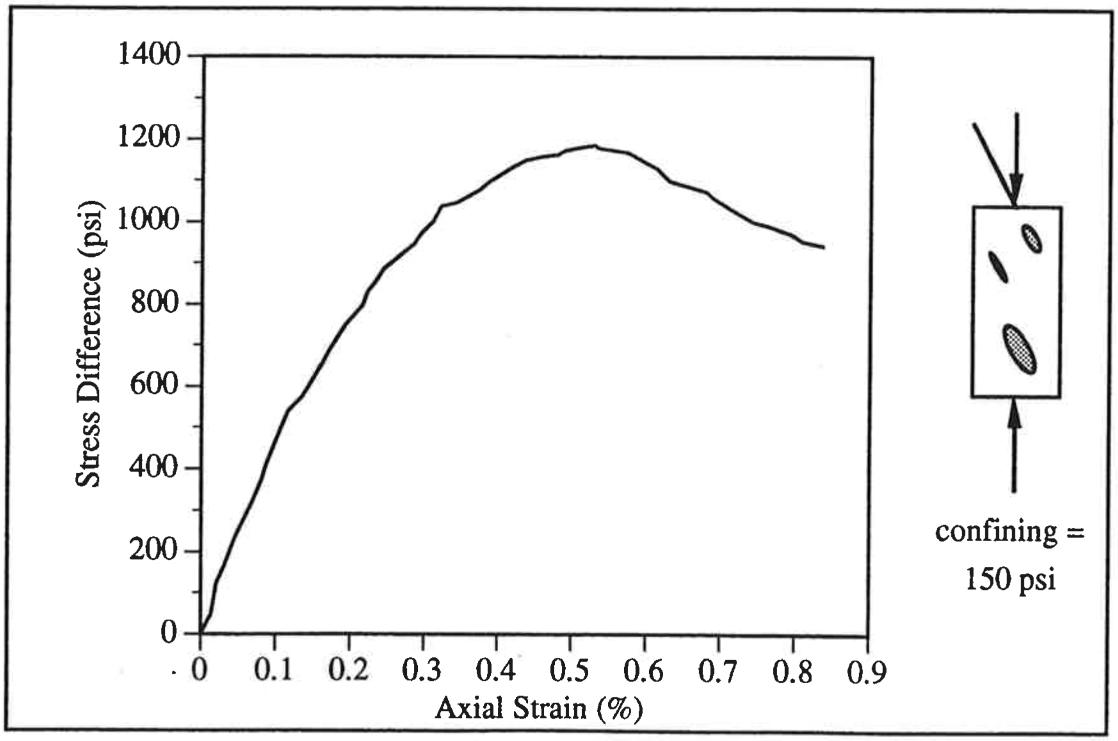

Figure B.25 Stress-Strain Curve for 1-30-150

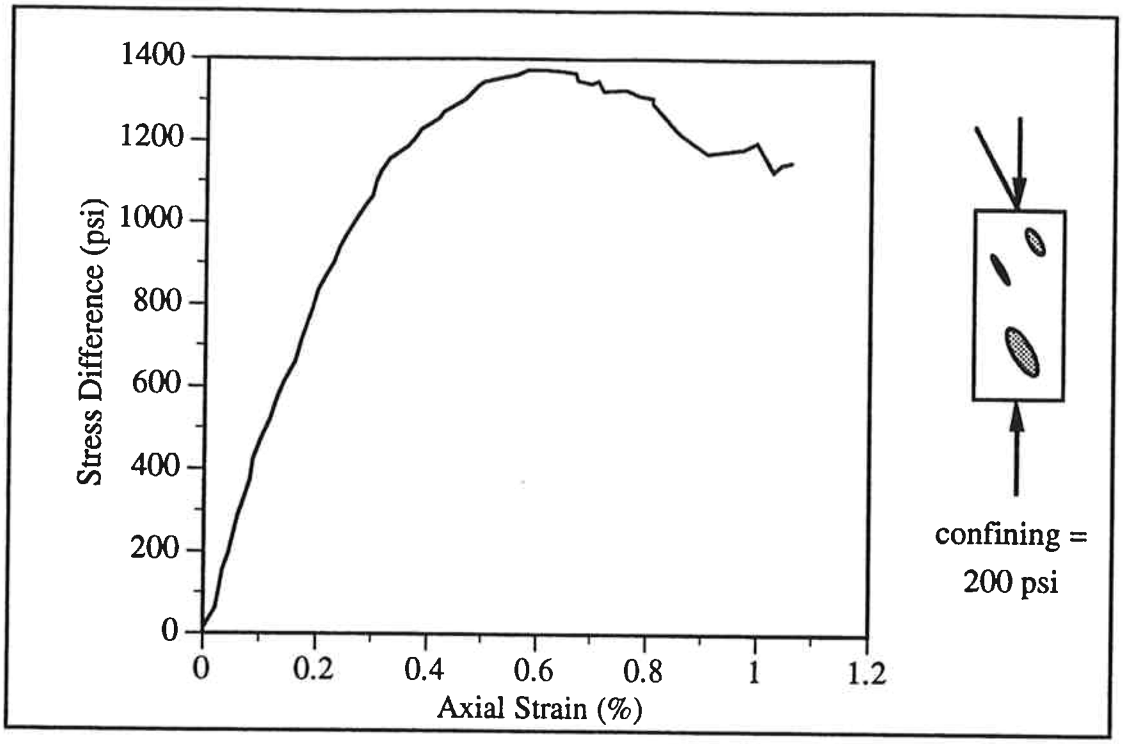

Figure B.26 Stress-Strain Curve for 1-30-200

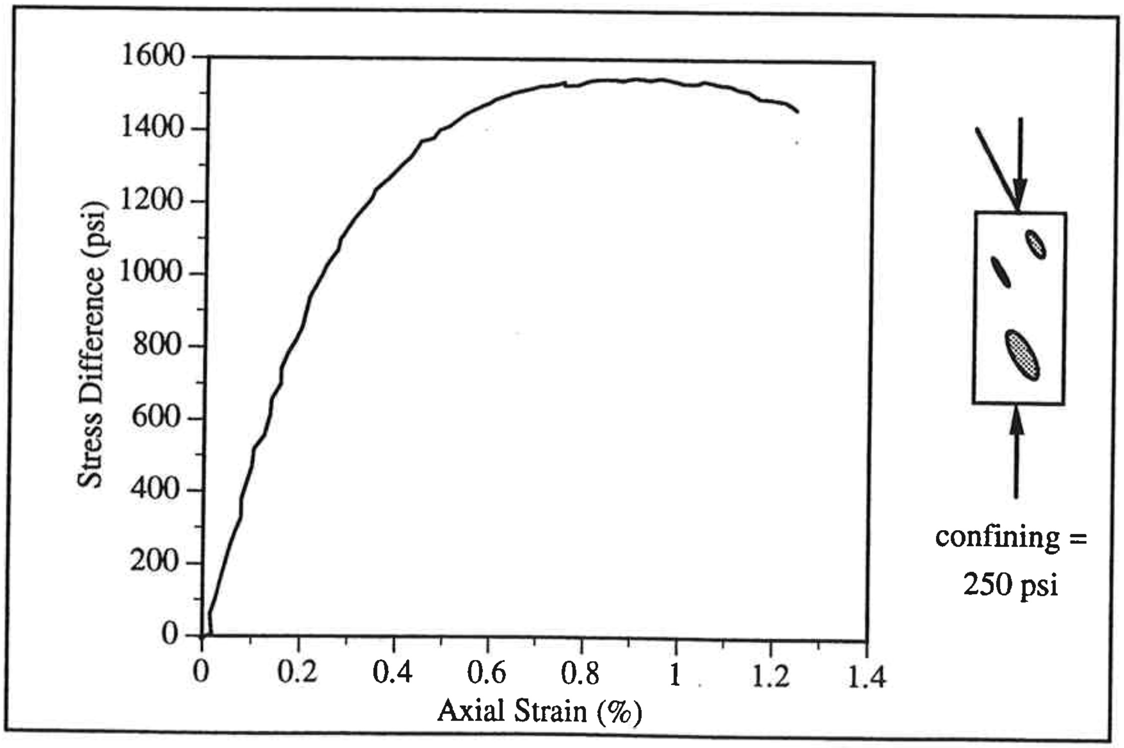

Figure B.27 Stress-Strain Curve for 1-30-250

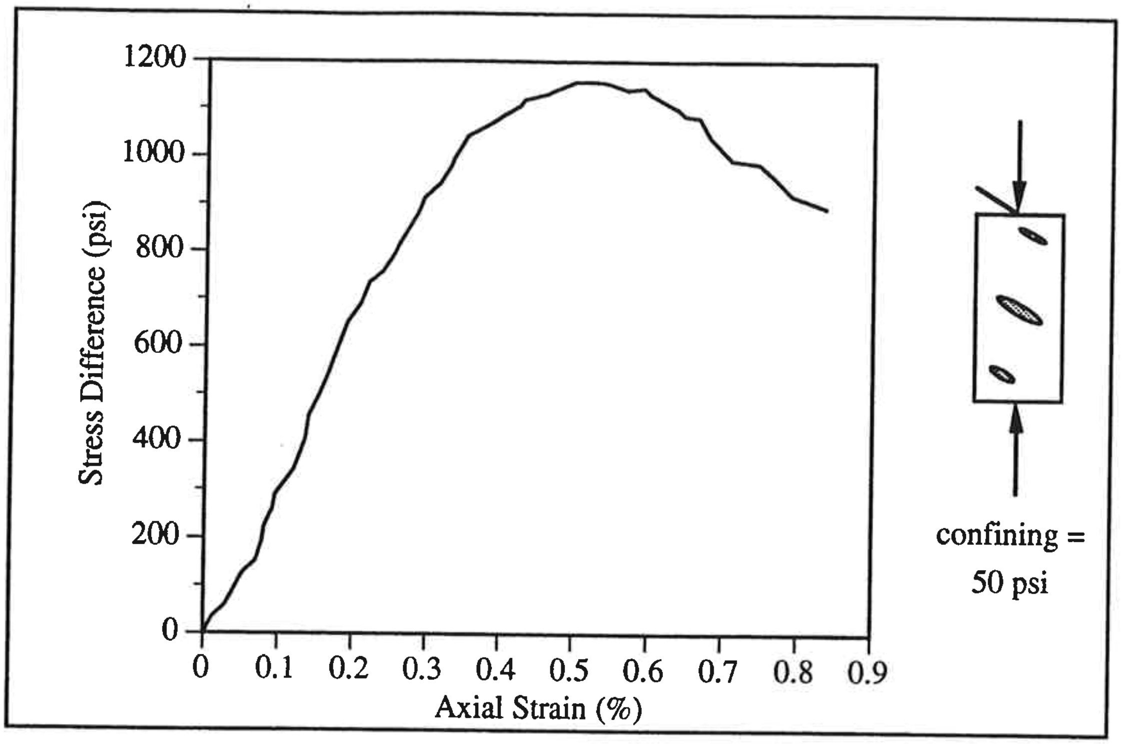

Figure B.28 Stress-Strain Curve for I-60-50

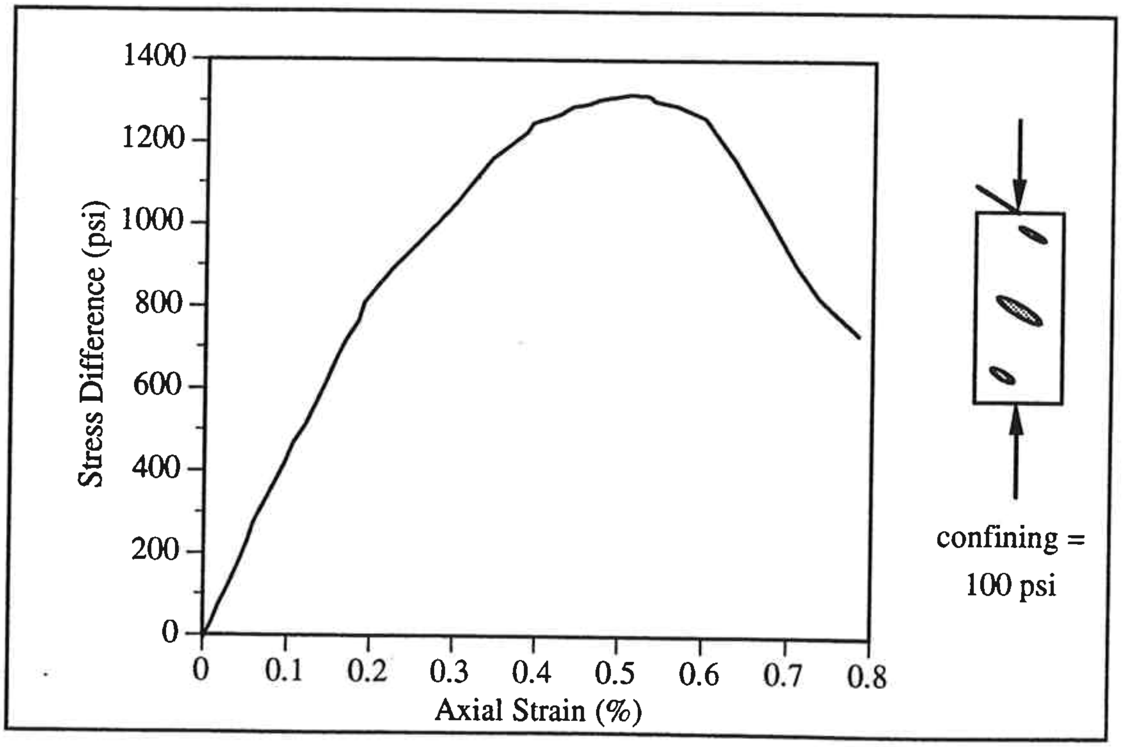

Figure B.29 Stress-Strain Curve for I-60-100

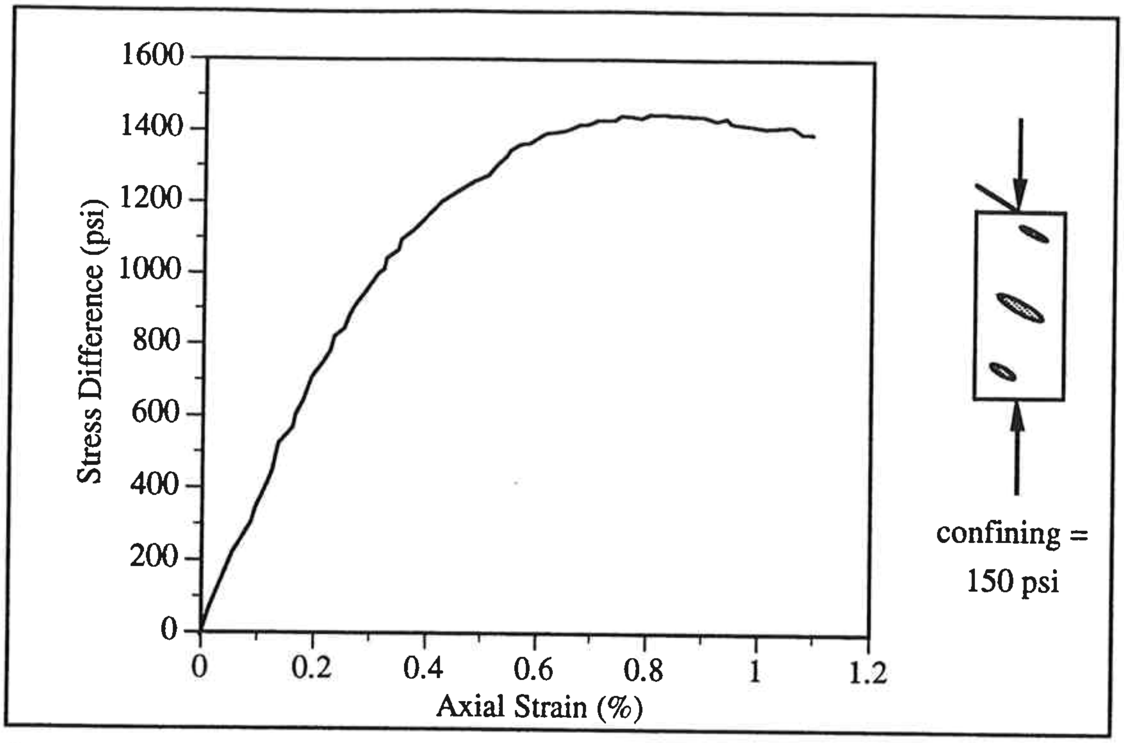

Figure B.30 Stress-Strain Curve for l-60-150

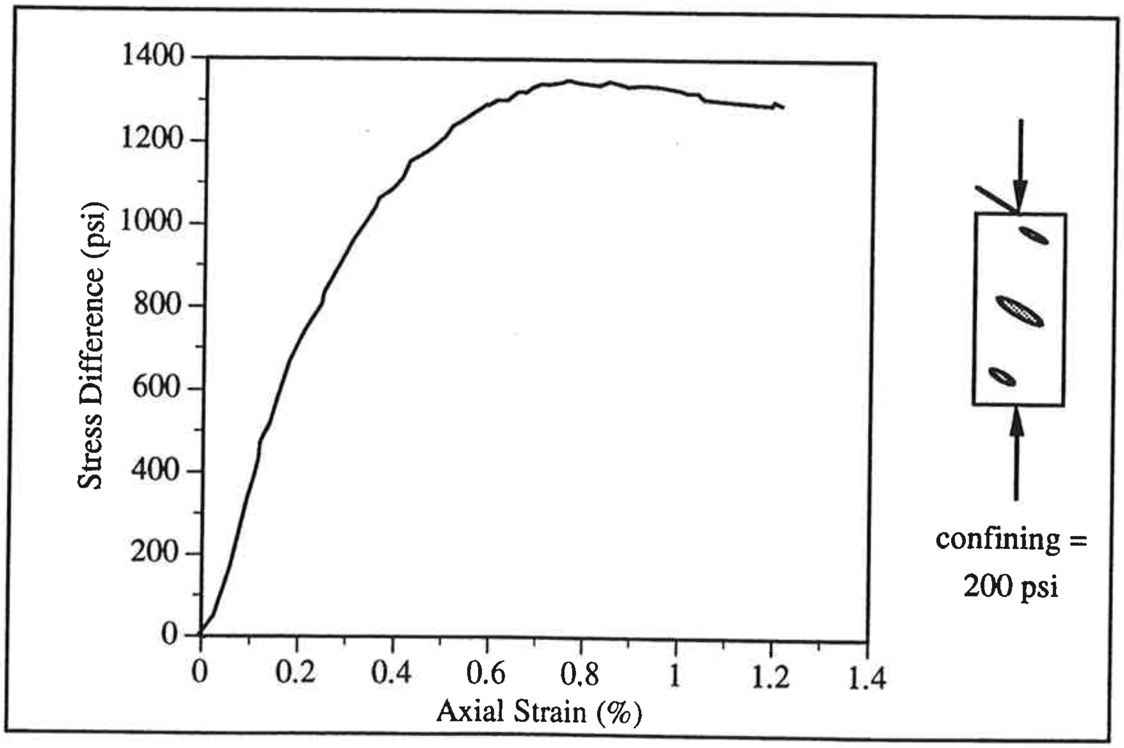

Figure B.31 Stress-Strain Curve for l-60-200

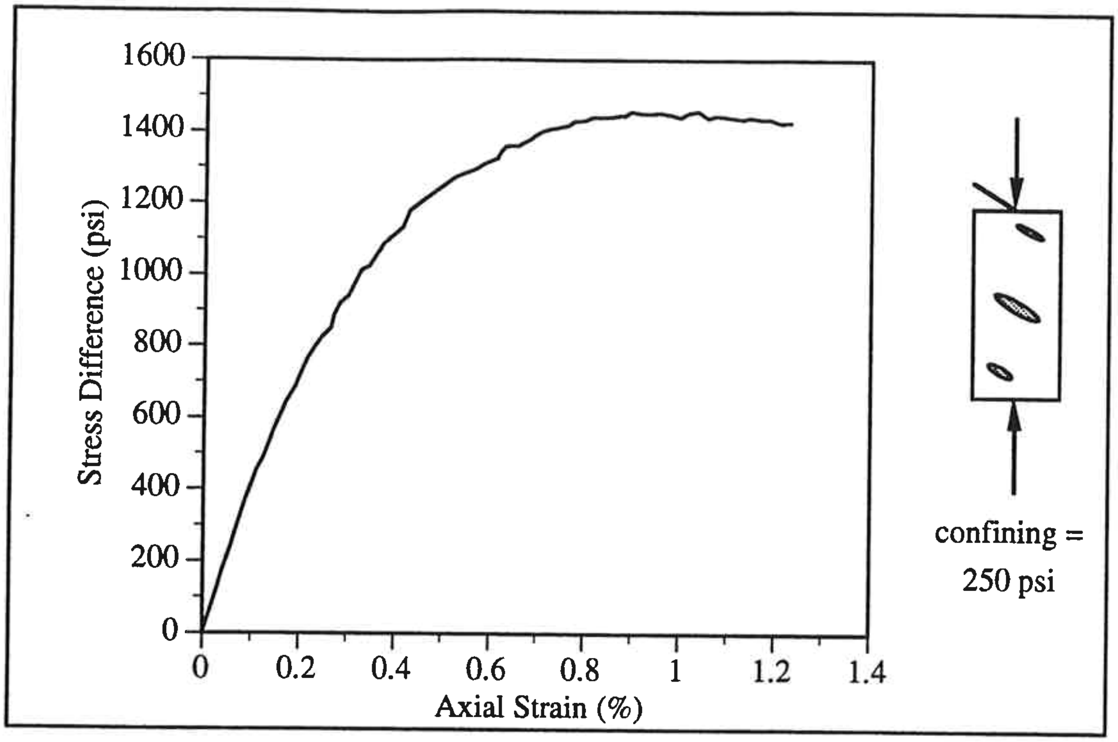

Figure B.32 Stress-Strain Curve for 1-60-250

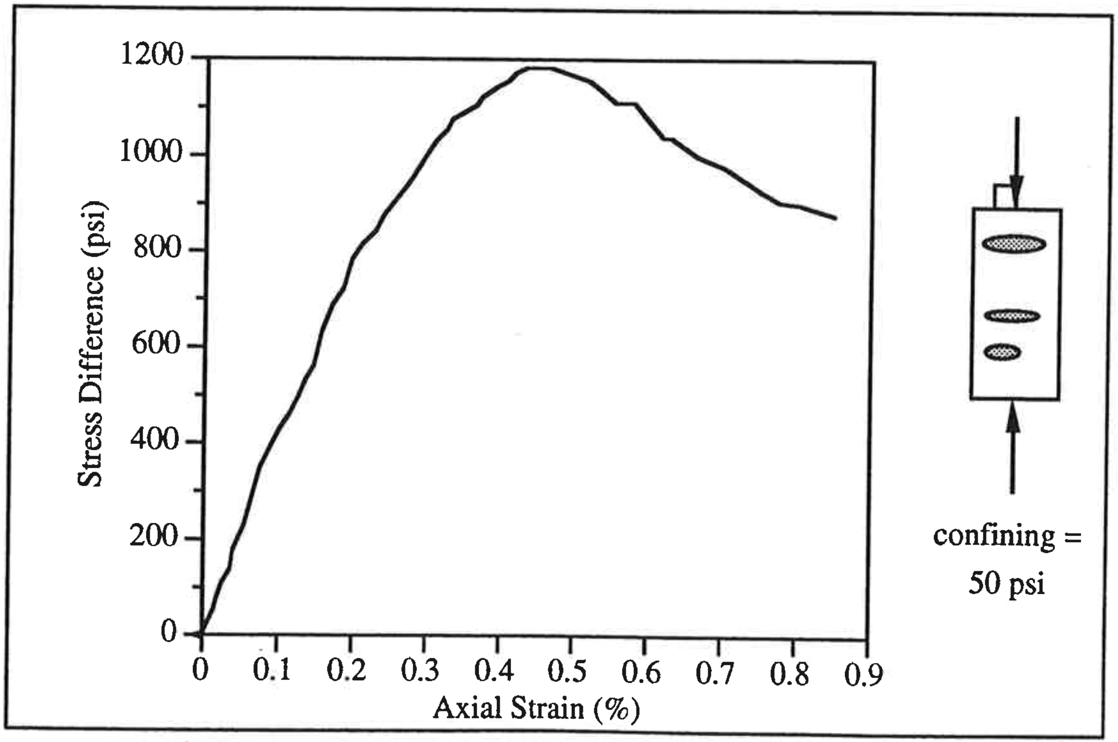

Figure B.33 Stress-Strain Curve for 1-60-50

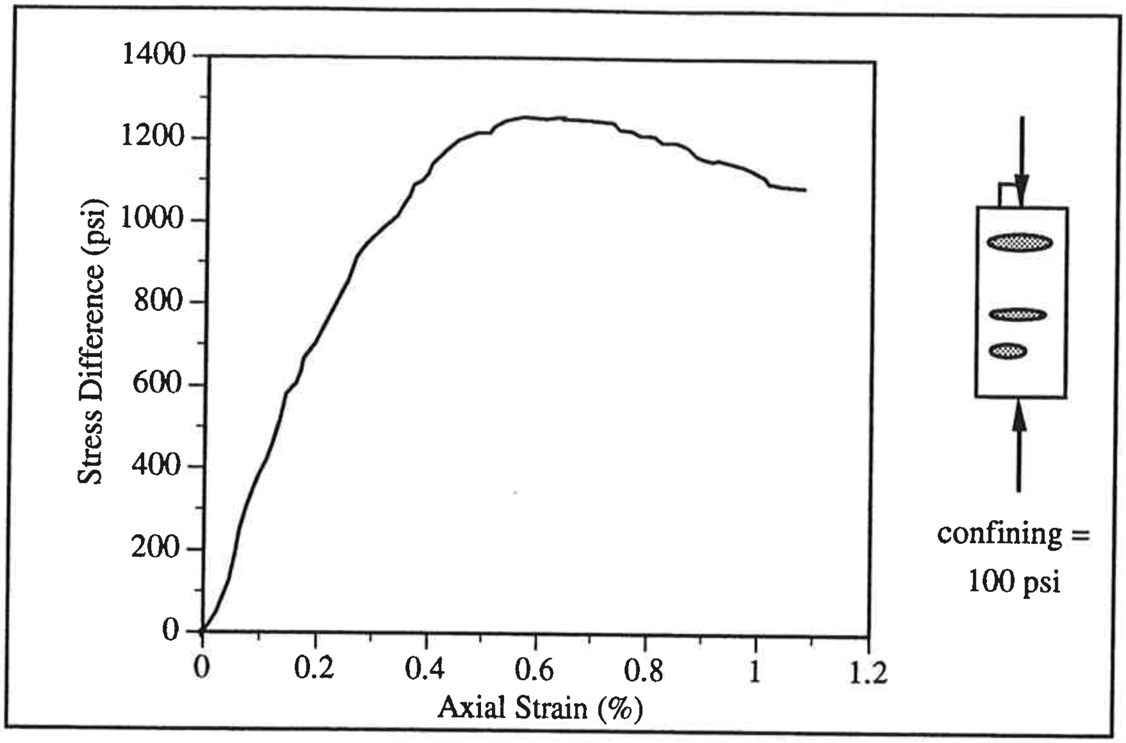

Figure B.34 Stress-Strain Curve for 1-90-100

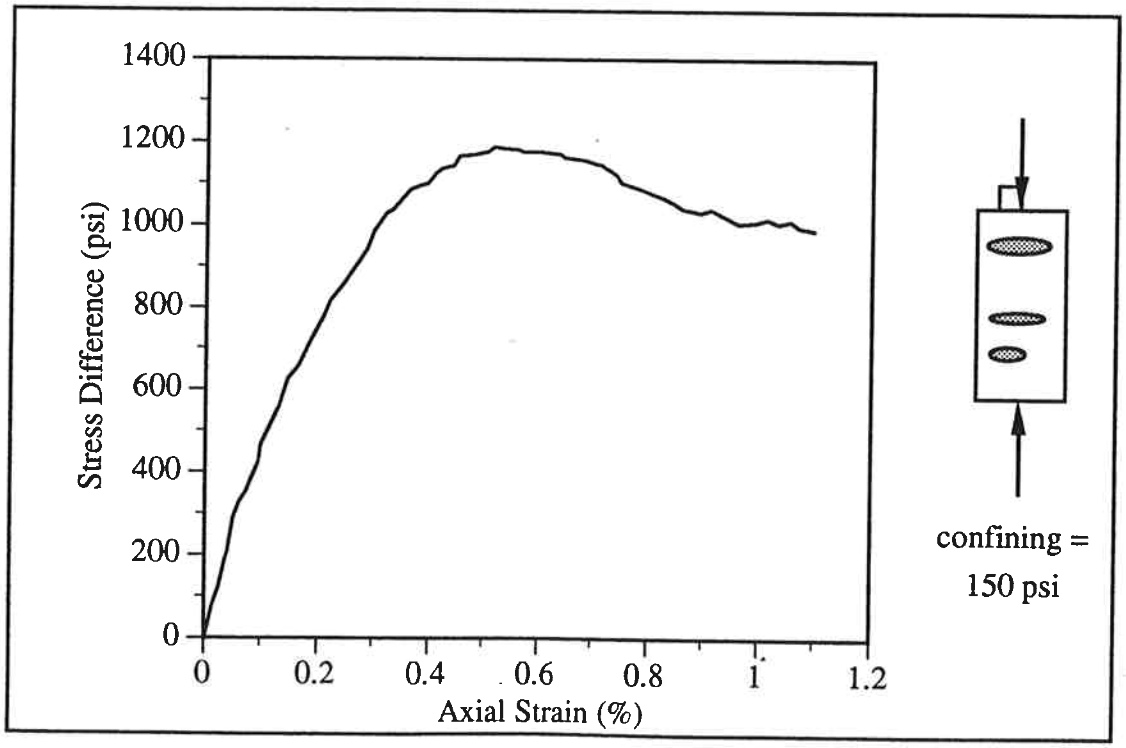

Figure B.35 Stress-Strain Curve for 1-90-150

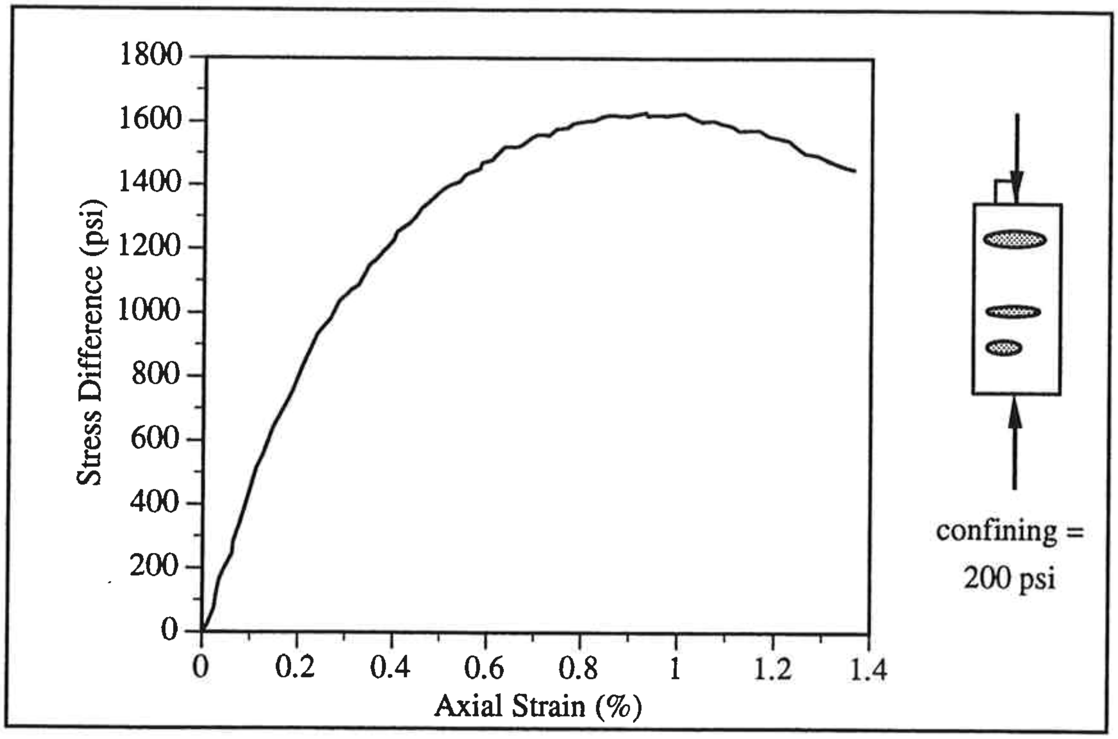

Figure B.36 Stress-Strain Curve for 1-90-200

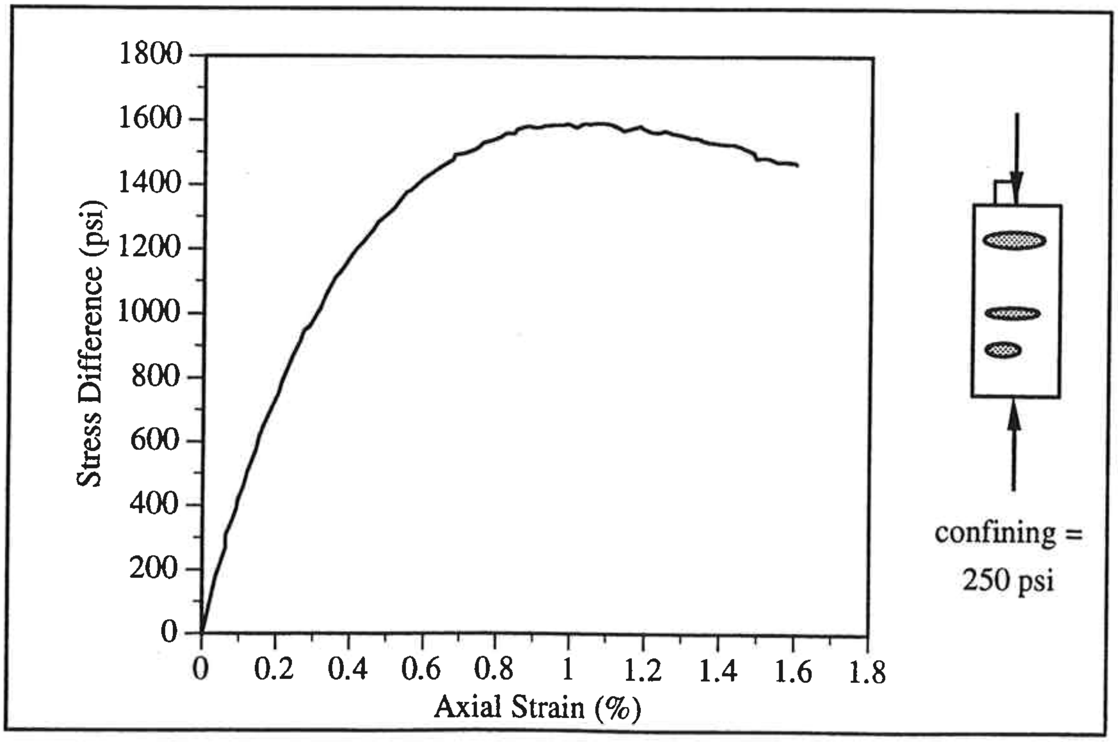

Figure B.37 Stress-Strain Curve for 1-90-250

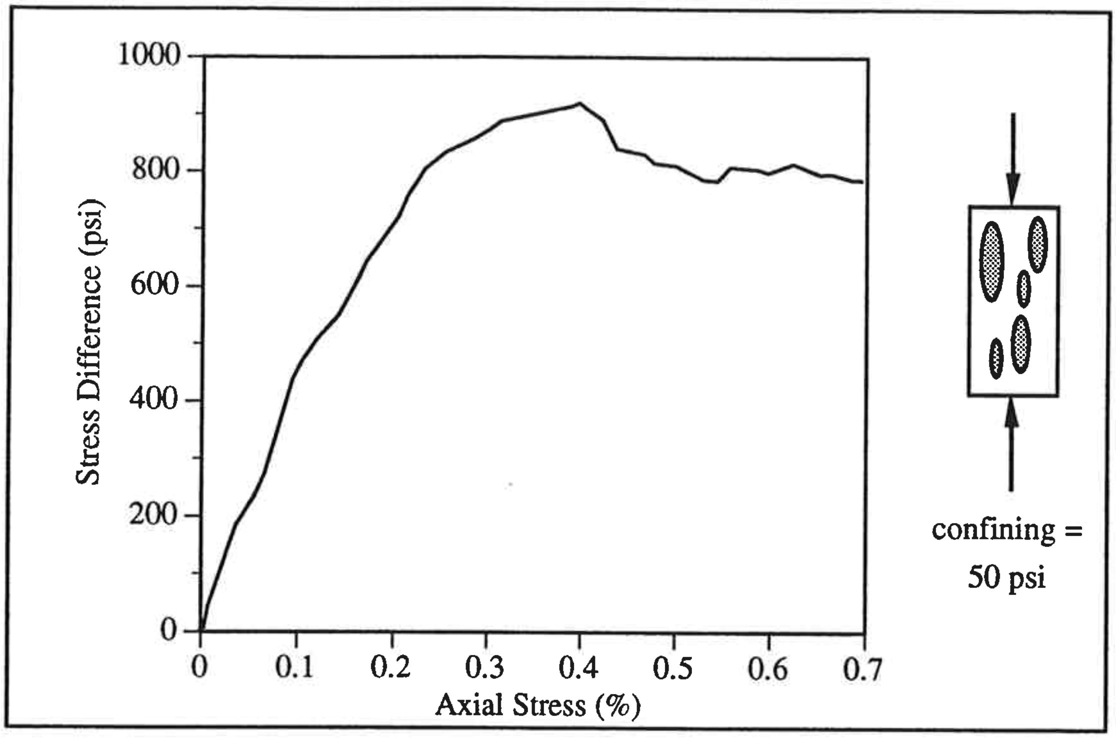

Figure B.38 Stress-Strain Curve for m-0-50

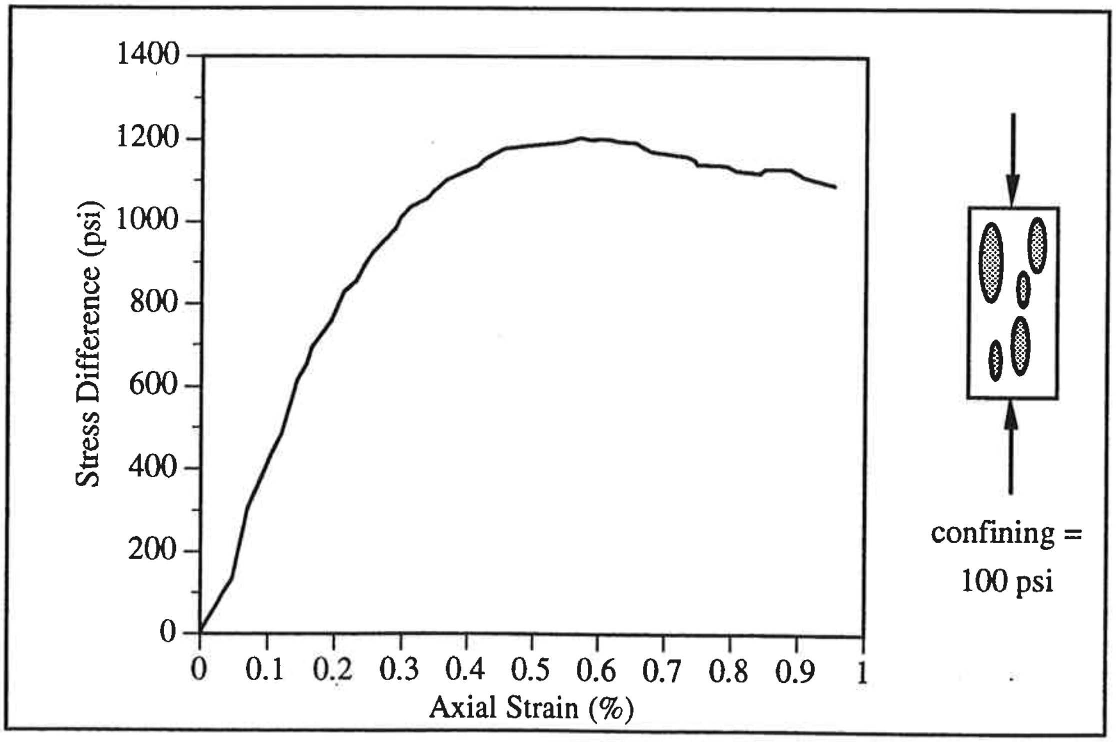

Figure B.39 Stress-Strain Curve for m-0-100

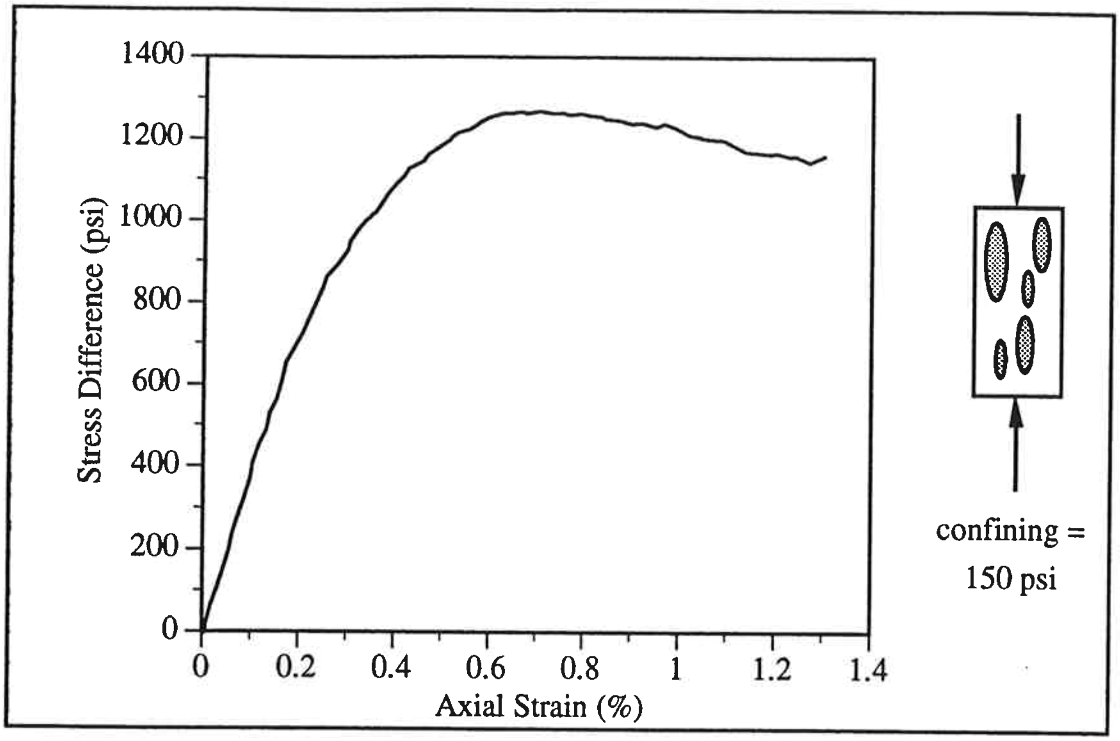

Figure B.40 Stress-Strain Curve for m-0-150

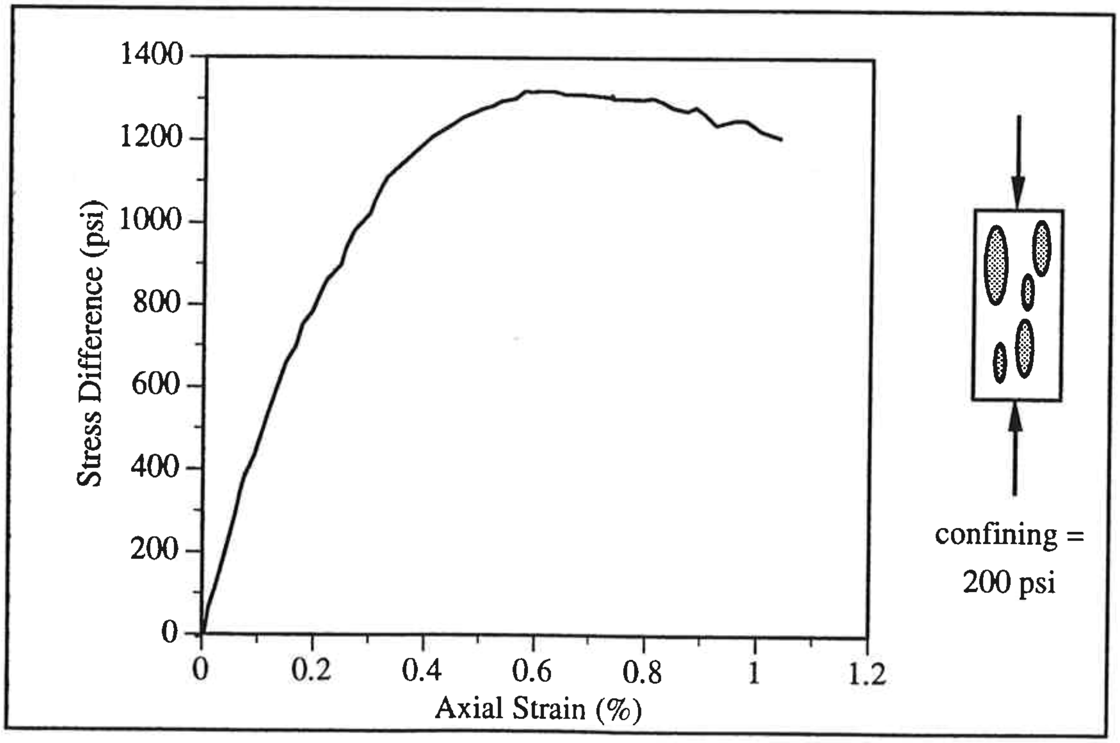

Figure B.41 Stress-Strain Curve for m-0-200

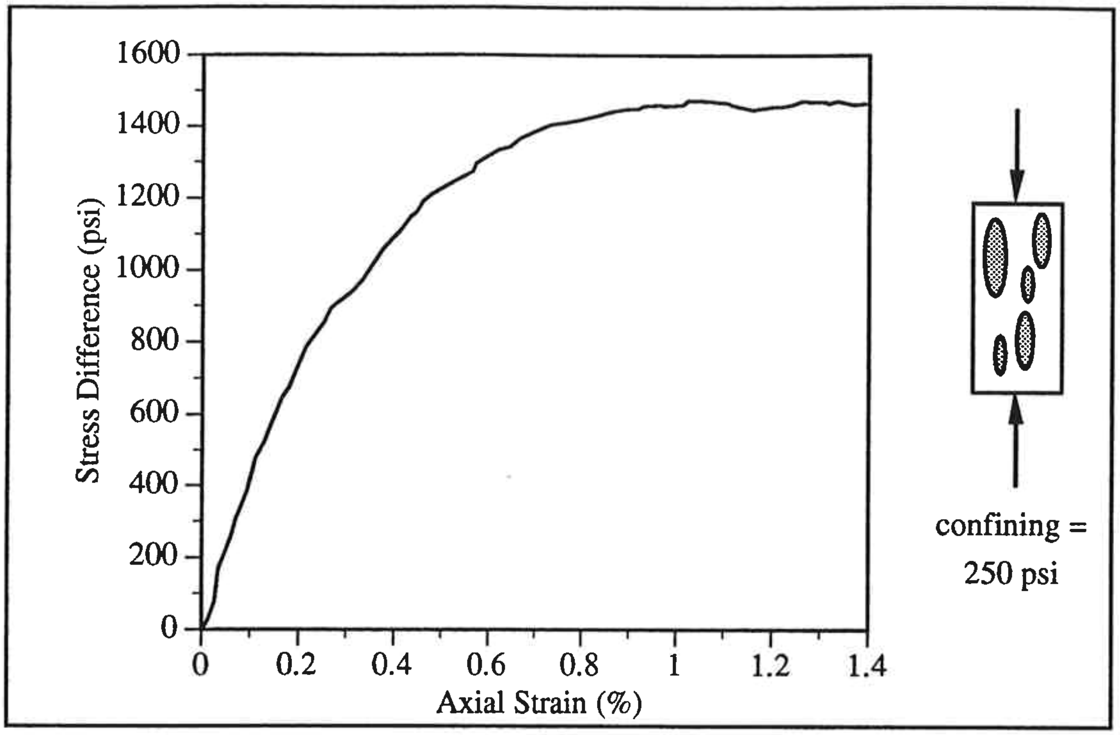

Figure B.42 Stress-Strain Curve for m-0-250

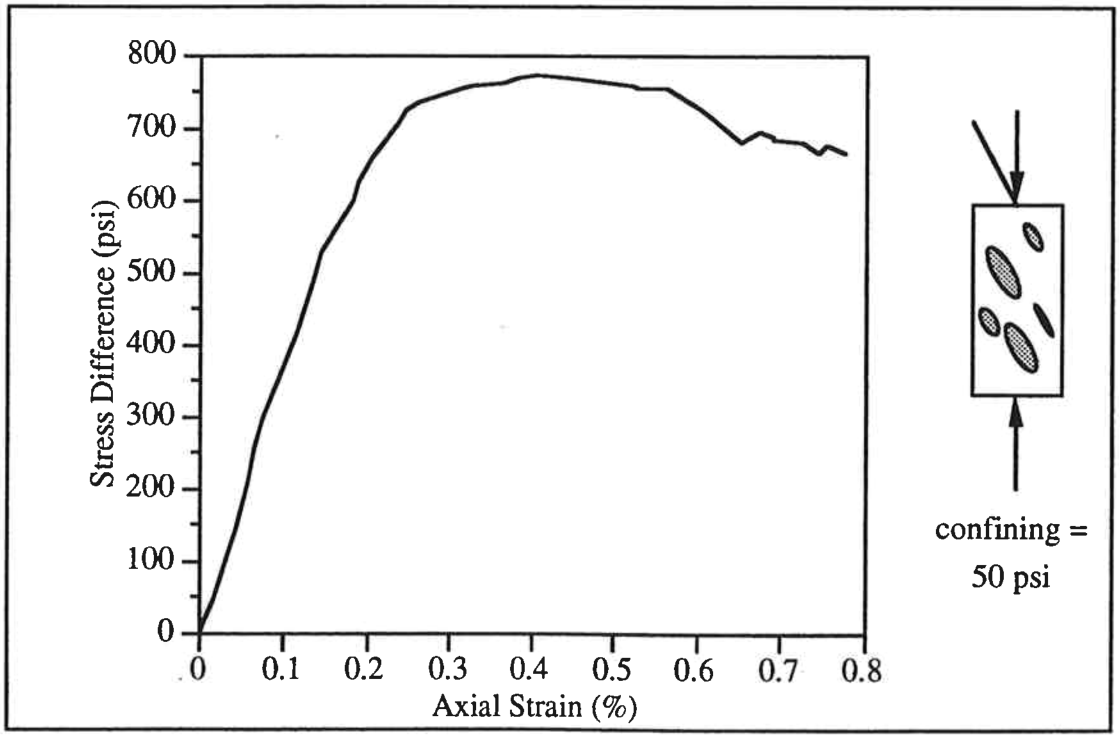

Figure B.43 Stress-Strain Curve for m-30-50

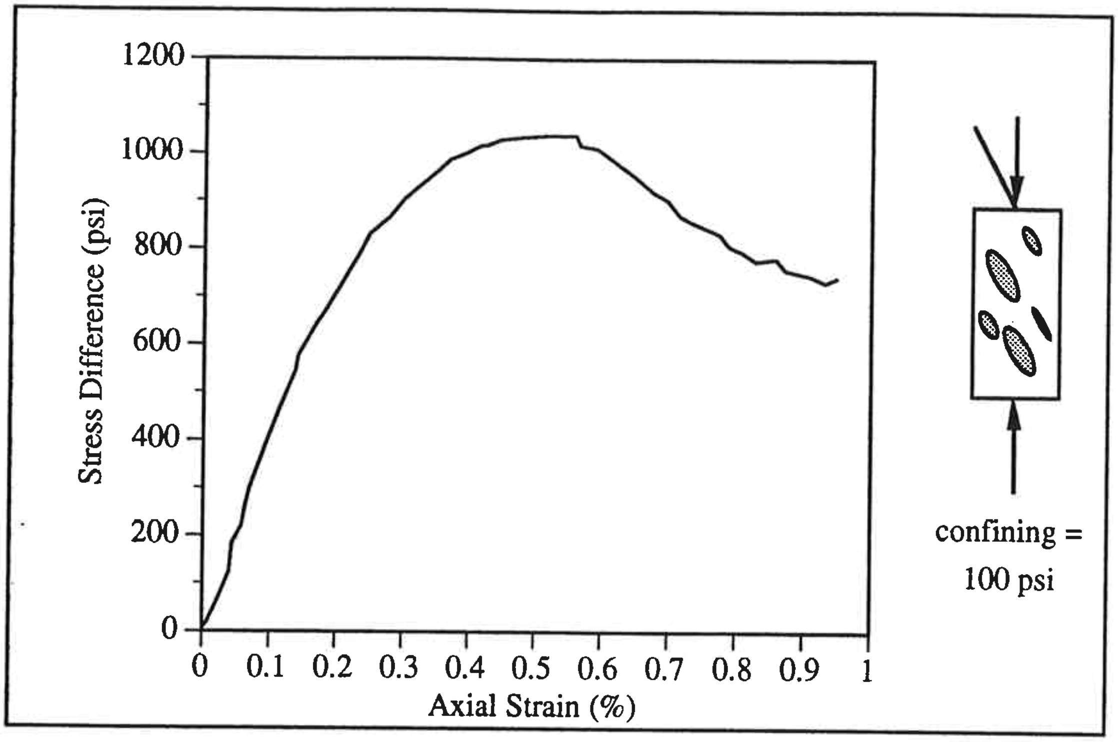

Figure B.44 Stress-Strain Curve for m-30-100

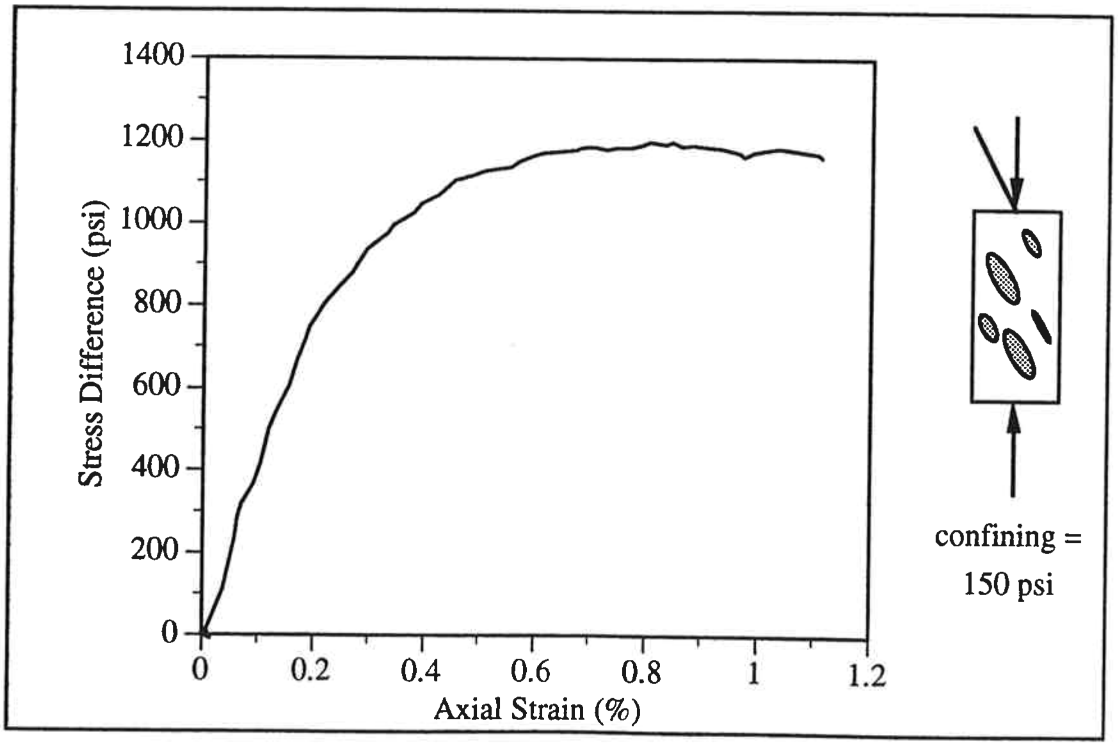

Figure B.45 Stress-Strain Curve for m-30-150

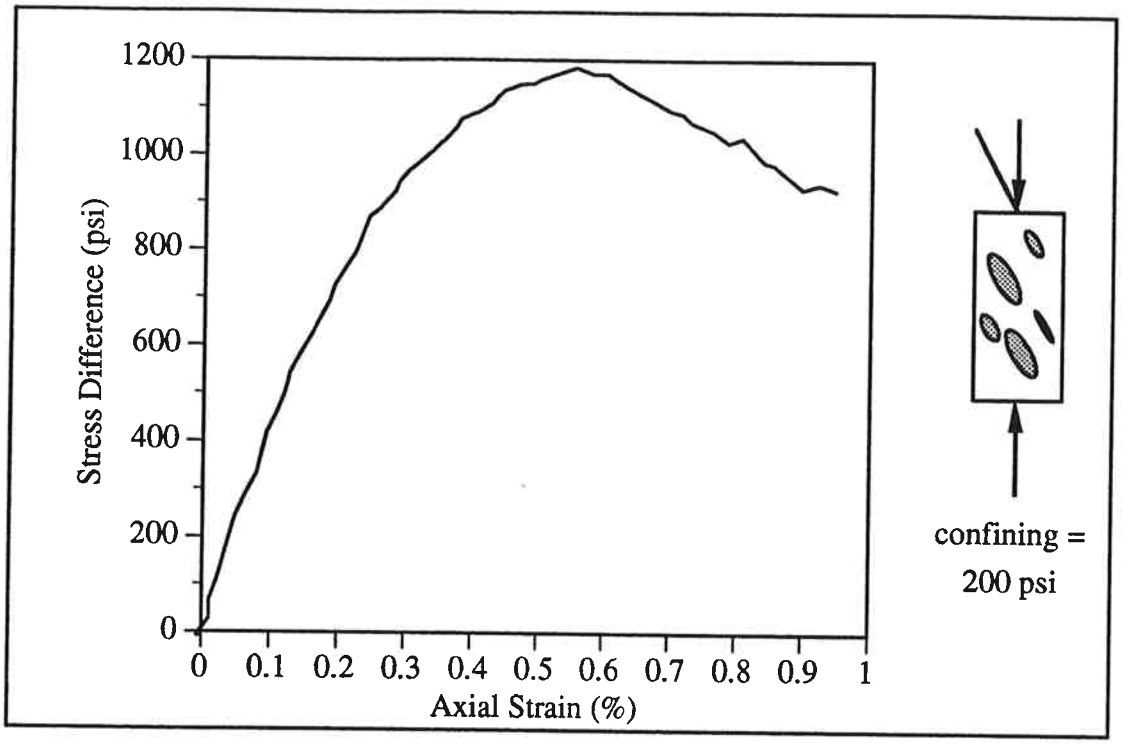

Figure B.46 Stress-Strain Curve for m-30-200

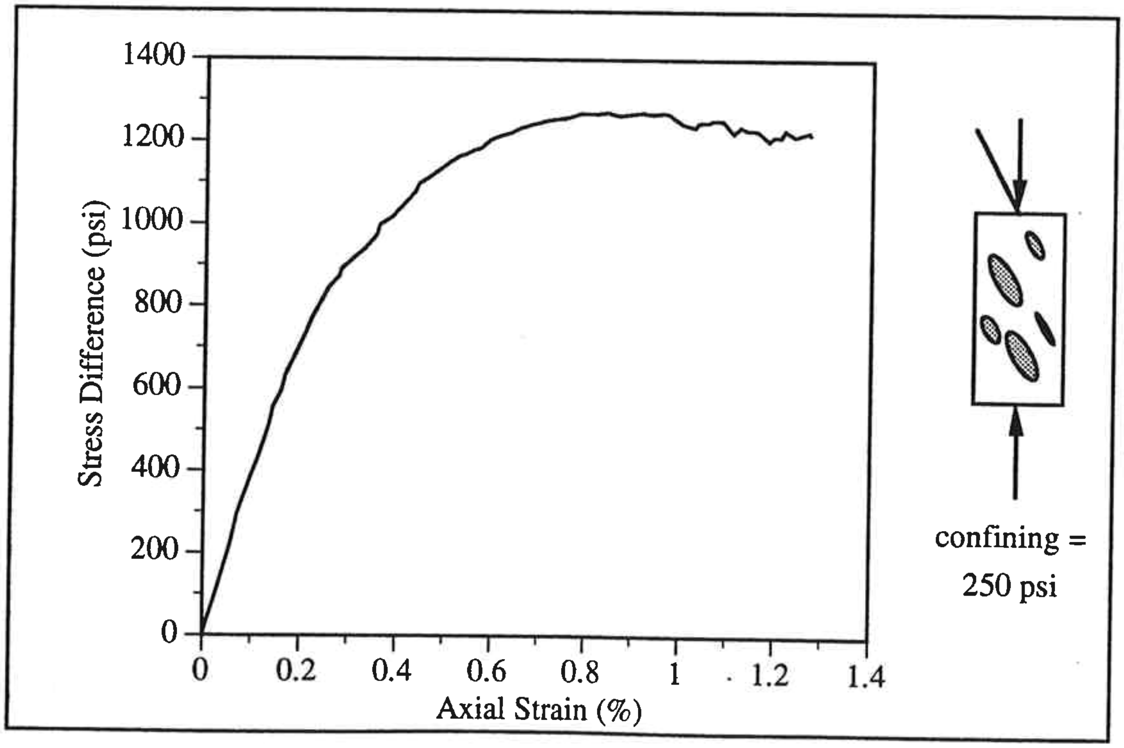

Figure B.47 Stress-Strain Curve for m-30-250

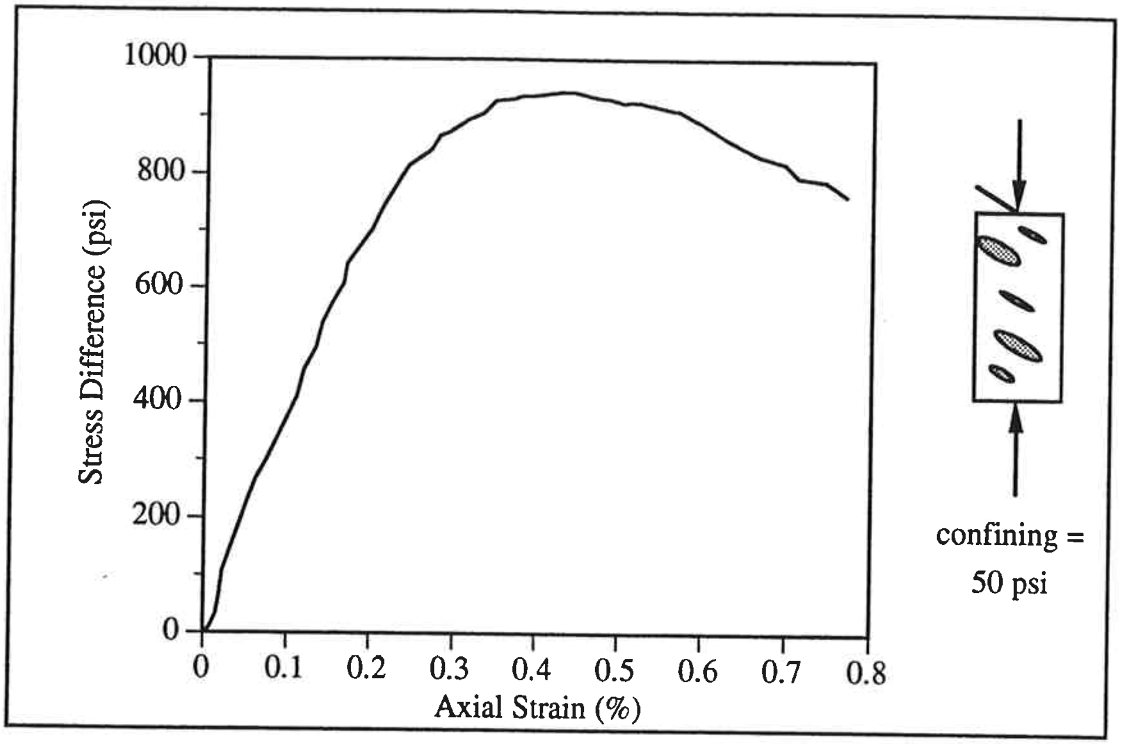

Figure B.48 Stress-Strain Curve for m-60-50

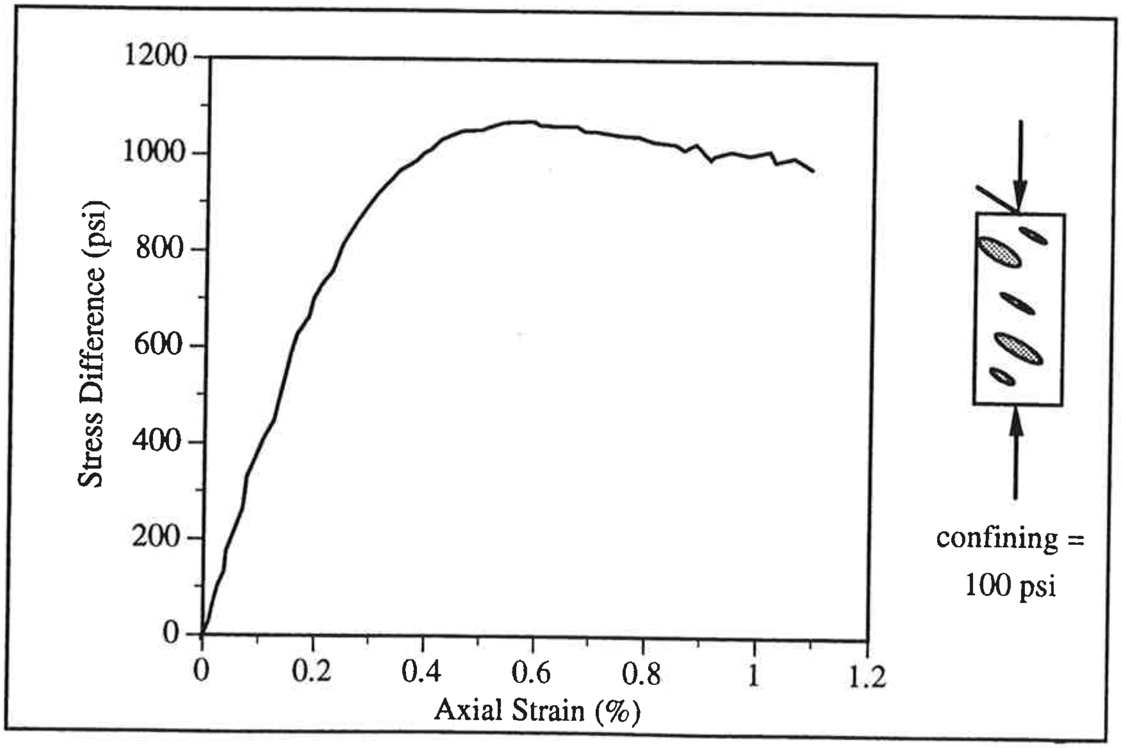

Figure B.49 Stress-Strain Curve for m-60-100

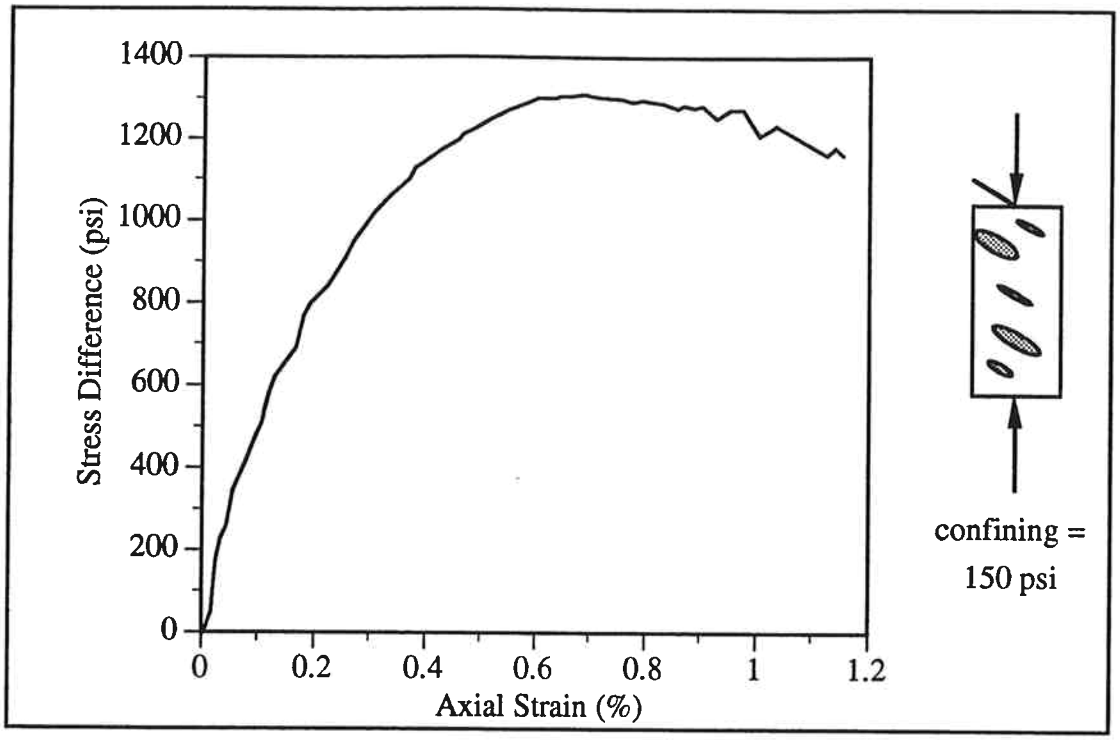

Figure B.50 Stress-Strain Curve for m-60-150

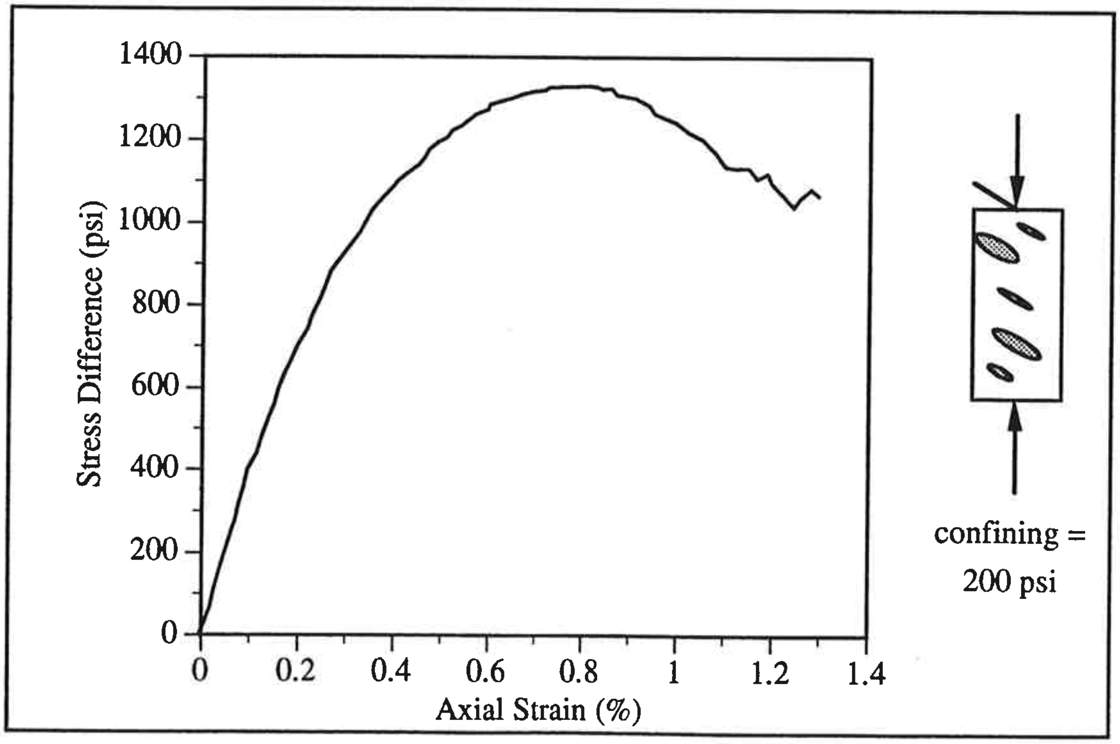

Figure B.51 Stress-Strain Curve for m-60-200

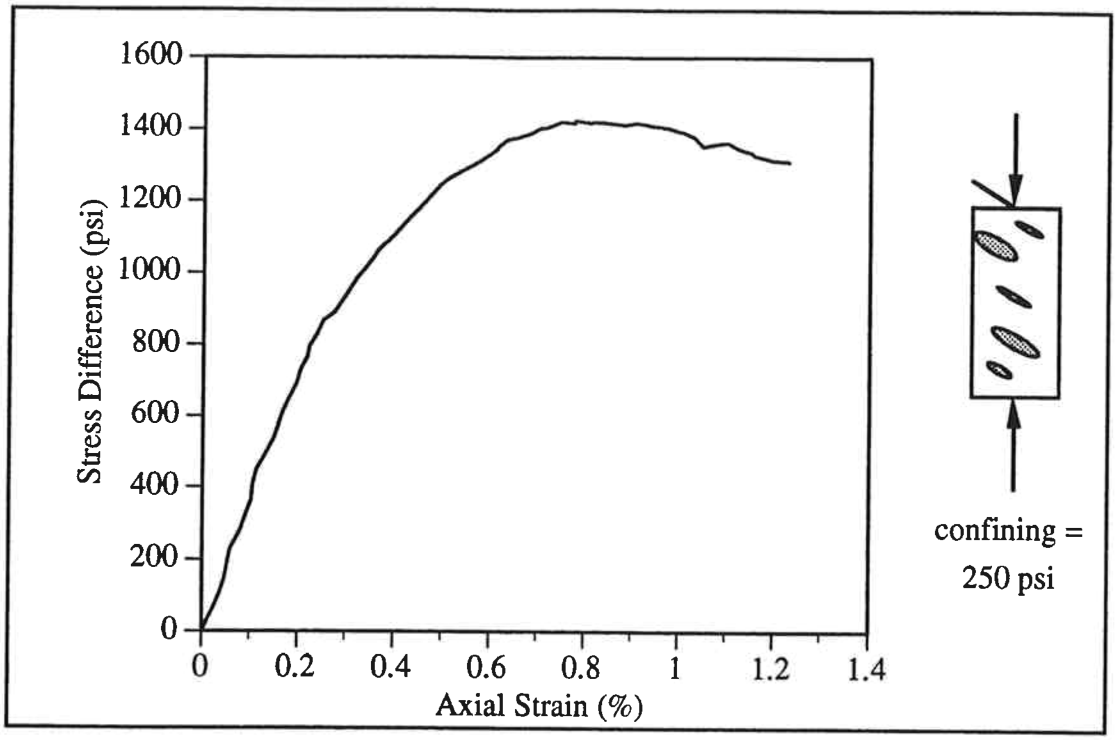

Figure B.52 Stress-Strain Curve for m-60-250

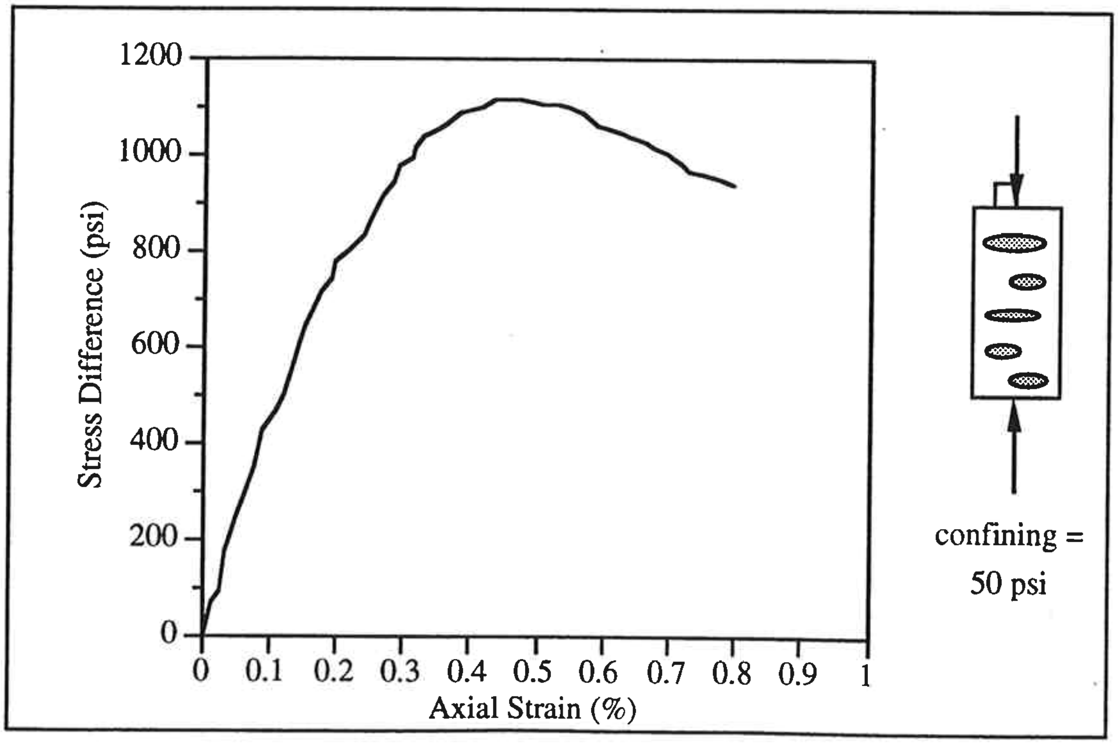

Figure B.53 Stress-Strain Curve for m-90-50

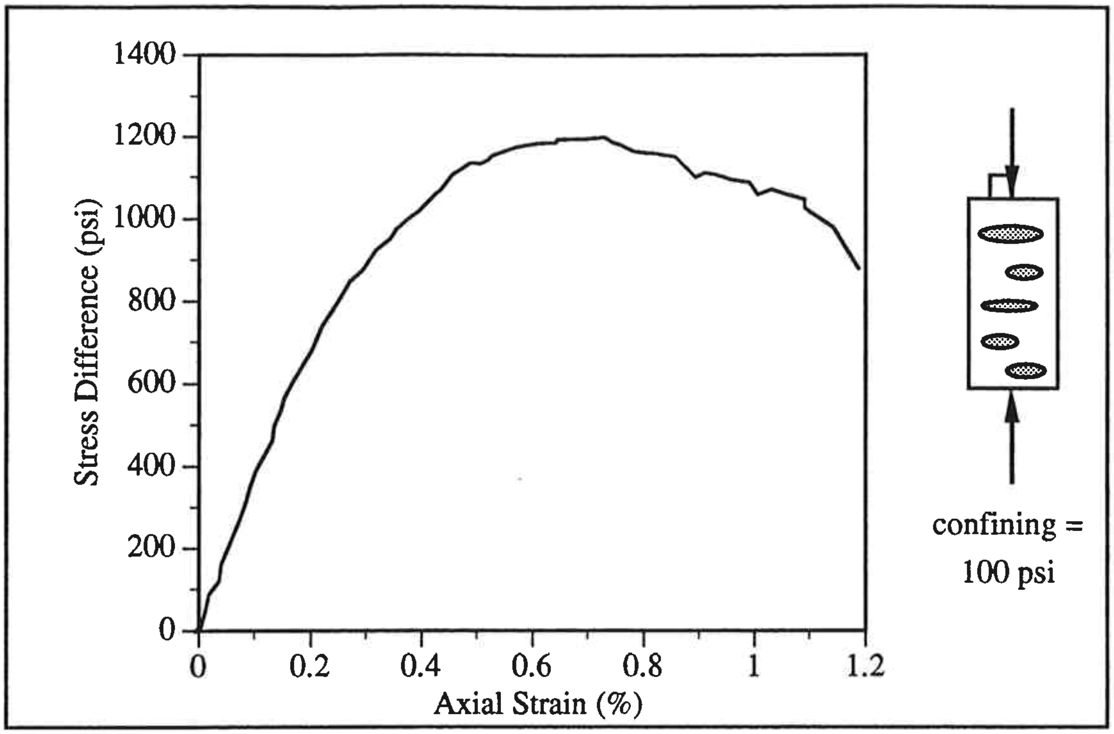

Figure B.54 Stress-Strain Curve for m-90-100

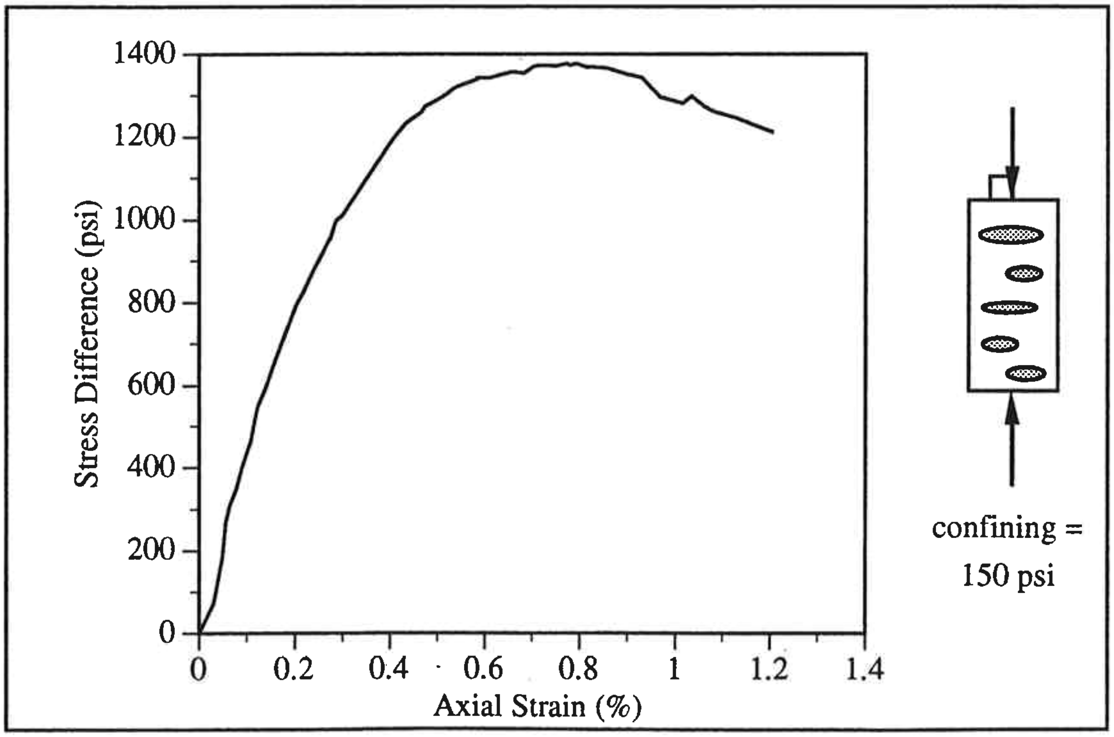

Figure B.55 Stress-Strain Curve for m-90-150

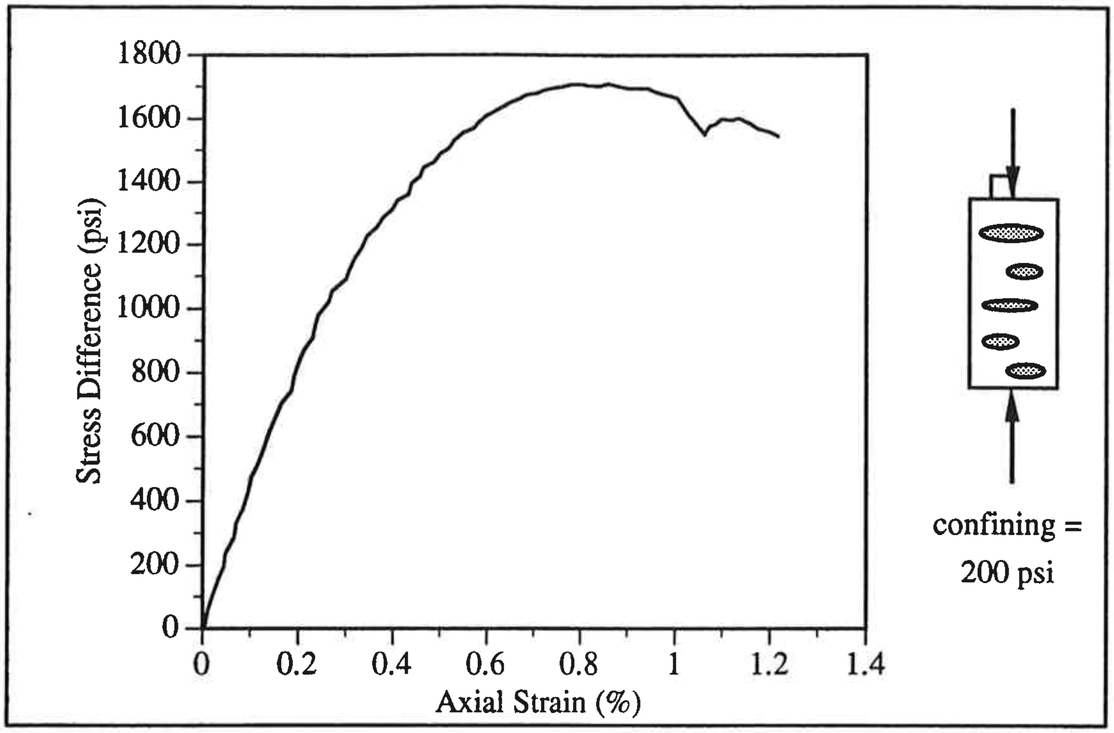

Figure B.56 Stress-Strain Curve for m-90-200

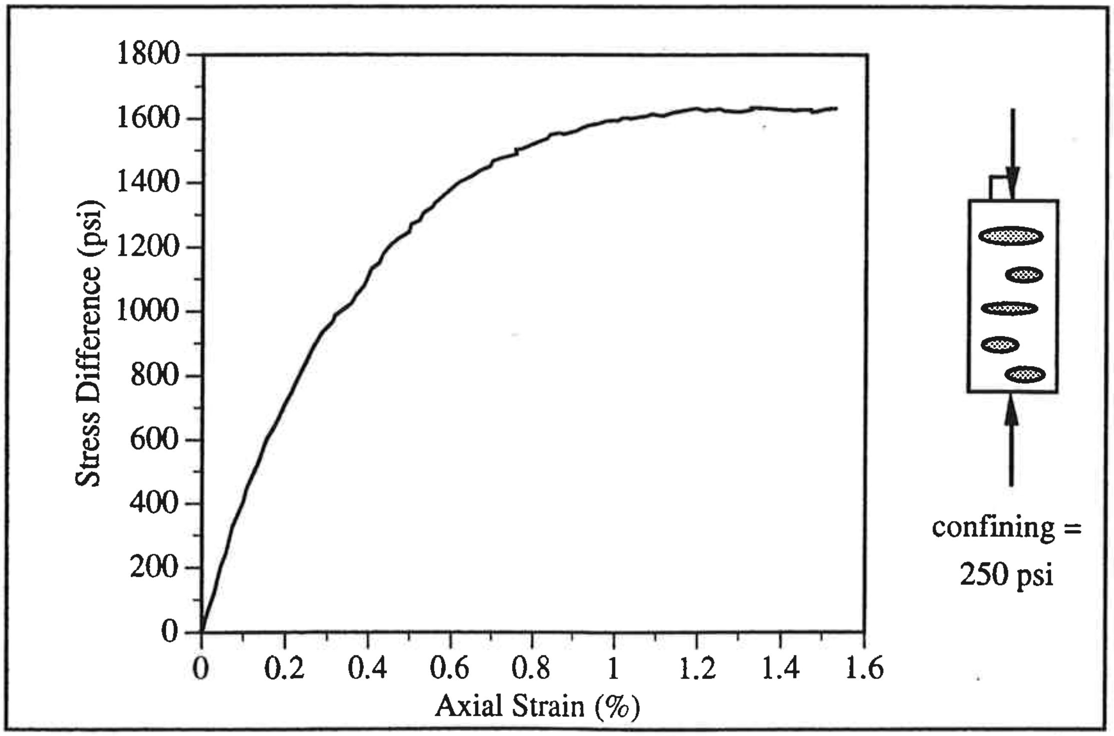

Figure B.57 Stress-Strain Curve for m-90-250

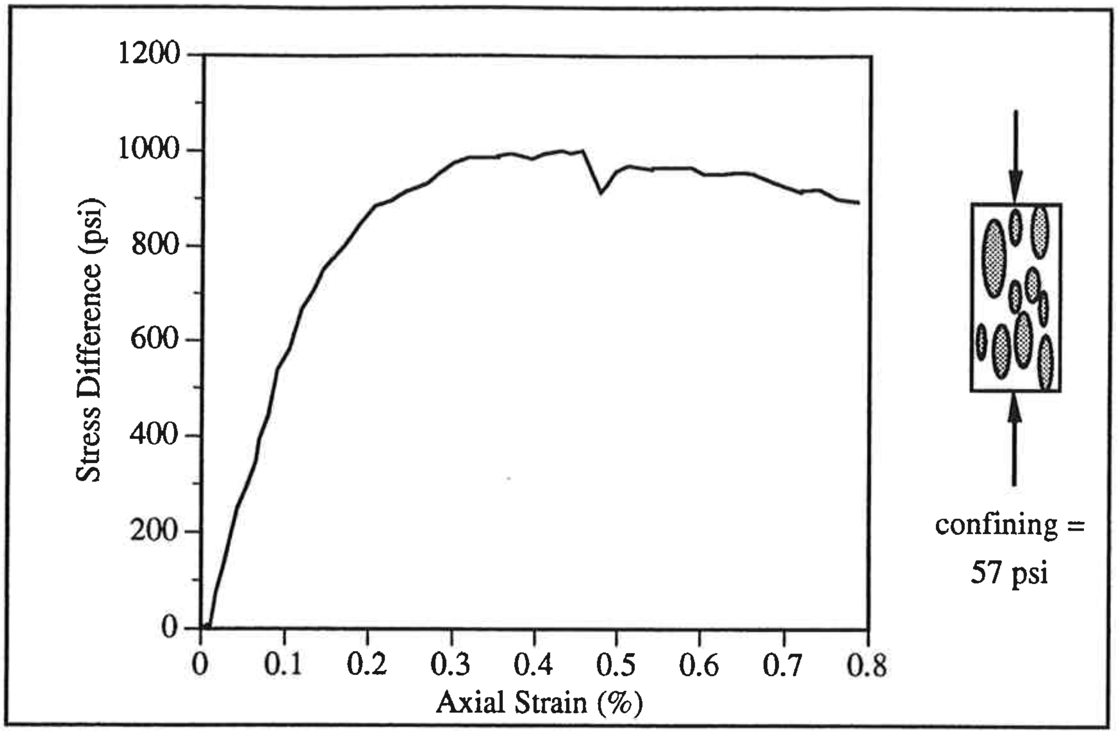

Figure B.58 Stress-Strain Curve for h-0-57

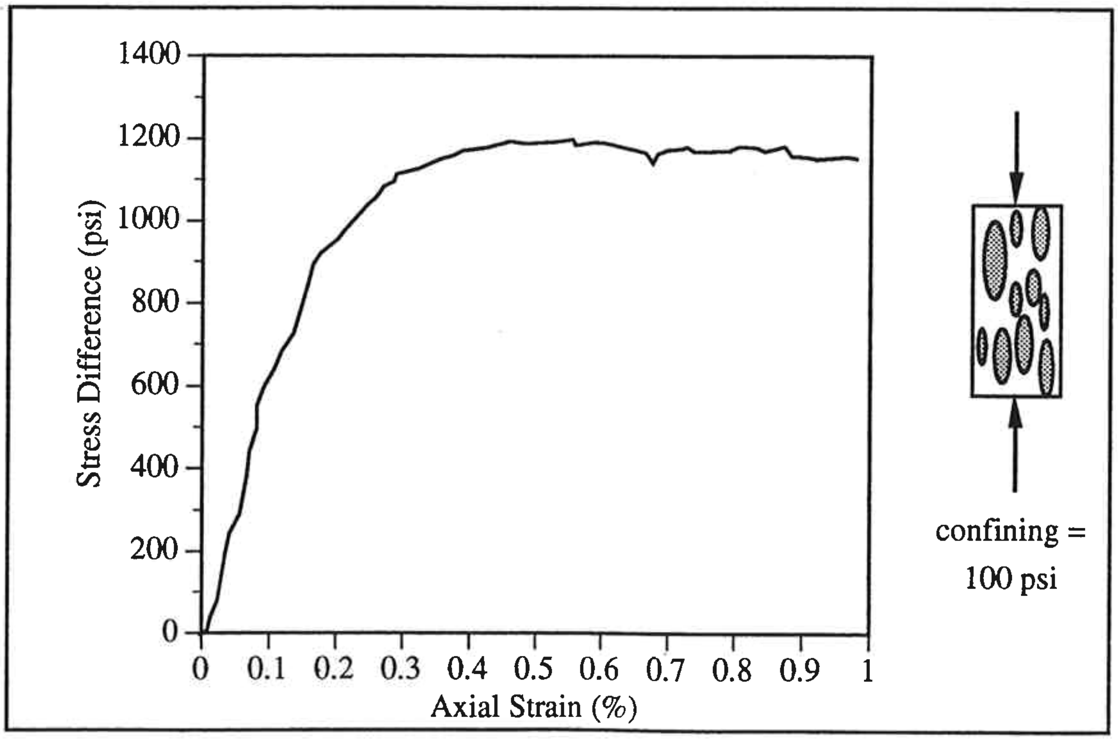

Figure B.59 Stress-Strain Curve for h-0-100

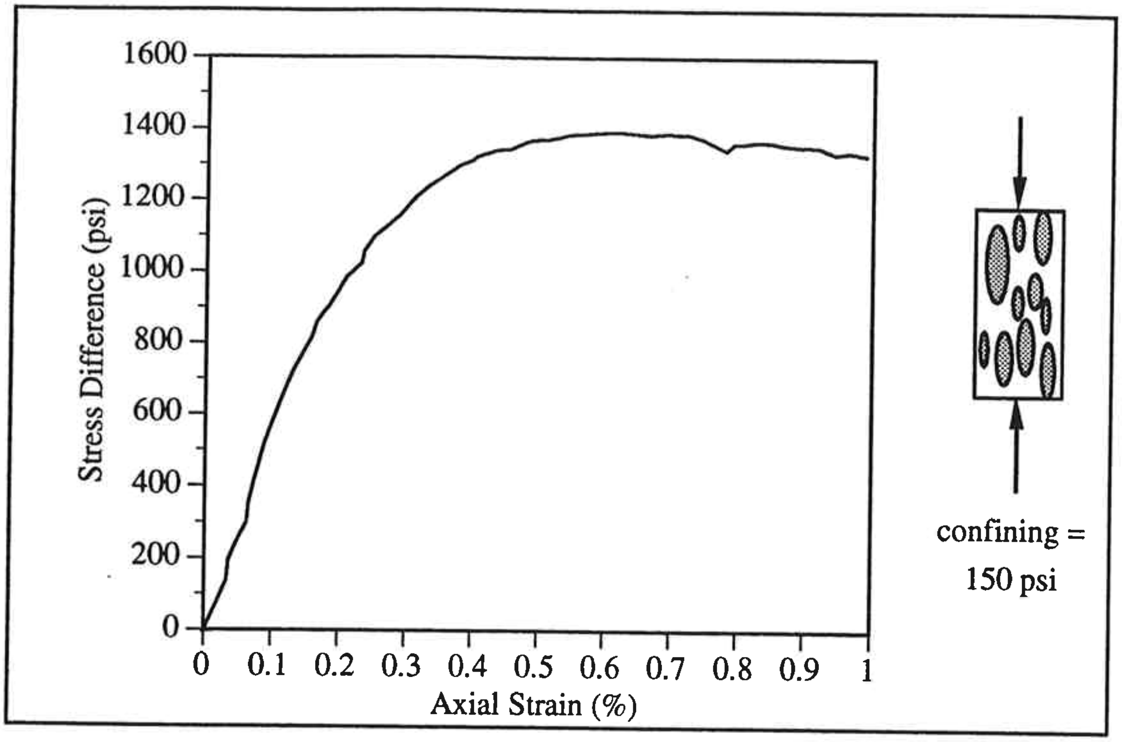

Figure B.60 Stress-Strain Curve for h-0-150

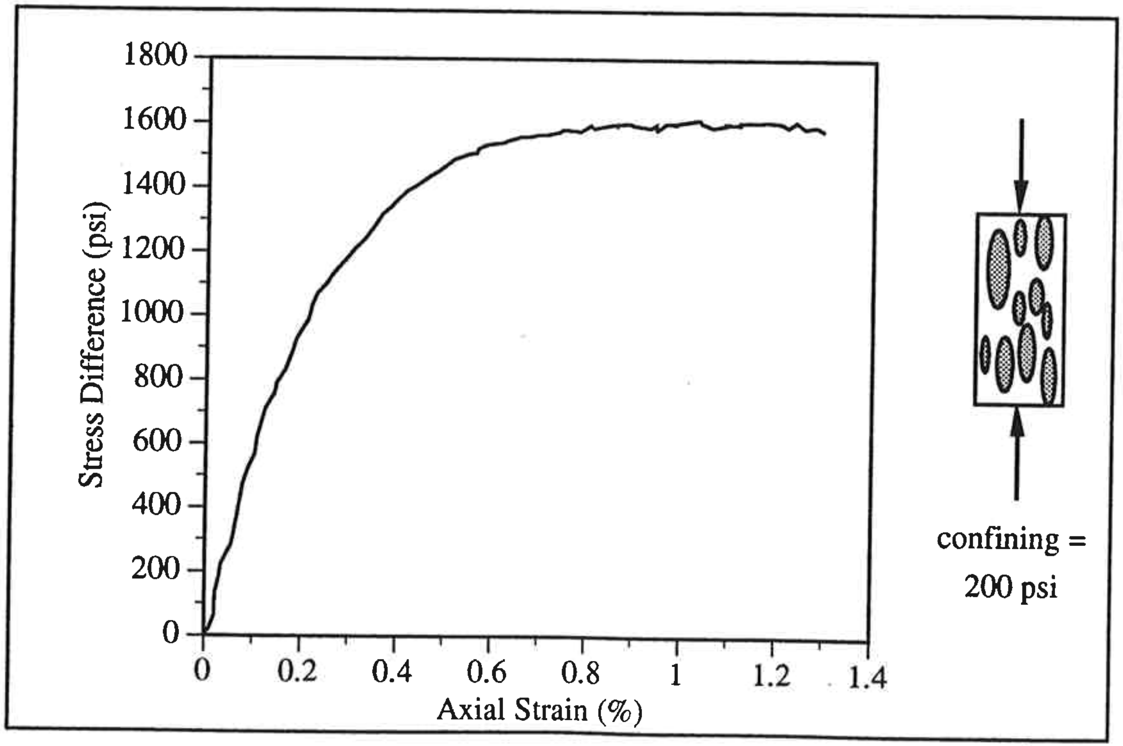

Figure B.61 Stress-Strain Curve for h-0-200

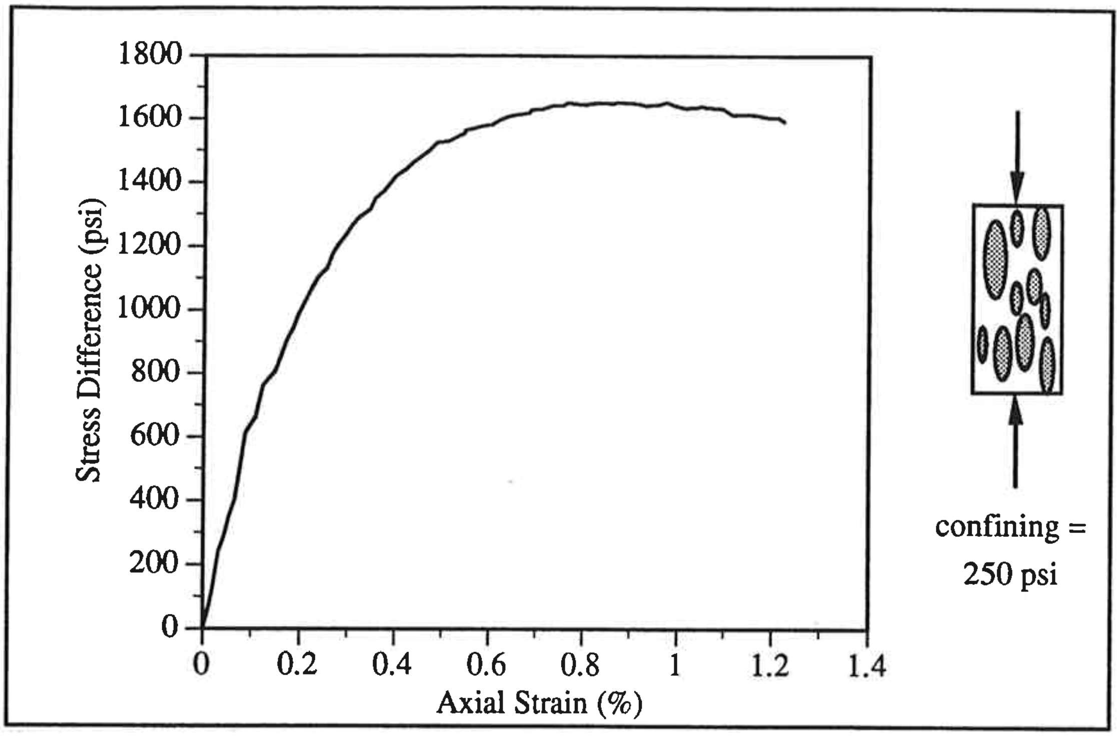

Figure B.62 Stress-Strain Curve for h-0-250

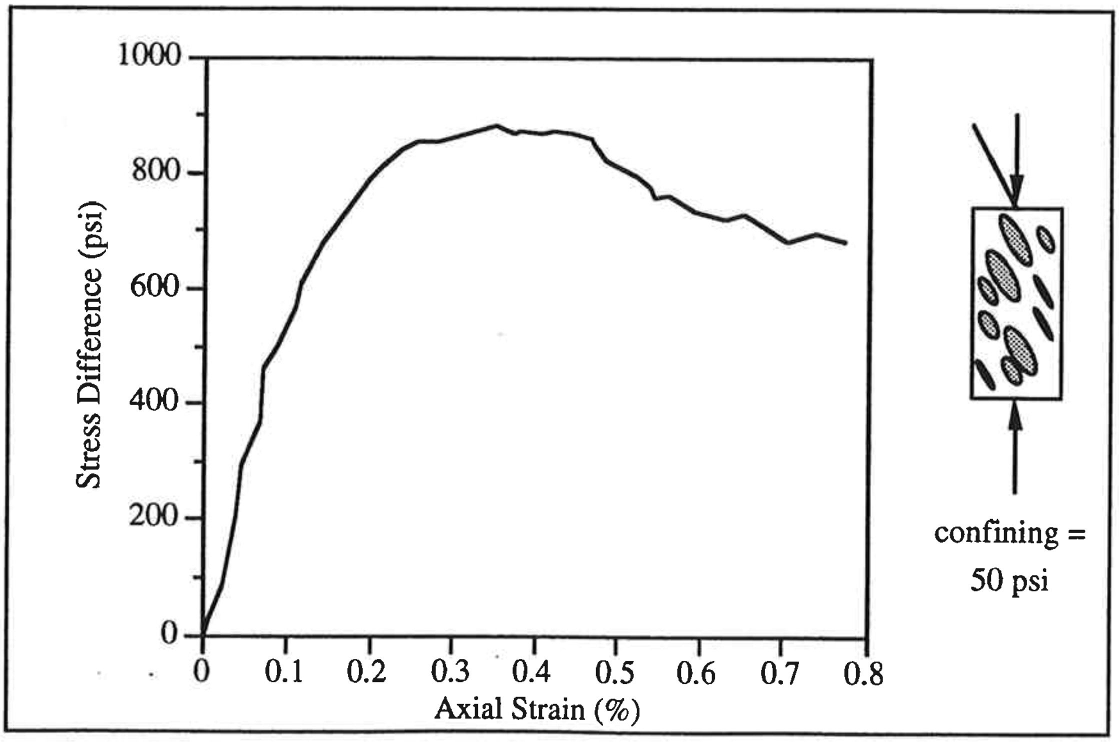

Figure B.63 Stress-Strain Curve for h-30-50

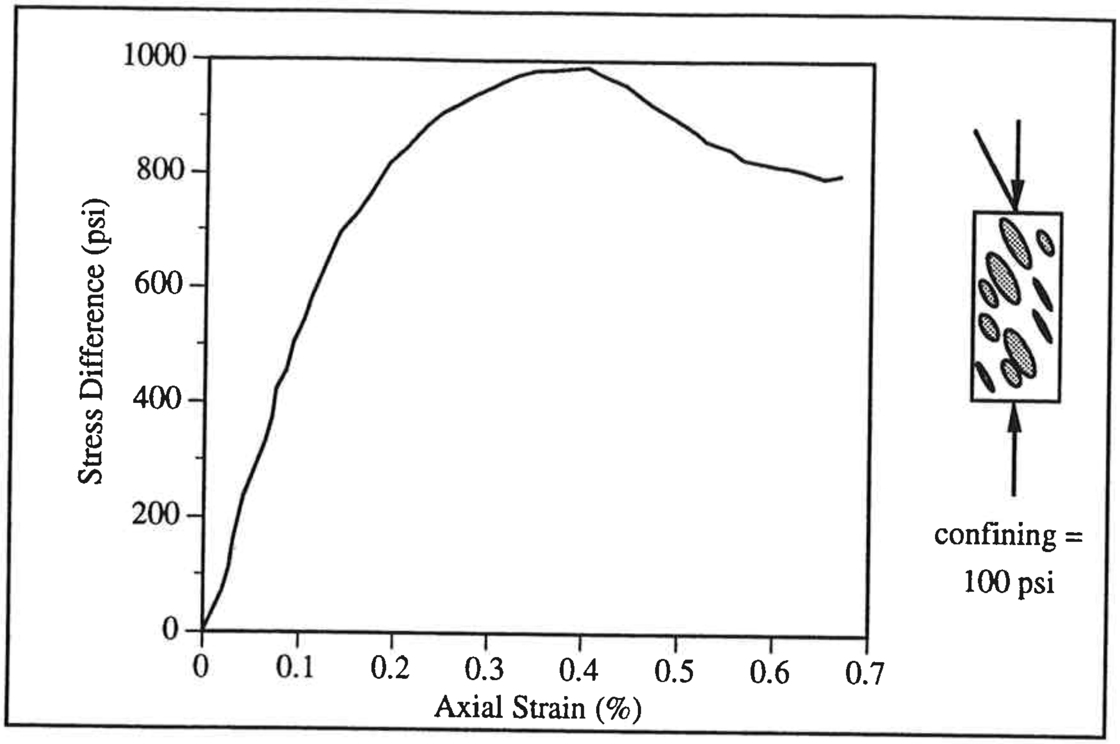

Figure B.64 Stress-Strain Curve for h-30-100

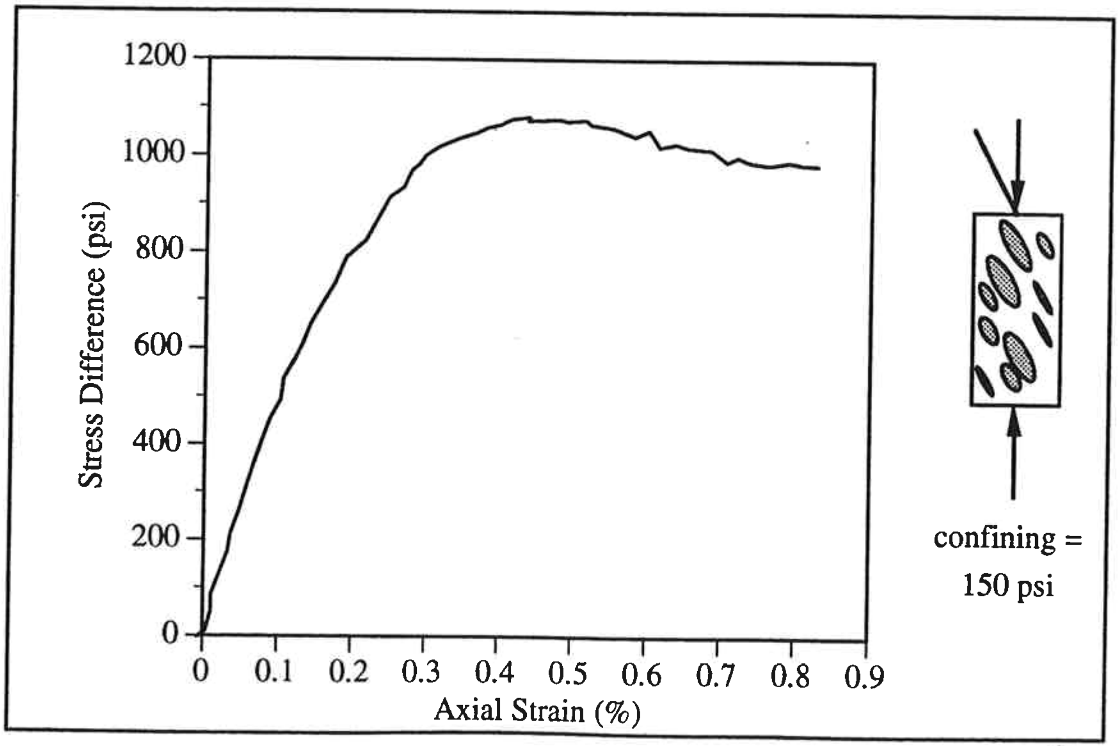

Figure B.65 Stress-Strain Curve for h-30-150

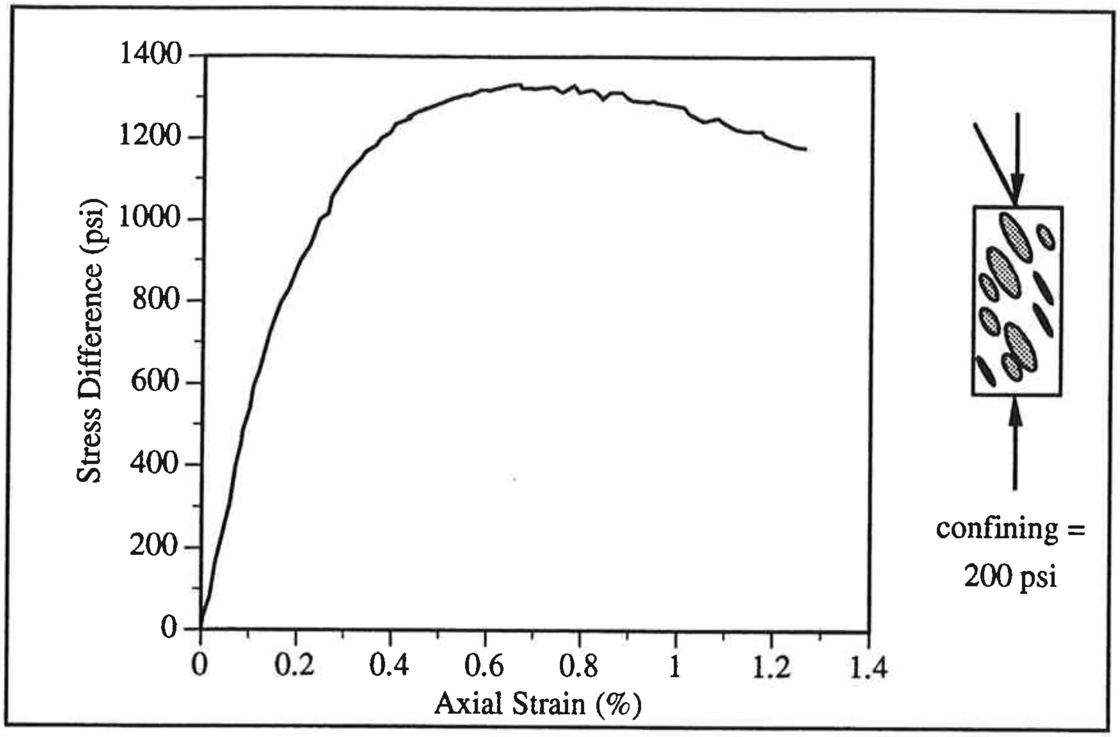

Figure B.66 Stress-Strain Curve for h-0-200

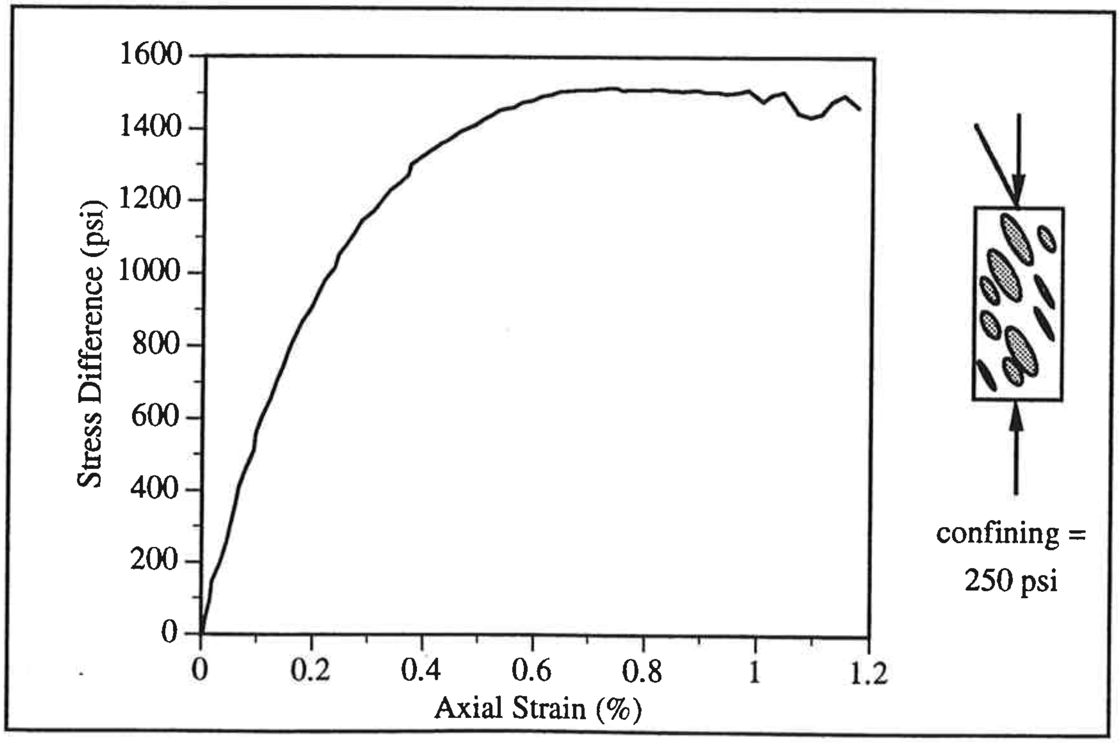

Figure B.67 Stress-Strain Curve for h-30-250

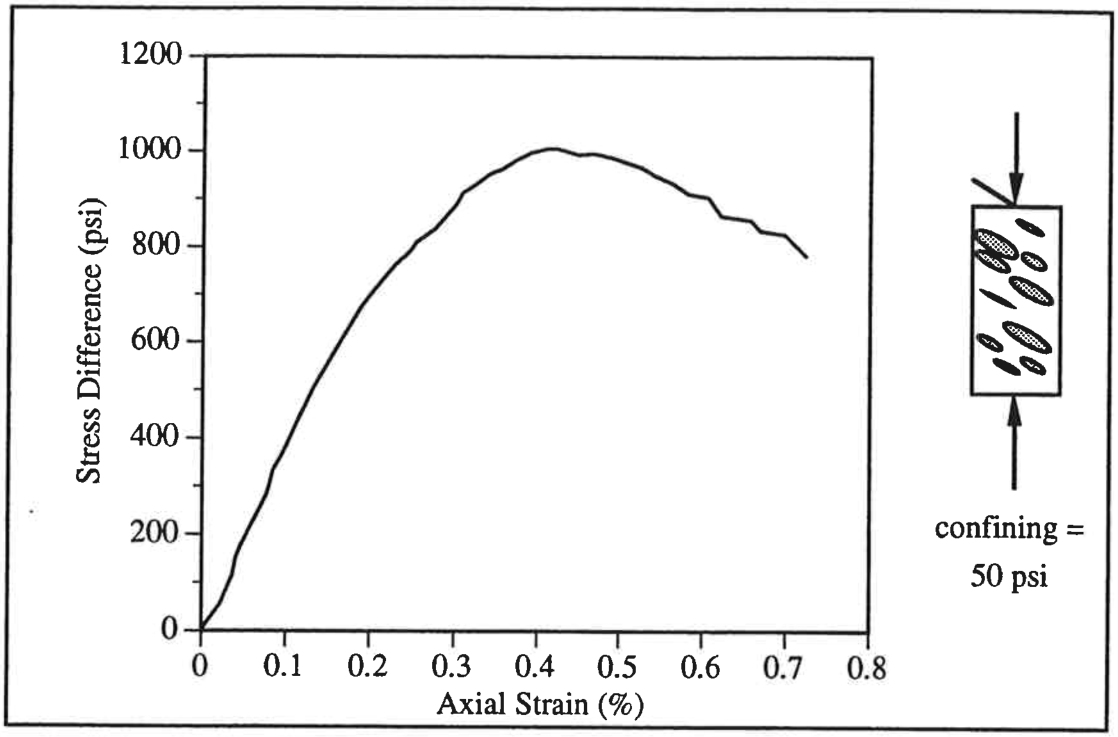

Figure B.68 Stress-Strain Curve for h-60-50

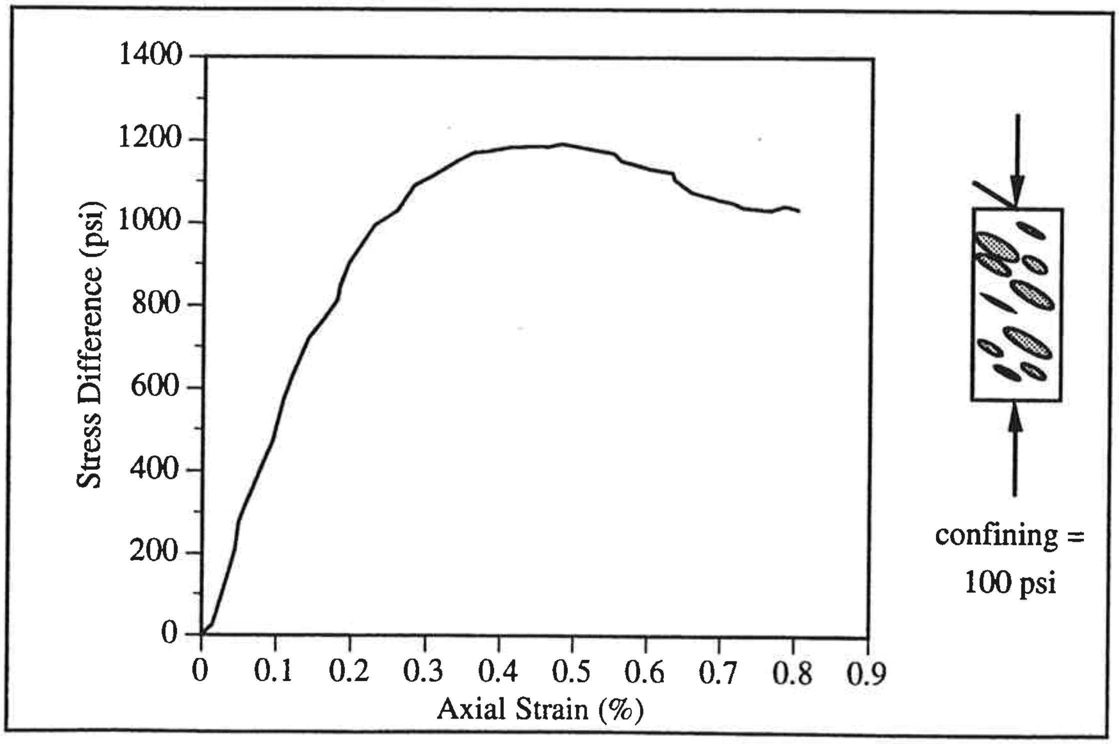

Figure B.69 Stress-Strain Curve for h-60-100

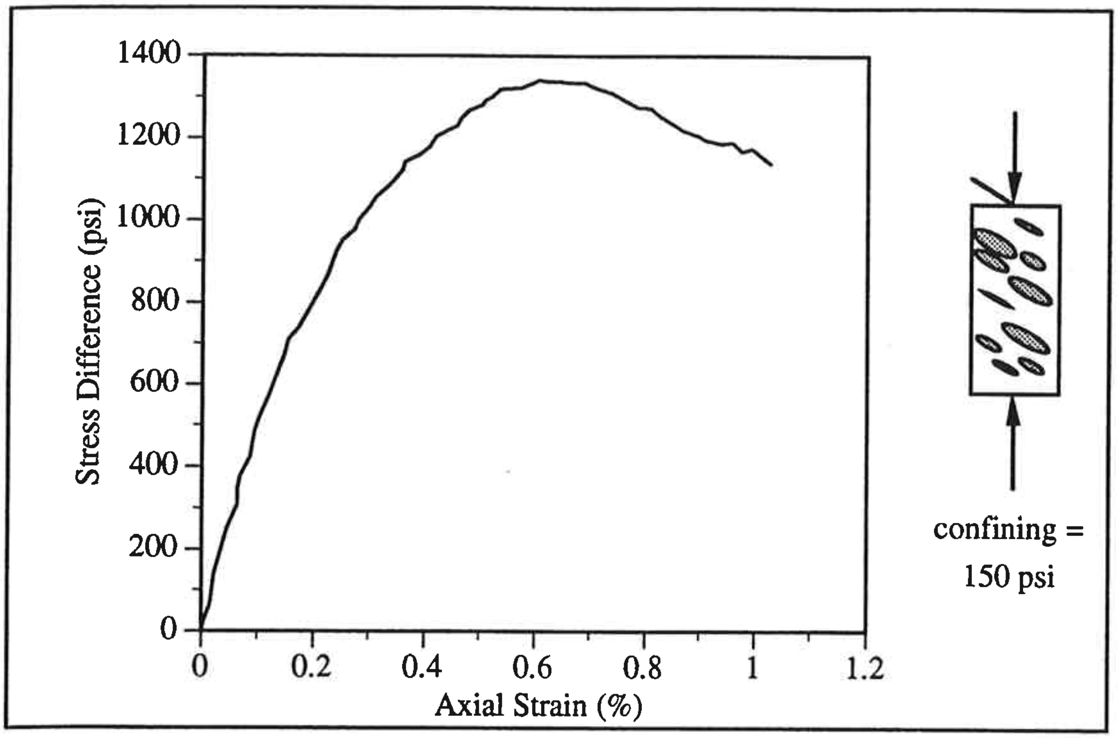

Figure B.70 Stress-Strain Curve for h-60-150

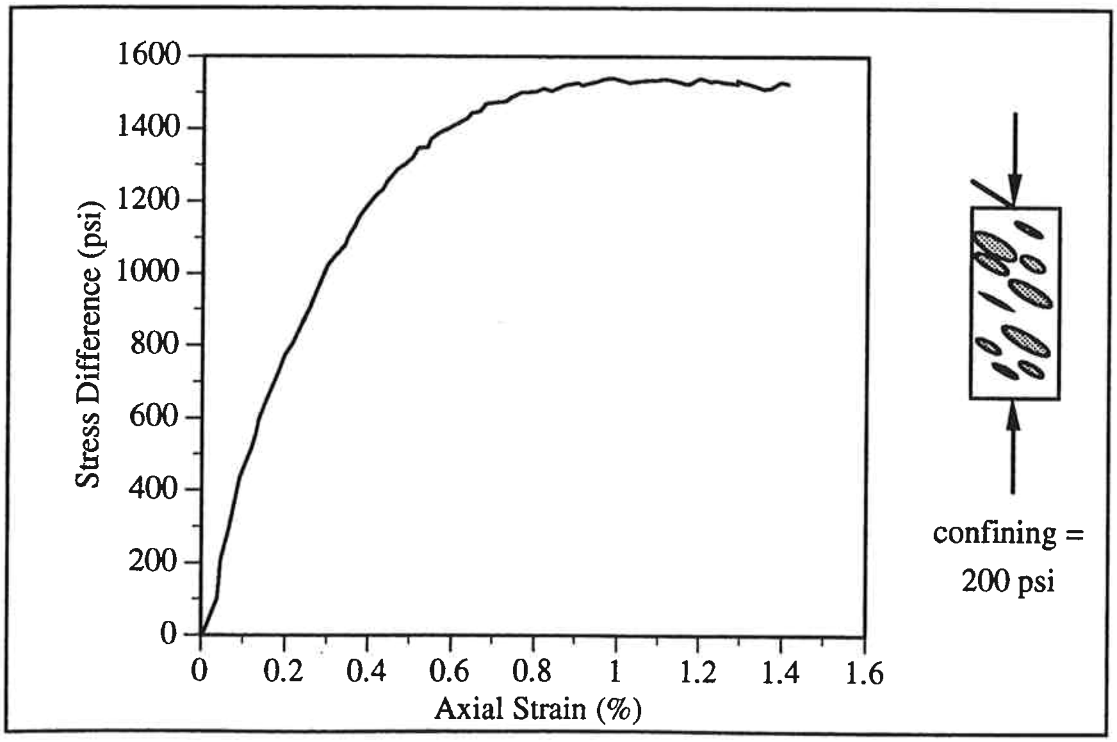

Figure B.71 Stress-Strain Curve for h-60-200

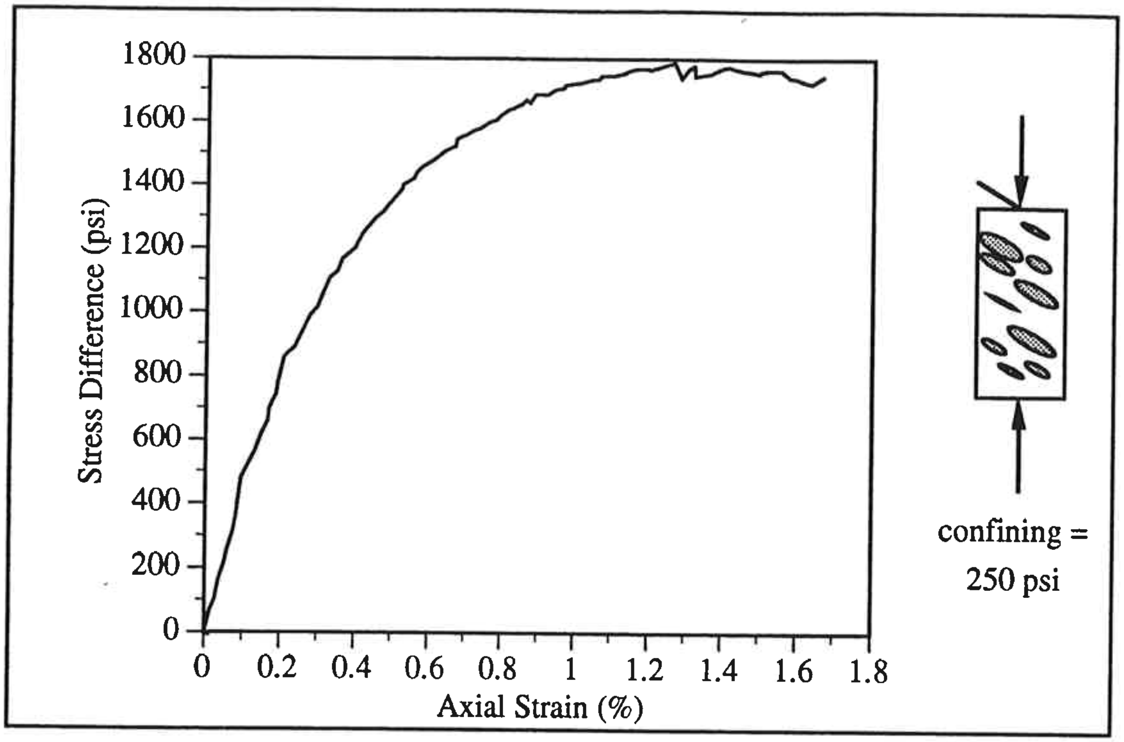

Figure B.72 Stress-Strain Curve for h-60-250

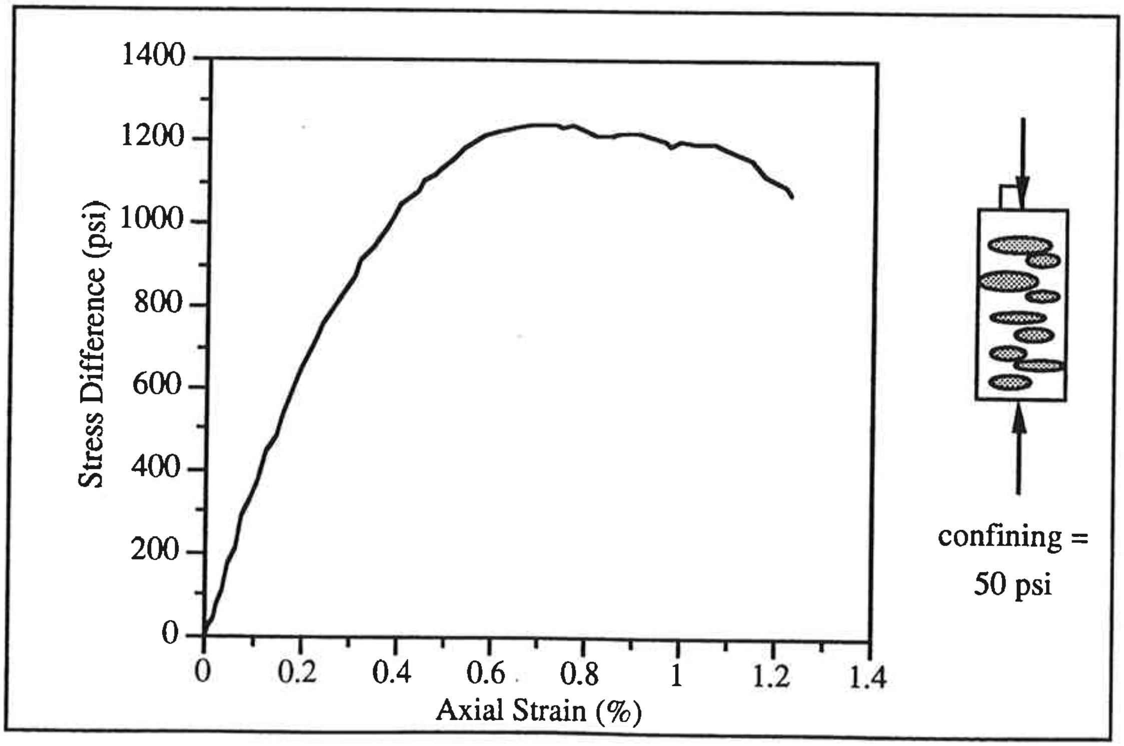

Figure B.73 Stress-Strain Curve for h-90-50

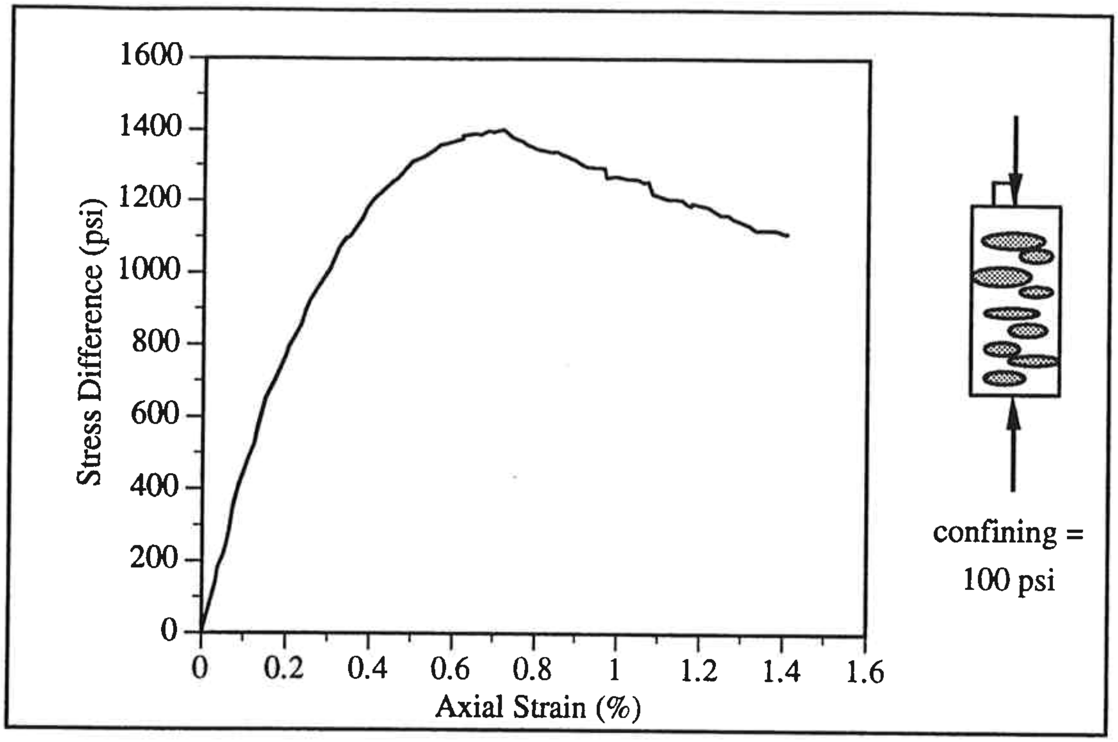

Figure B.74 Stress-Strain Curve for h-90-100

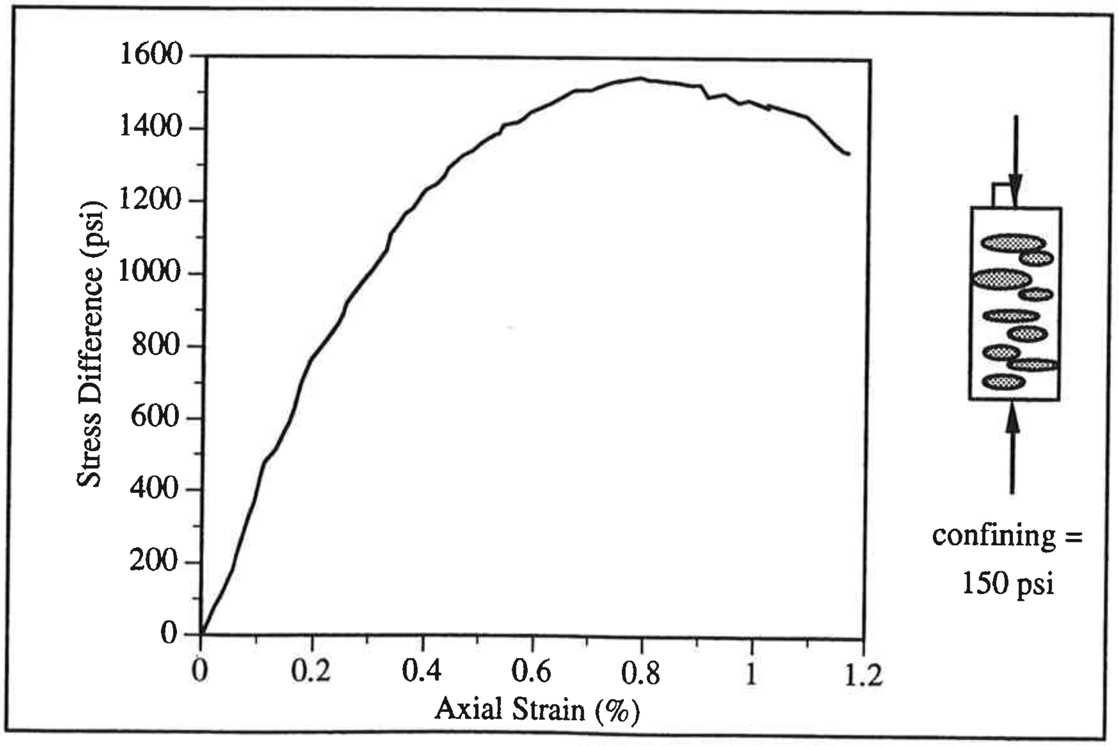

Figure B.75 Stress-Strain Curve for h-90-150

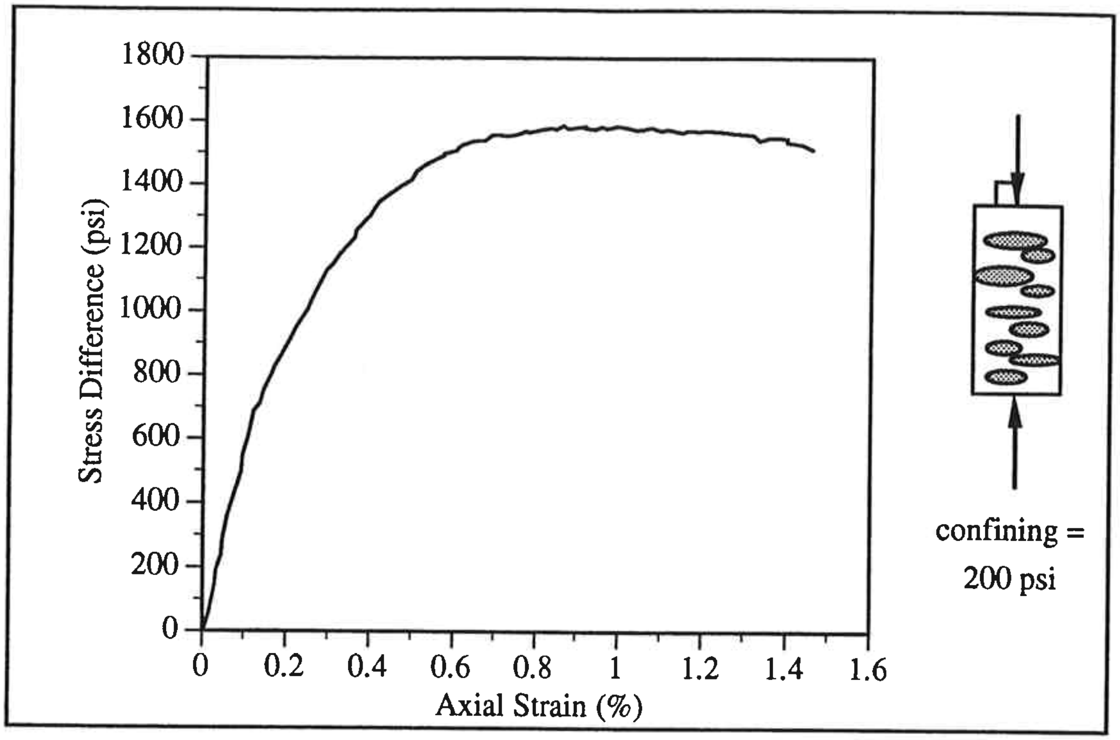

Figure B.76 Stress-Strain Curve for h-90-200

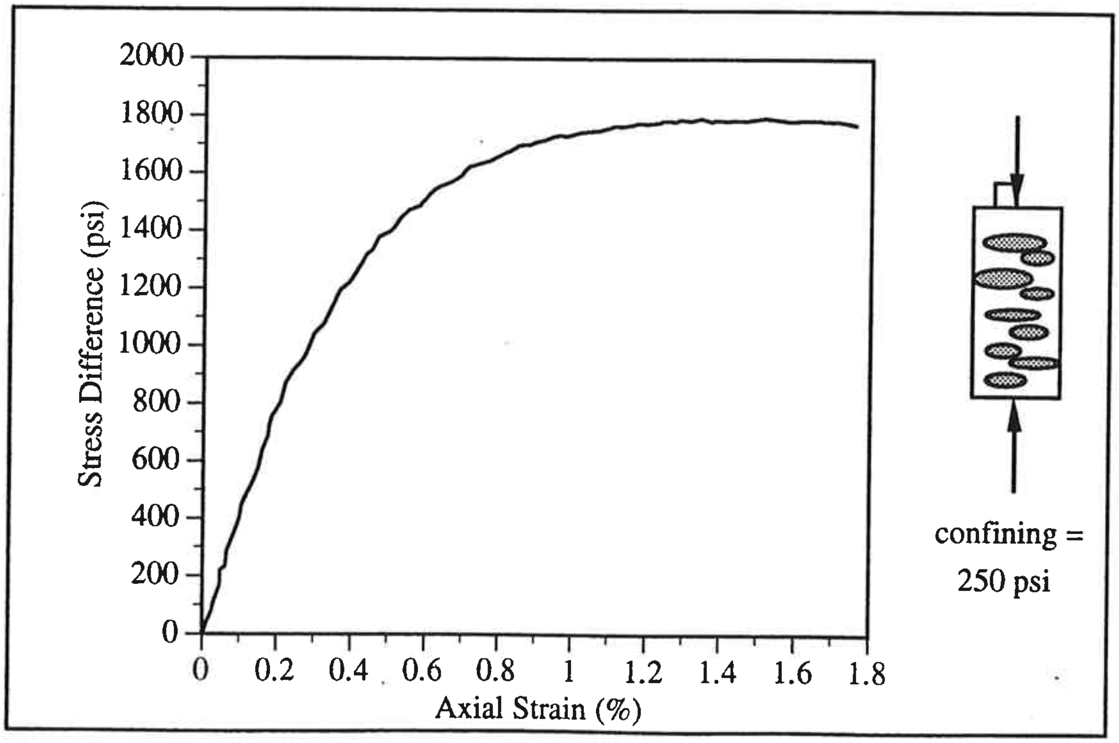

Figure B.77 Stress-Strain Curve for h-90-250

APPENDIX C

Strength Data - Compressive Strength versus Confining Stress and Mohr Circle Plots for the Physical Models

The strength results for all the tested physical model specimens are presented in this appendix. The results are presented in tabular form, as plots of compressive strength versus confining stress and as Mohr Circles. Table C.1 presents the values of compressive strength (i.e. σ_1 at failure) for the matrix specimens, and the block specimen compressive strengths are given in Table C.2. The compressive strength of each block-in-matrix specimen is presented in Table C.3.

Figures C.1 through C.14 are plots of compressive strength versus confining stress (i.e. σ_1 versus σ_3 at failure). Each plot represents one specimen type, i.e. each plot shows specimens with approximately the same block proportion and orientation. A schematic specimen sketch accompanies each plot to ease identification. Vogler and Kovari (1981) suggest that these plots be used to calculate the angle of internal friction (ϕ) and cohesion (c) for each specimen type. This is accomplished by determining the slope (m) and intercept (b) of the least squares linear regression line for each data set and then using the following formulas:

$$\phi = \arcsin\left(\frac{m-1}{m+1}\right) \tag{C.1}$$

$$c = b\left(\frac{1-\sin\phi}{2\cos\phi}\right). \tag{C.2}$$

These values are shown on each plot along with the correlation coefficient (R). The correlation coefficient is a measure of how well the data fit the least-squares line. A coefficient of exactly one indicates perfect fit, and as the fit becomes less ideal the correlation coefficient decreases. The correlation coefficients for these plots are all reasonably close to one indicating good data fit.

The strength results are summarized in Table C.4.

An additional presentation of the data is made in Figures C.15 through C.28. Mohr circles and a failure envelope for each specimen type are plotted in these figures.

Appendix C Strength Data - Compressive Strength versus Confining Stress and Mohr Circle Plots for the Physical Models

Table C.1

Compressive Strengths of Matrix Specimens

Specimen	Compressive Strength (psi)
matrix-50	1106
matrix-100	1364
matrix-125	1309
matrix-150	1360
matrix-200	1499
matrix-225	1642
matrix-250	1591

Table C.2

Compressive Strengths of Block Specimens

Specimen	Compressive Strength (psi)
block-0	1866
block-50	2142
block-75	2141
block-100	2225
block-125	2142
block-150	2520
block-175	2633
block-200	2752
block-225	2775
block-250	2919

Appendix C Strength Data - Compressive Strength versus Confining Stress and Mohr Circle Plots for the Physical Models

Table C.3 Compressive Strengths of Block-in-Matrix Specimens

Specimen	Compressive Strength (psi)
l-0-50	1261
l-0-100	1374
l-0-150	1471
l-0-200	1579
l-0-250	1804
l-30-50	1069
l-30-100	1345
l-30-150	1332
l-30-200	1574
l-30-250	1798
l-60-50	1206
l-60-100	1411
l-60-150	1597
l-60-200	1548
l-60-250	1717
l-90-50	1234
l-90-100	1356
l-90-150	1336
l-90-200	1811
l-90-250	1848
m-0-50	970
m-0-100	1300
m-0-150	1418
m-0-200	1517
m-0-250	1726
m-30-50	819
m-30-100	1139
m-30-150	1345
m-30-200	1377
m-30-250	1523
m-60-50	995
m-60-100	1168
m-60-150	1463
m-60-200	1534
m-60-250	1672
m-90-50	1167
m-90-100	1298
m-90-150	1526
m-90-200	1909
m-90-250	1892
h-0-57	1070
h-0-100	1297
h-0-150	1545
h-0-200	1817
h-0-250	1909
h-30-50	930
h-30-100	1086
h-30-150	1227
h-30-200	1530
h-30-250	1768
h-60-50	1053
h-60-100	1290
h-60-150	1495
h-60-200	1748
h-60-250	2040
h-90-50	1297
h-90-100	1507
h-90-150	1699
h-90-200	1770
h-90-250	2050

Appendix C Strength Data - Compressive Strength versus Confining Stress and Mohr Circle Plots for the Physical Models

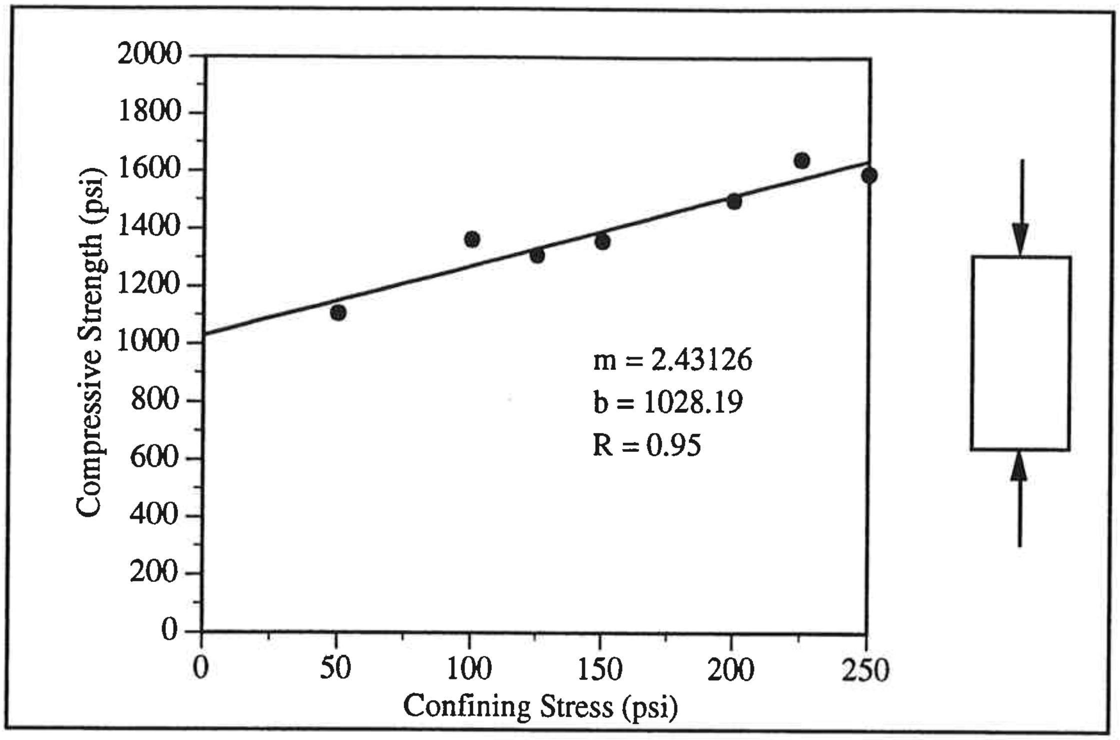

Figure C.1 Compressive Strength versus Confining Stress - Matrix Component

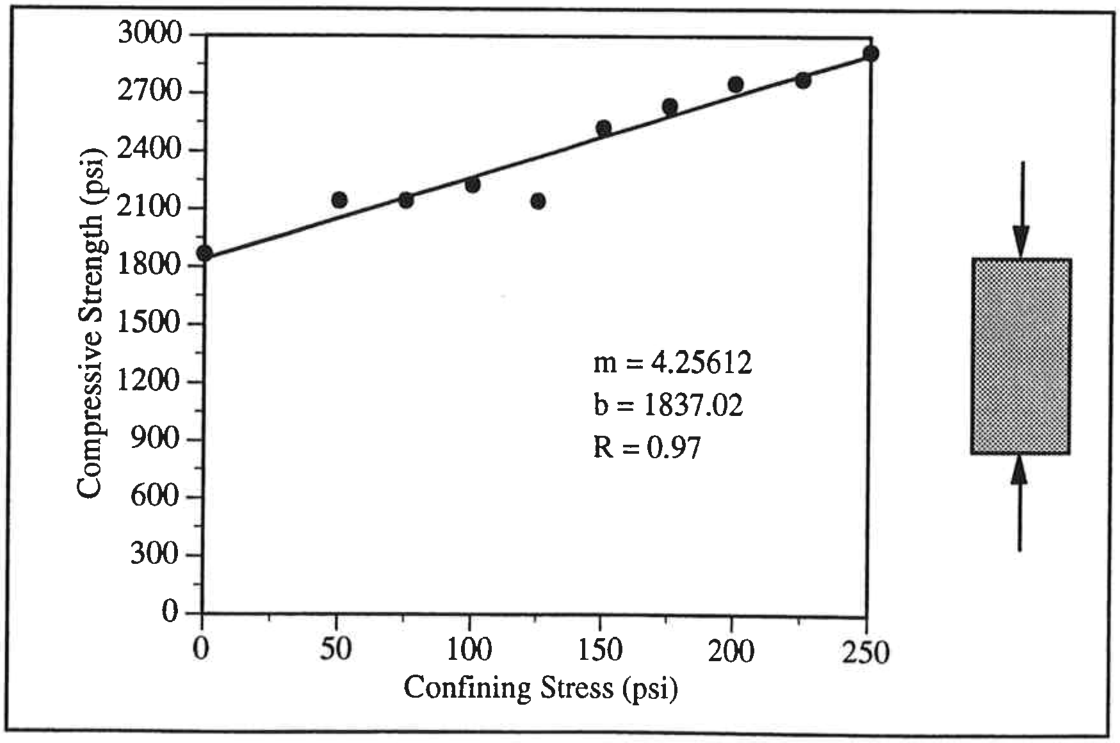

Figure C.2 Compressive Strength versus Confining Stress - Block Component

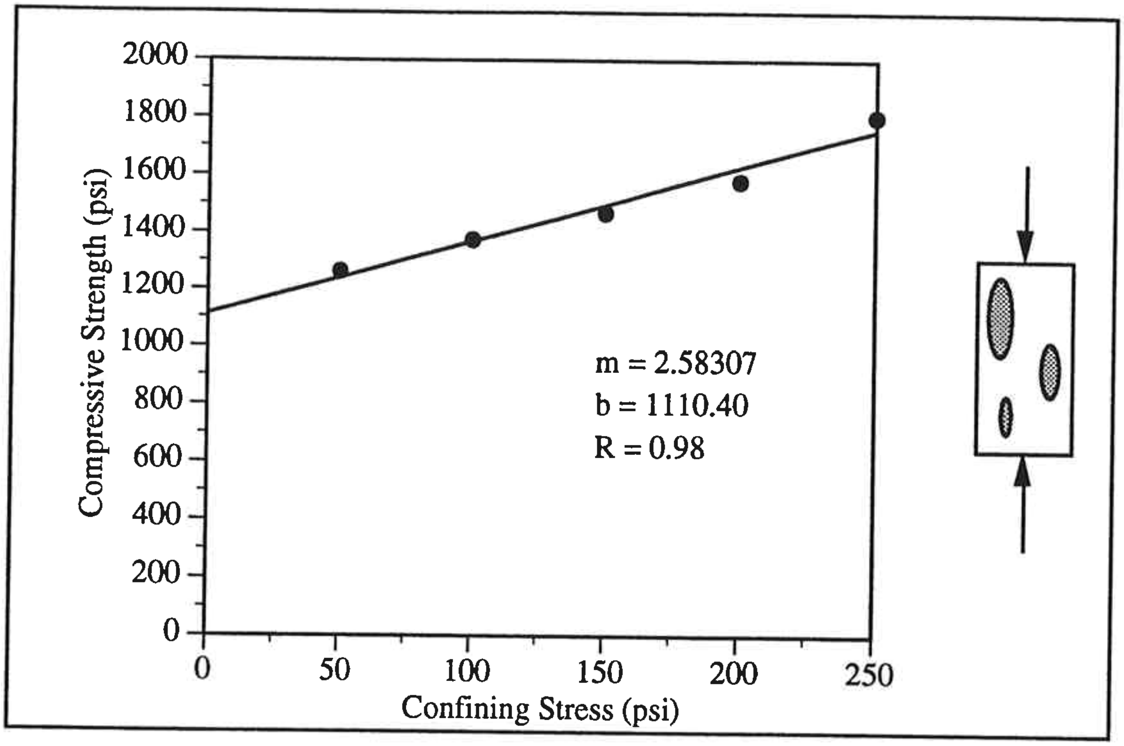

Figure C.3 Compressive Strength versus Confining Stress - 1-0 Specimens

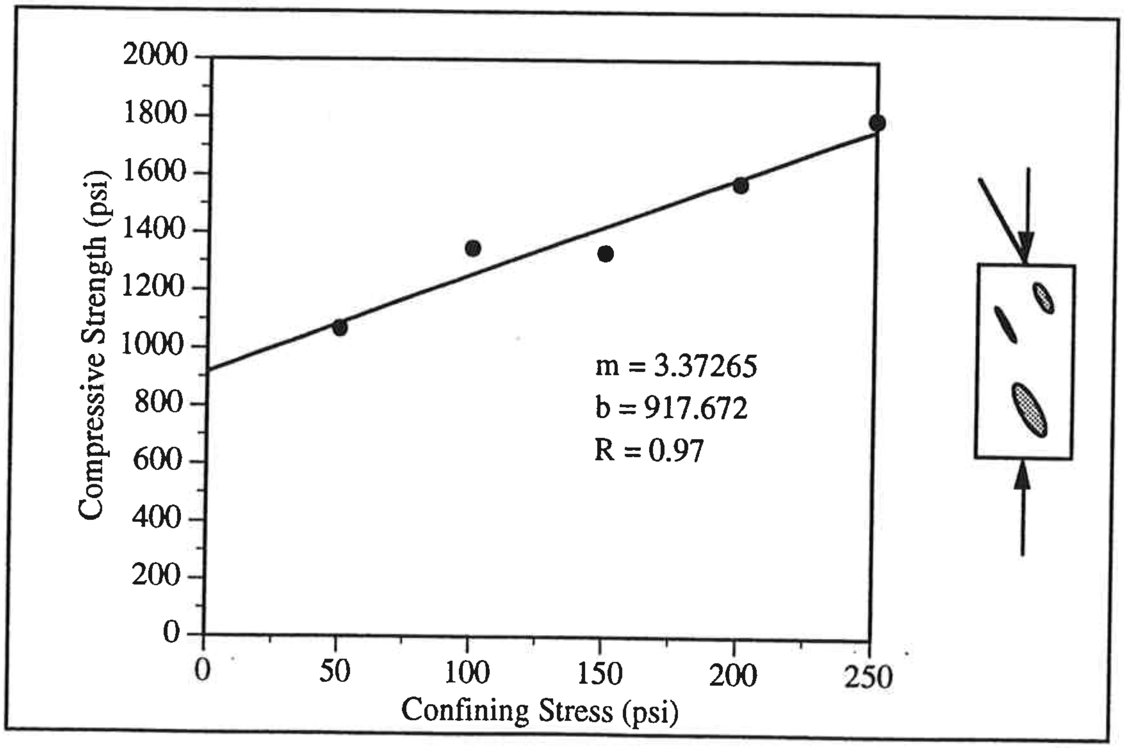

Figure C.4 Compressive Strength versus Confining Stress - 1-30 Specimens

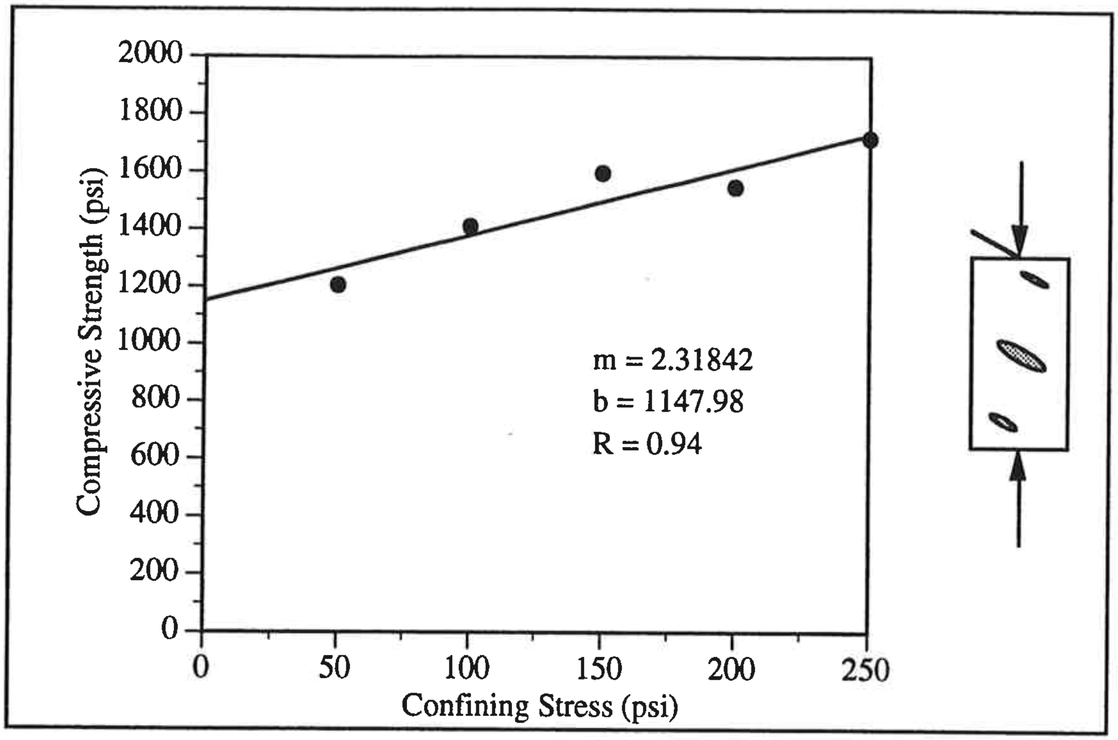

Figure C.5 Compressive Strength versus Confining Stress - 1-60 Specimens

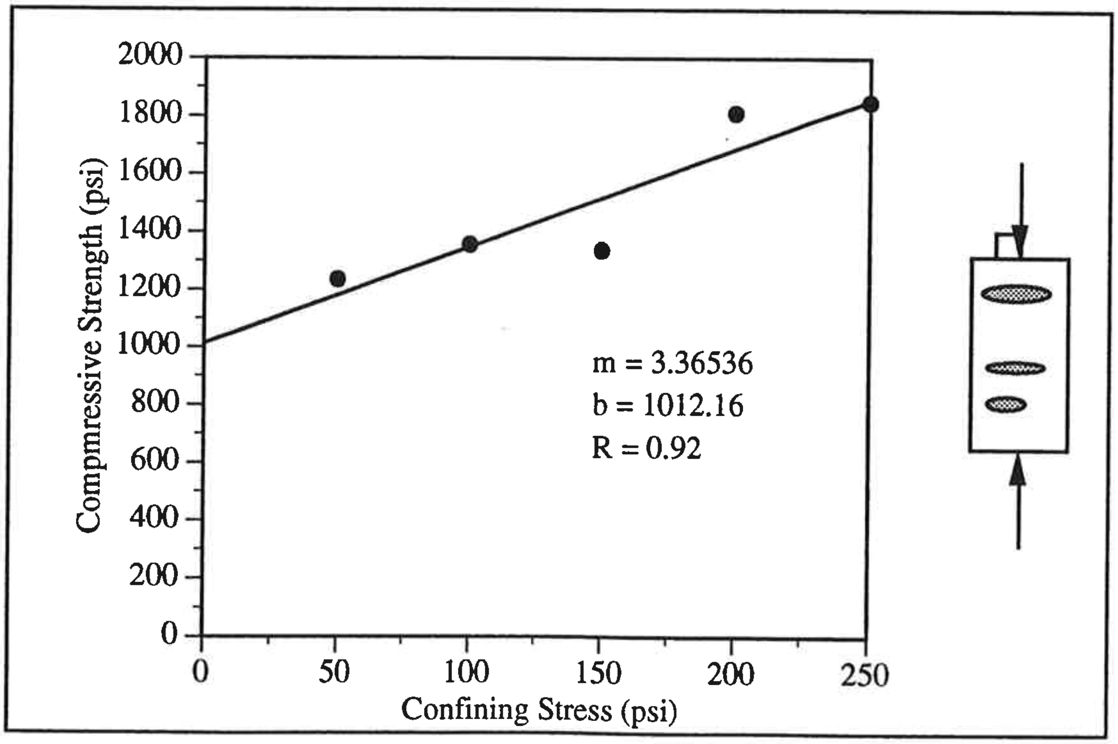

Figure C.6 Compressive Strength versus Confining Stress - 1-90 Specimens

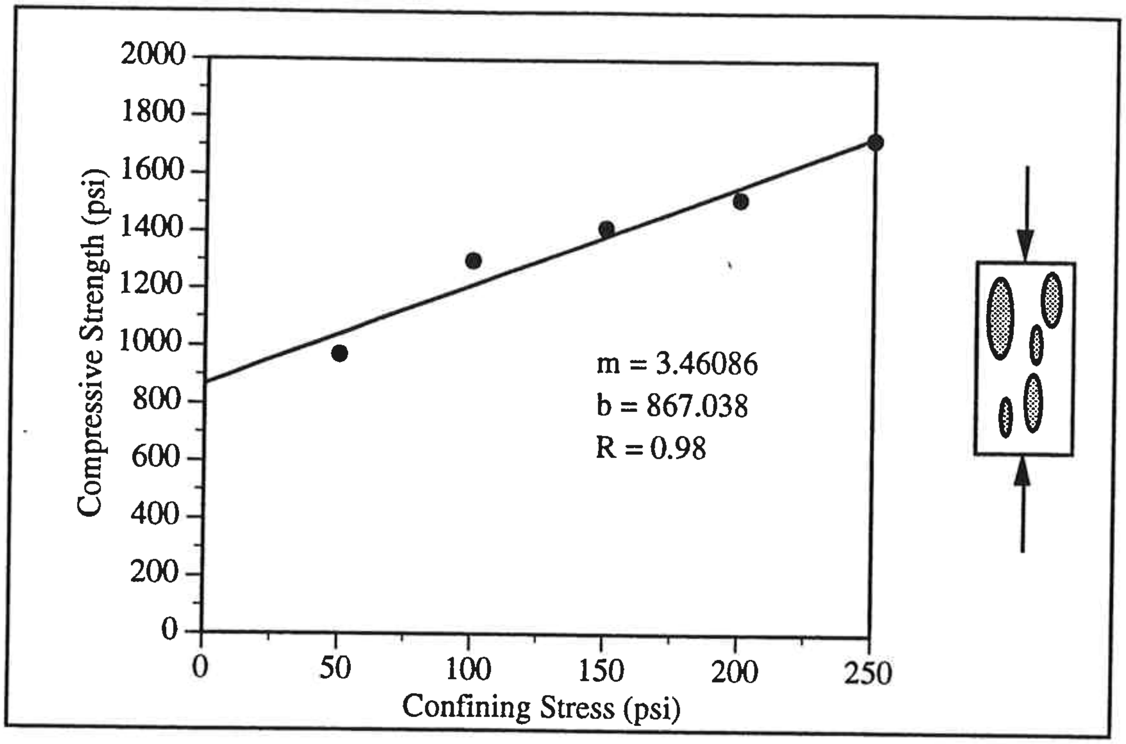

Figure C.7 Compressive Strength versus Confining Stress - m-0 Specimens

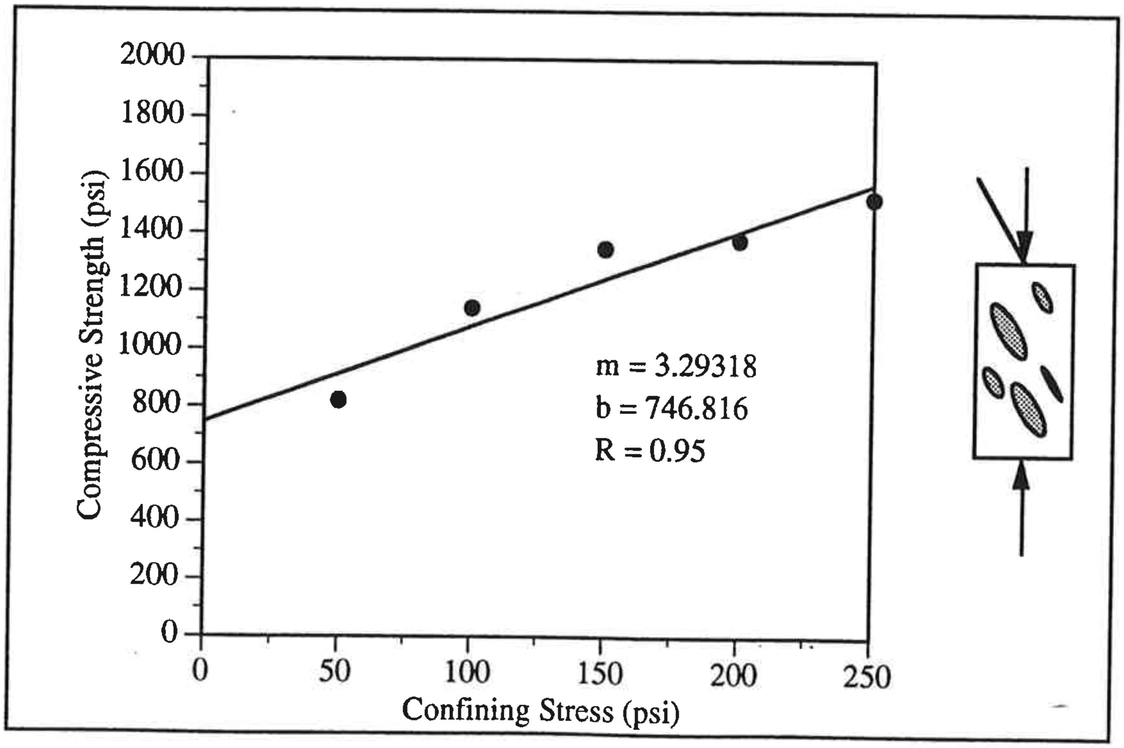

Figure C.8 Compressive Strength versus Confining Stress - m-30 Specimens

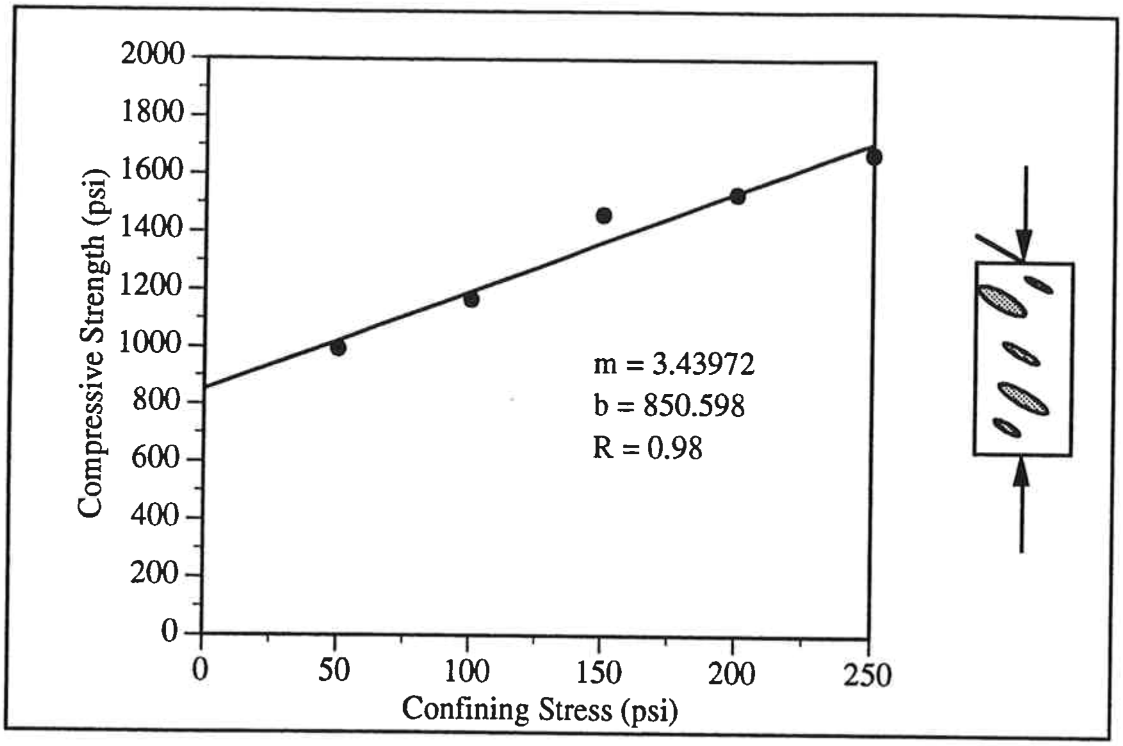

Figure C.9 Compressive Strength versus Confining Stress - m-60 Specimens

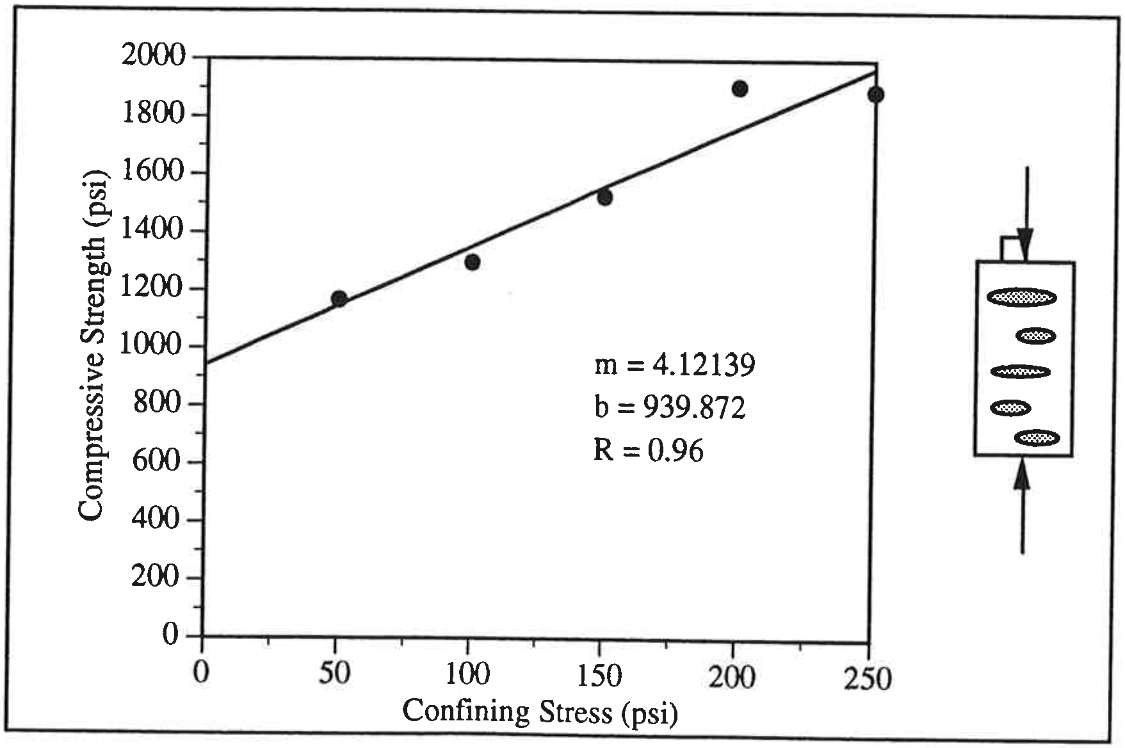

Figure C.10 Compressive Strength versus Confining Stress - m-90 Specimens

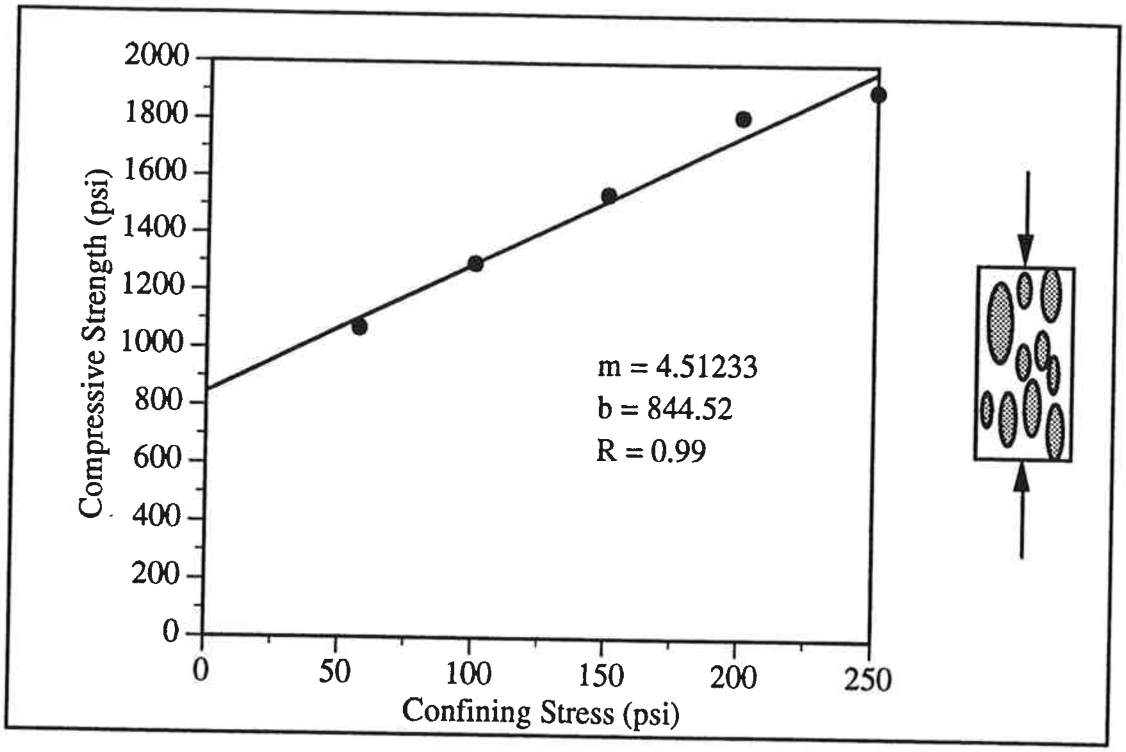

Figure C.11 Compressive Strength versus Confining Stress - h-0 Specimens

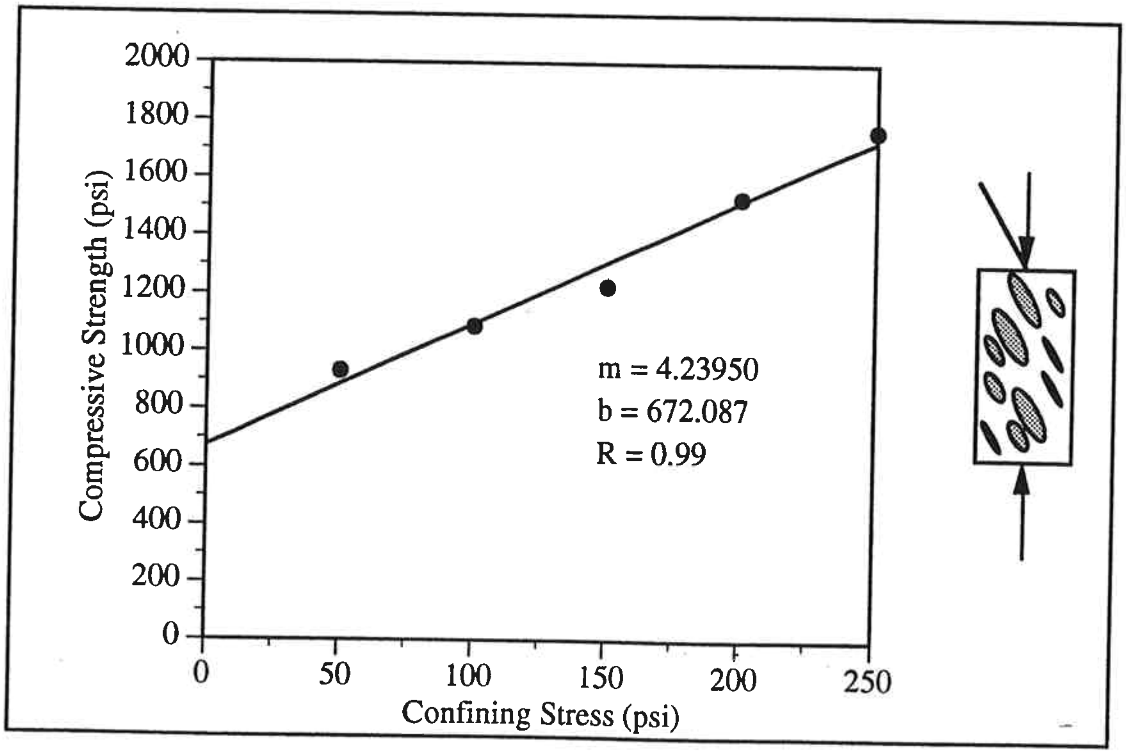

Figure C.12 Compressive Strength versus Confining Stress - h-30 Specimens

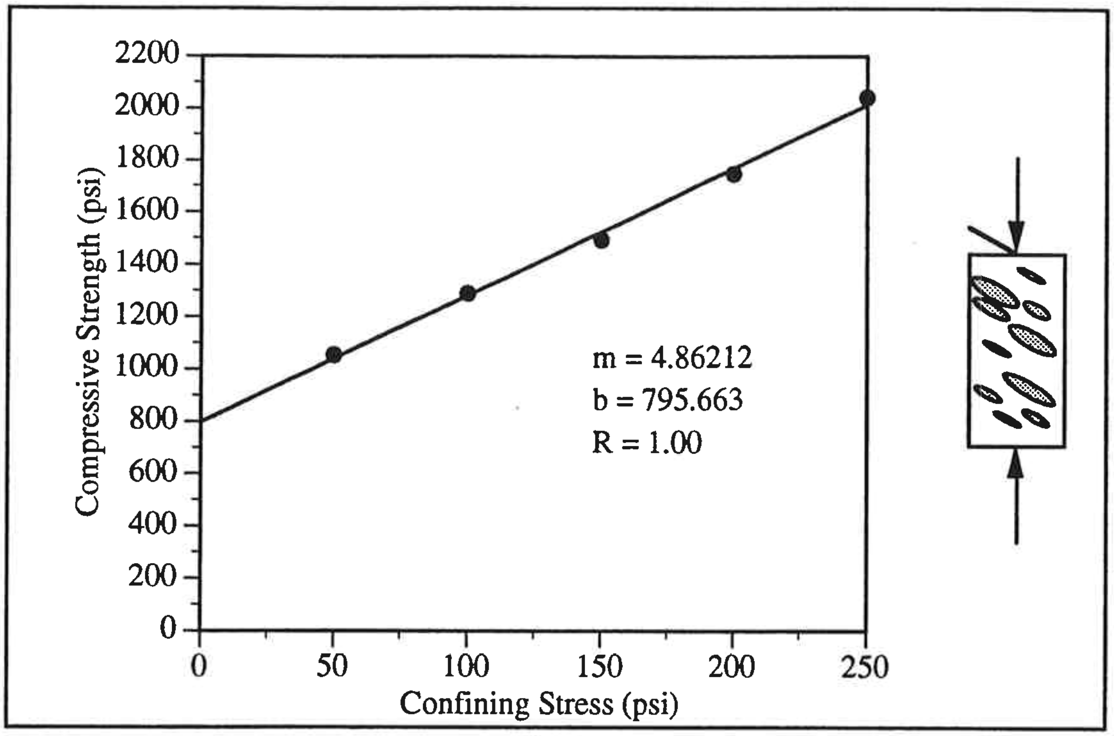

Figure C.13 Compressive Strength versus Confining Stress - h-60 Specimens

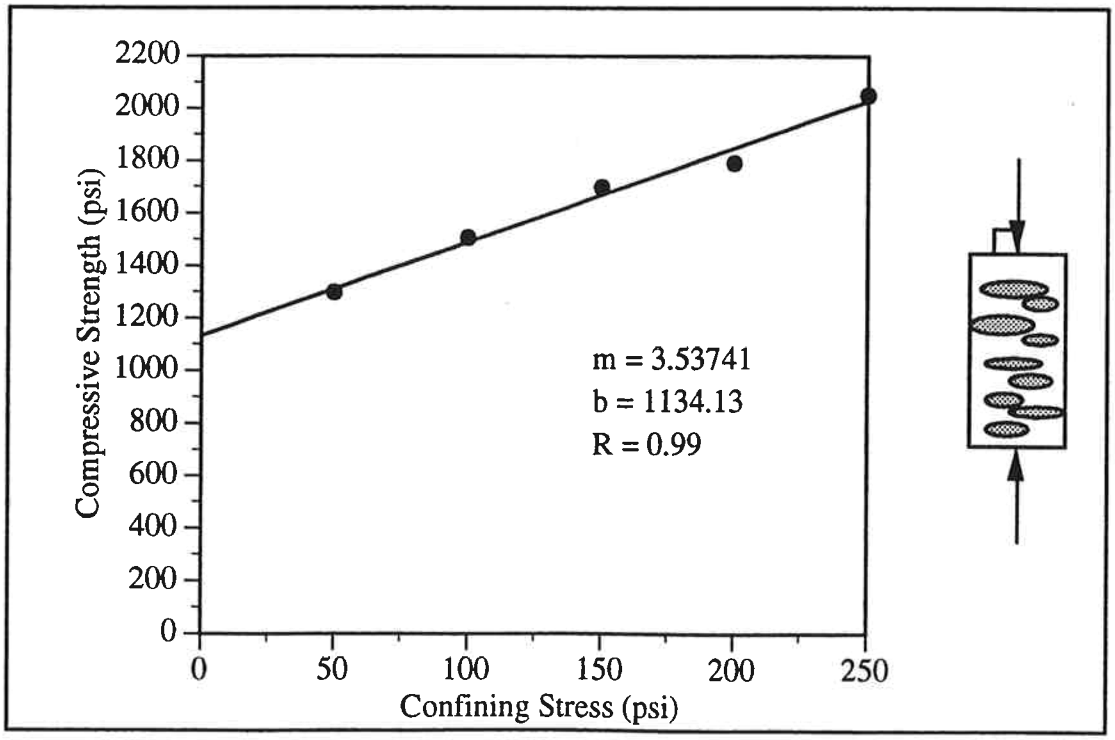

Figure C.14 Compressive Strength versus Confining Stress - h-90 Specimens

Appendix C Strength Data - Compressive Strength versus Confining Stress and Mohr Circle Plots for the Physical Models

Table C.4 Cohesion and Angle of Internal Friction Values for Different Specimen Types

Specimen Type	Average Block Proportion	m	b	c (psi)	ϕ (°)
matrix	0%	2.43126	1028.19	330	24.7
block	100%	4.25612	1837.02	445	38.3
l-0	29%	2.58307	1110.40	345	26.2
l-30	31%	3.37265	917.672	250	32.9
l-60	33%	2.31842	1147.98	377	23.4
l-90	29%	3.36536	1012.16	276	32.8
m-0	50%	3.46086	867.038	233	33.5
m-30	53%	3.29318	746.816	206	32.3
m-60	54%	3.43972	850.598	229	33.3
m-90	57%	4.12139	939.872	231	37.6
h-0	72%	4.51233	844.512	199	39.6
h-30	74%	4.23950	672.087	163	38.2
h-60	73%	4.86212	795.663	180	41.2
h-90	71%	3.53741	1134.13	302	34.0

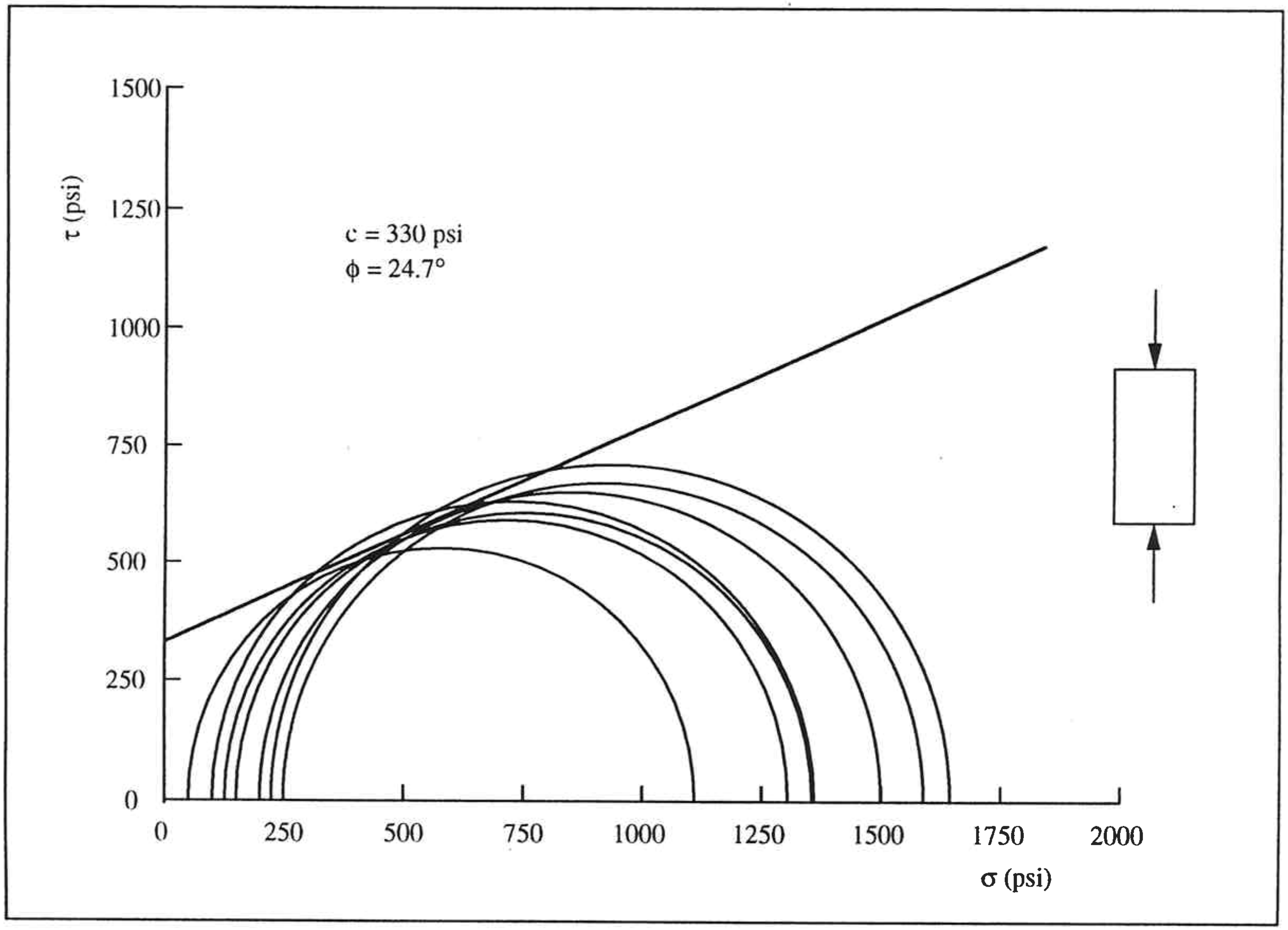

Figure C.15 Mohr Circles and Failure Envelope - Matrix Component

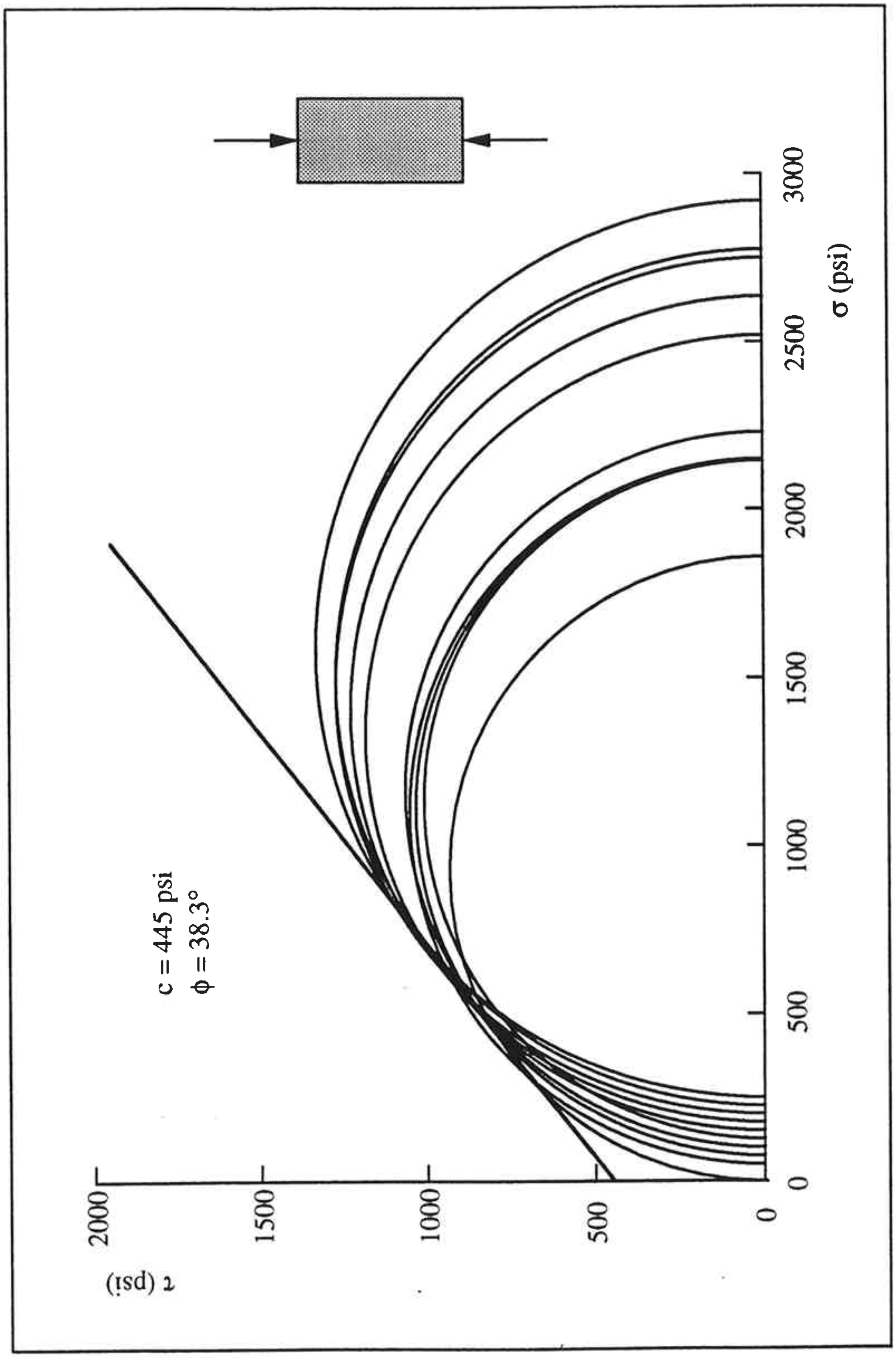

Figure C.16 Mohr Circles and Failure Envelope - Block Component

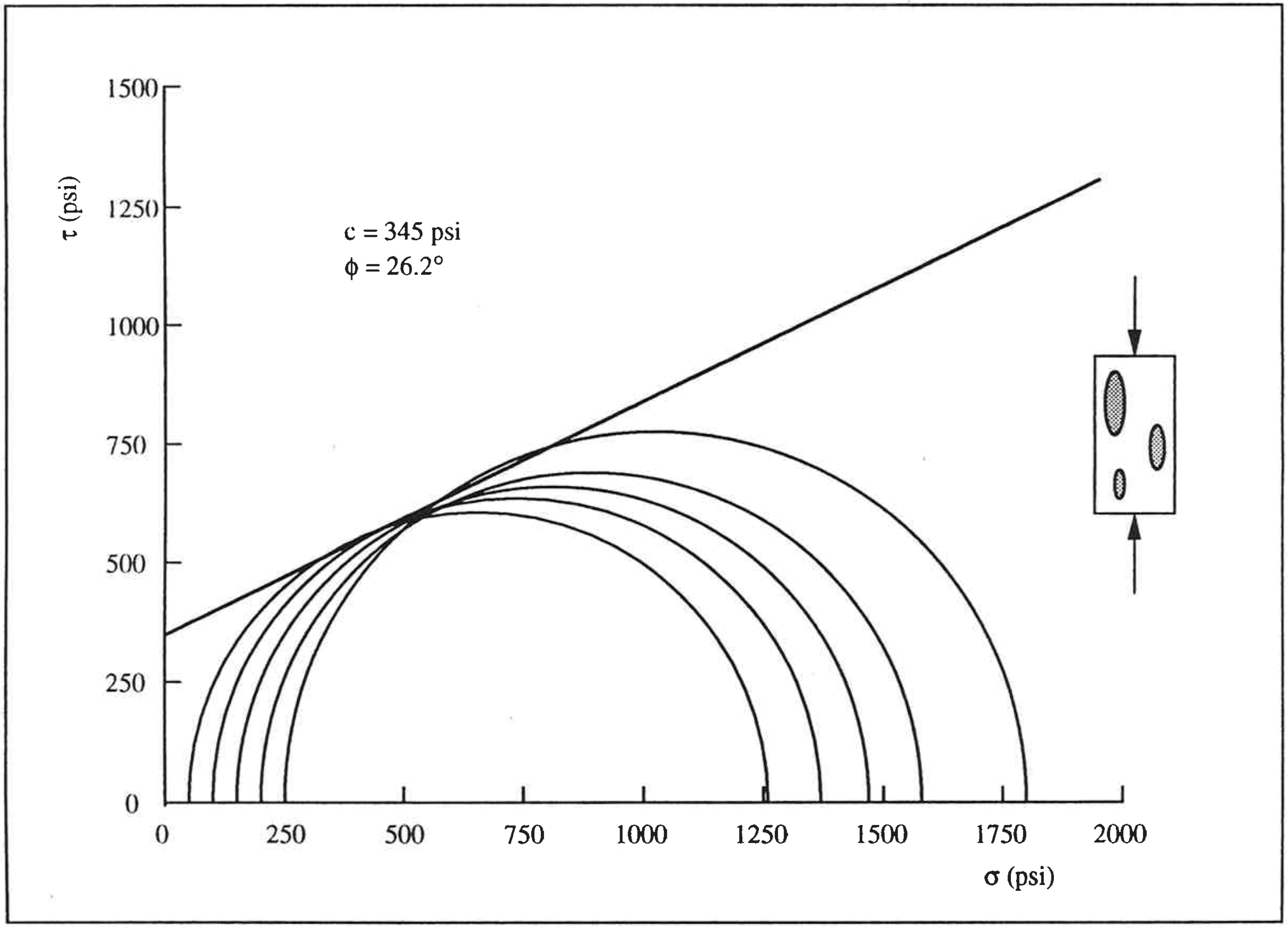

Figure C.17 Mohr Circles and Failure Envelope - 1-0 Specimens

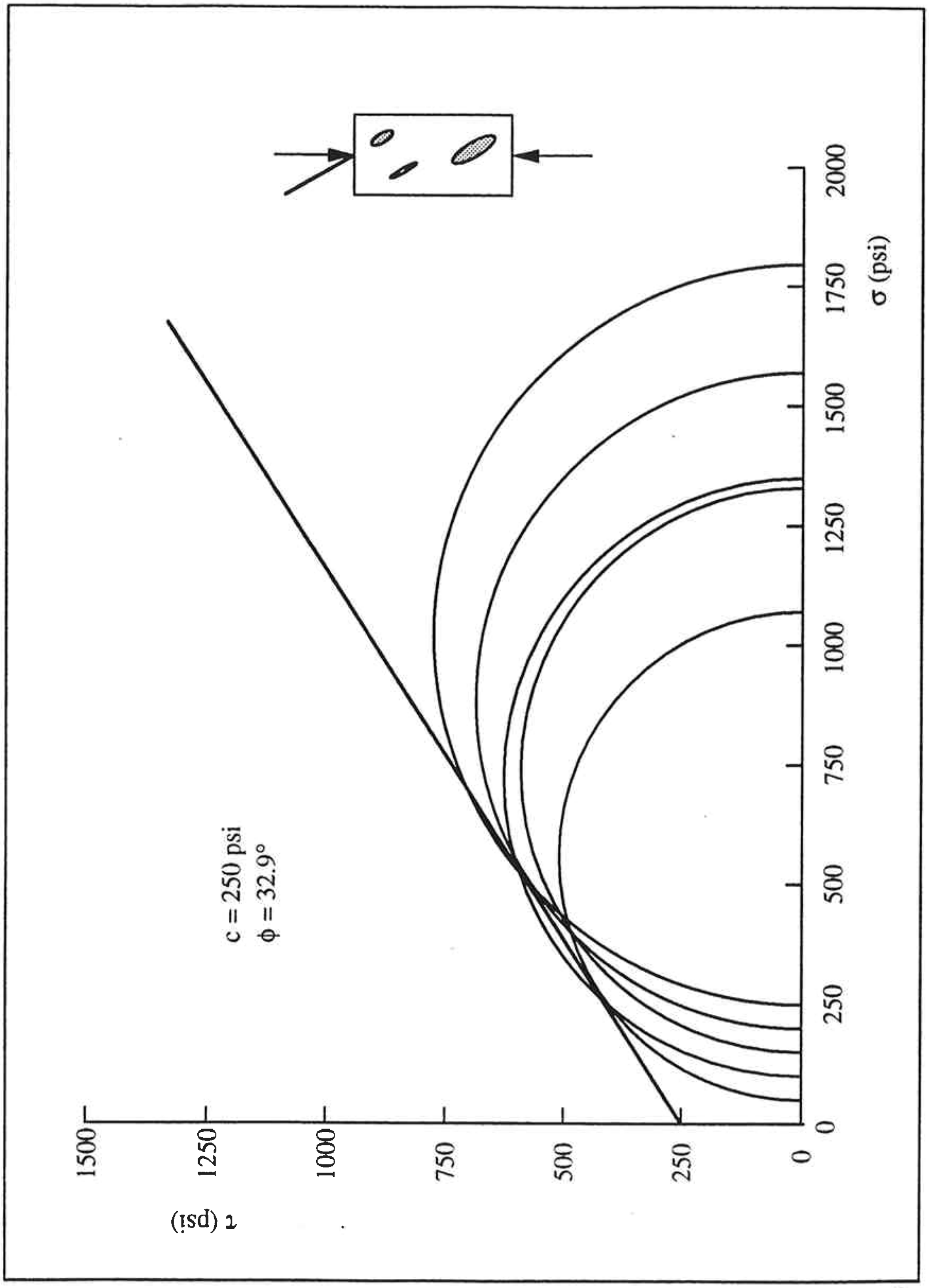

Figure C.18 Mohr Circles and Failure Envelope - 1-30 Specimens

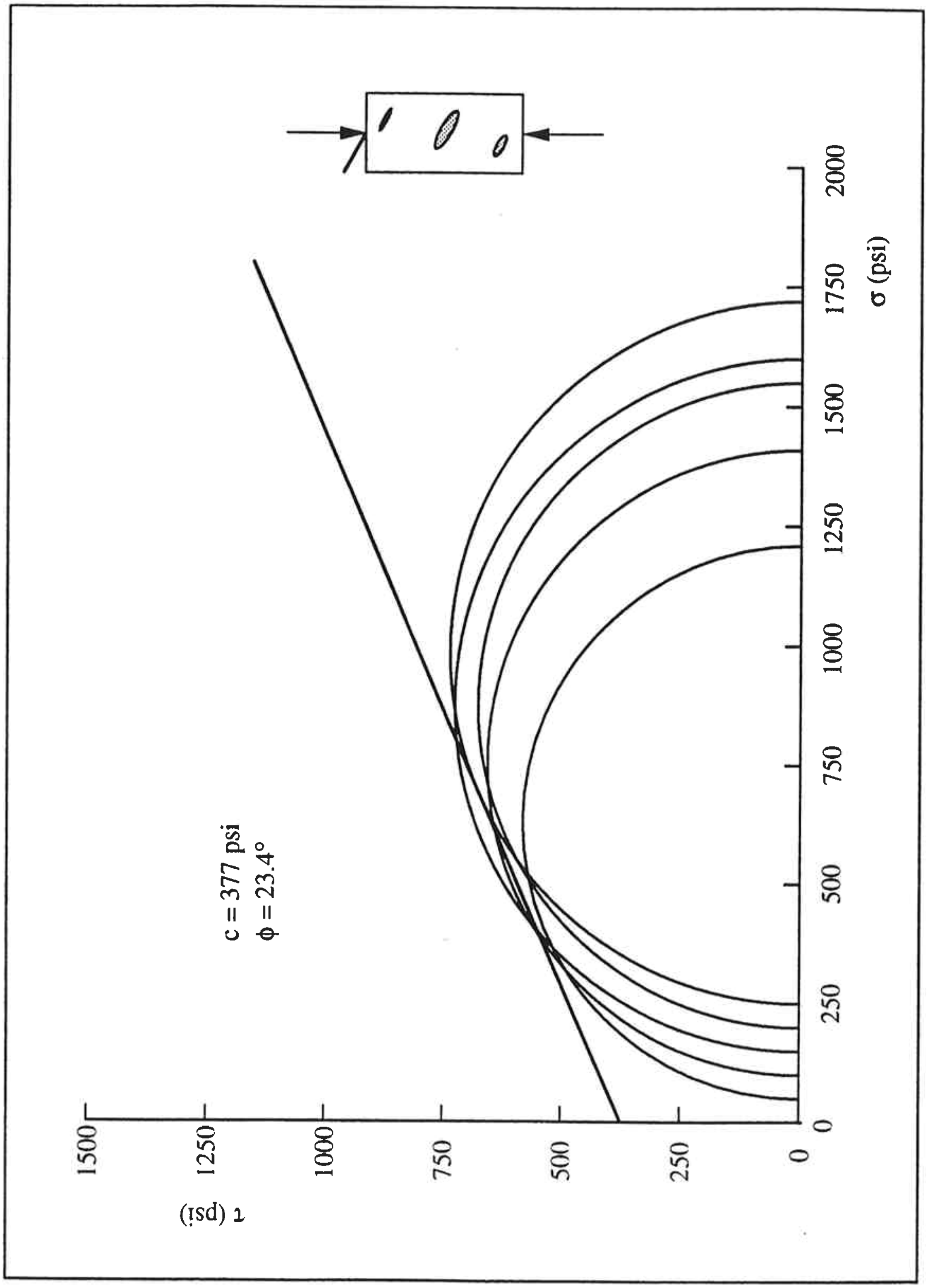

Figure C.19 Mohr Circles and Failure Envelope - 1-60 Specimens

Appendix C Strength Data - Compressive Strength versus Confining Stress and Mohr Circle Plots for the Physical Models

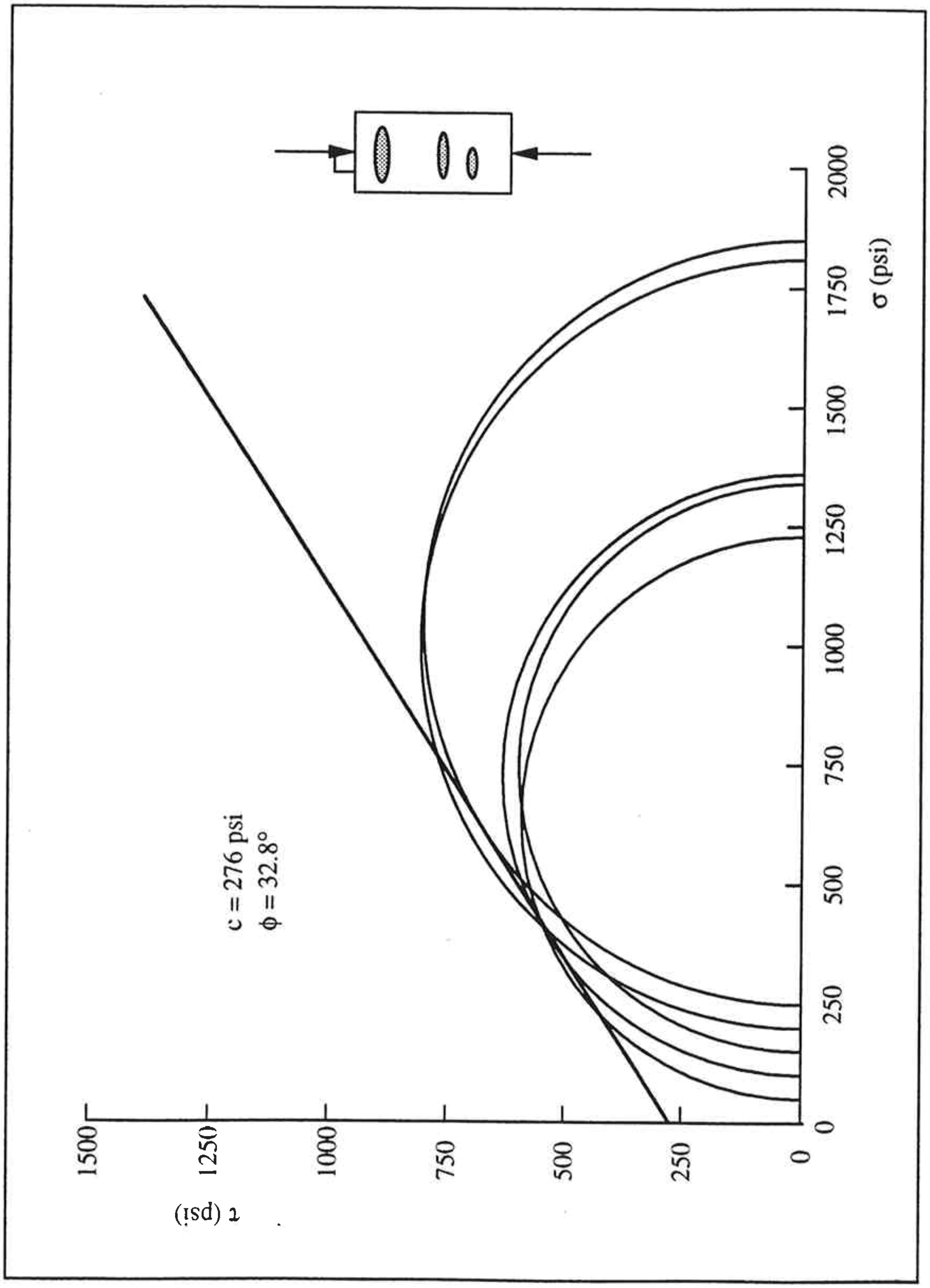

Figure C.20 Mohr Circles and Failure Envelope - 1-90 Specimens

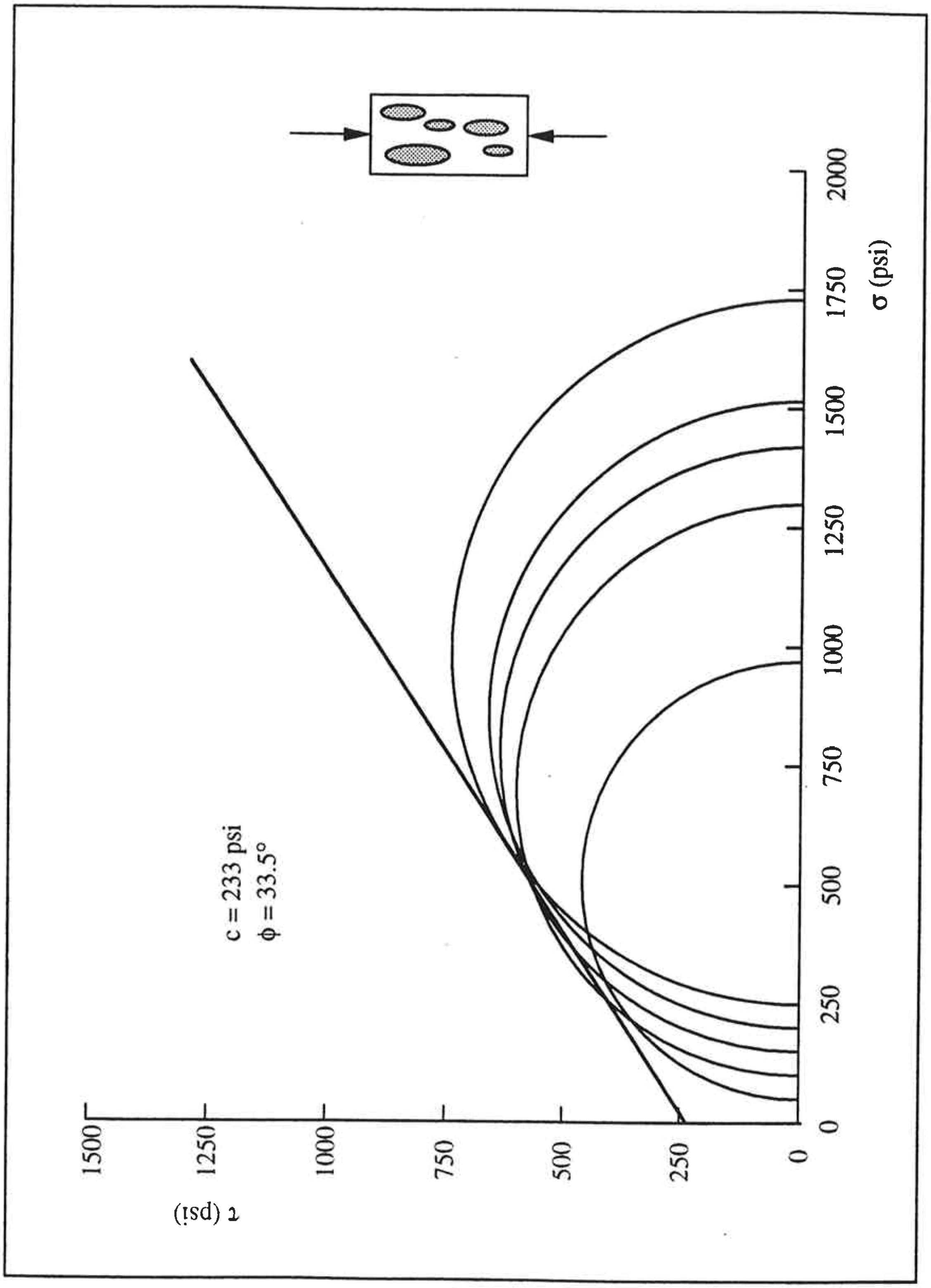

Figure C.21 Mohr Circles and Failure Envelope - m-0 Specimens

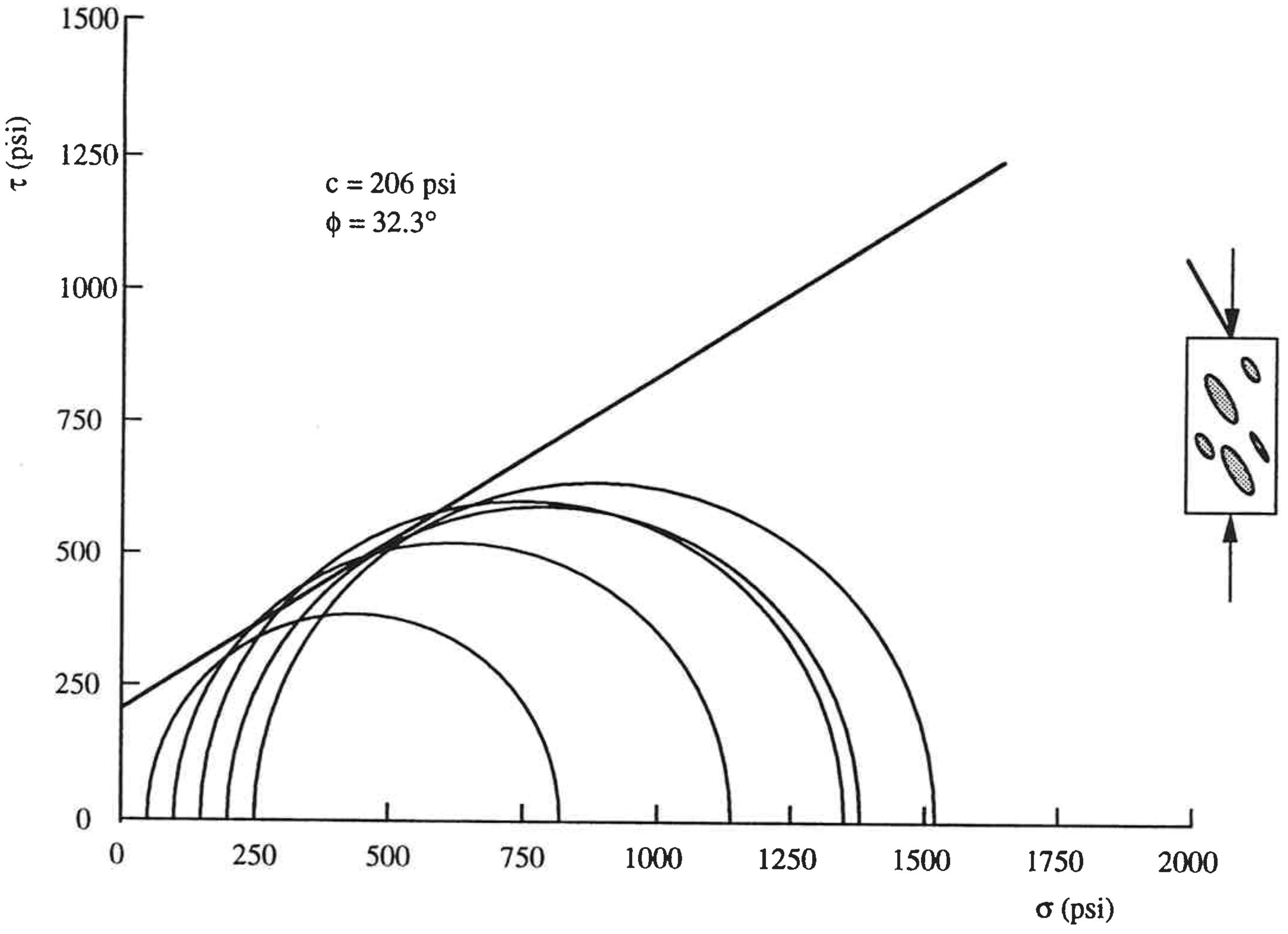

Figure C.22 Mohr Circles and Failure Envelope - m-30 Specimens

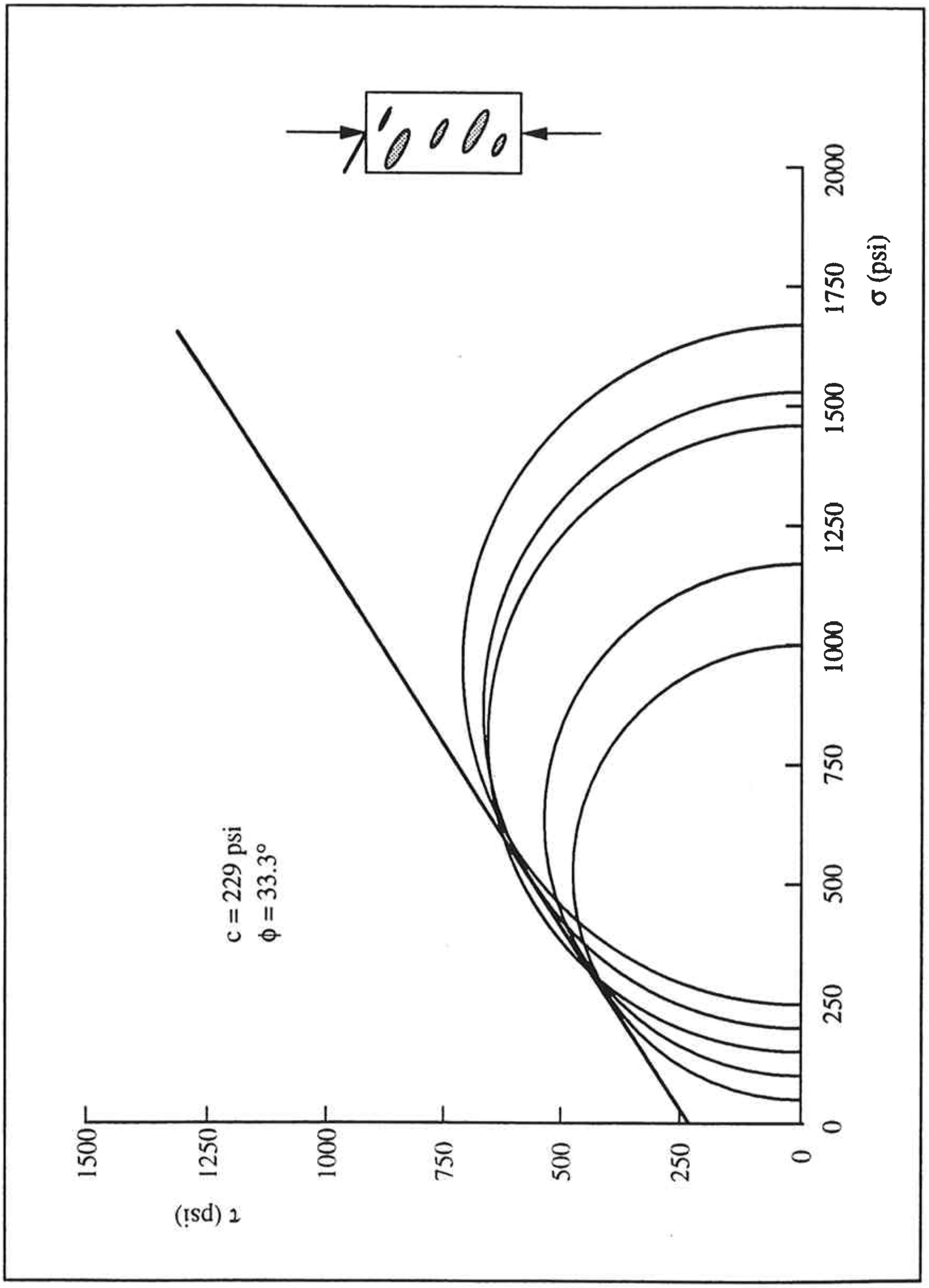

Figure C.23 Mohr Circles and Failure Envelope - m-60 Specimens

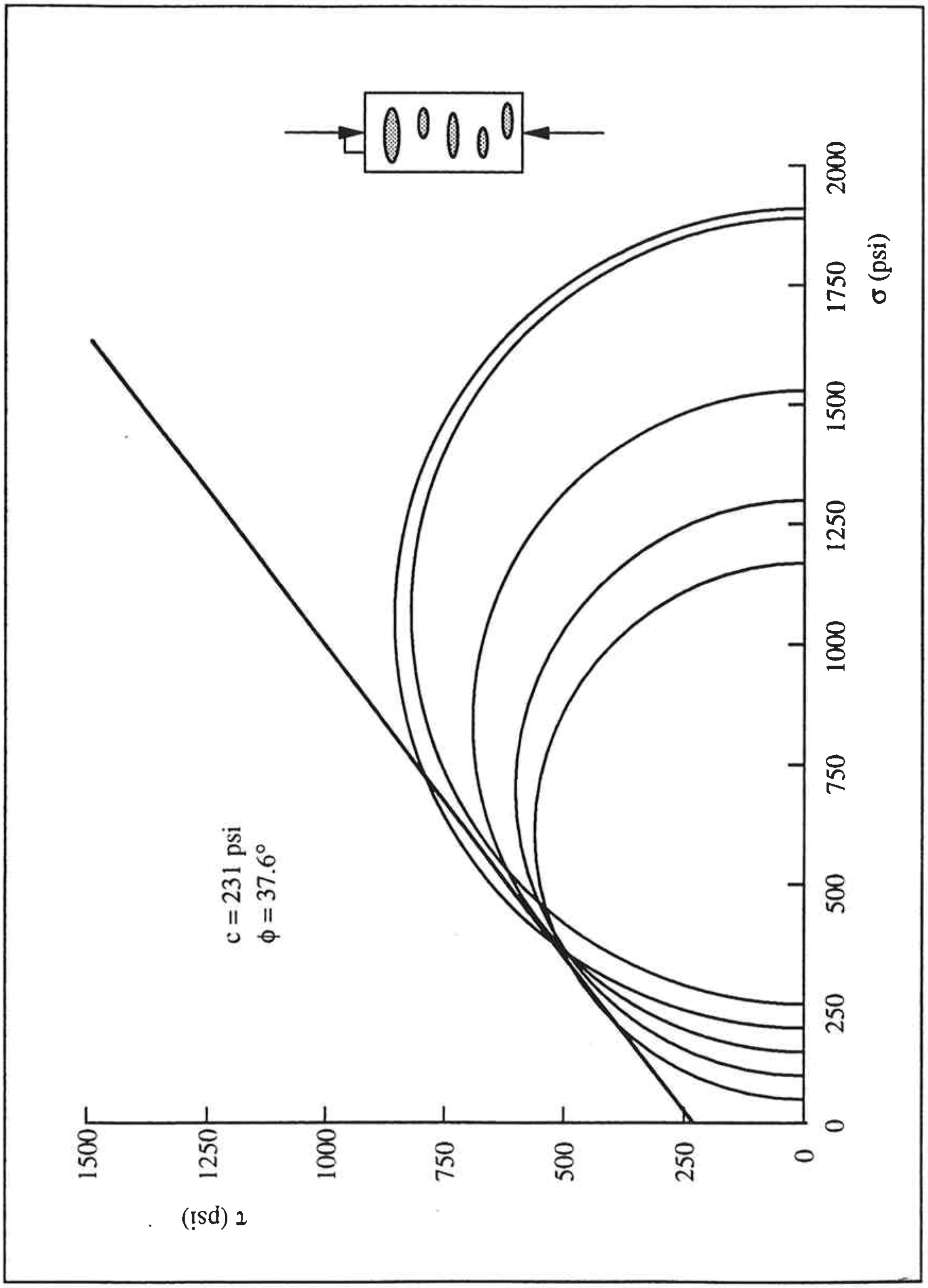

Figure C. 24 Mohr Circles and Failure Envelope - m-90 Specimens

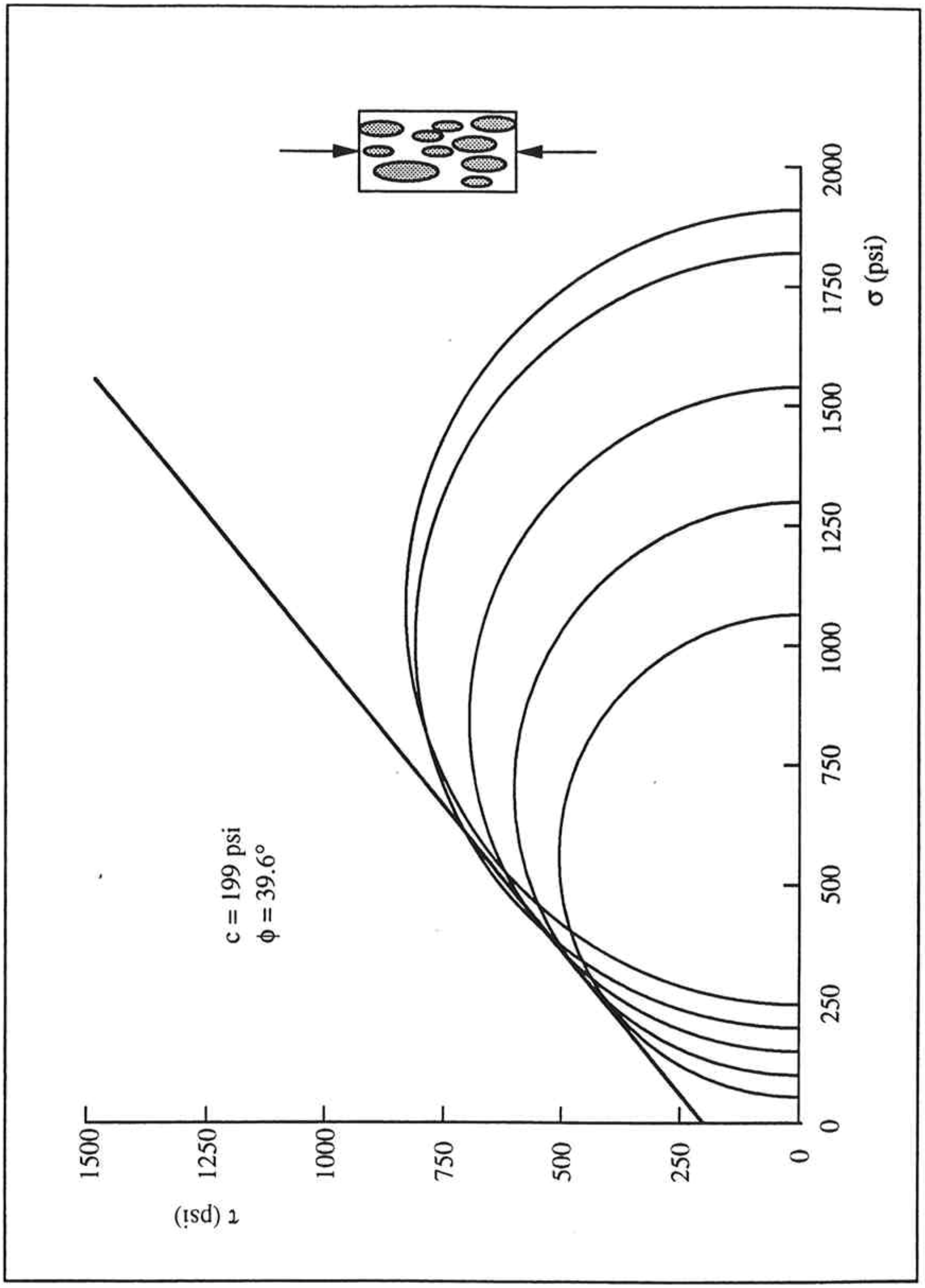

Figure C.25 Mohr Circles and Failure Envelope - h-0 Specimens

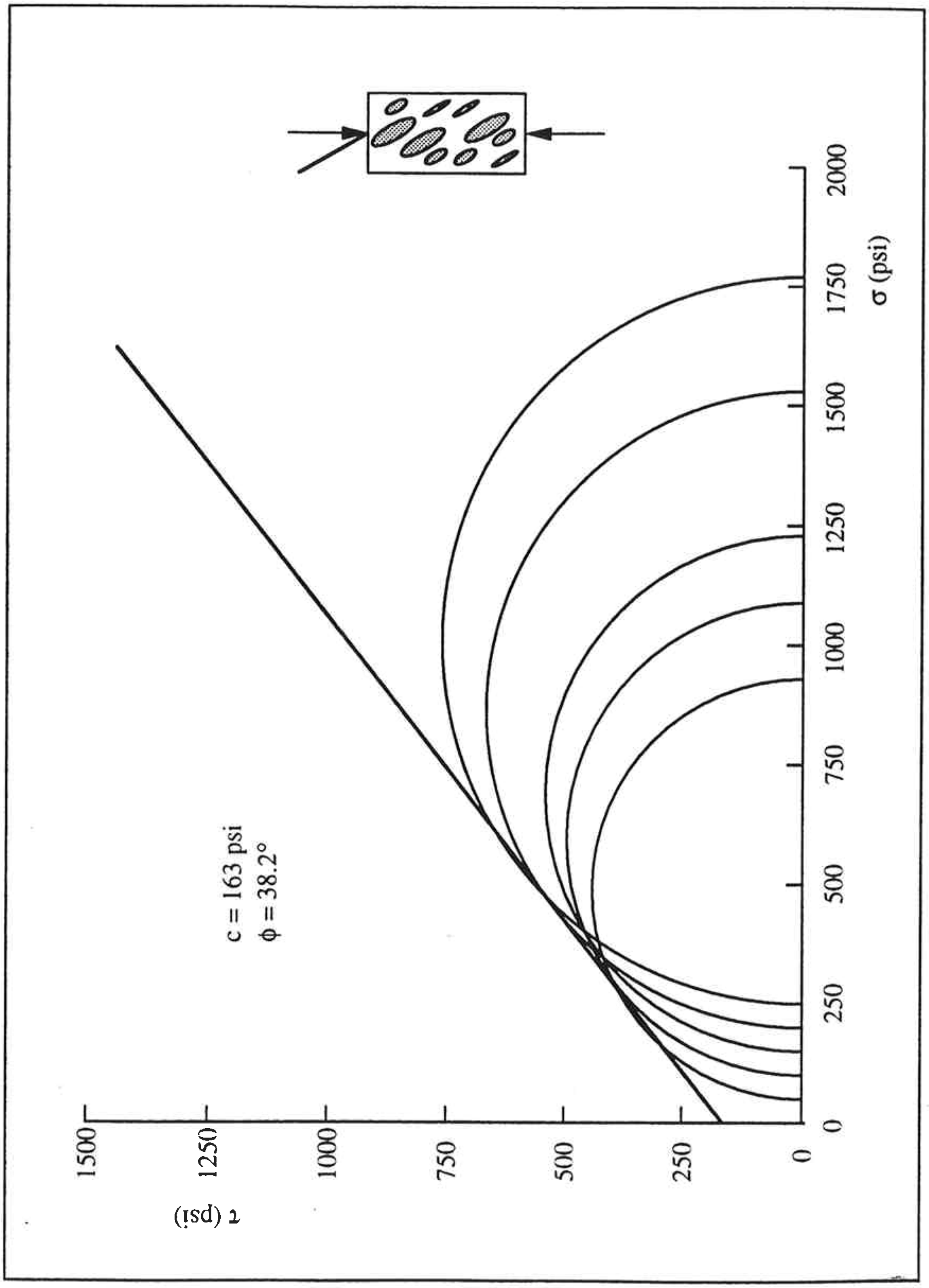

Figure C. 26 Mohr Circles and Failure Envelope - h-30 Specimens

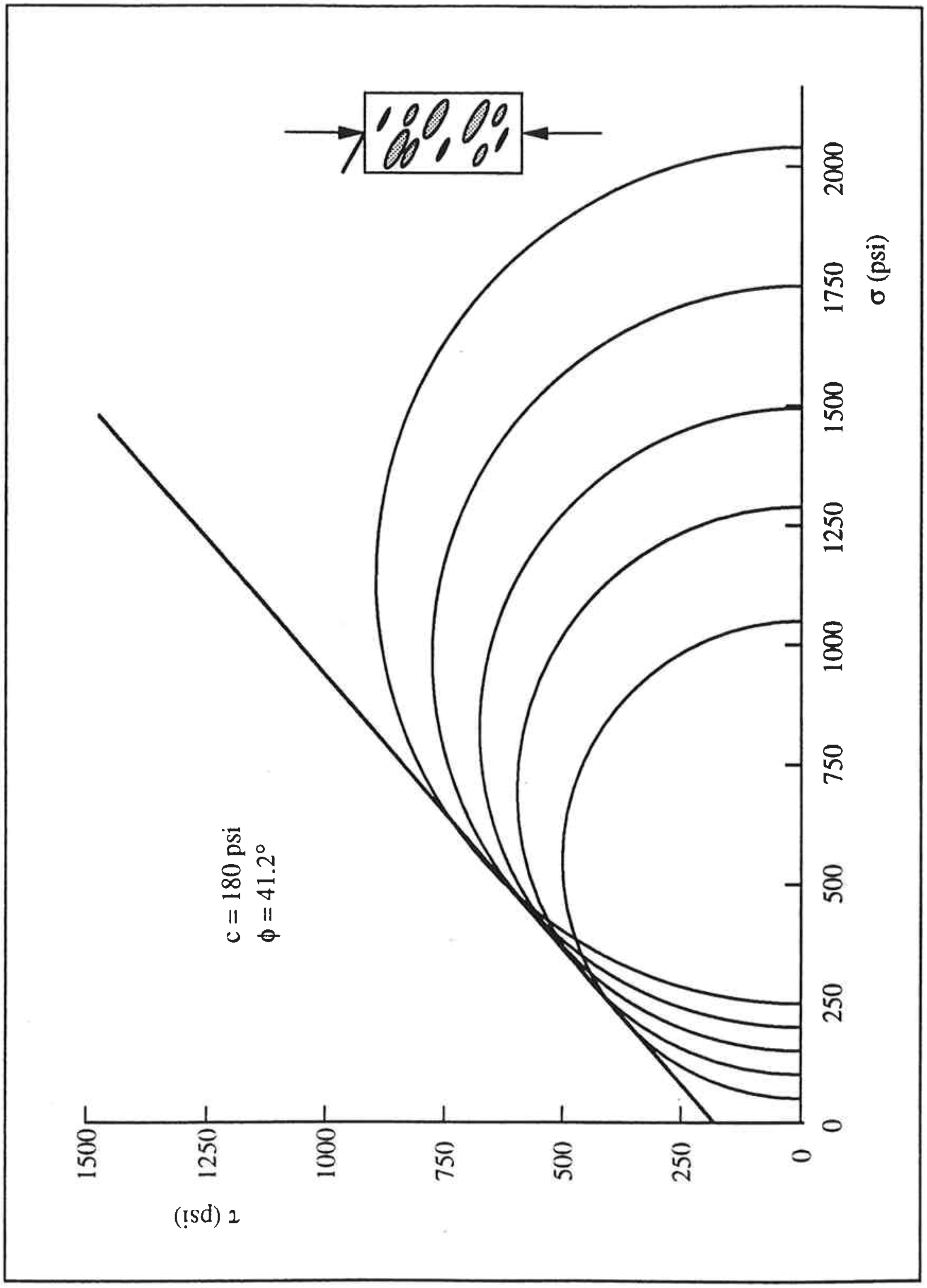

Figure C. 27 Mohr Circles and Failure Envelope - h-60 Specimens

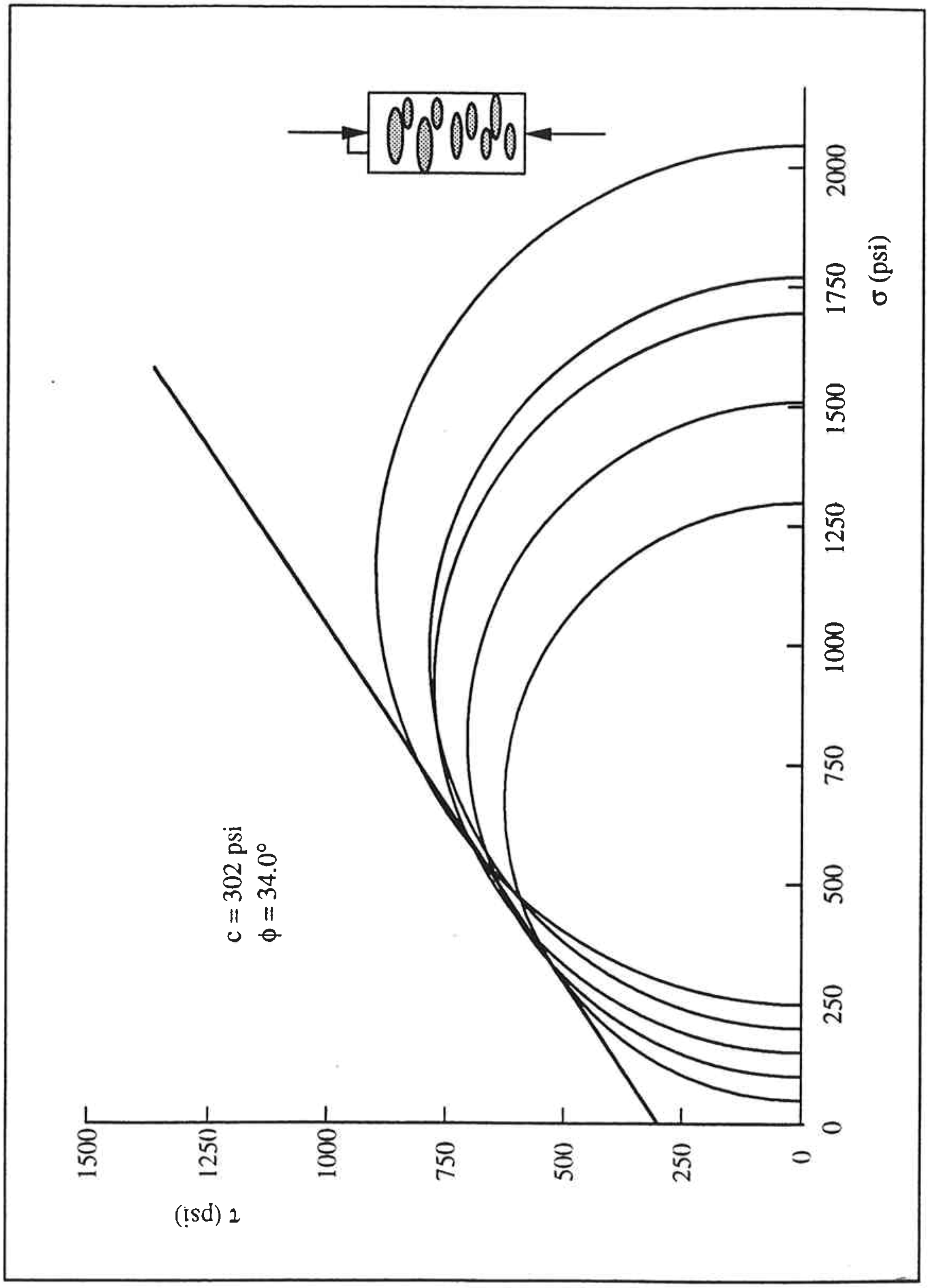

Figure C.28 Mohr Circles and Failure Envelope - h-90 Specimens

APPENDIX D

Photographs and Tracings of Failed Specimens

This appendix contains photographs of the 77 failed physical model specimens and surface tracings of 58 of the 60 block-in-matrix specimens. The tracings were made by covering each specimen with clear plastic wrap, and then sketching the outlines of the blocks and the surface expression of the failure "plane" with a permanent marking pen. The plastic wrap was then unrolled, taped to a white board and reduced by photocopying. The idea to trace the specimens' surfaces using plastic wrap was suggested and used initially by my colleague Ed Medley. The tracings done by him that are reproduced in this section are identified.

It was not feasible to trace the h-60-150 specimen or the h-90-100 specimen. They were broken during testing and/or removal from the triaxial cell to such an extreme that it was impossible to reconstitute the specimen fragments into a sufficiently cylindrical form to be plastic wrapped and traced.

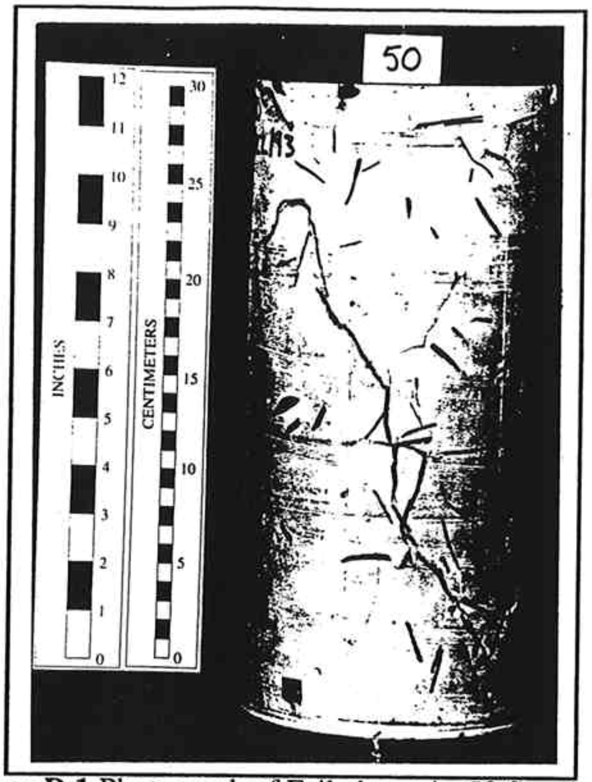

Figure D.1 Photograph of Failed matrix-50 Specimen

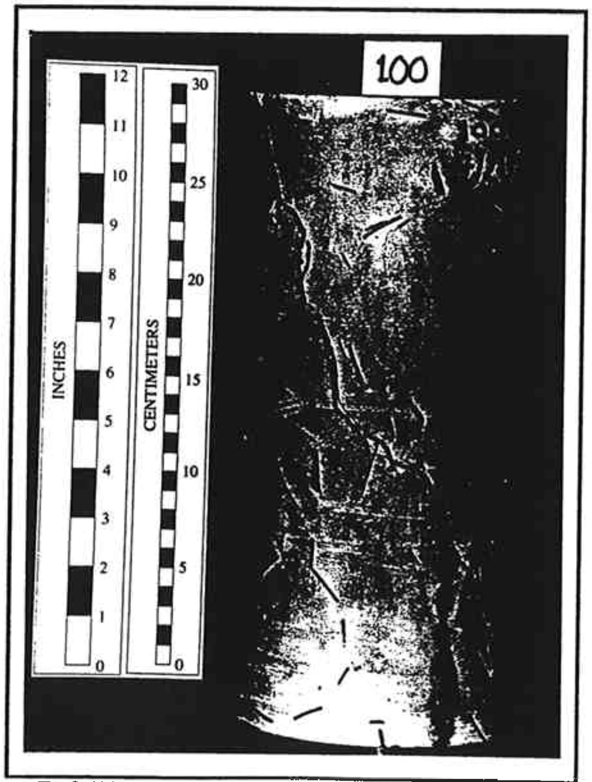

Figure D.2 Photograph of Failed matrix-100 Specimen

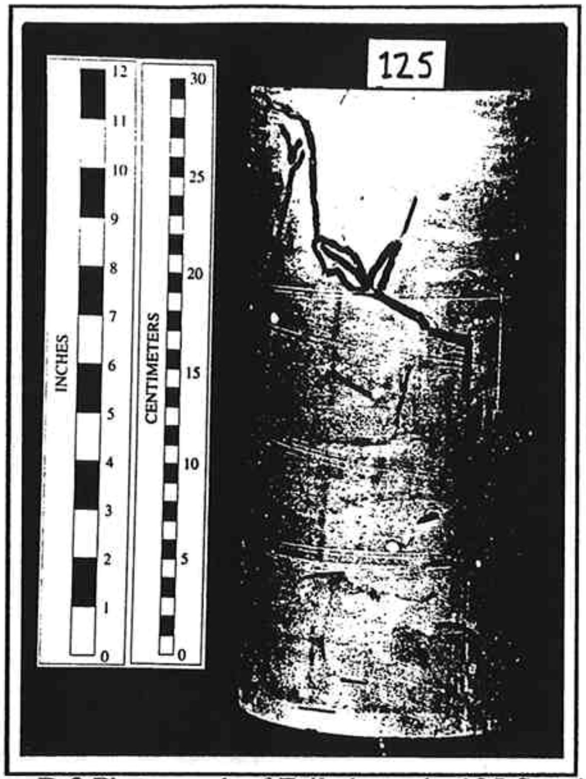

Figure D.3 Photograph of Failed matrix-125 Specimen

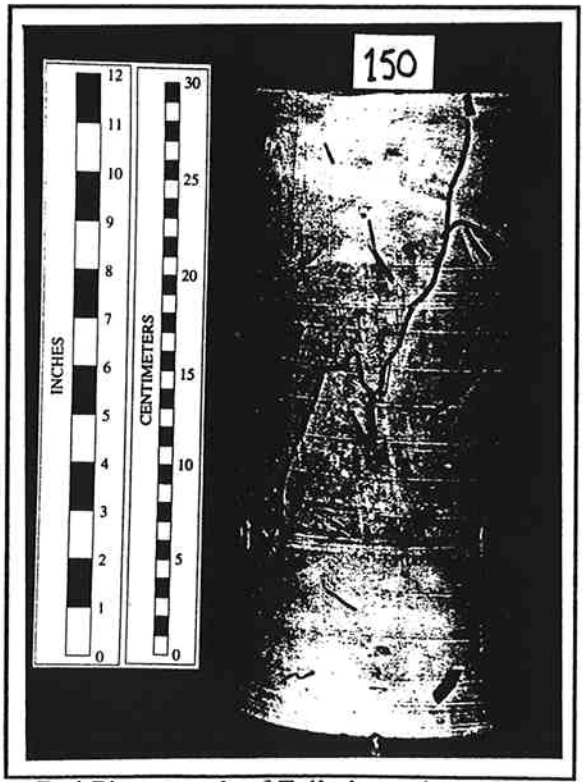

Figure D.4 Photograph of Failed matrix-150 Specimen

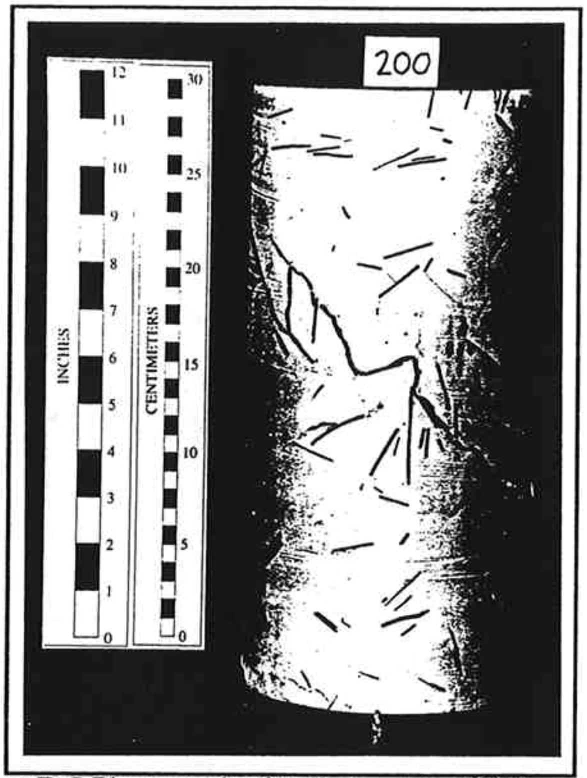

Figure D.5 Photograph of Failed matrix-200 Specimen

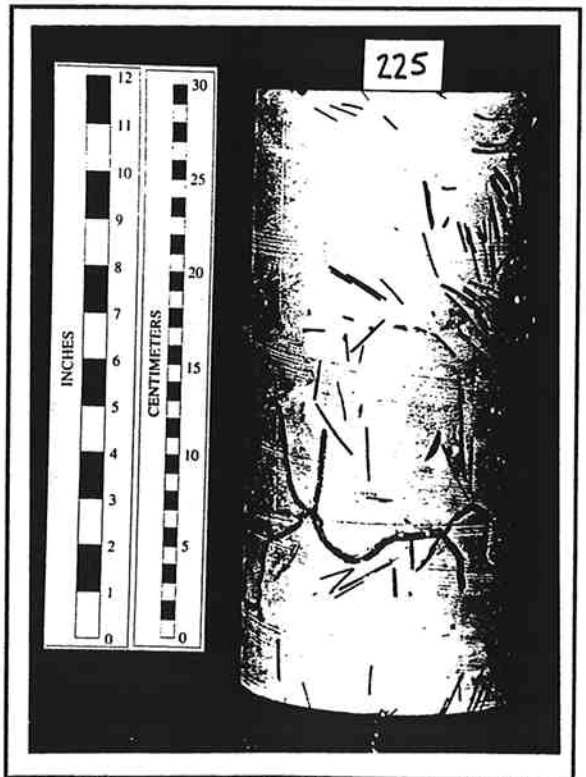

Figure D.6 Photograph of Failed matrix-225 Specimen

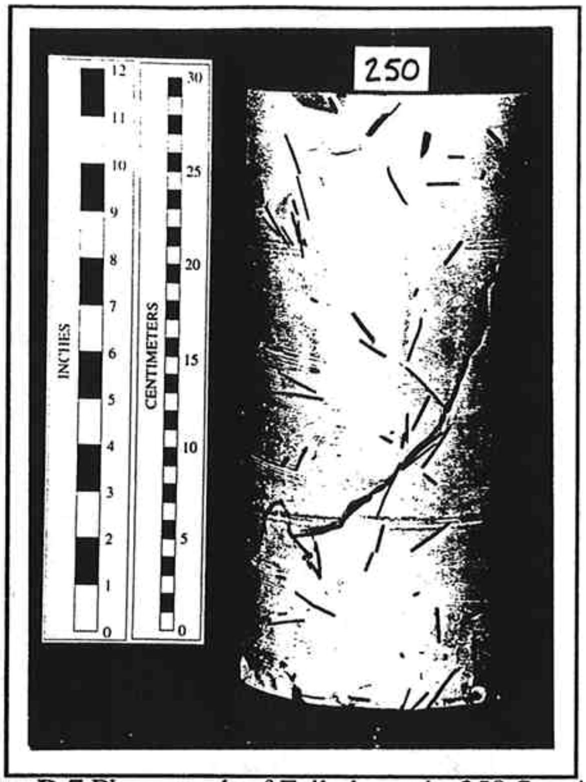

Figure D.7 Photograph of Failed matrix-250 Specimen

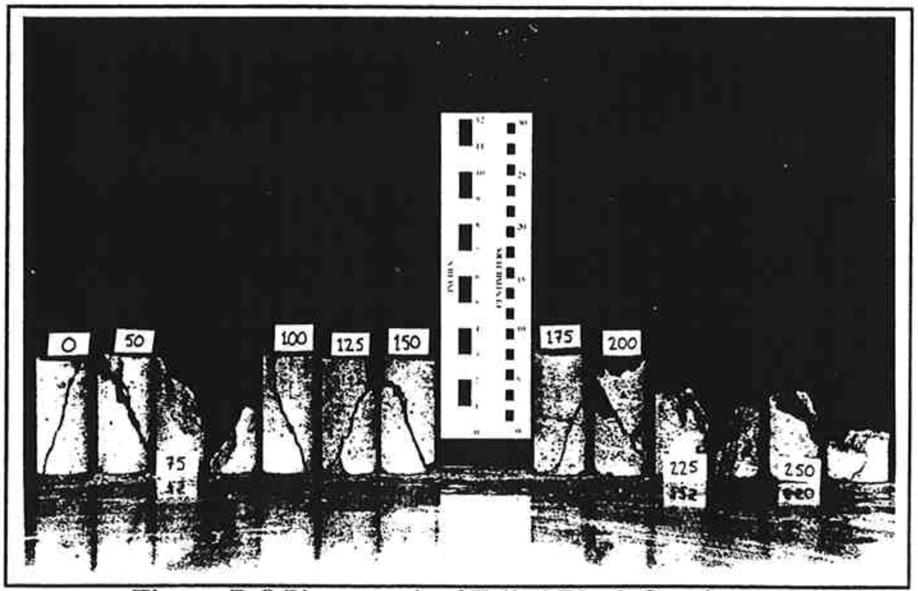

Figure D.8 Photograph of Failed Block Specimens

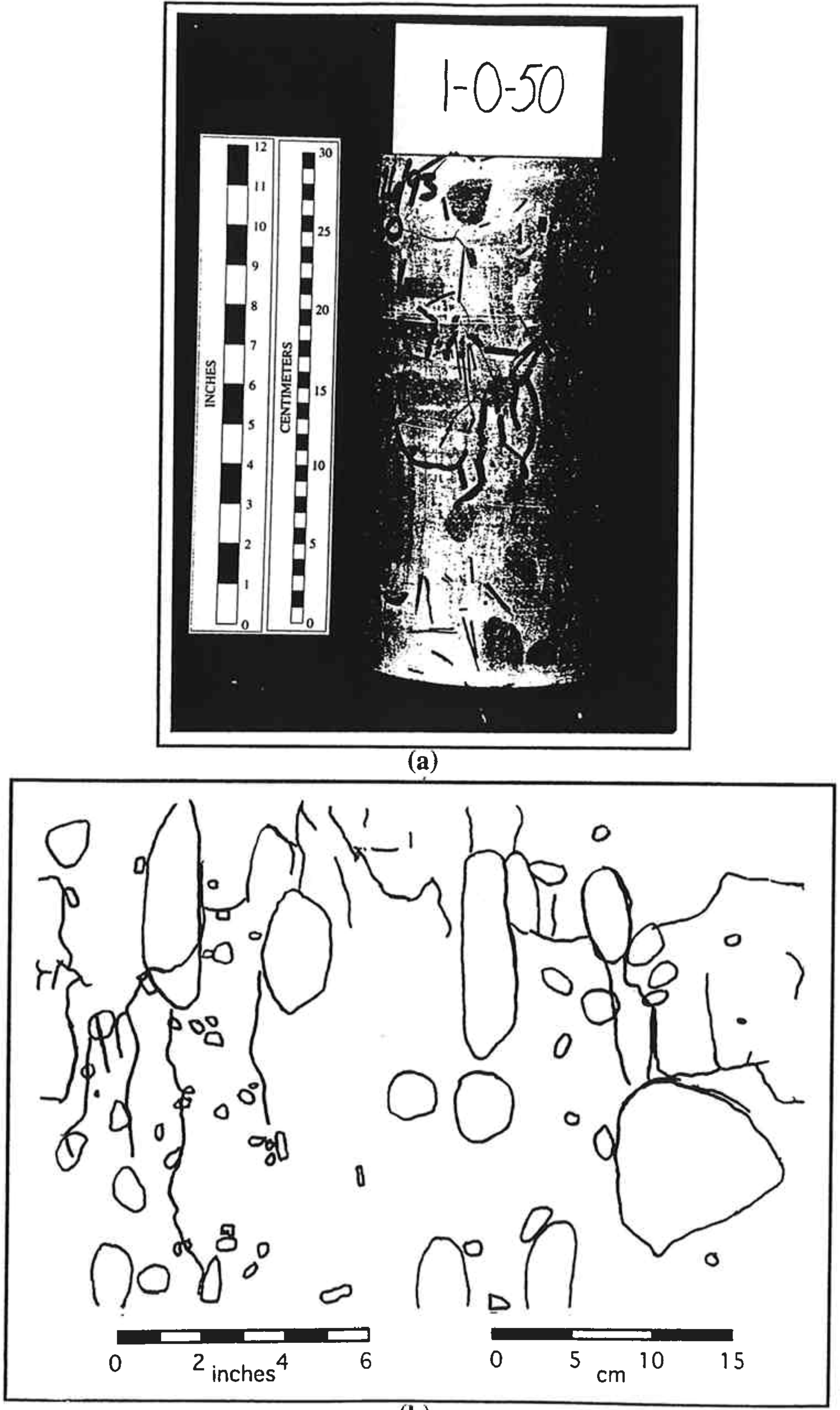

(a)

(b)

Figure D.9 (**a**) Photograph and (**b**) Tracing of Failed Specimen 1-0-50

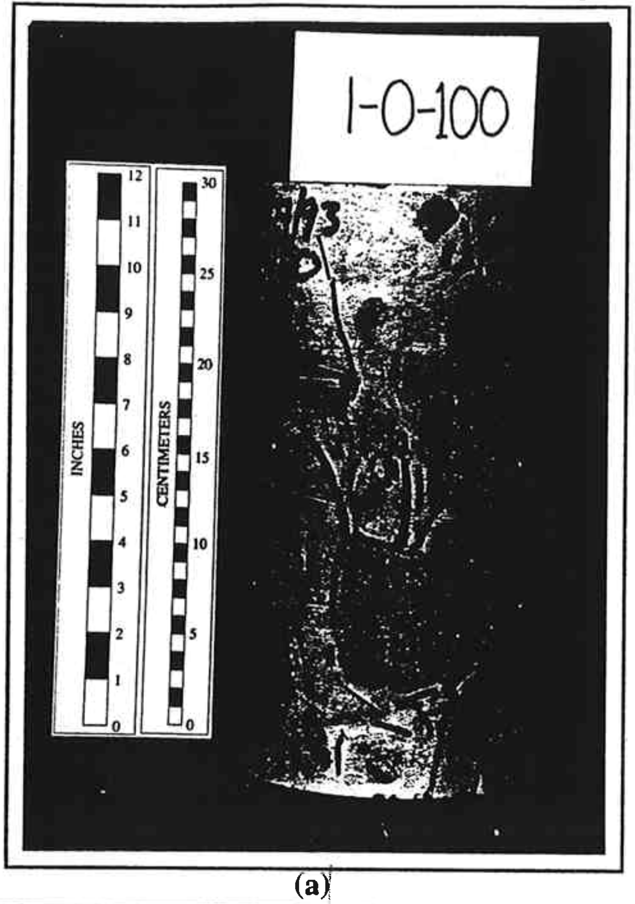

(a)

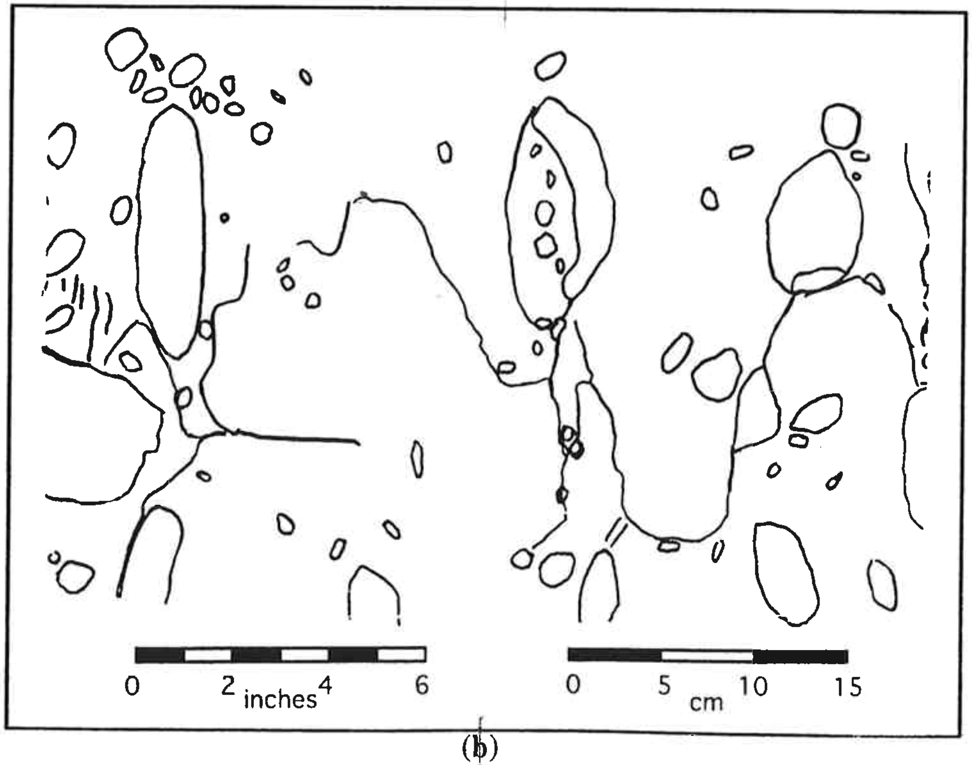

(b)

Figure D.10 (a) Photograph and **(b)** Tracing of Failed Specimen 1-0-100

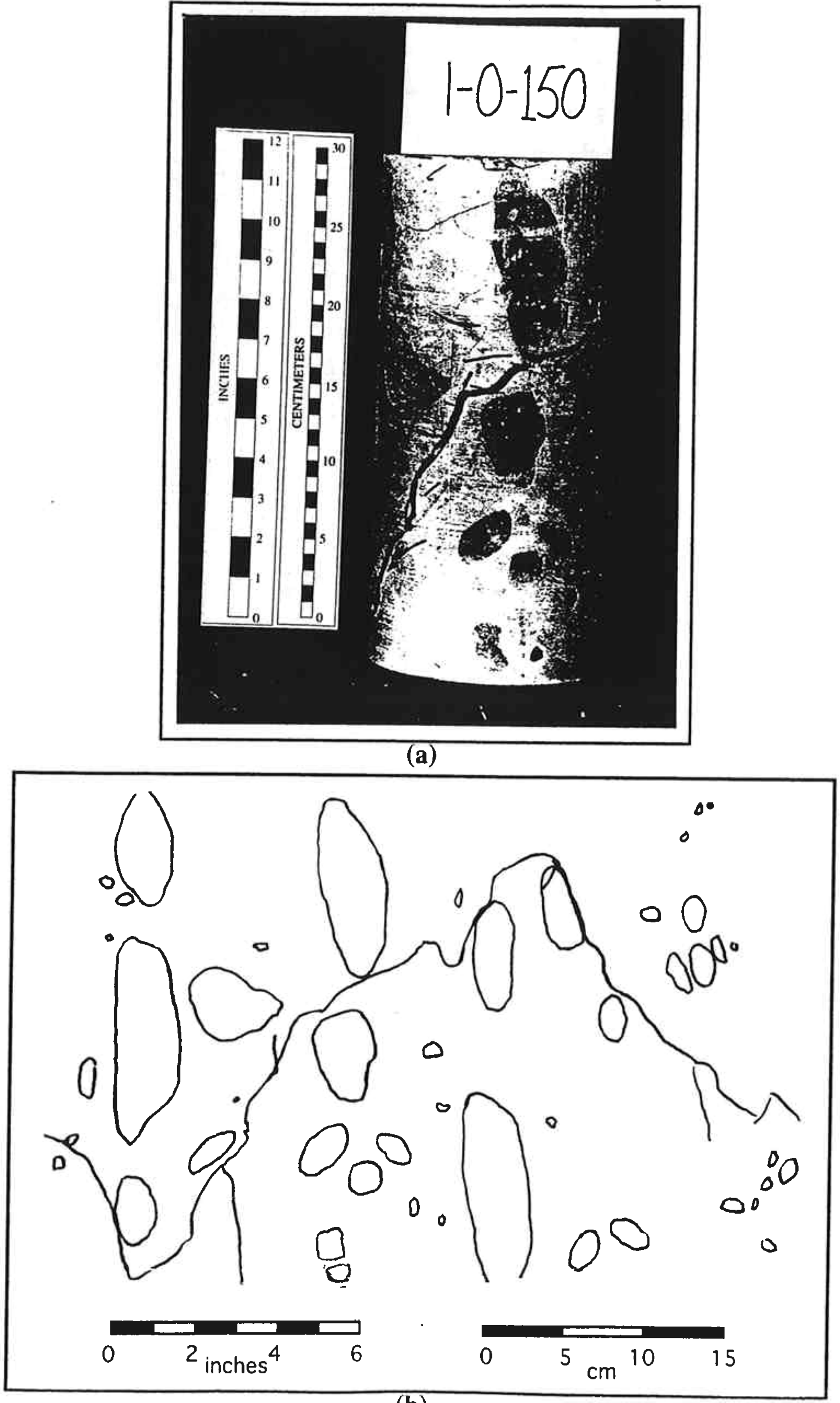

(a)

(b)

Figure D.11 (a) Photograph and **(b)** Tracing of Failed Specimen 1-0-150

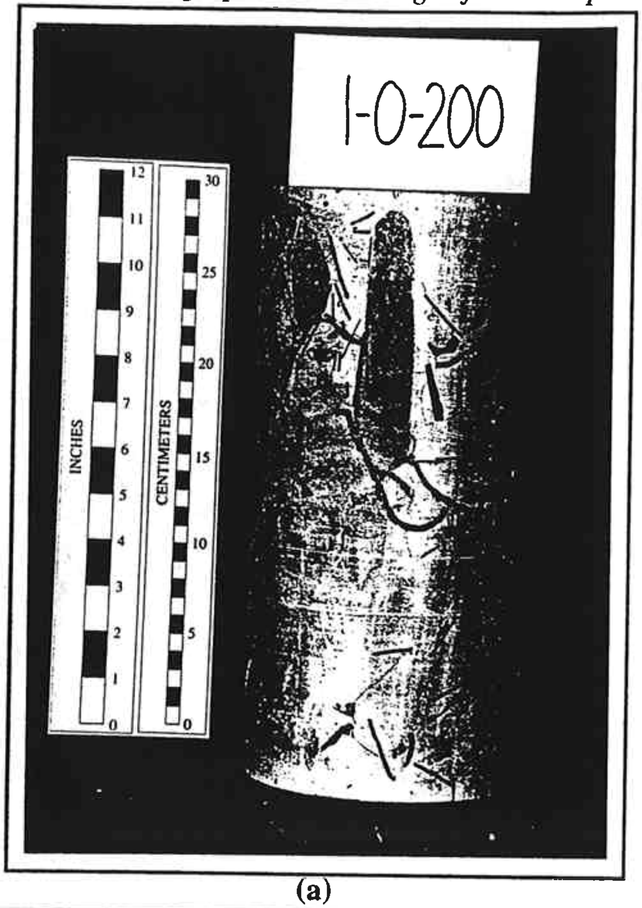

(a)

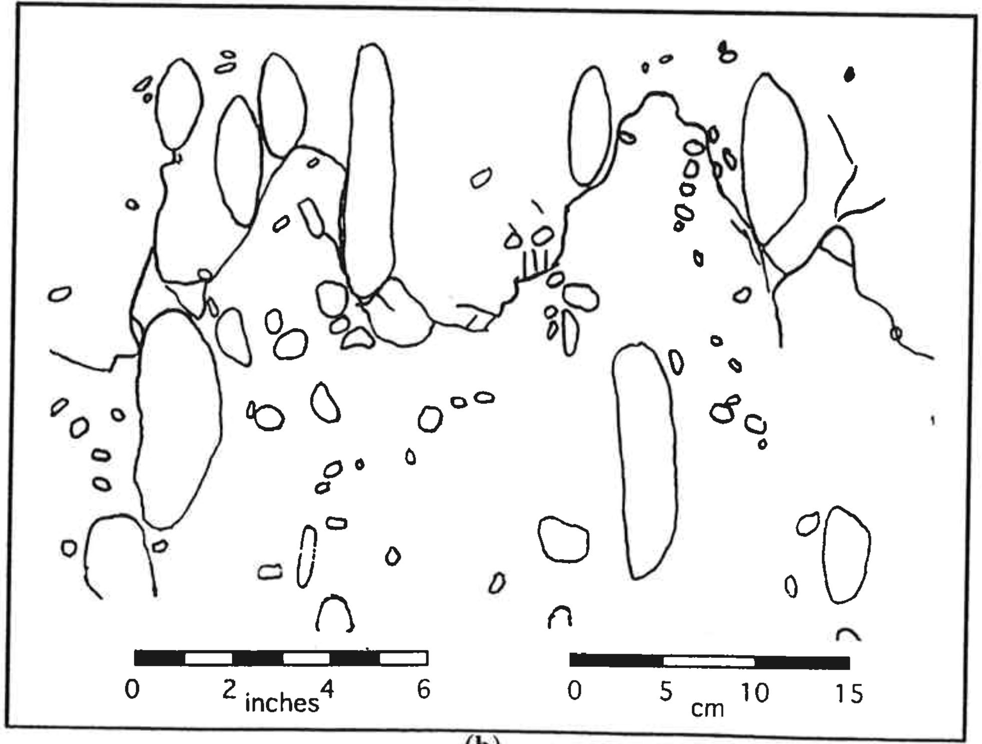

(b)

Figure D.12 (a) Photograph and **(b)** Tracing of Failed Specimen 1-0-200

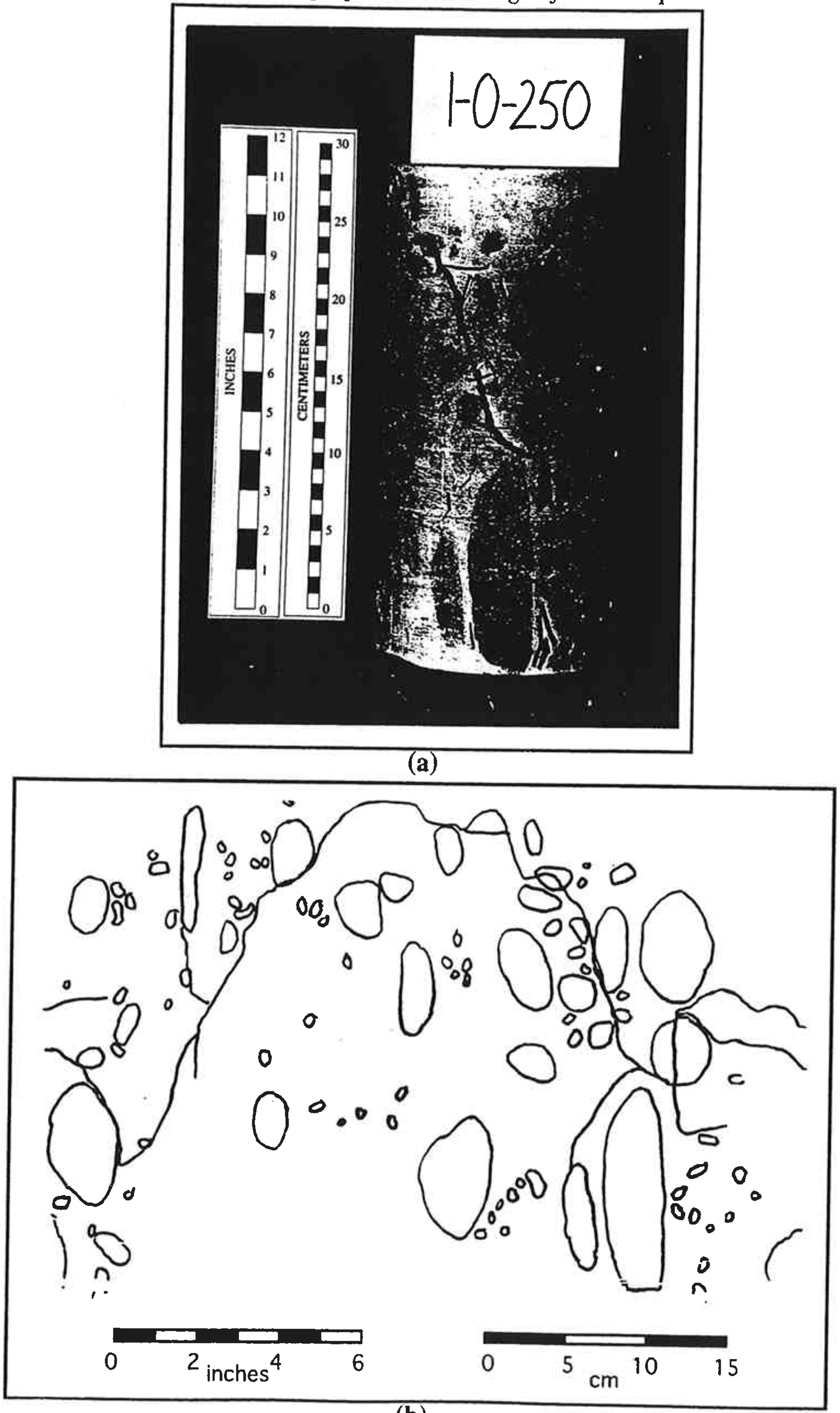

(a)

(b)

Figure D.13 (a) Photograph and **(b)** Tracing of Failed Specimen 1-0-250

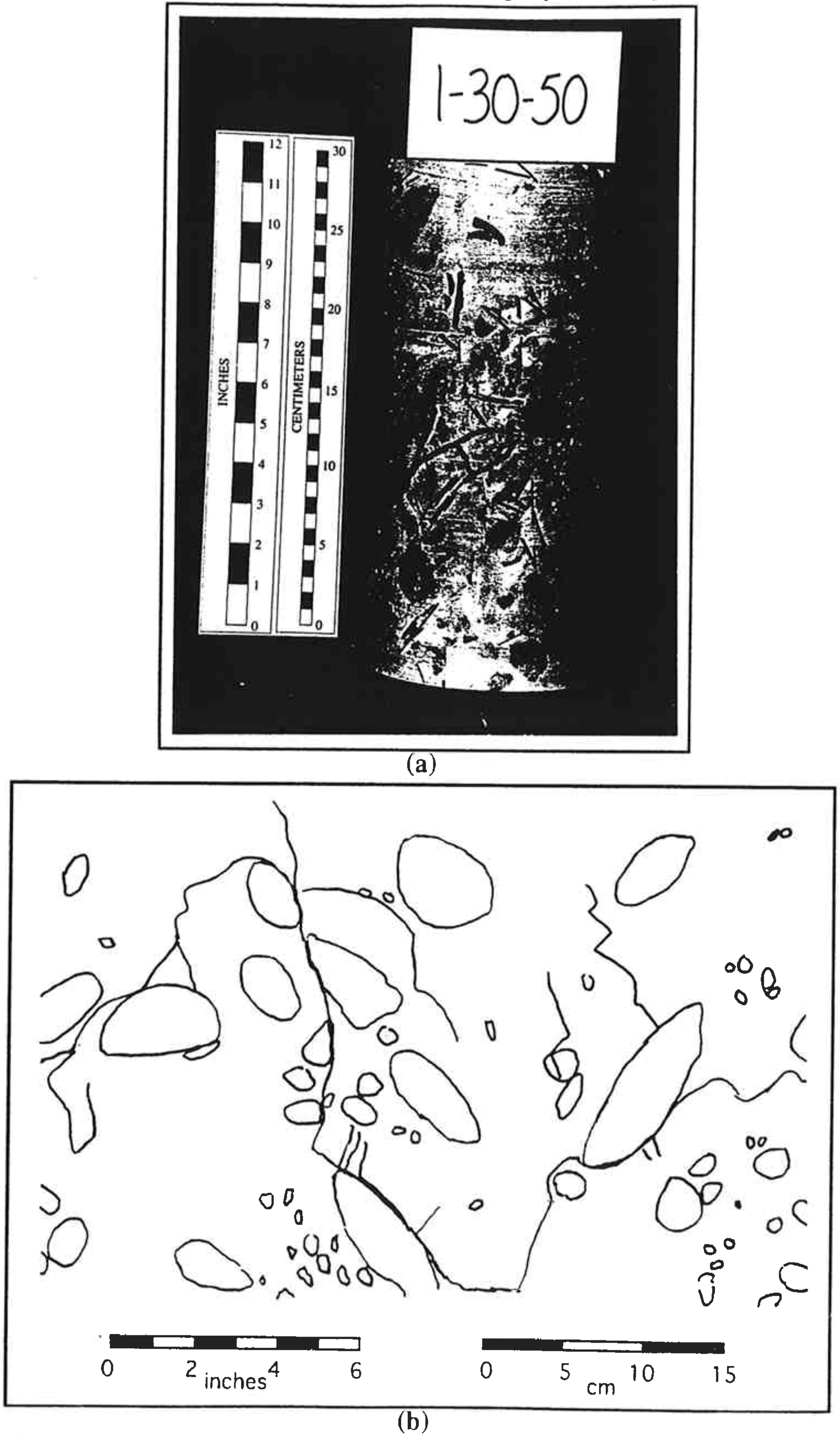

(a)

(b)

Figure D.14 (a) Photograph and **(b)** Tracing of Failed Specimen 1-30-50

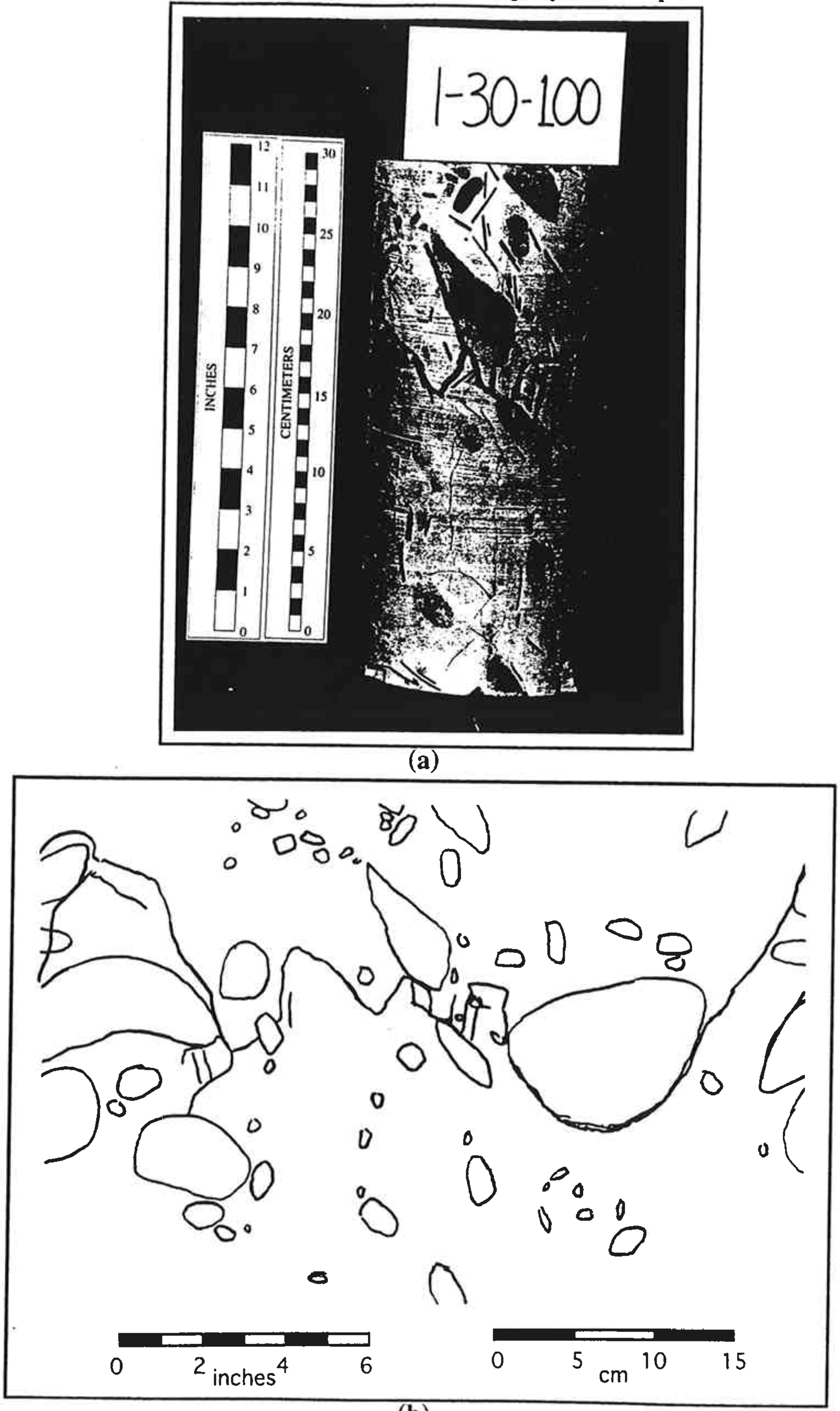

(a)

(b)

Figure D.15 (a) Photograph and **(b)** Tracing of Failed Specimen 1-30-100

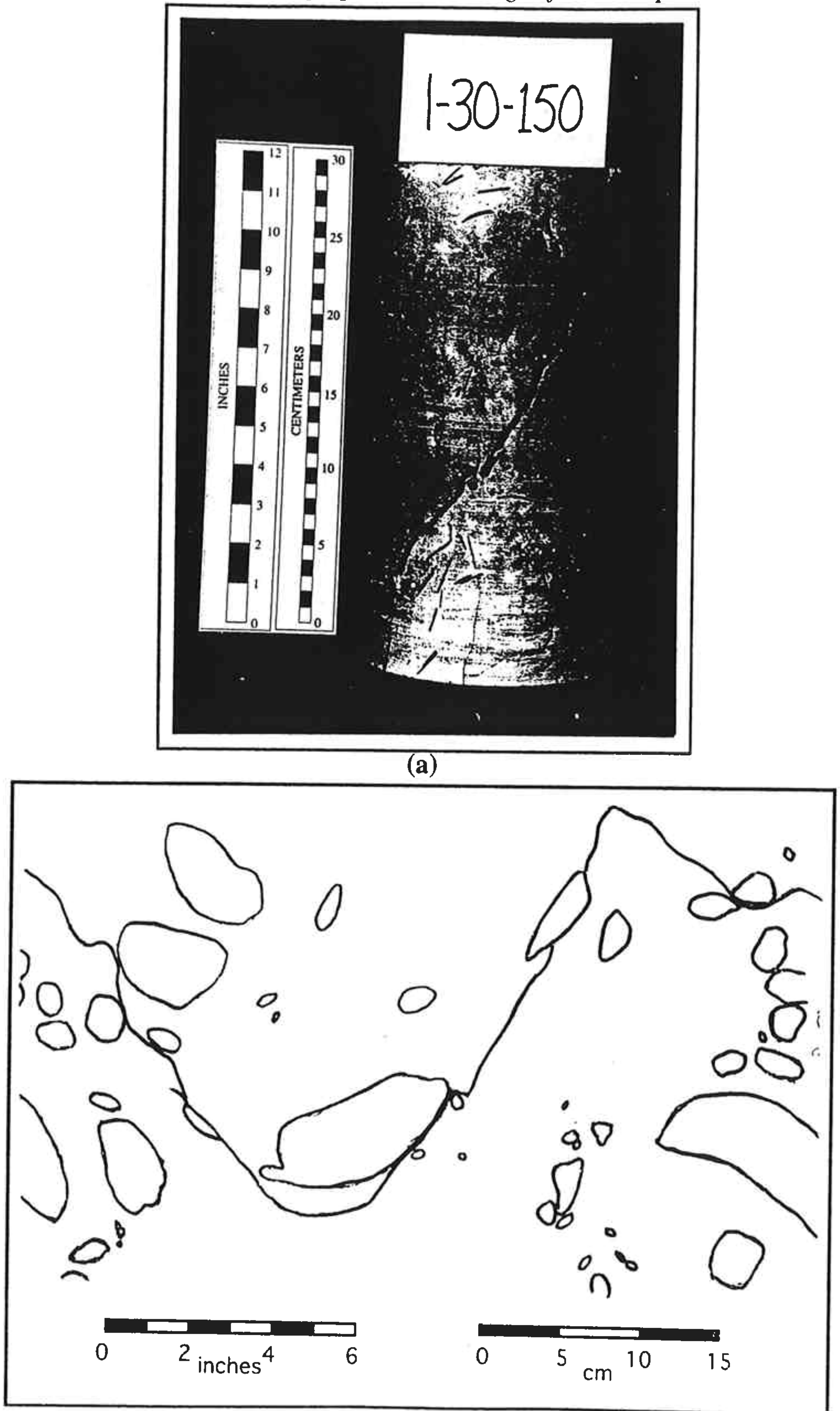

(a)

(b) courtesy of Ed Medley

Figure D.16 (a) Photograph and **(b)** Tracing of Failed Specimen 1-30-150

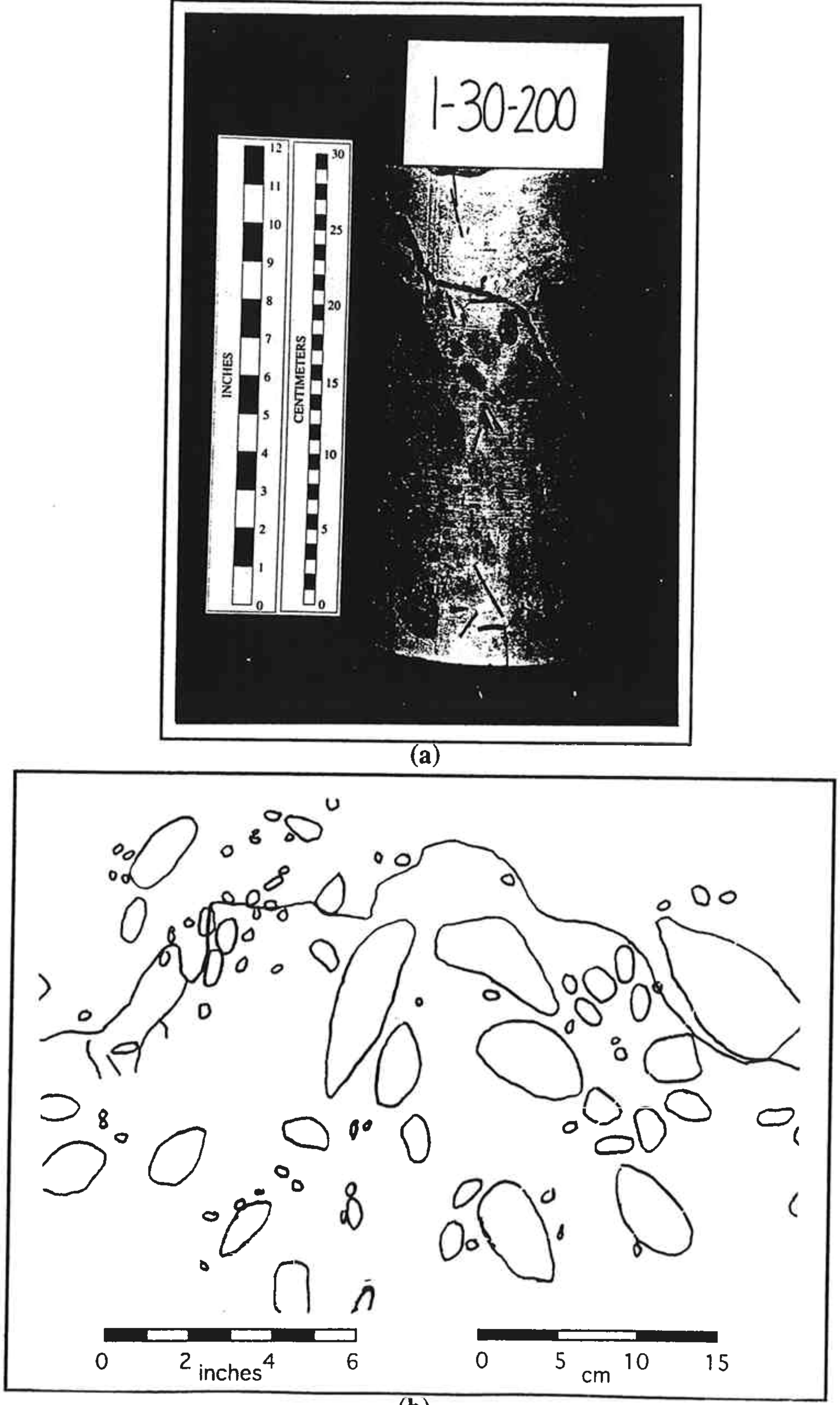

(a)

(b)

Figure D.17 (a) Photograph and **(b)** Tracing of Failed Specimen 1-30-200

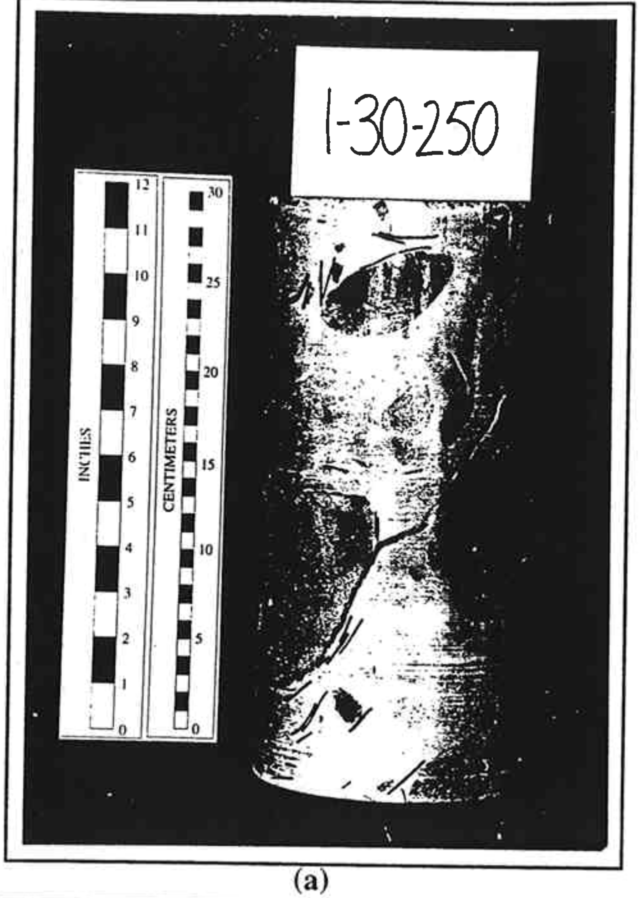

(a)

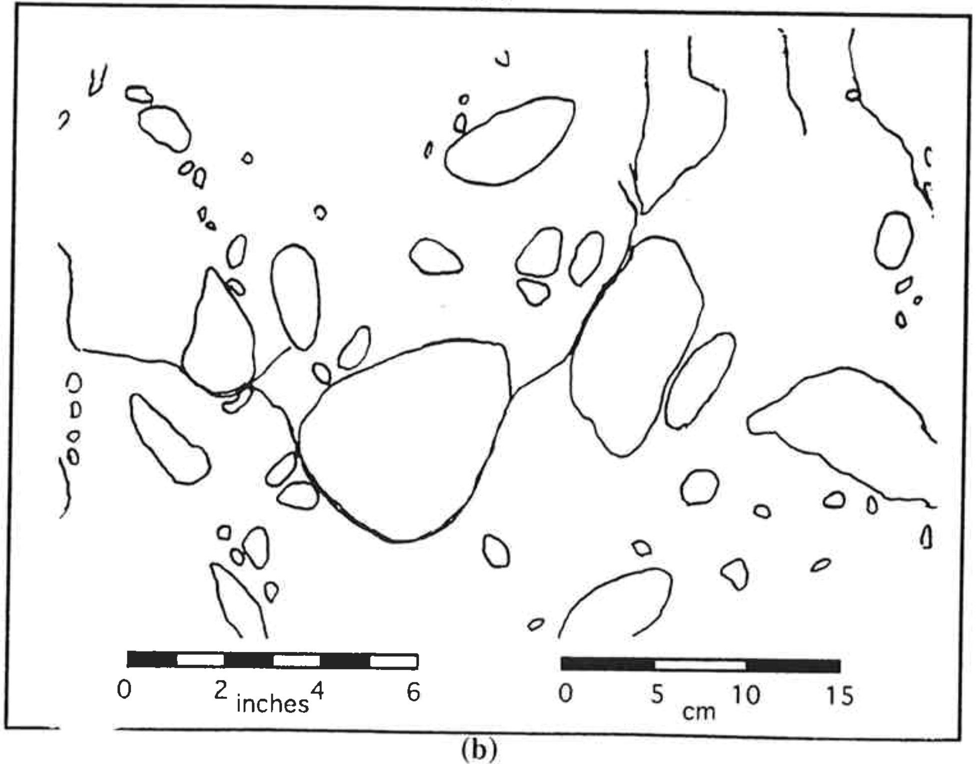

(b)

Figure D.18 (a) Photograph and (b) Tracing of Failed Specimen 1-30-250

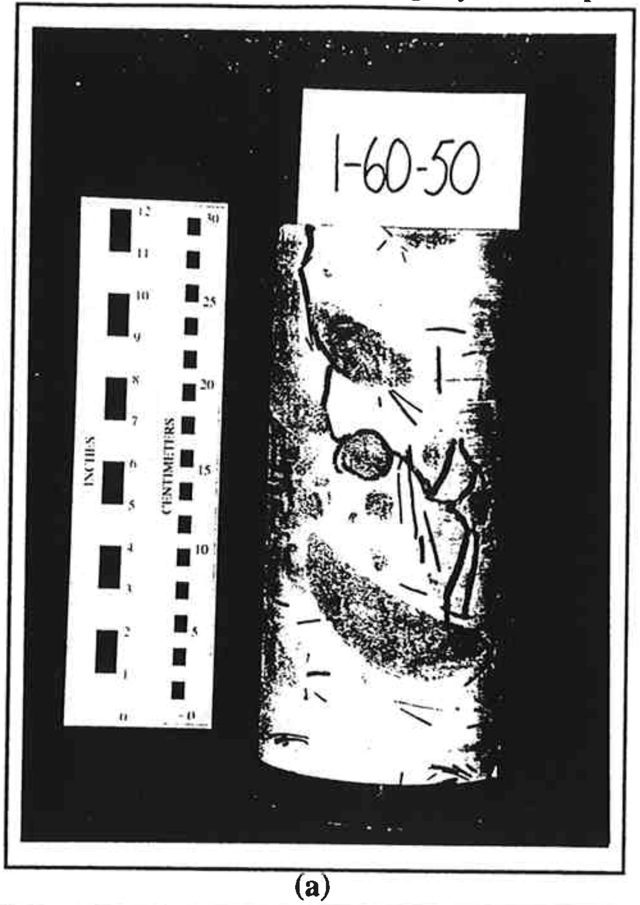

(a)

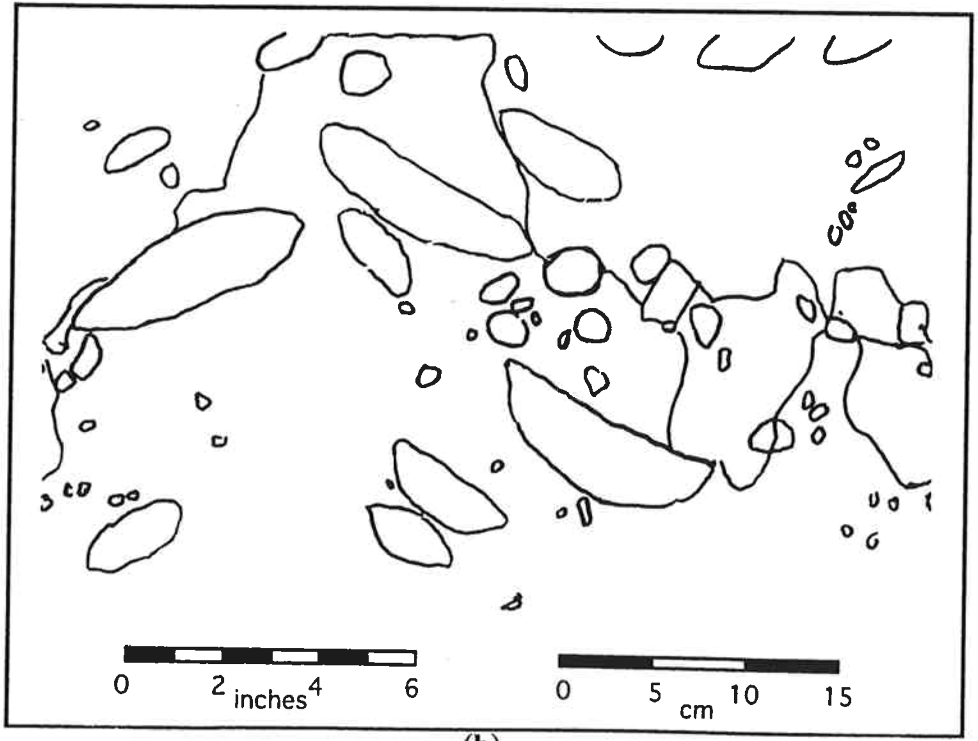

(b)

Figure D.19 (a) Photograph and (b) Tracing of Failed Specimen 1-60-50

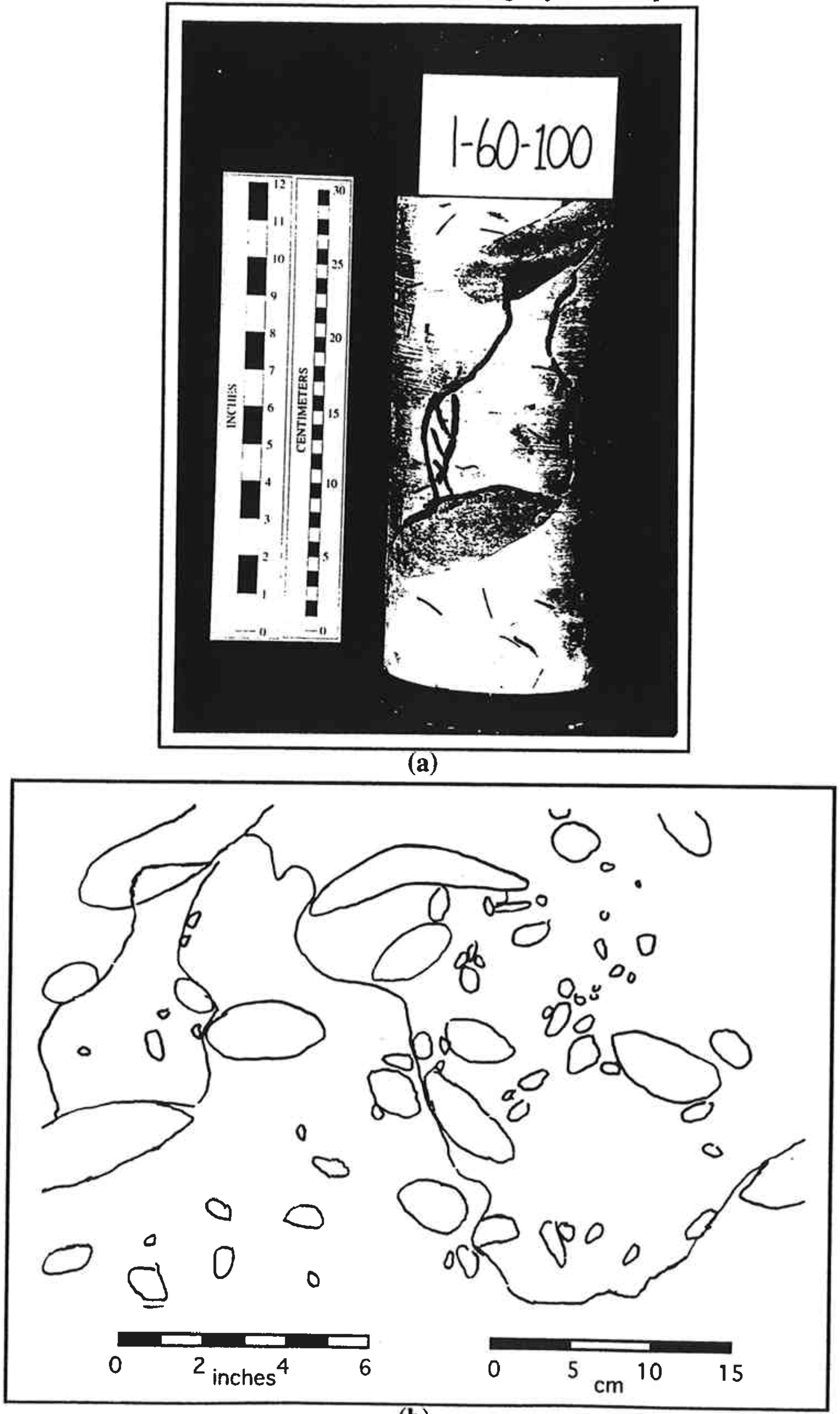

(a)

(b)

Figure D.20 (a) Photograph and **(b)** Tracing of Failed Specimen 1-60-100

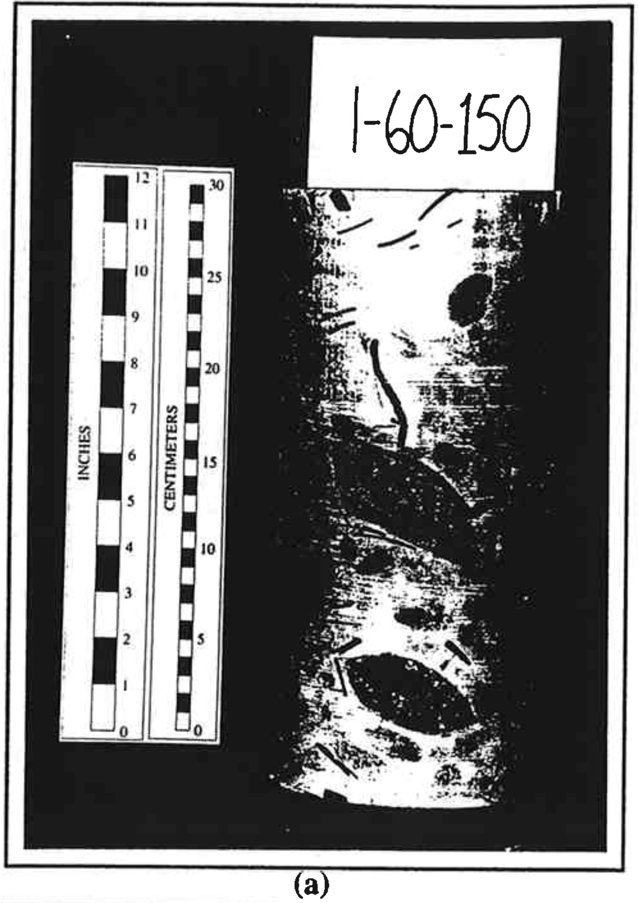

(a)

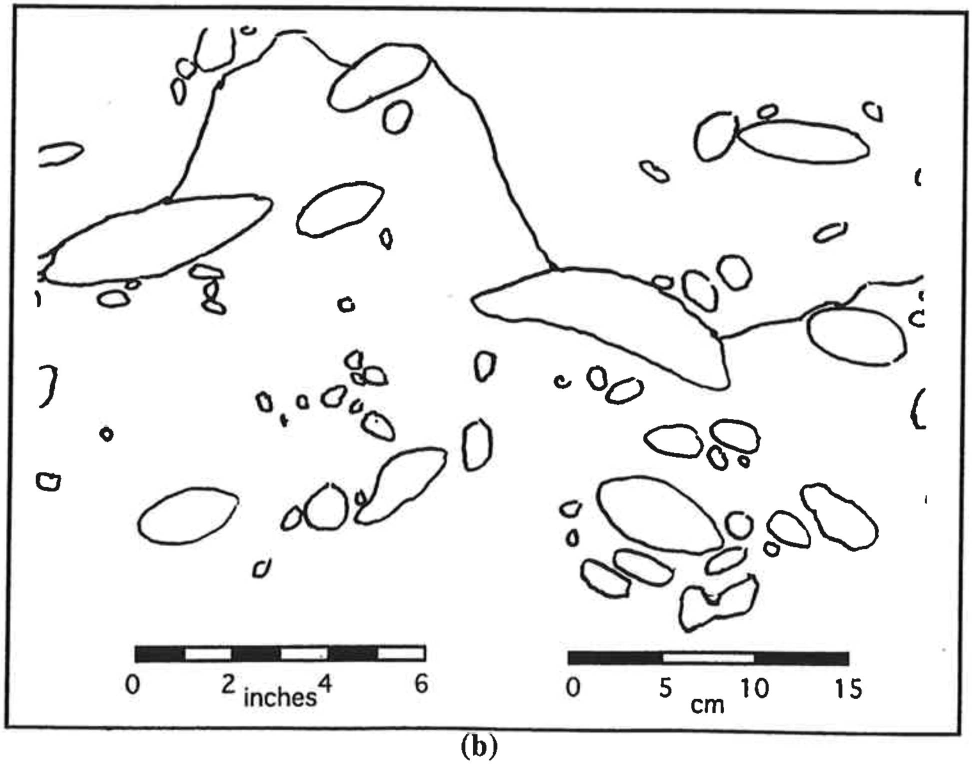

(b)

Figure D.21 (a) Photograph and **(b)** Tracing of Failed Specimen 1-60-150

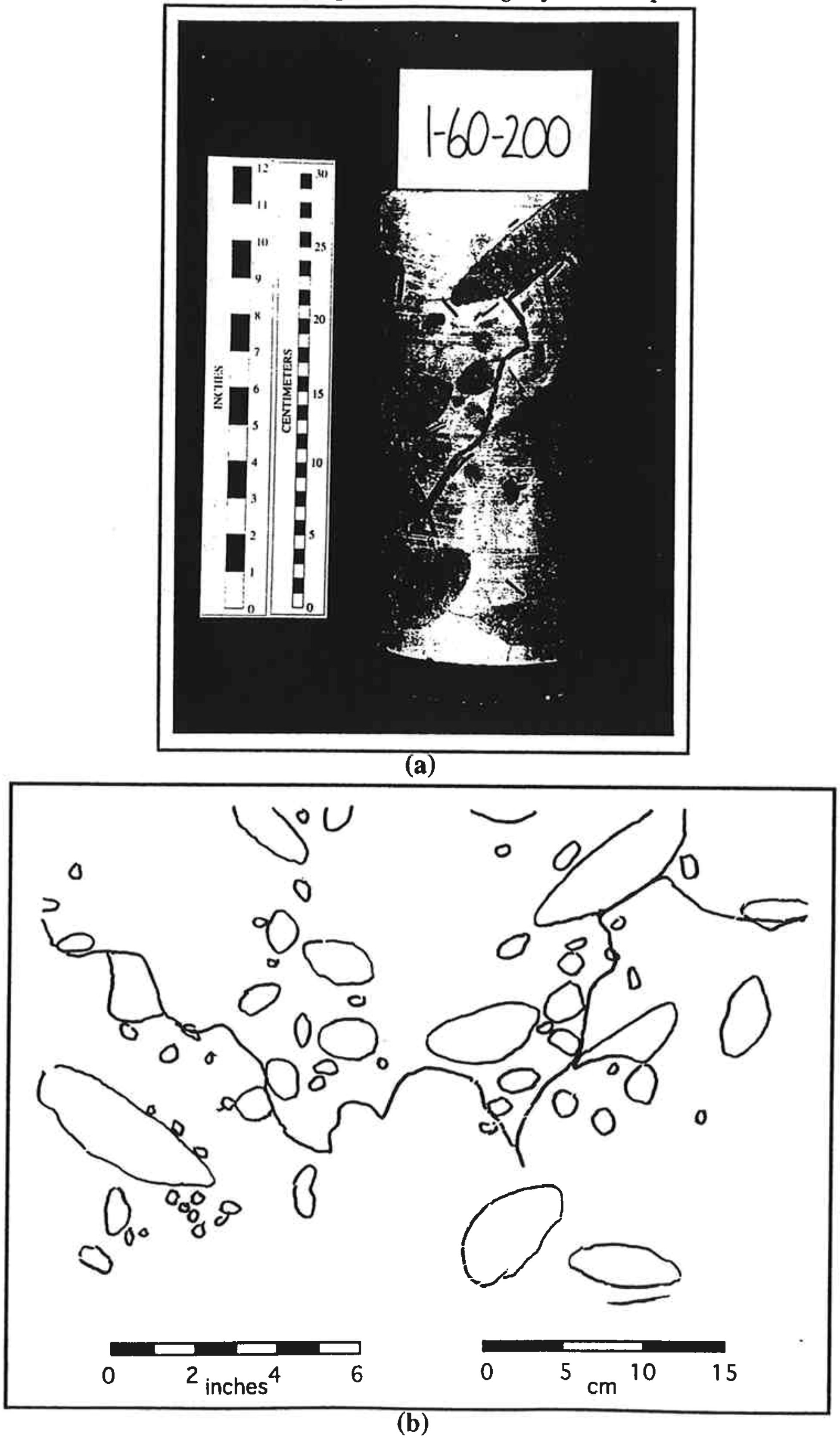

(a)

(b)

Figure D.22 **(a)** Photograph and **(b)** Tracing of Failed Specimen 1-60-200

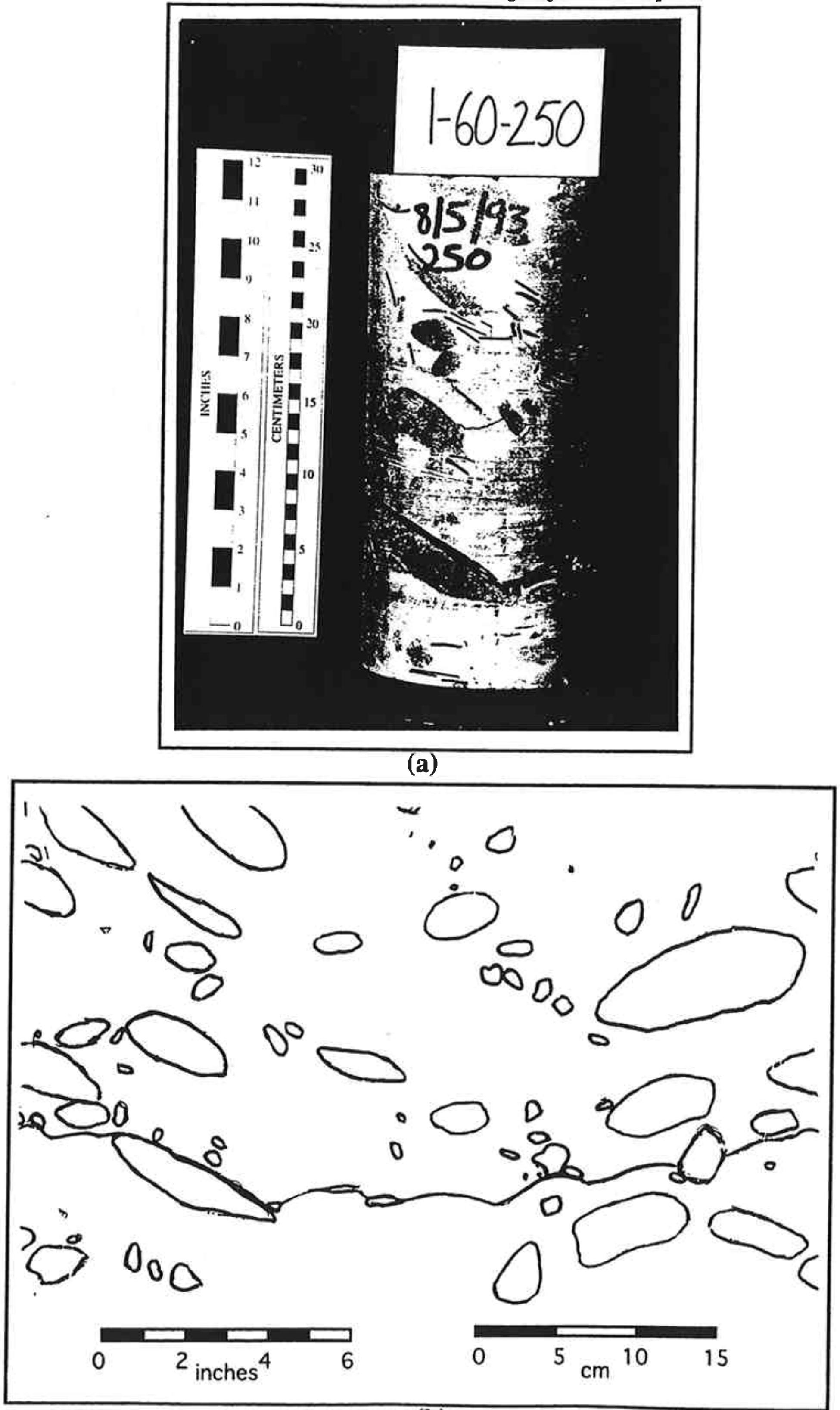

(a)

(b) courtesy of Ed Medley

Figure D.23 **(a)** Photograph and **(b)** Tracing of Failed Specimen 1-60-250

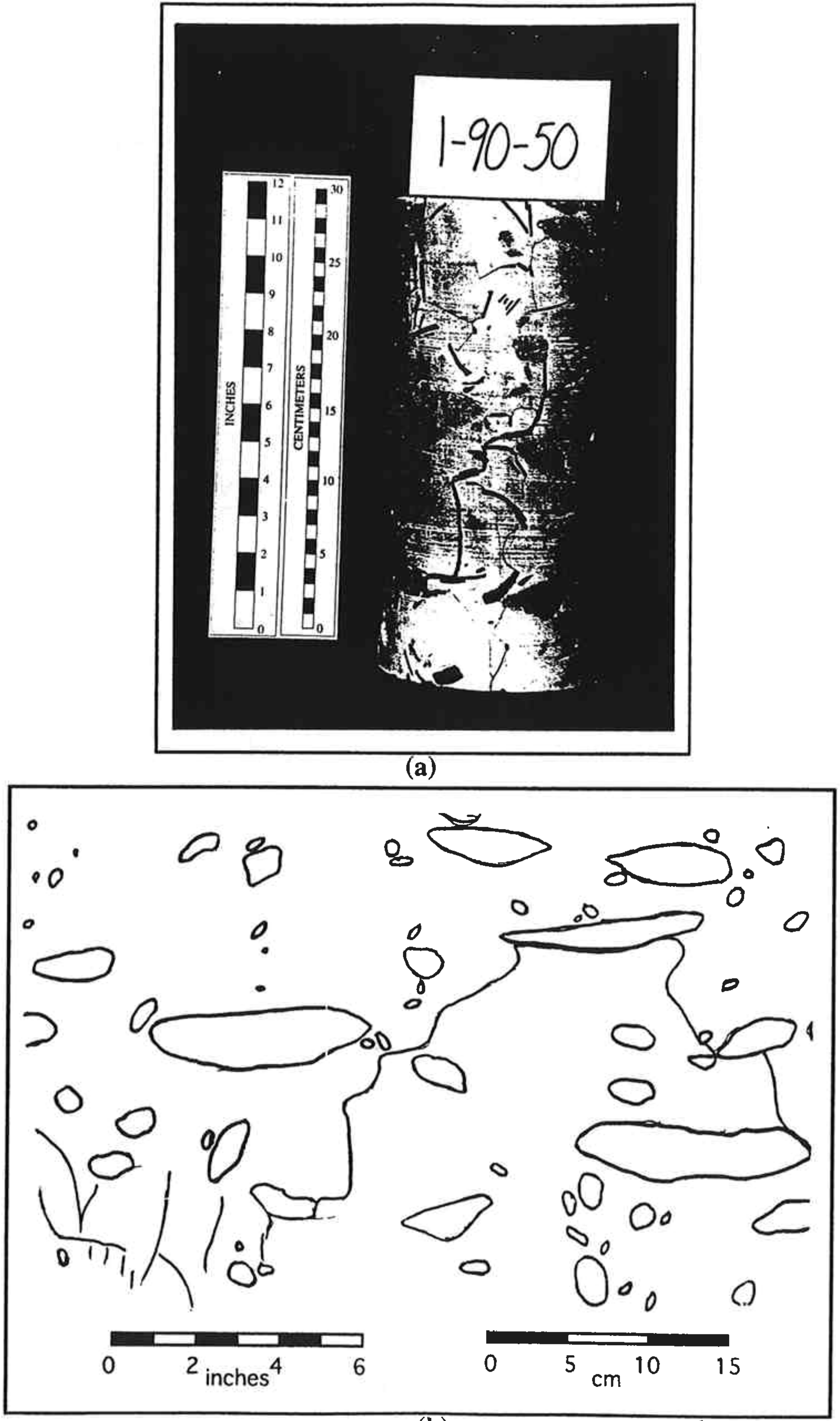

(a)

(b) courtesy of Ed Medley

Figure D.24 (a) Photograph and **(b)** Tracing of Failed Specimen 1-90-50

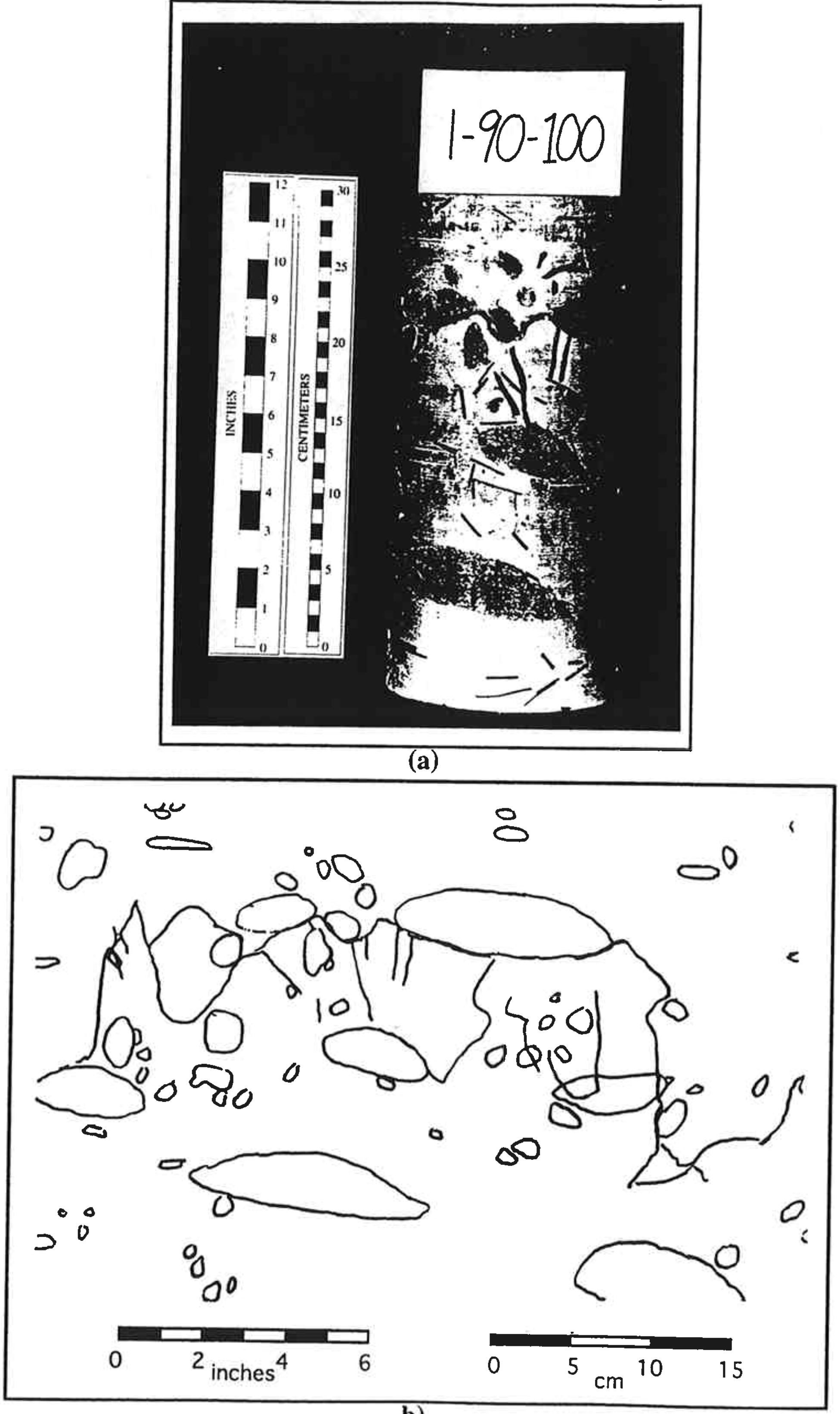

Figure D.25 **(a)** Photograph and **(b)** Tracing of Failed Specimen 1-90-100

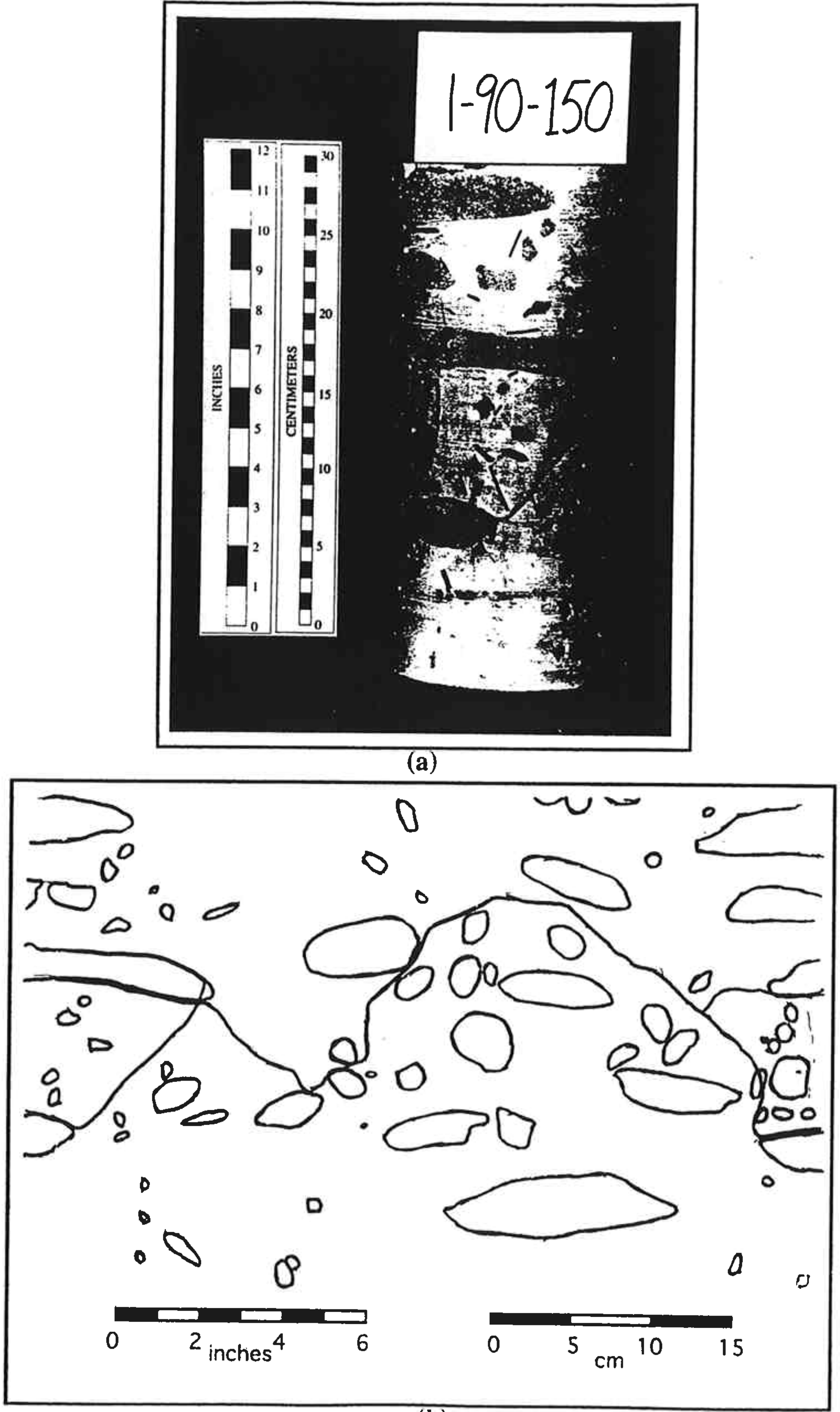

(a)

(b) courtesy of Ed Medley

Figure D.26 (**a**) Photograph and (**b**) Tracing of Failed Specimen 1-90-150

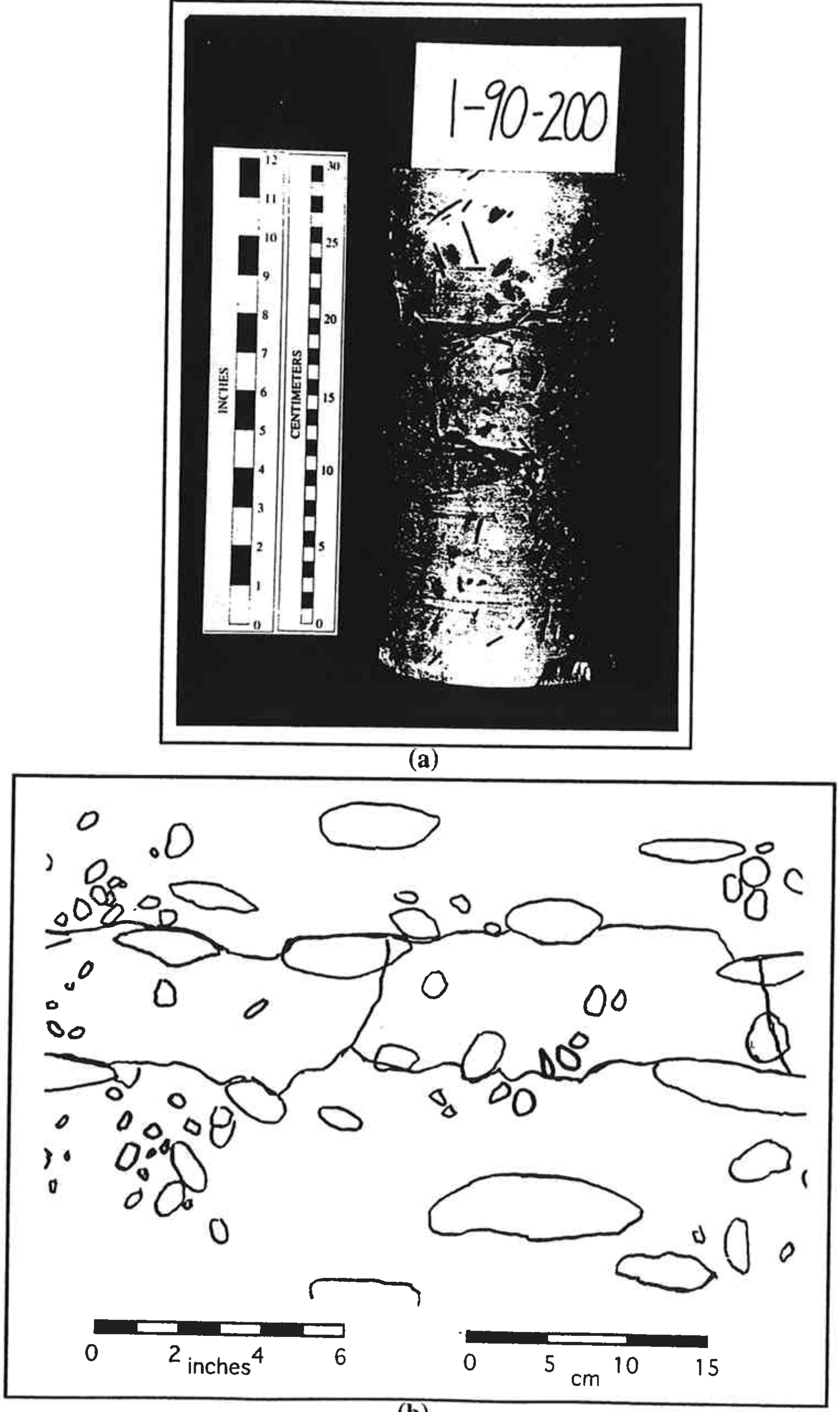

(a)

(b)

Figure D.27 (a) Photograph and **(b)** Tracing of Failed Specimen 1-90-200

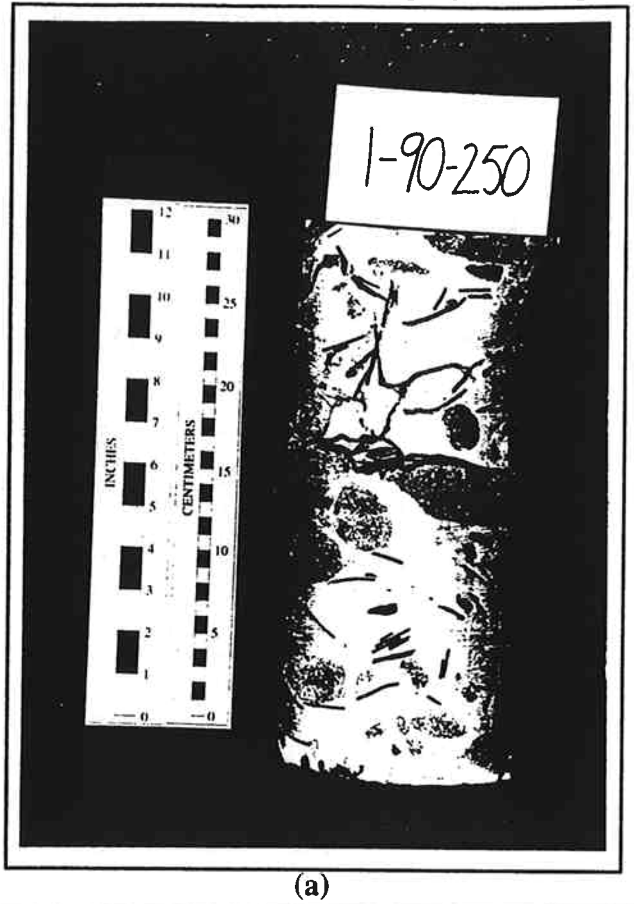

(a)

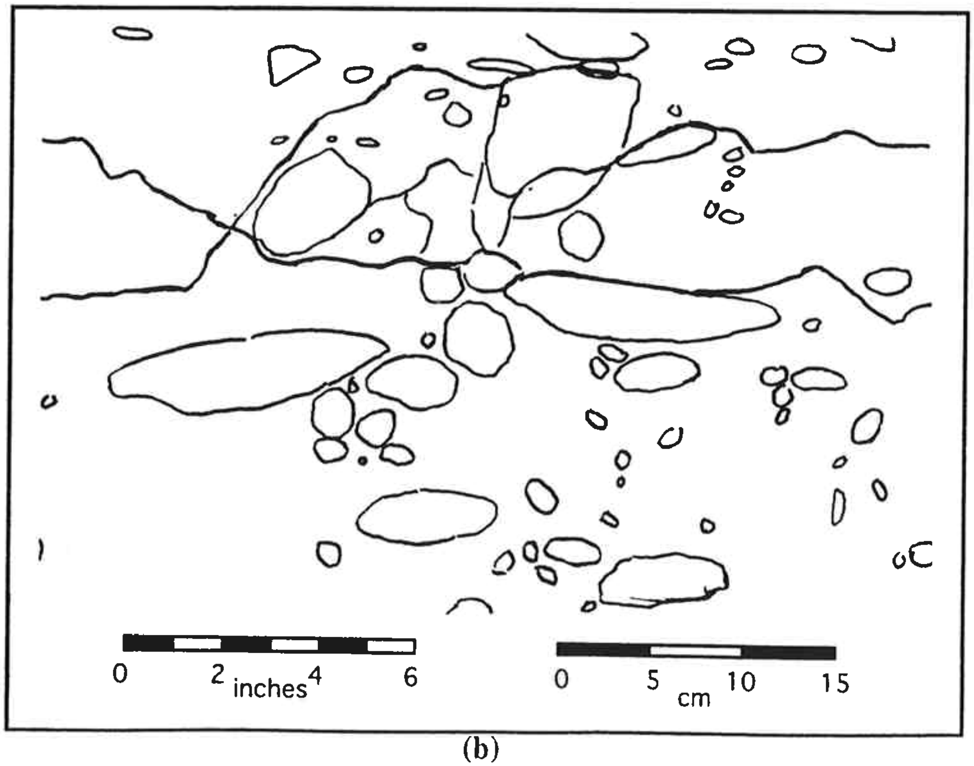

(b)

Figure D.28 (a) Photograph and **(b)** Tracing of Failed Specimen 1-90-250

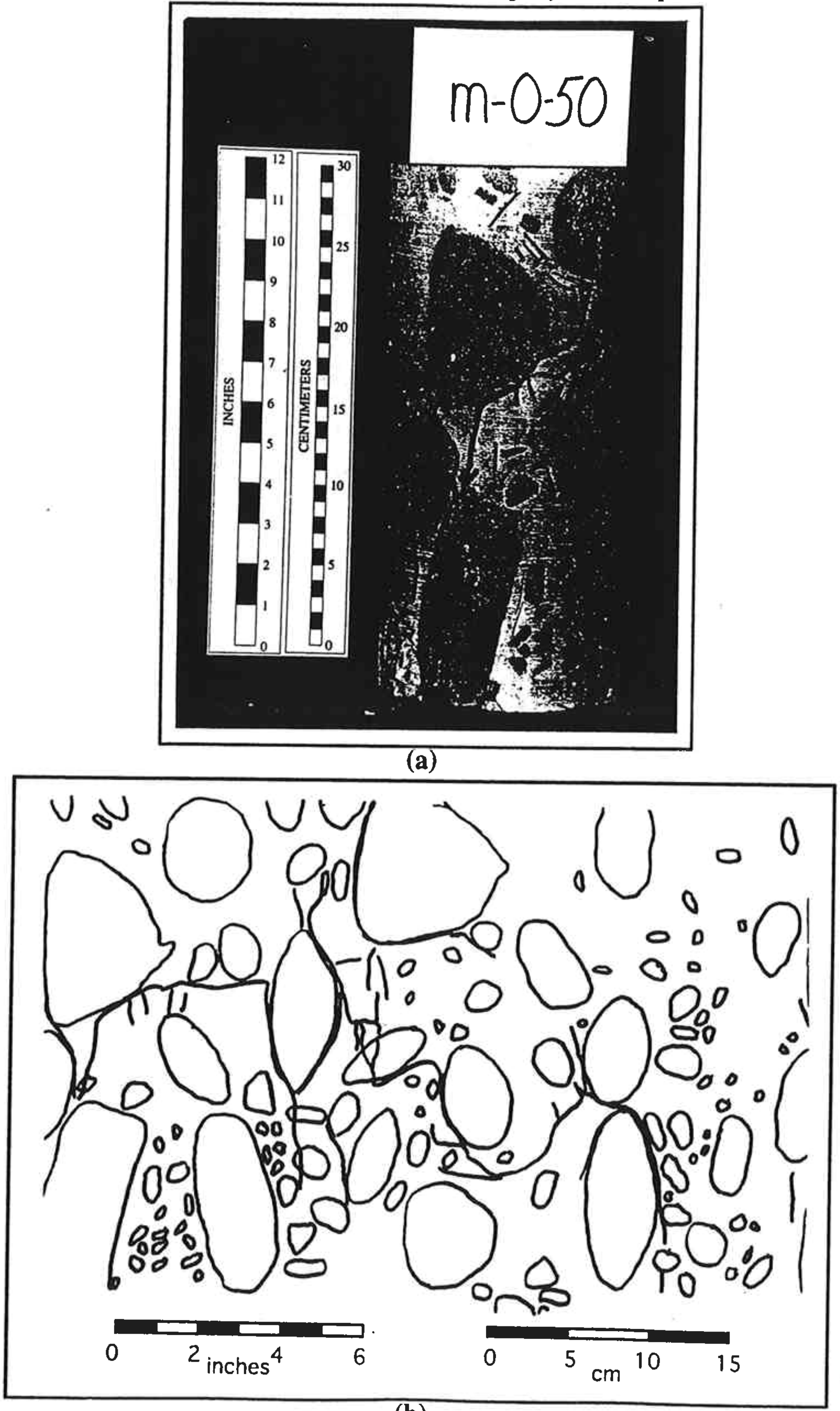

(a)

(b)

Figure D.29 (a) Photograph and **(b)** Tracing of Failed Specimen m-0-50

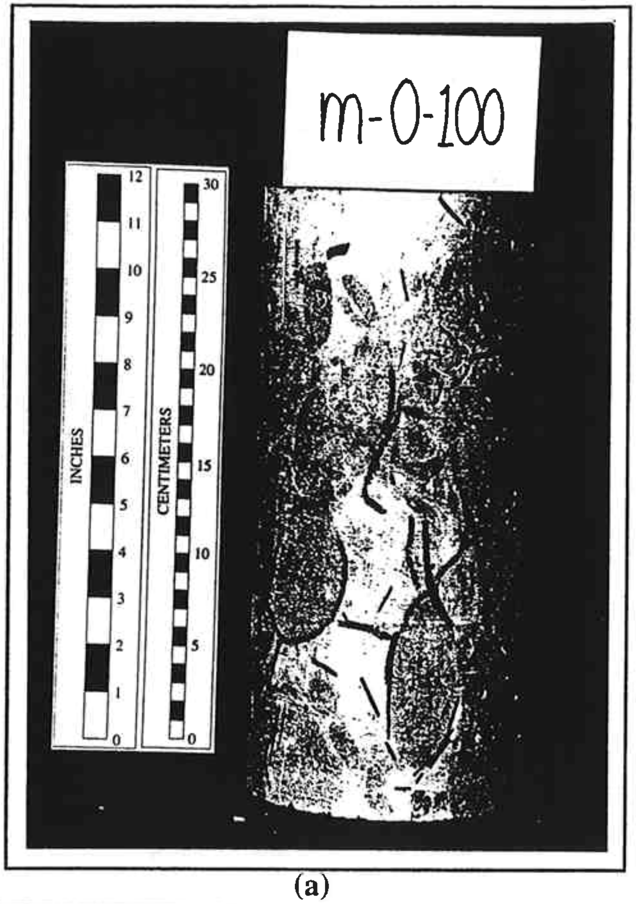

(a)

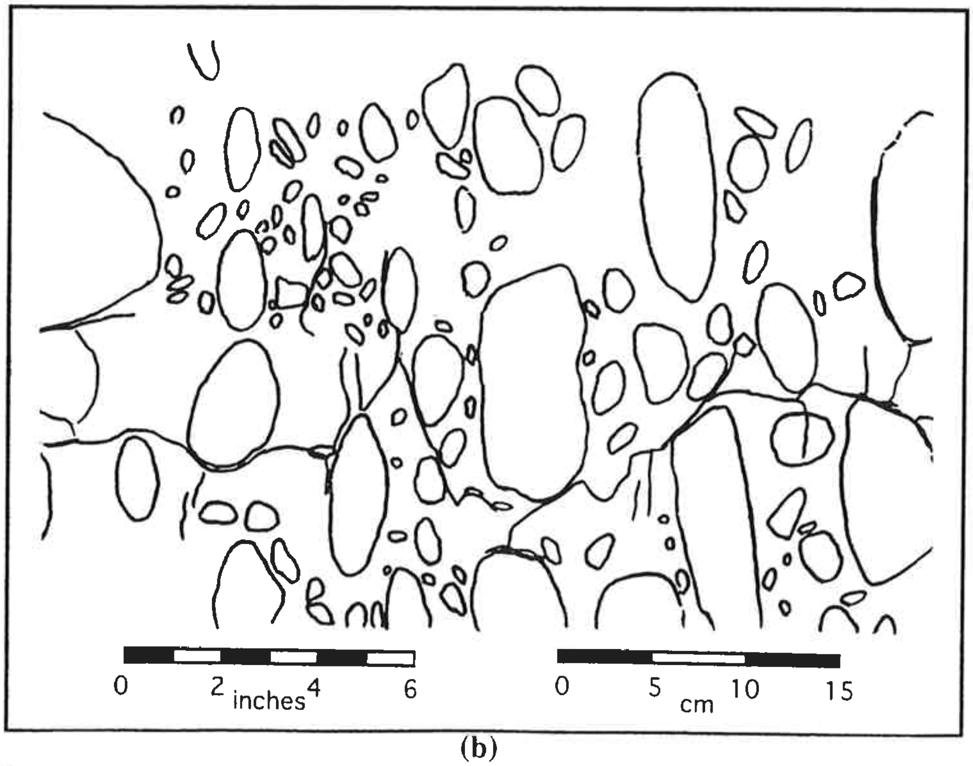

(b)

Figure D.30 **(a)** Photograph and **(b)** Tracing of Failed Specimen m-0-100

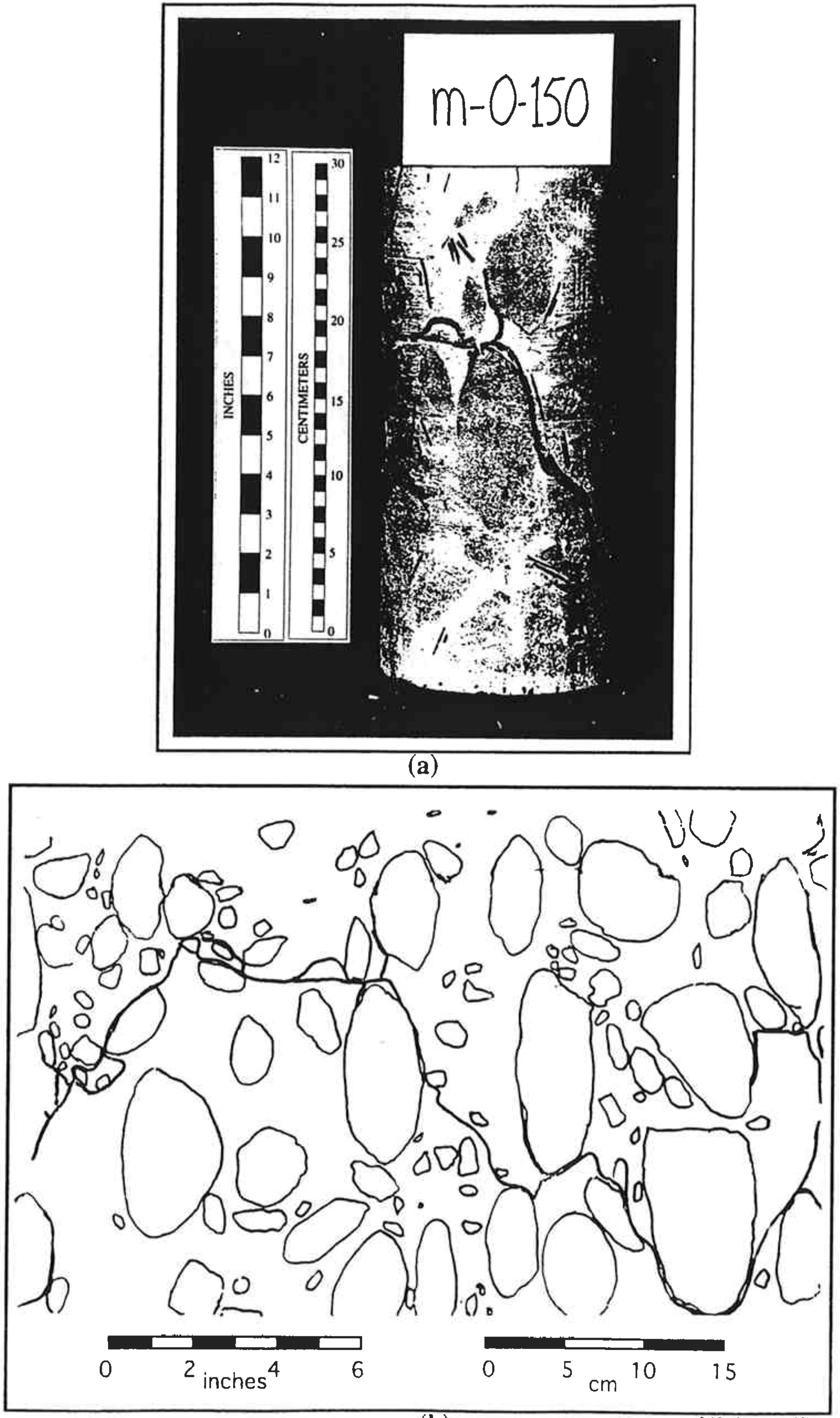

(a)

(b)

courtesy of Ed Medley

Figure D.31 (a) Photograph and (b) Tracing of Failed Specimen m-0-150

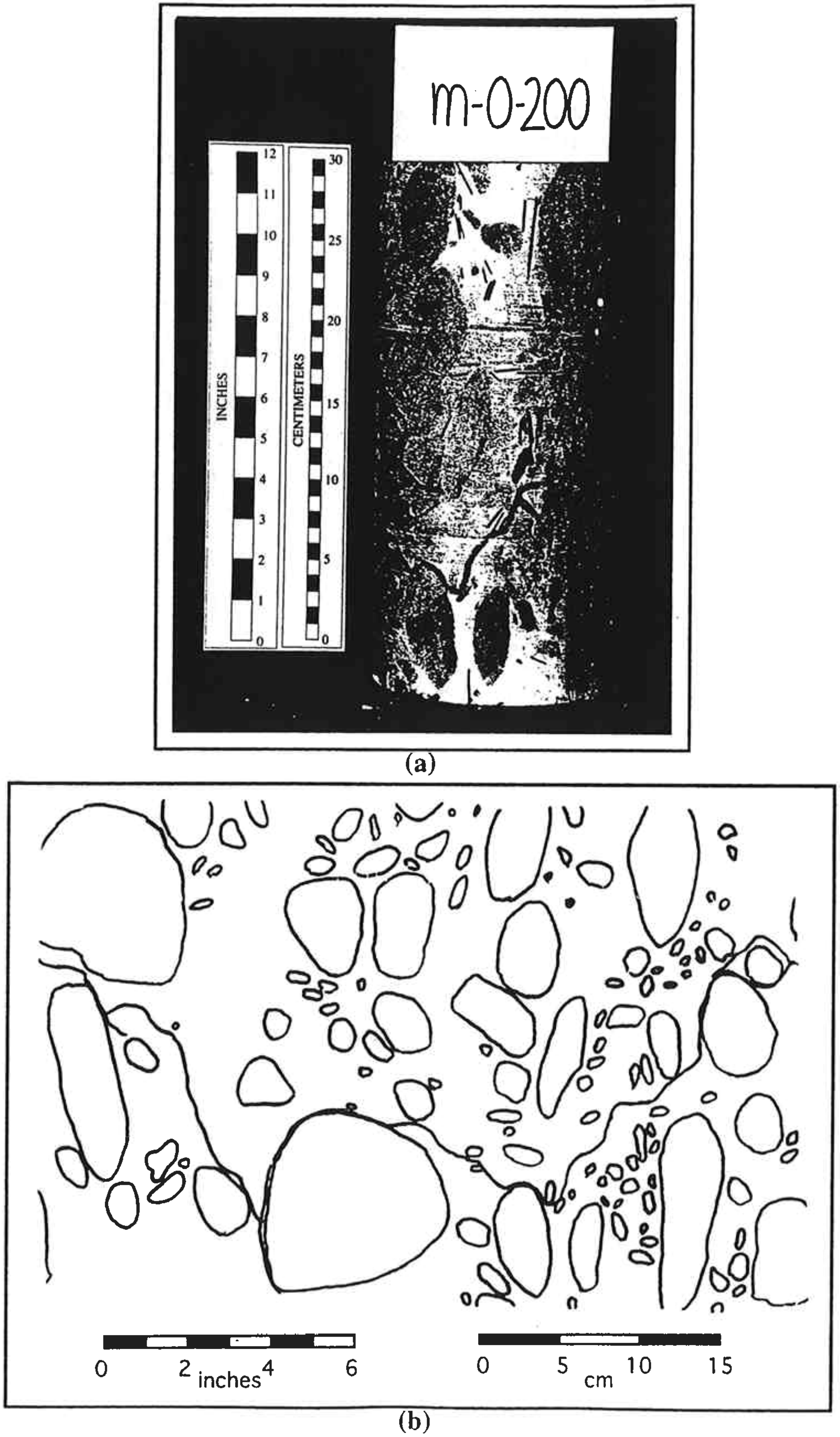

(a)

(b)

Figure D.32 (a) Photograph and **(b)** Tracing of Failed Specimen m-0-200

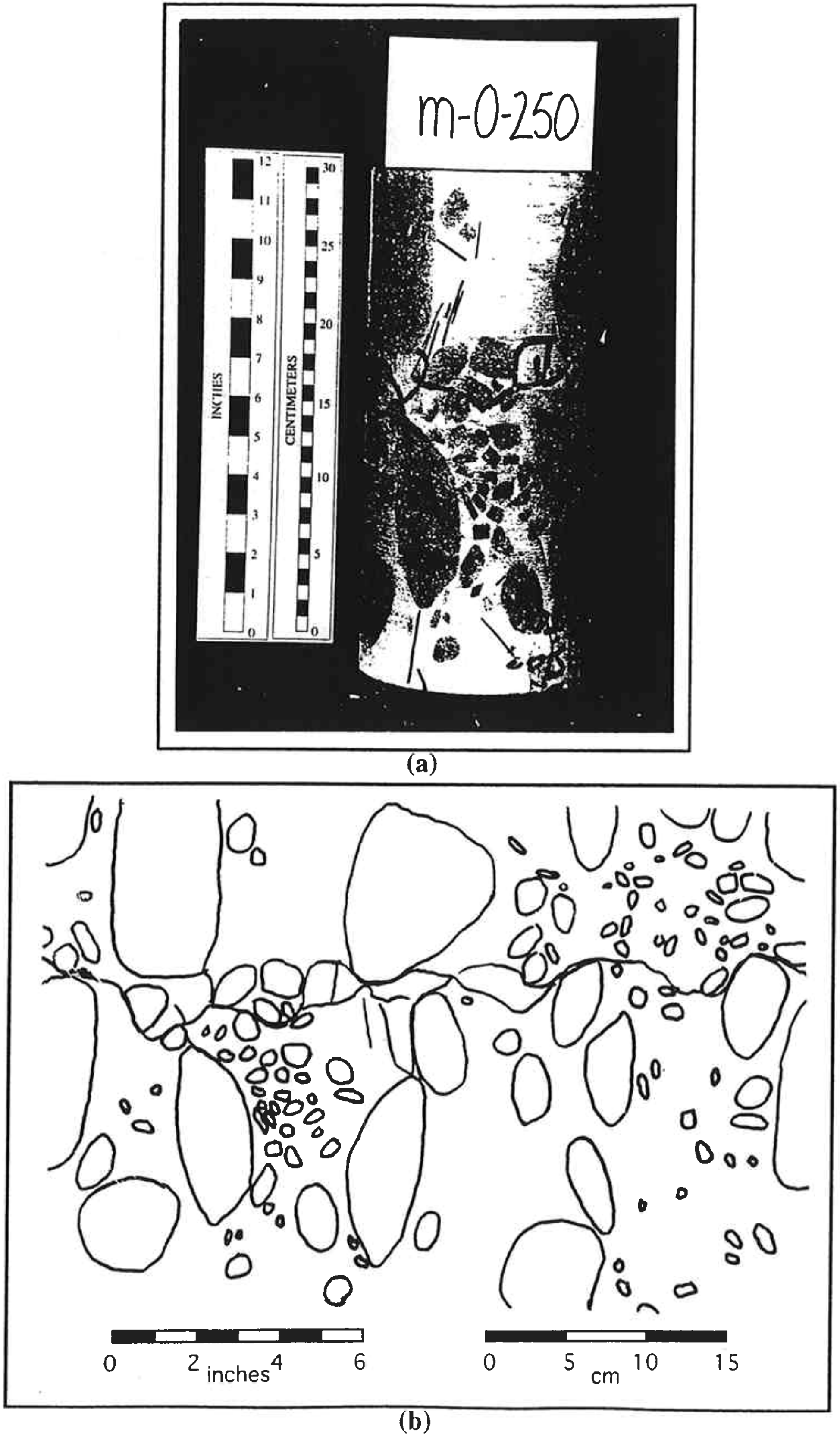

(a)

(b)

Figure D.33 (a) Photograph and **(b)** Tracing of Failed Specimen m-0-250

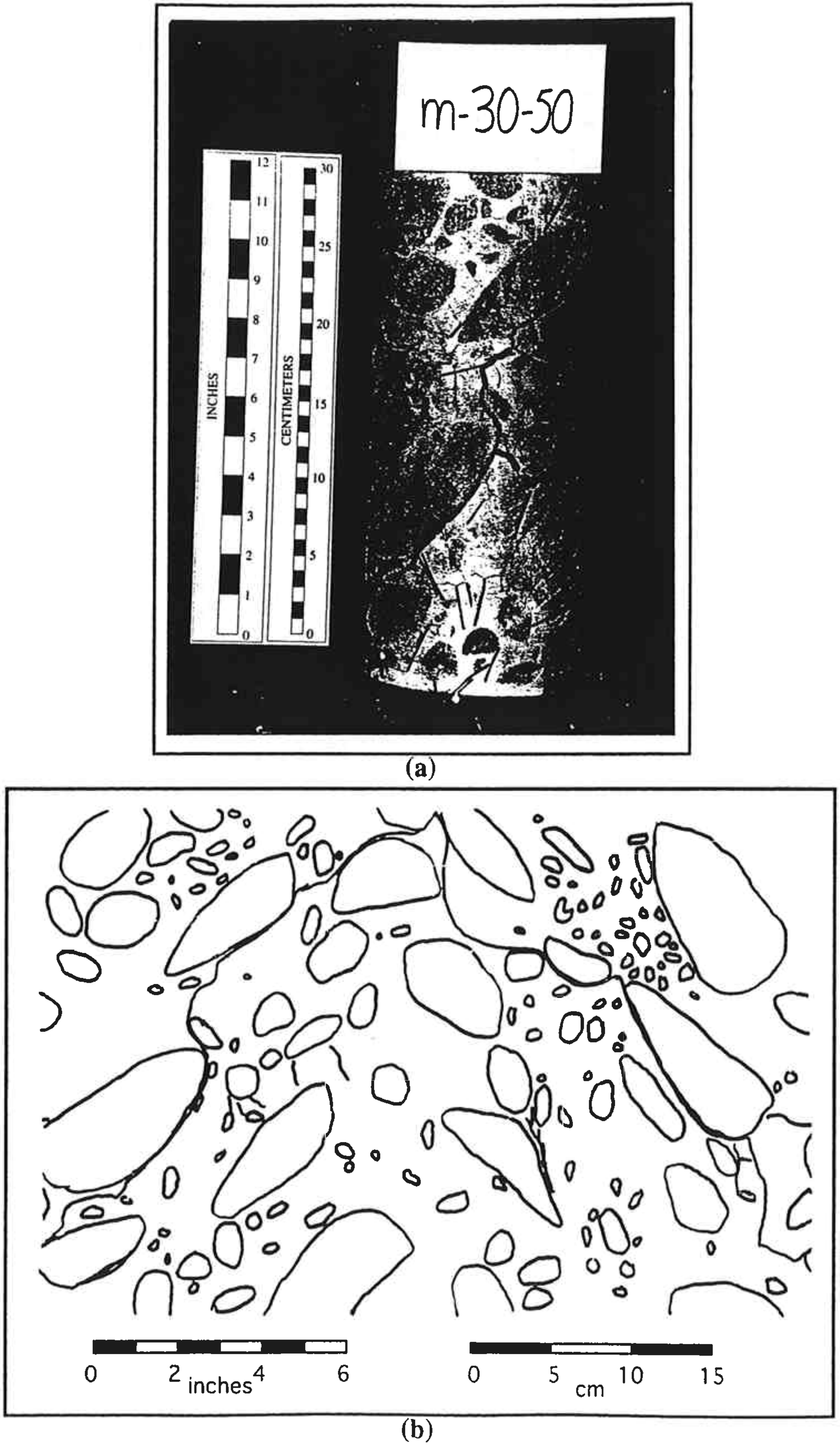

(a)

(b)

Figure D.34 (a) Photograph and **(b)** Tracing of Failed Specimen m-30-50

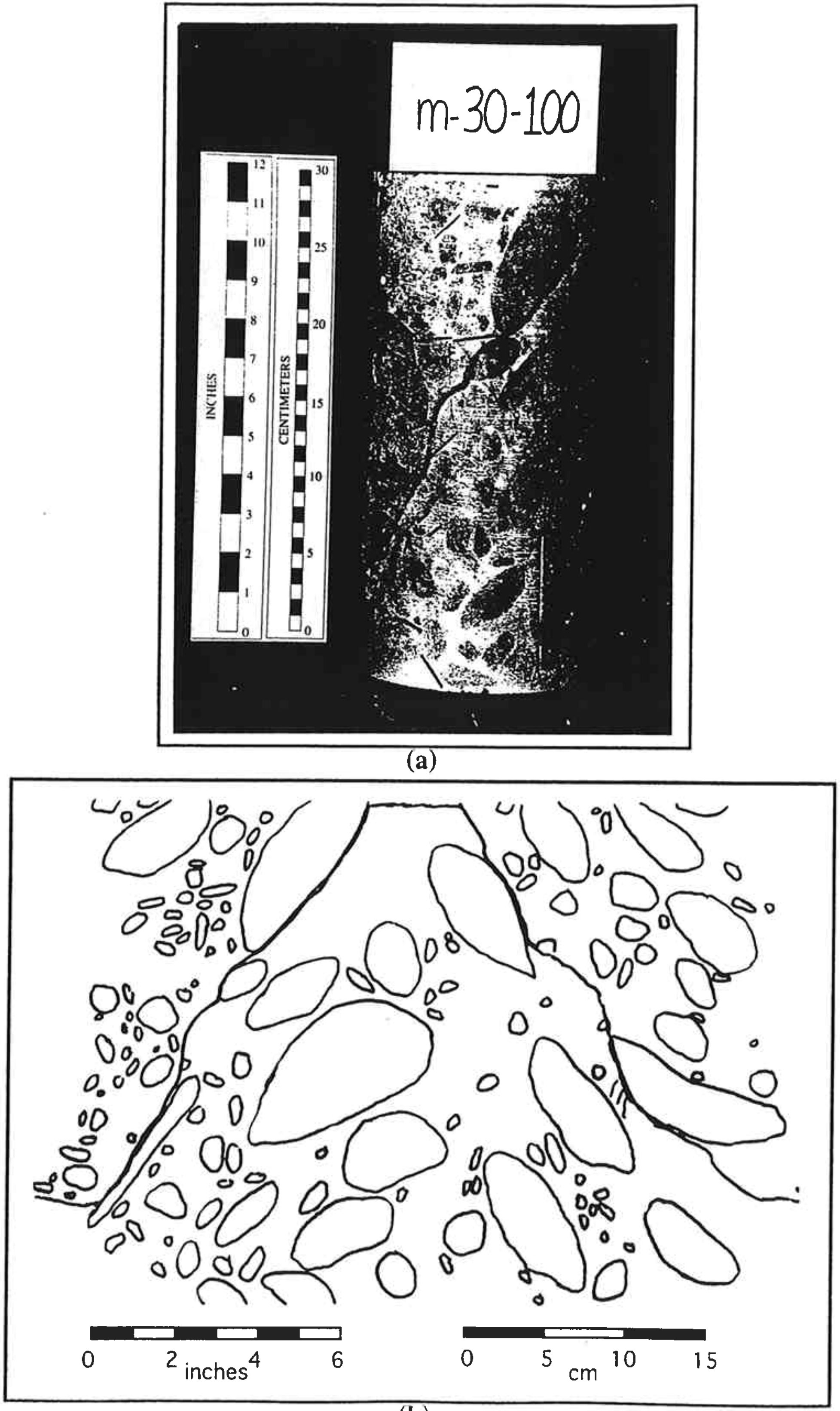

(a)

(b)

Figure D.35 **(a)** Photograph and **(b)** Tracing of Failed Specimen m-30-100

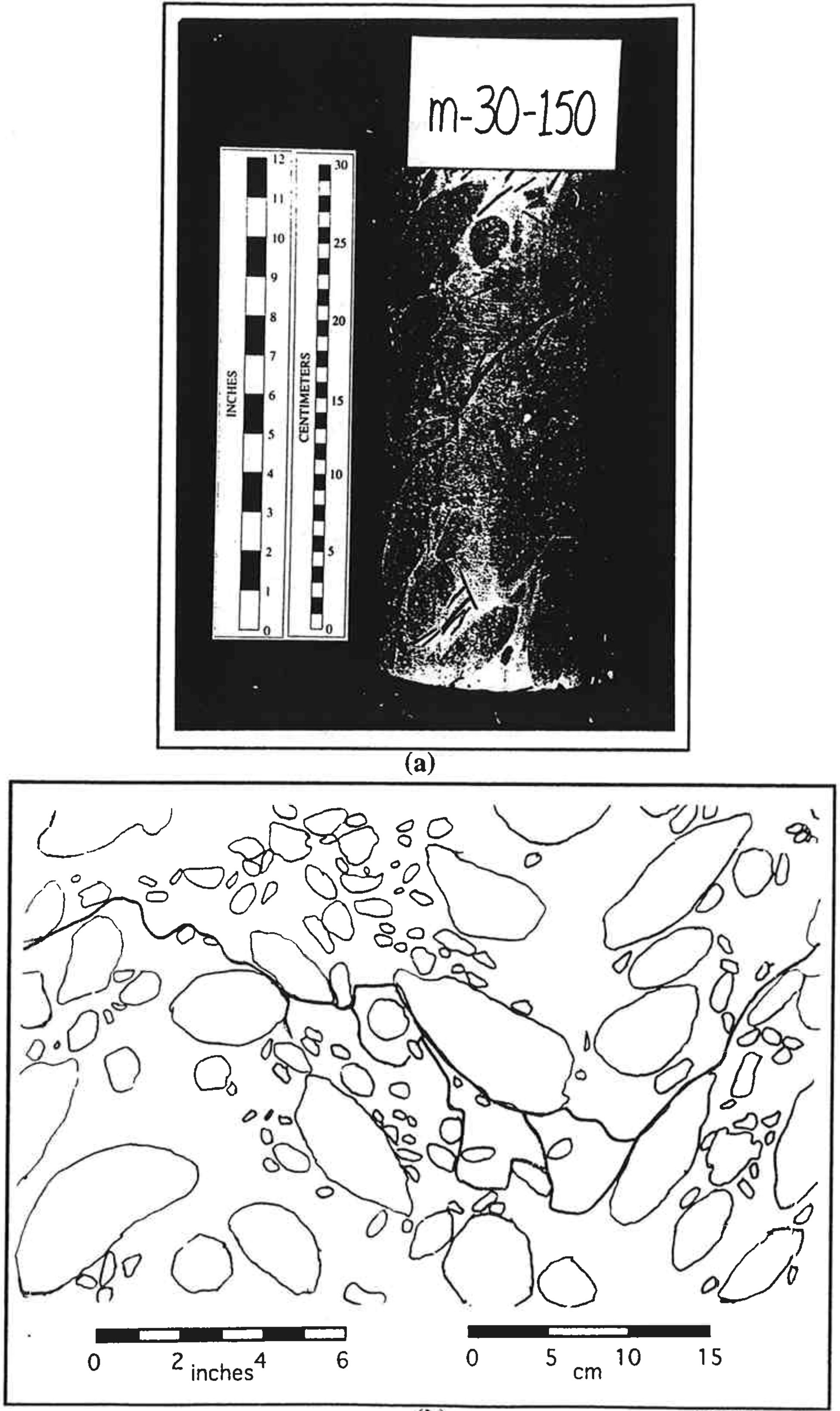

(a)

(b)

courtesy of Ed Medley

Figure D.36 (a) Photograph and **(b)** Tracing of Failed Specimen m-30-150

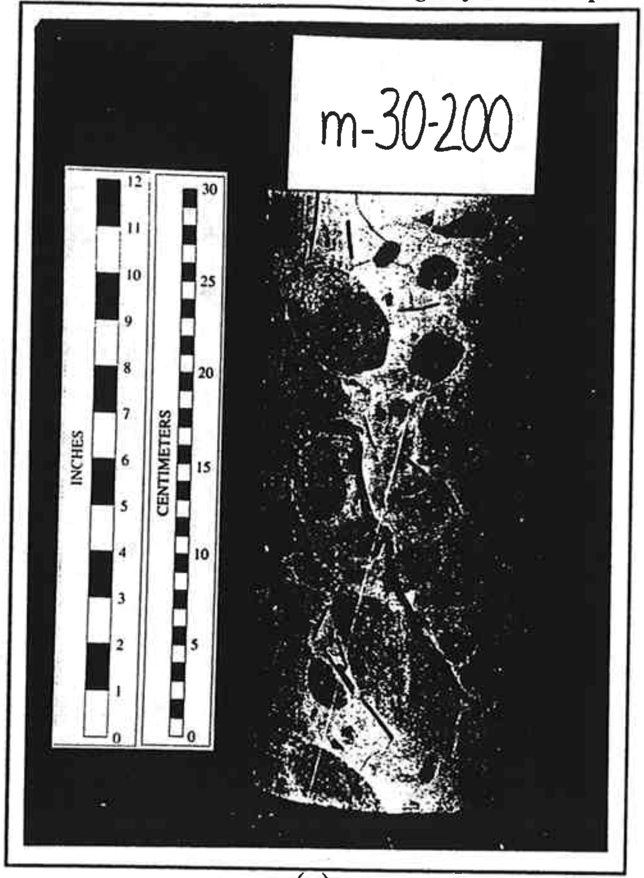

(a)

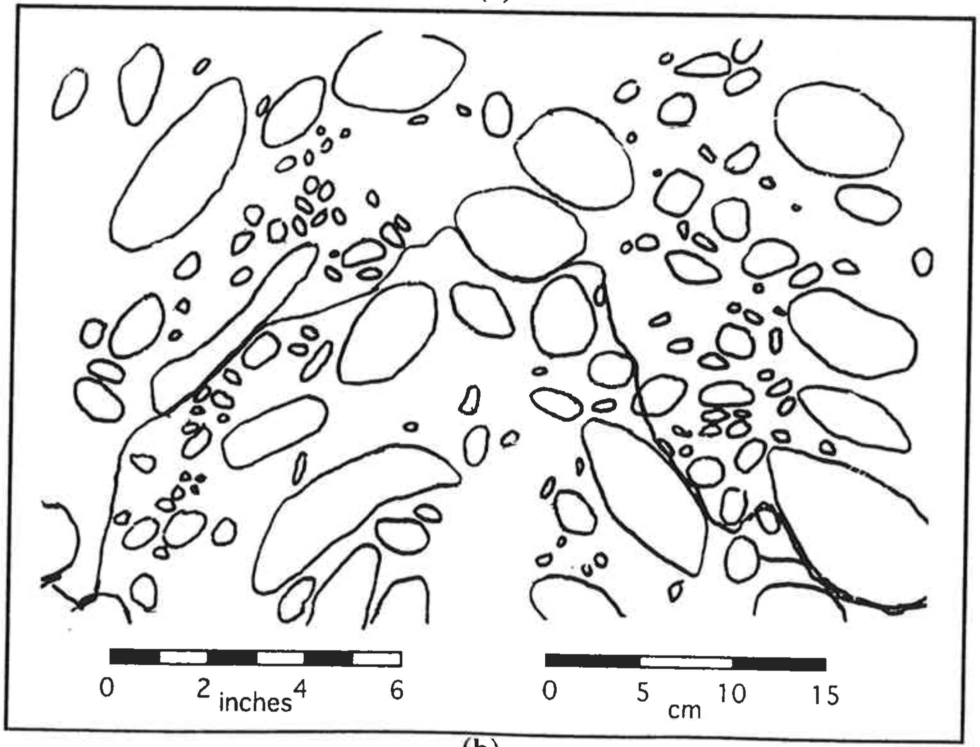

(b)

Figure D.37 (a) Photograph and **(b)** Tracing of Failed Specimen m-30-200

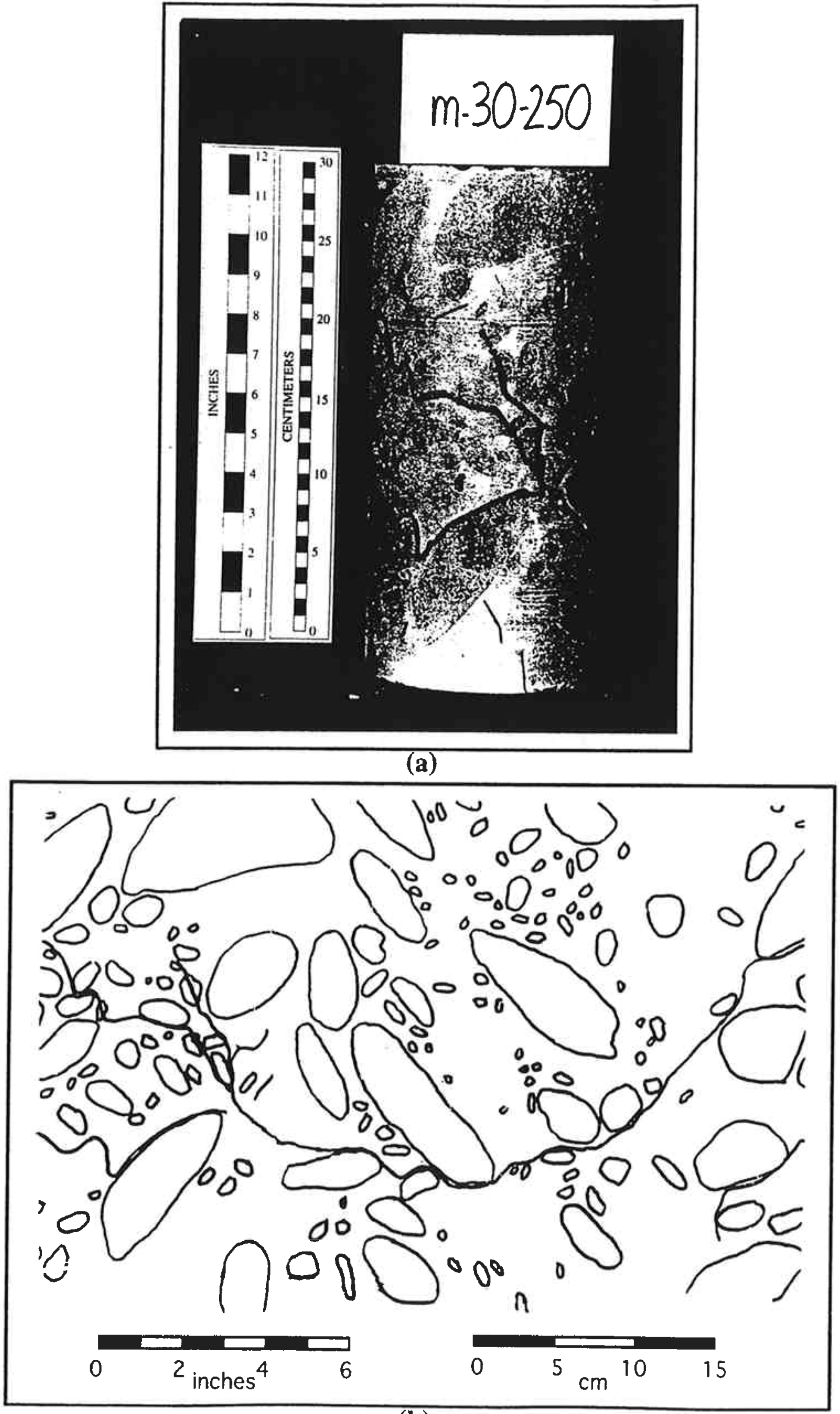

(a)

(b)

Figure D.38 (a) Photograph and (b) Tracing of Failed Specimen m-30-250

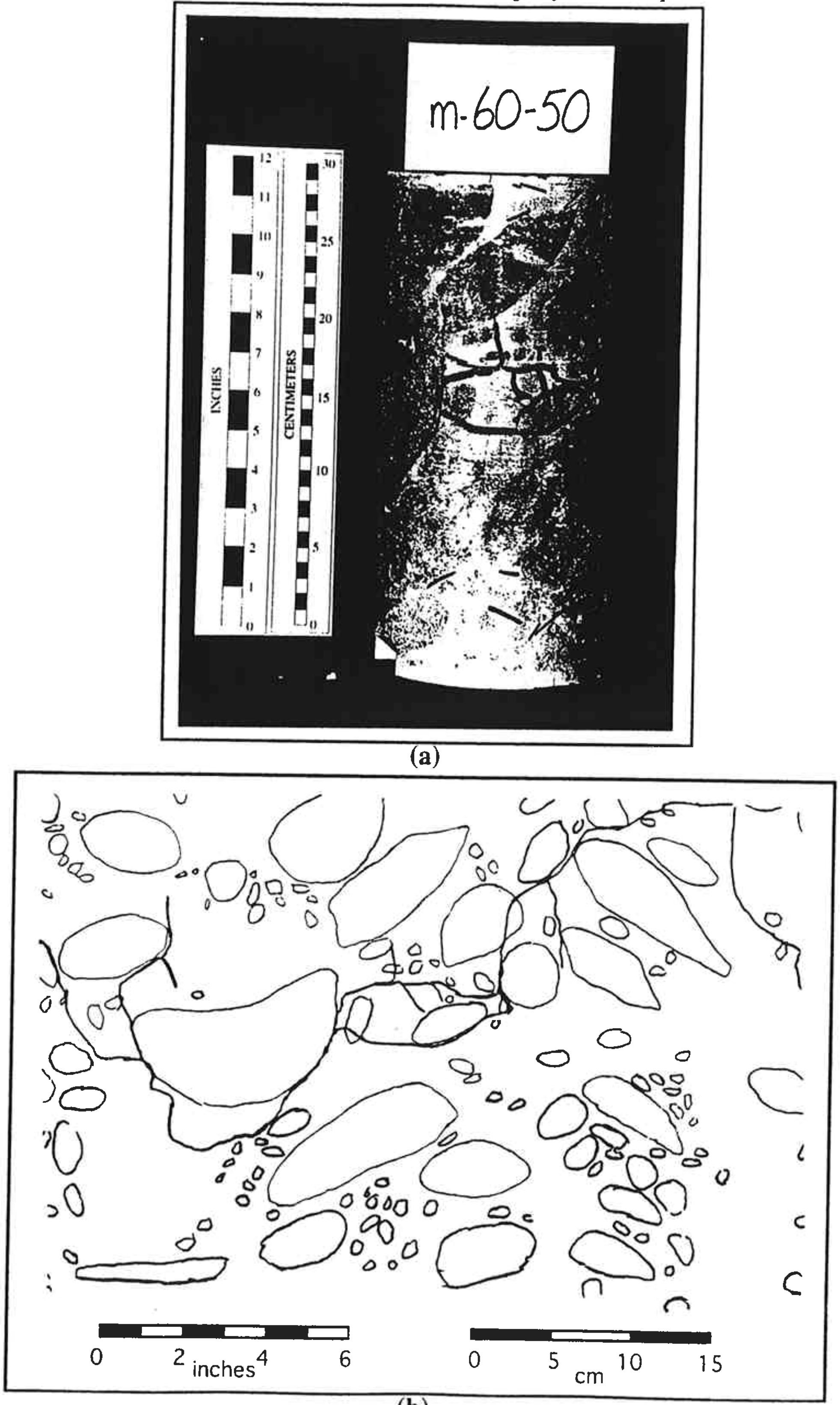

(a)

(b)

Figure D.39 (a) Photograph and **(b)** Tracing of Failed Specimen m-60-50

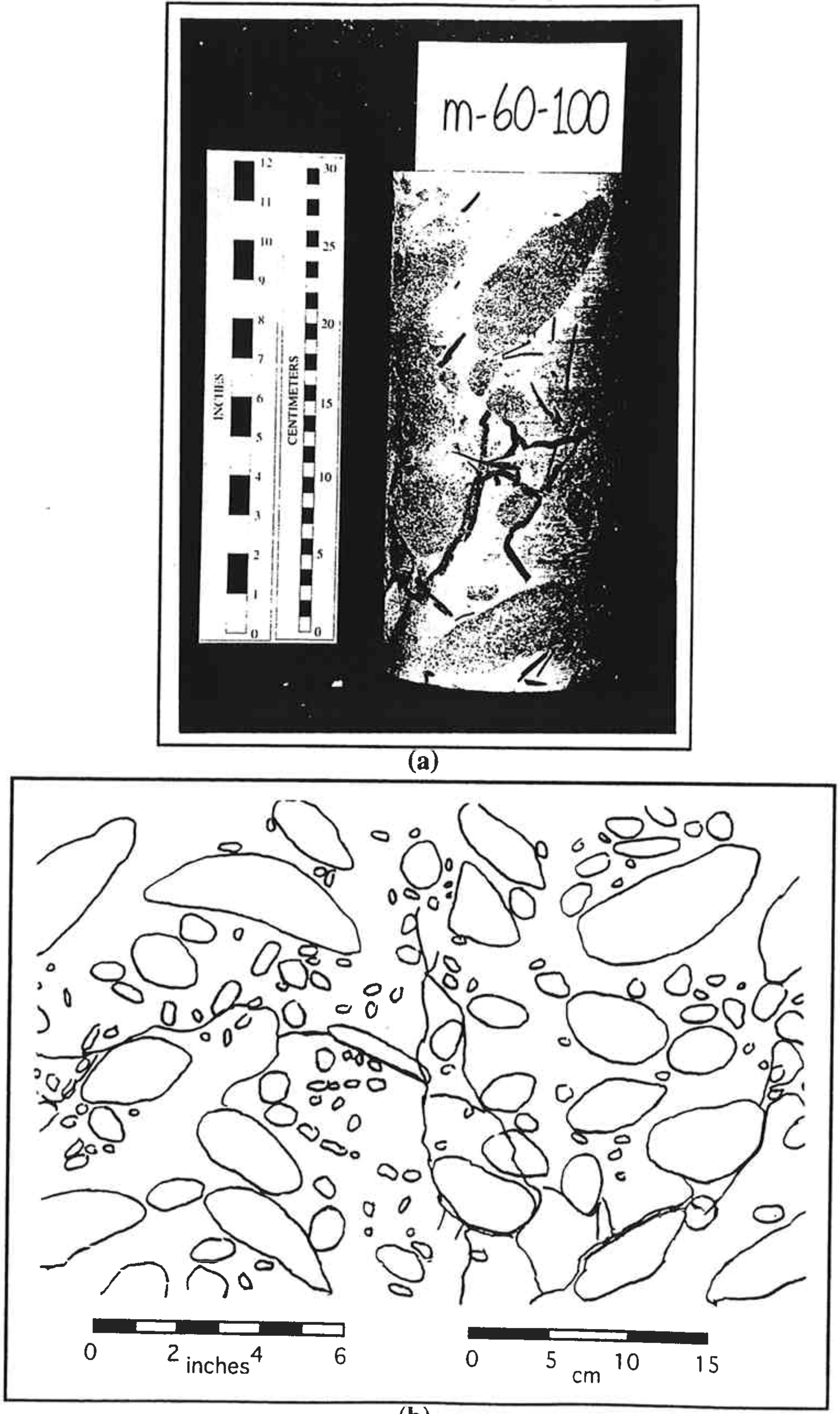

(a)

(b)

Figure D.40 (a) Photograph and **(b)** Tracing of Failed Specimen m-60-100

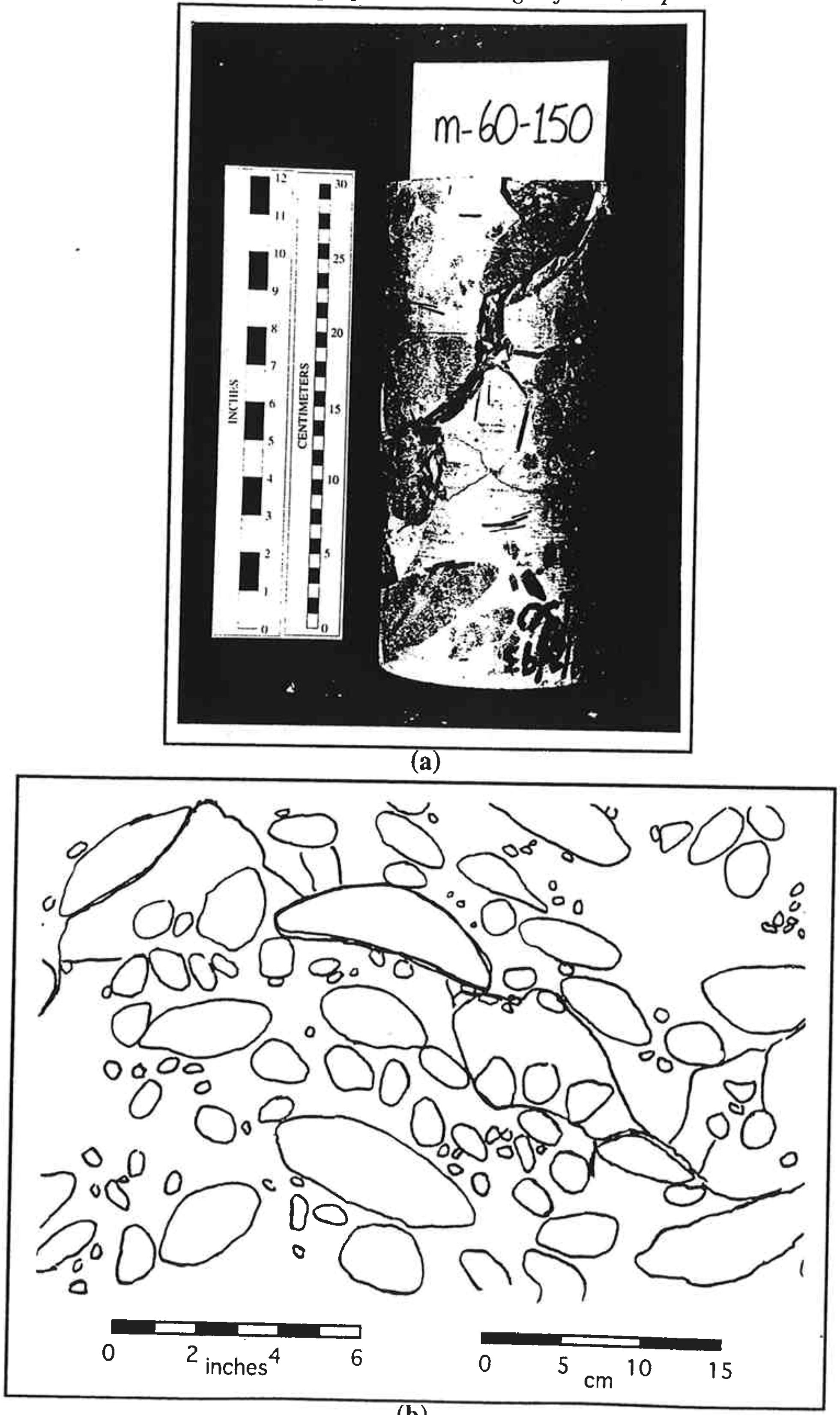

(a)

(b)

Figure D.41 **(a)** Photograph and **(b)** Tracing of Failed Specimen m-60-150

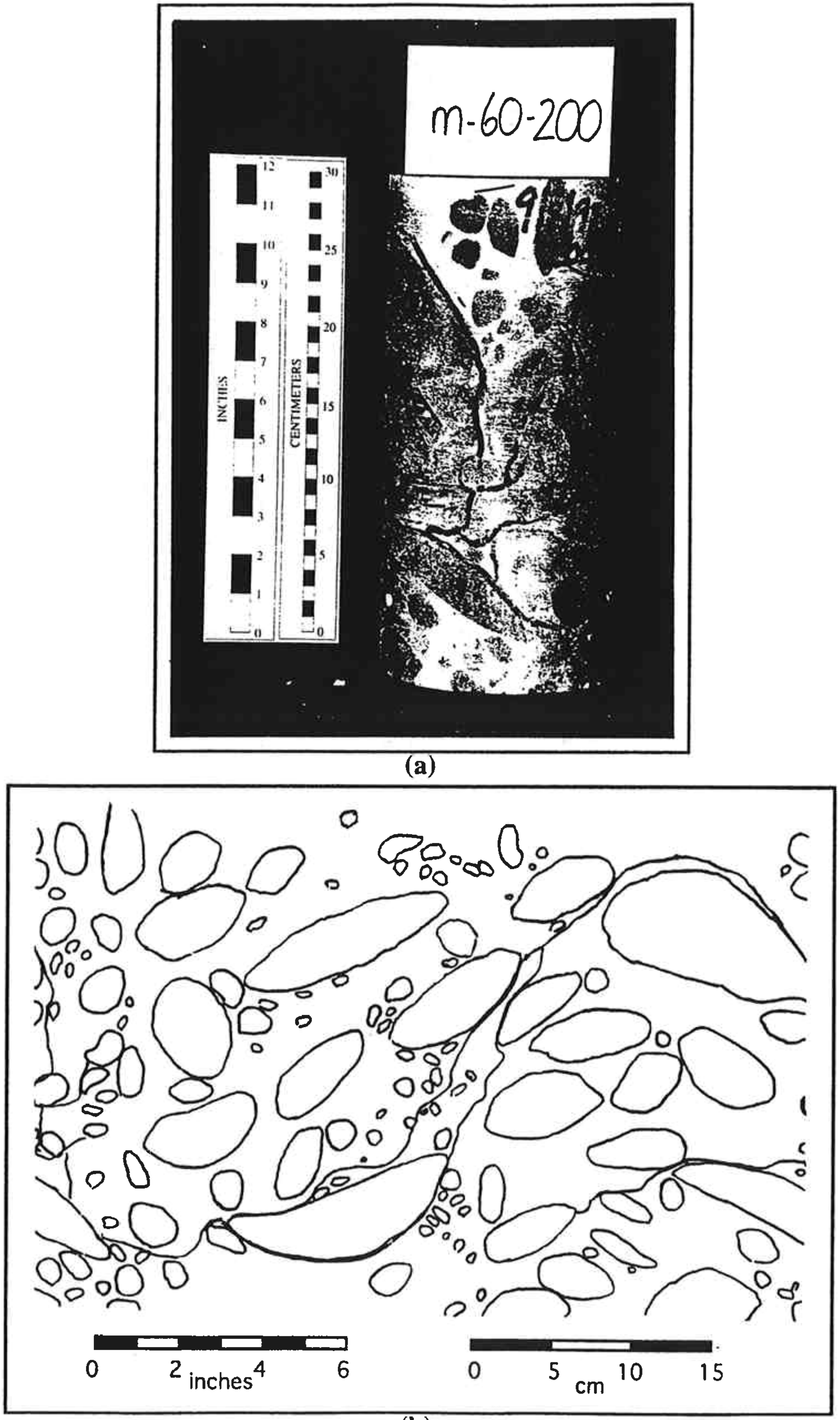

(a)

(b)

Figure D.42 (**a**) Photograph and (**b**) Tracing of Failed Specimen m-60-200

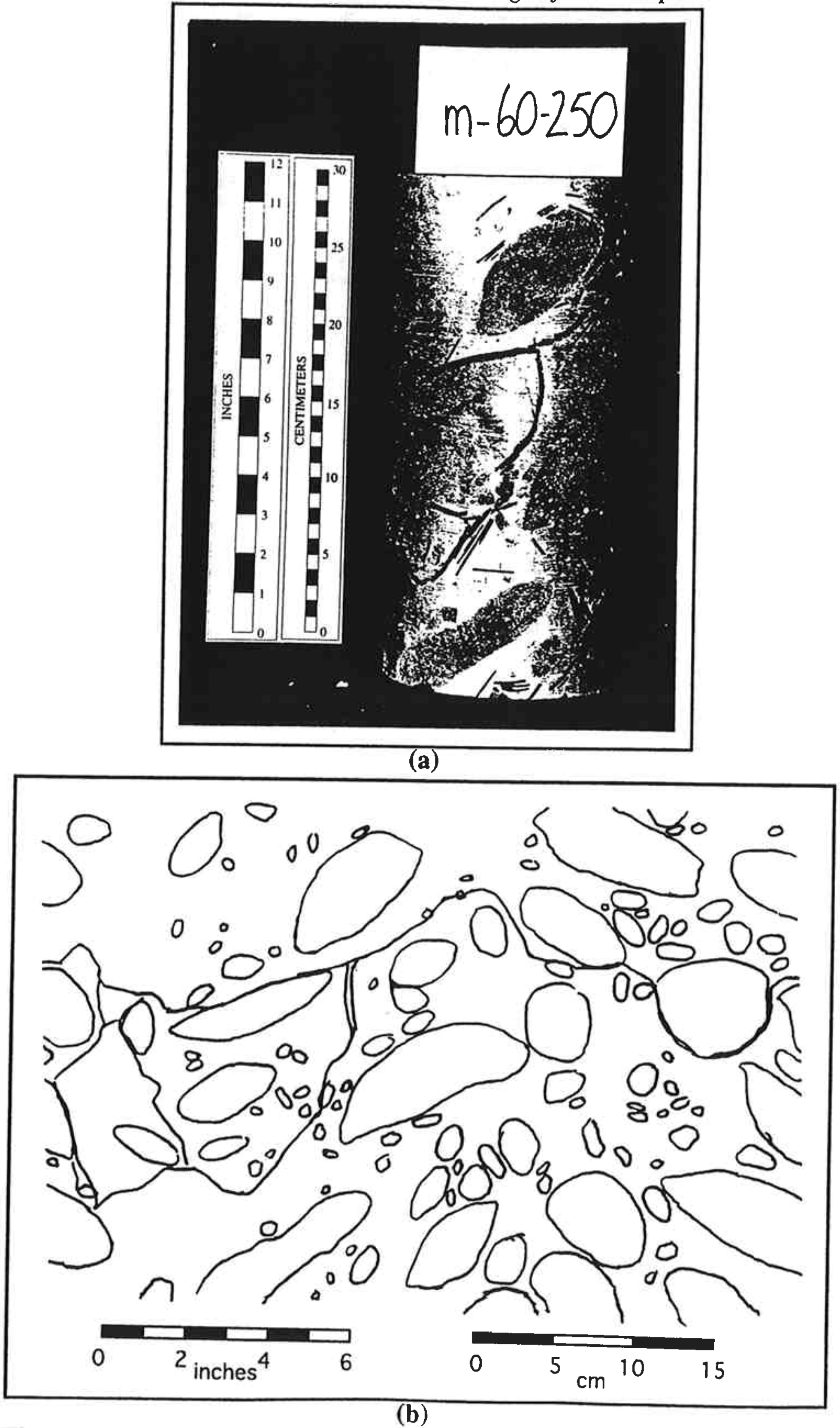

(a)

(b)

Figure D.43 (a) Photograph and **(b)** Tracing of Failed Specimen m-60-250

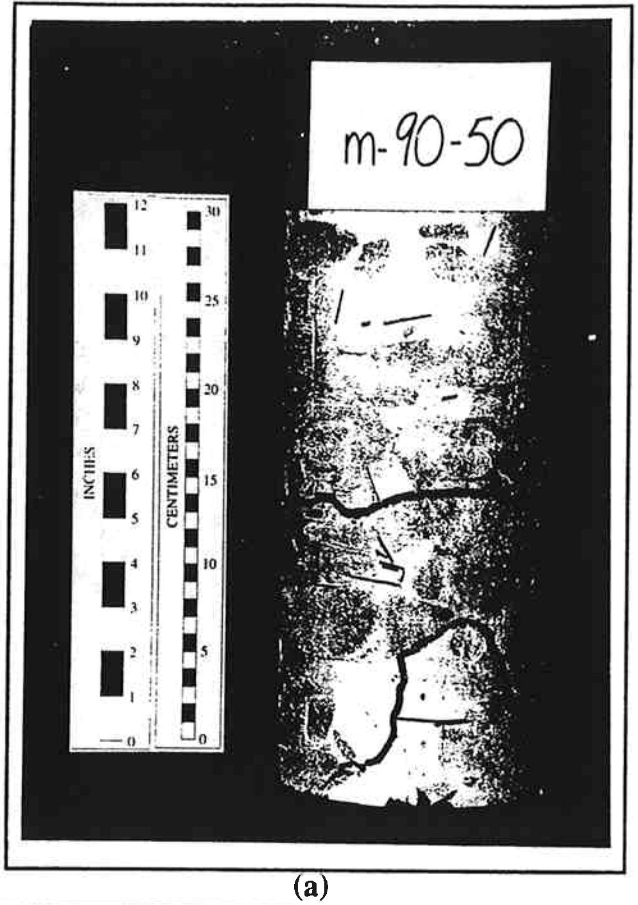

(a)

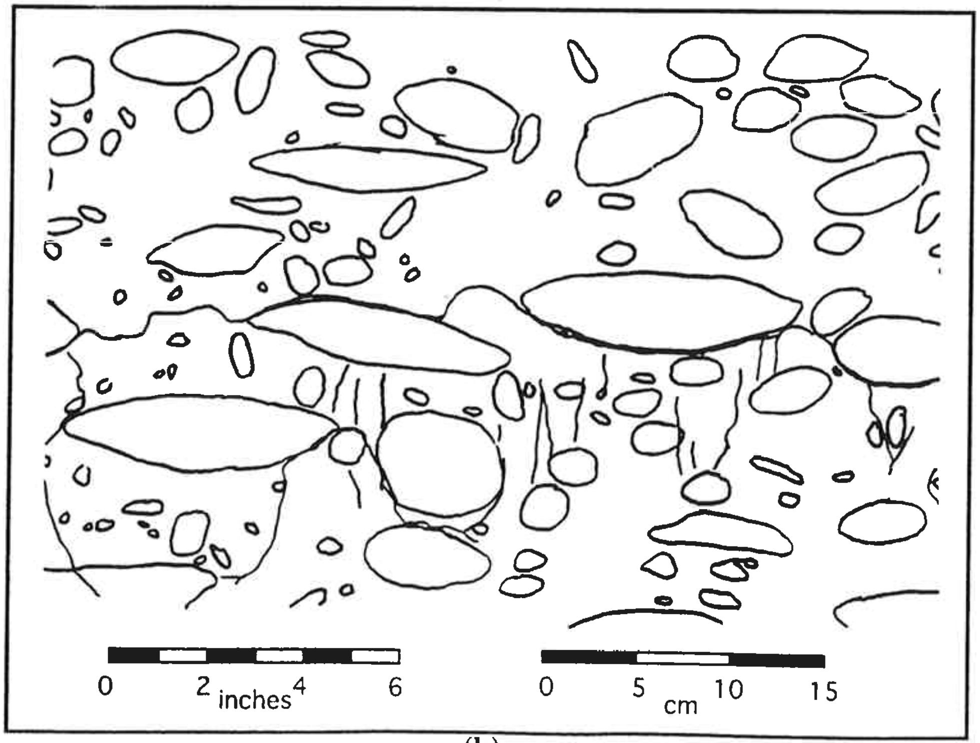

(b)

Figure D.44 (**a**) Photograph and (**b**) Tracing of Failed Specimen m-90-50

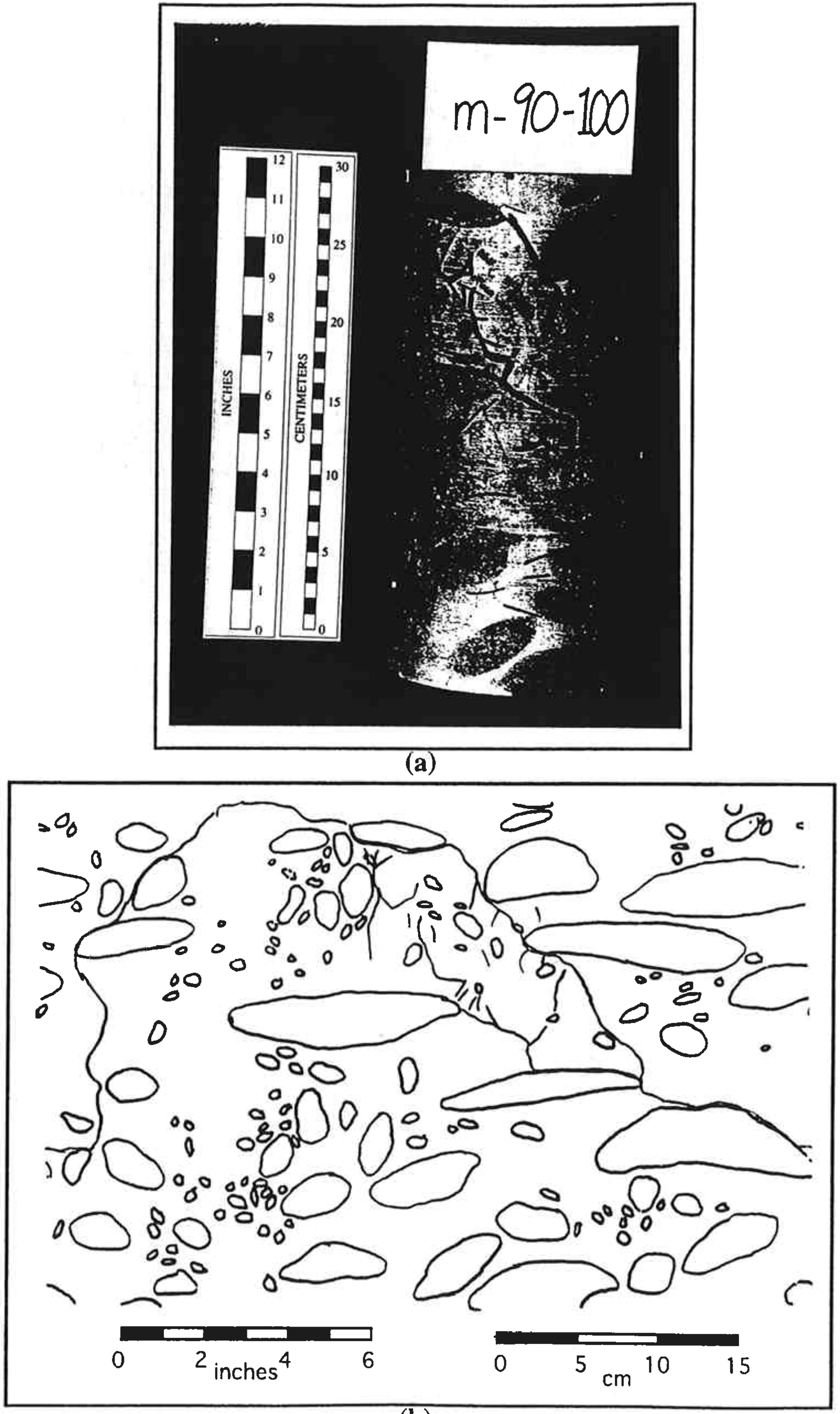

(a)

(b)

Figure D.45 **(a)** Photograph and **(b)** Tracing of Failed Specimen m-90-100

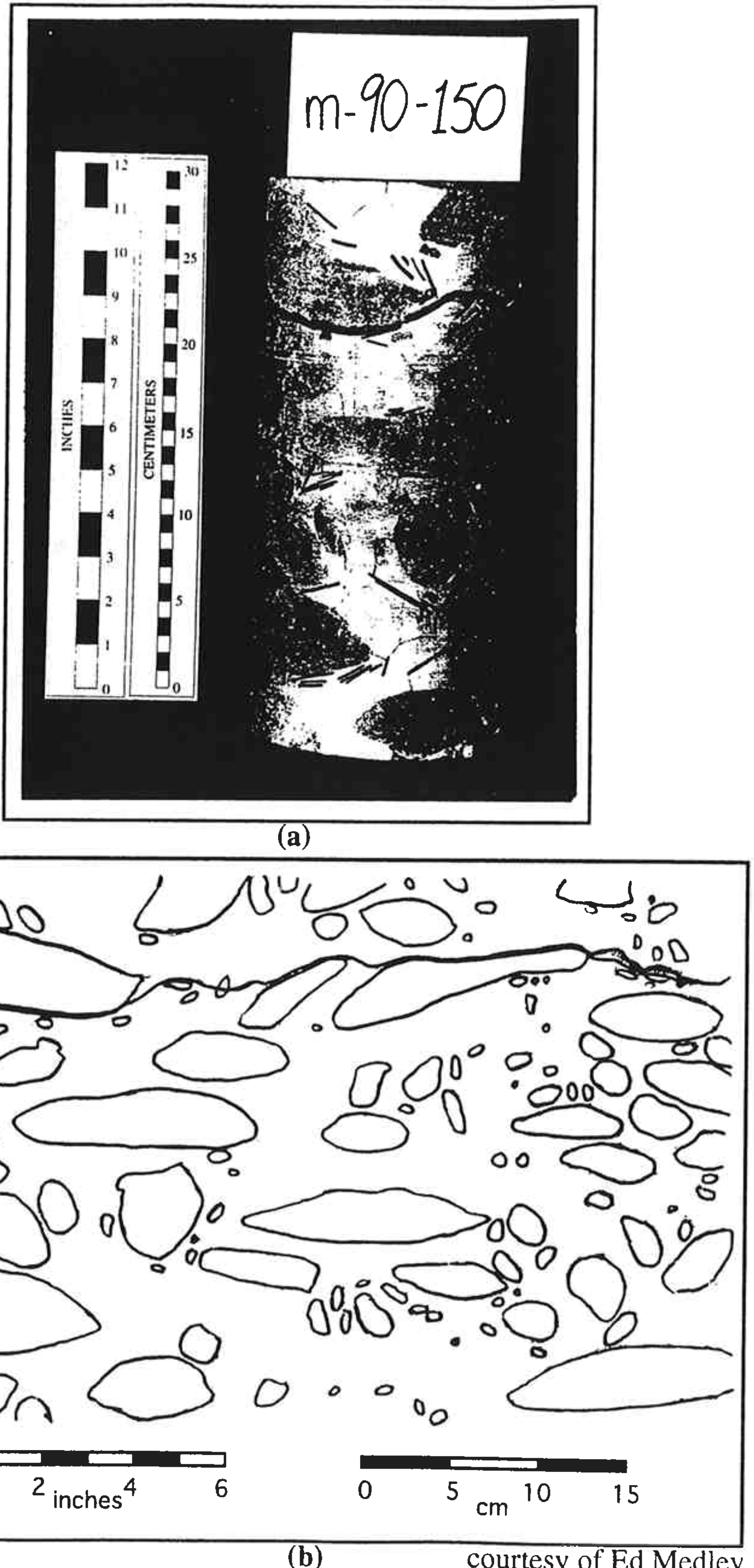

(a)

(b) courtesy of Ed Medley

Figure D.46 **(a)** Photograph and **(b)** Tracing of Failed Specimen m-90-150

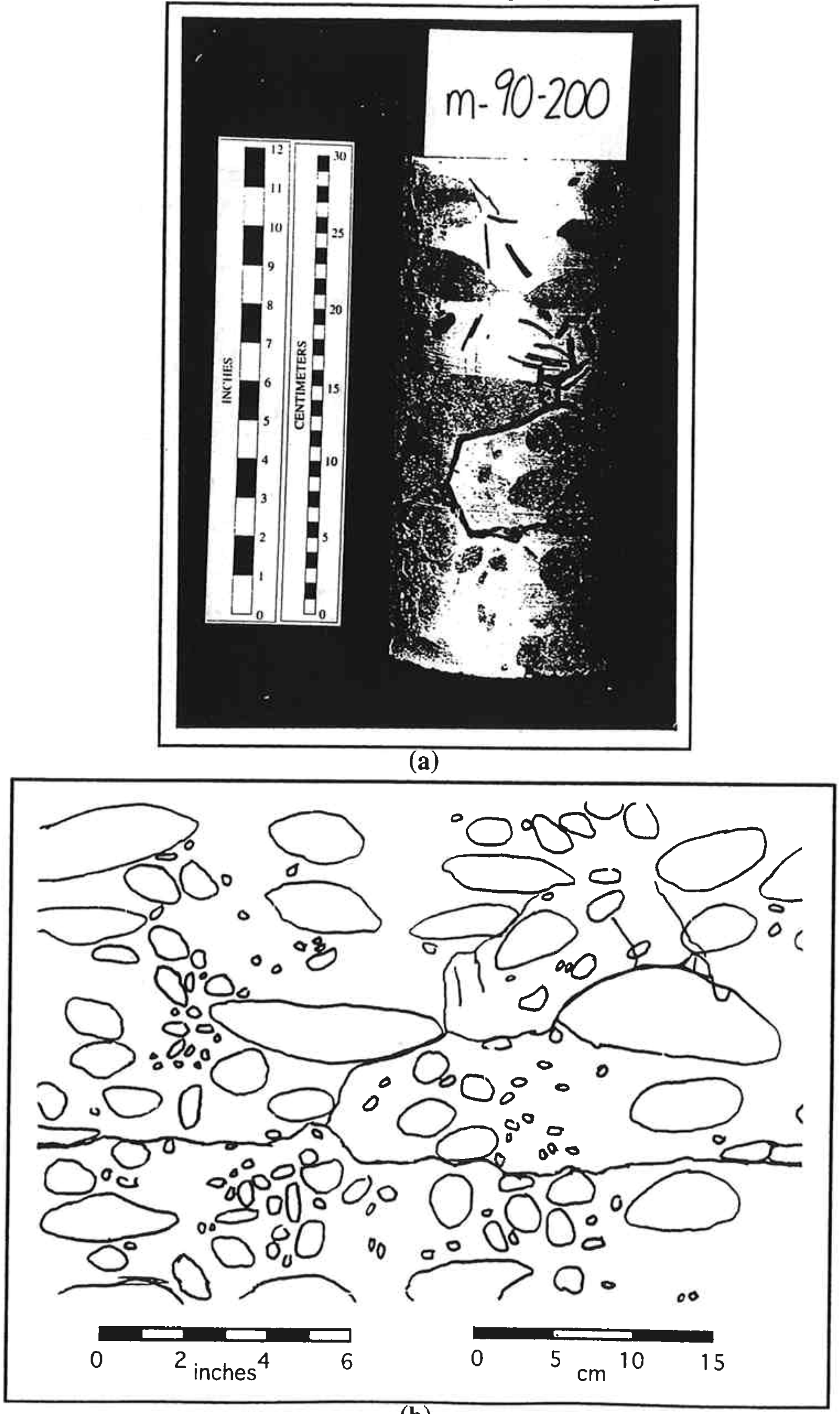

(a)

(b)

Figure D.47 (**a**) Photograph and (**b**) Tracing of Failed Specimen m-90-200

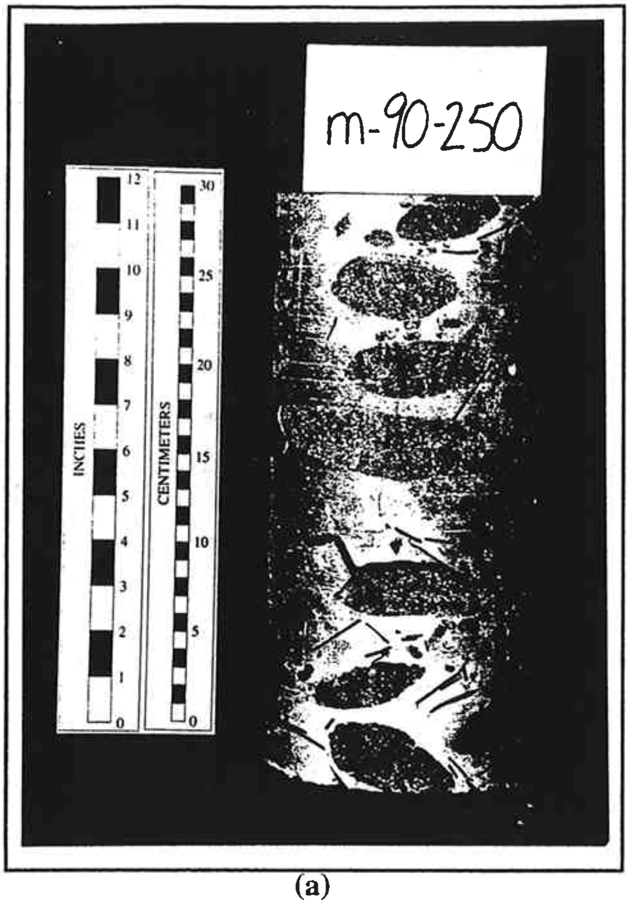

(a)

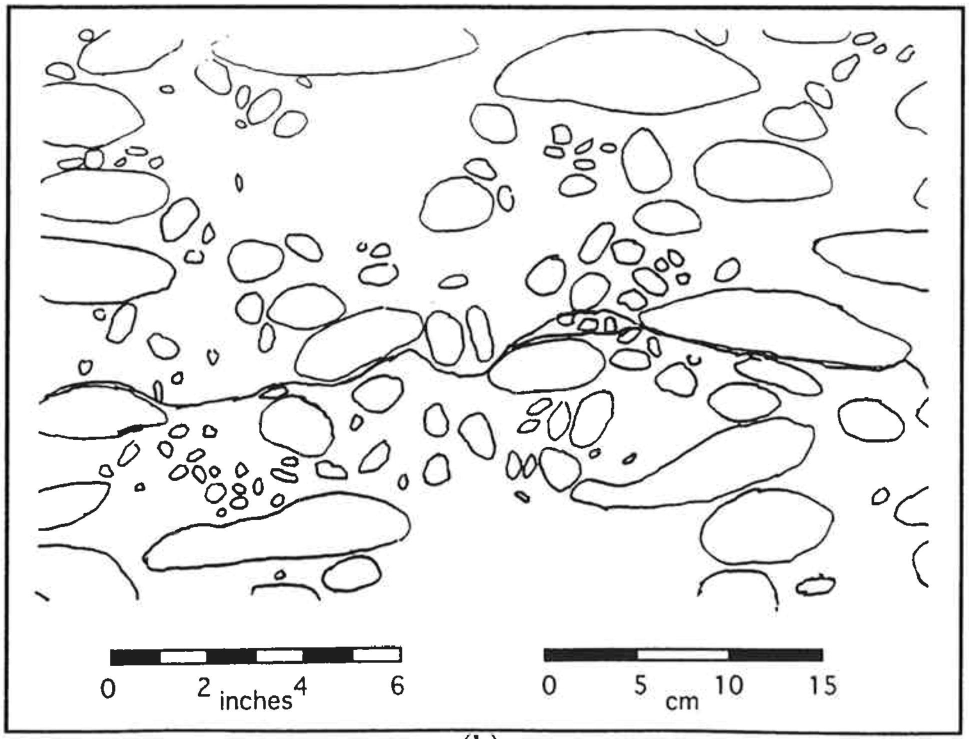

(b)

Figure D.48 (a) Photograph and **(b)** Tracing of Failed Specimen m-90-250

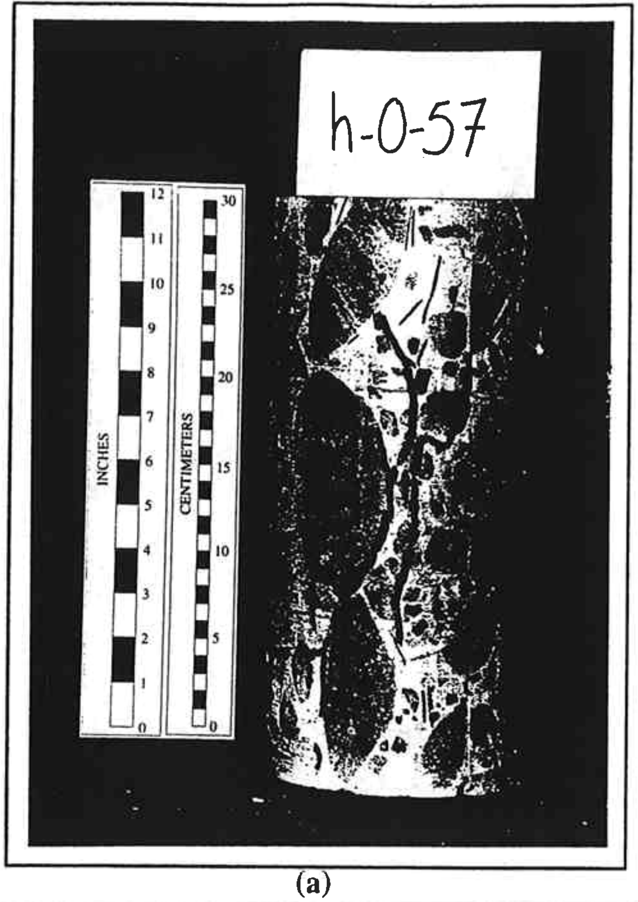

(a)

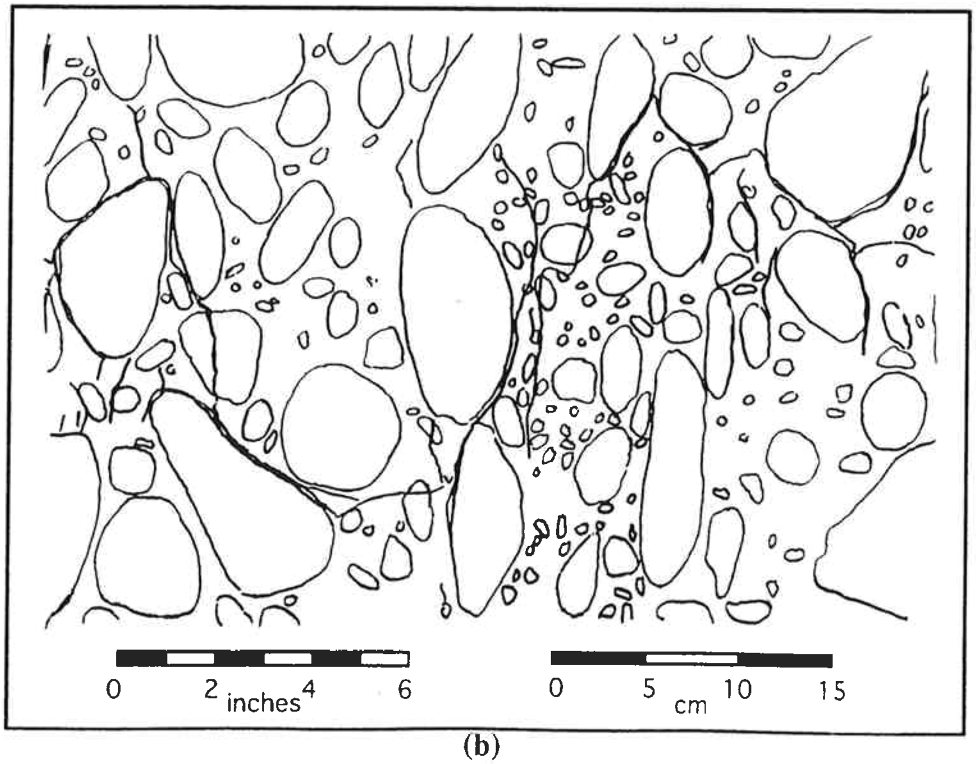

(b)

Figure D.49 (a) Photograph and (b) Tracing of Failed Specimen h-0-57

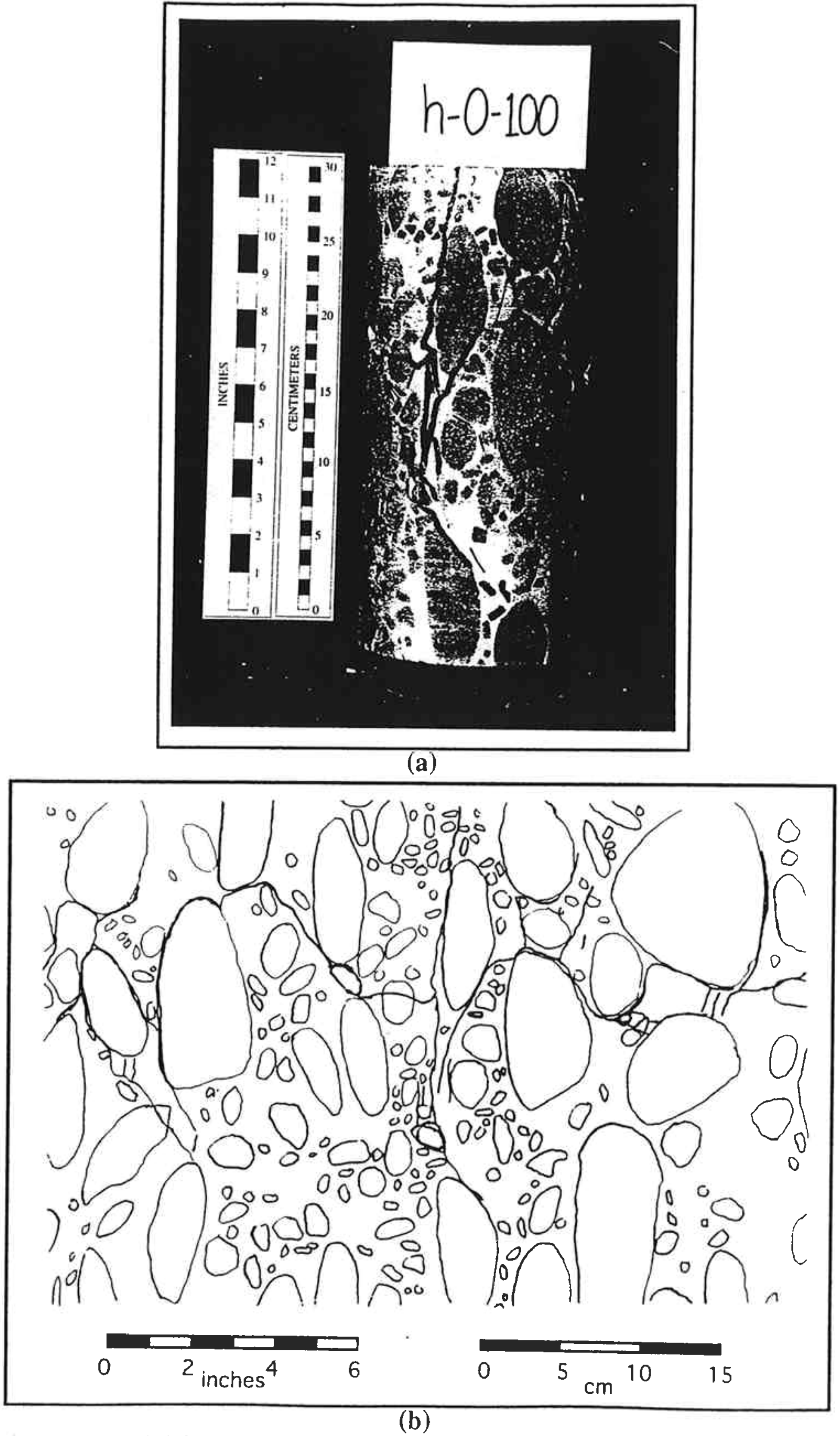

Figure D.50 (a) Photograph and **(b)** Tracing of Failed Specimen h-0-100

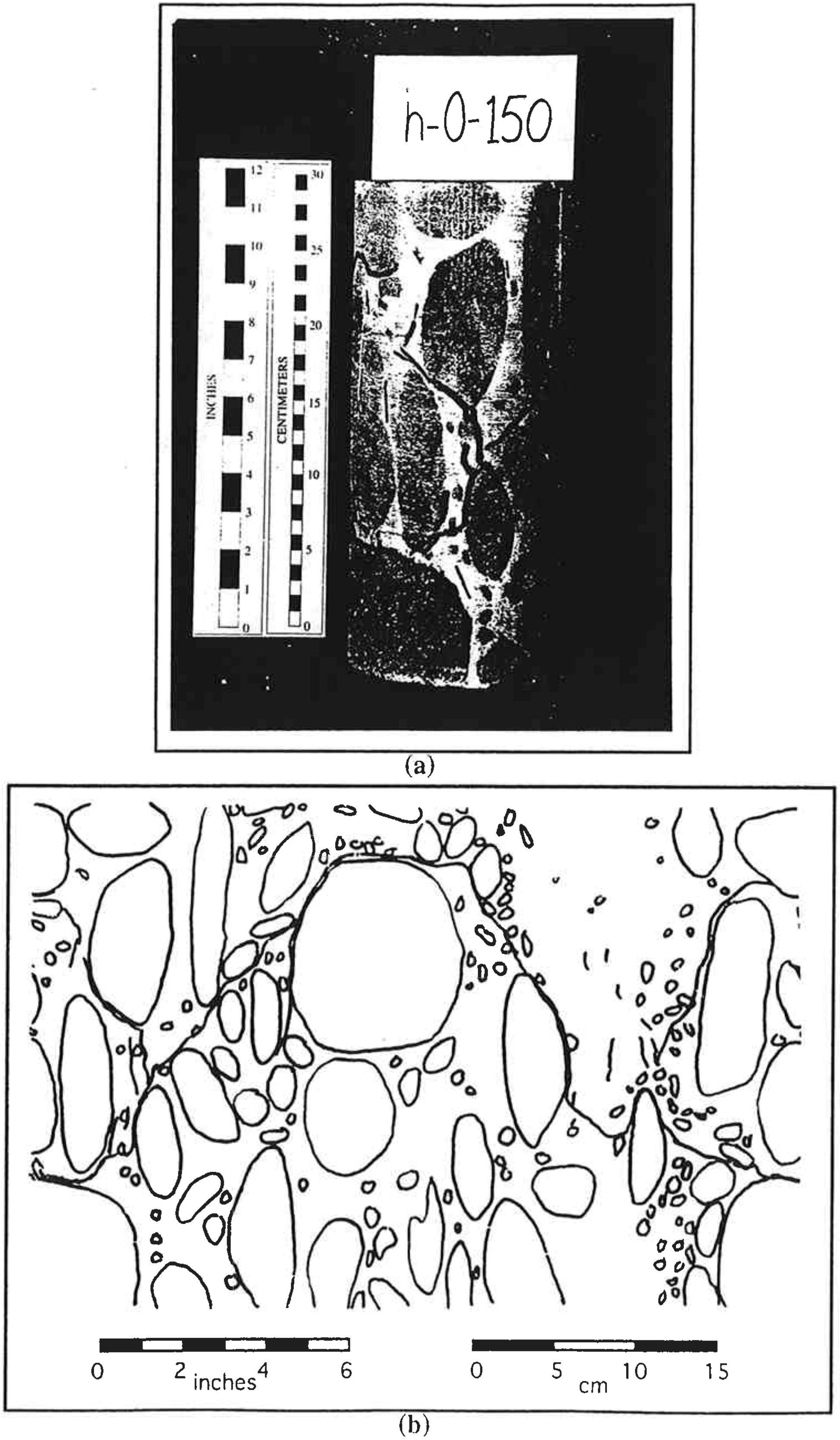

(a)

(b)

Figure D.51 (a) Photograph and **(b)** Tracing of Failed Specimen h-0-150

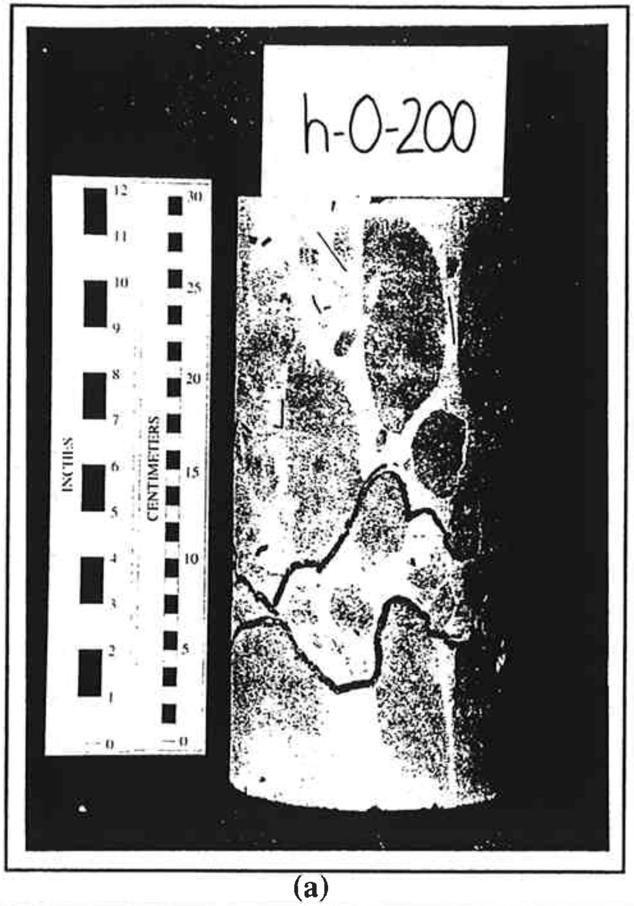

(a)

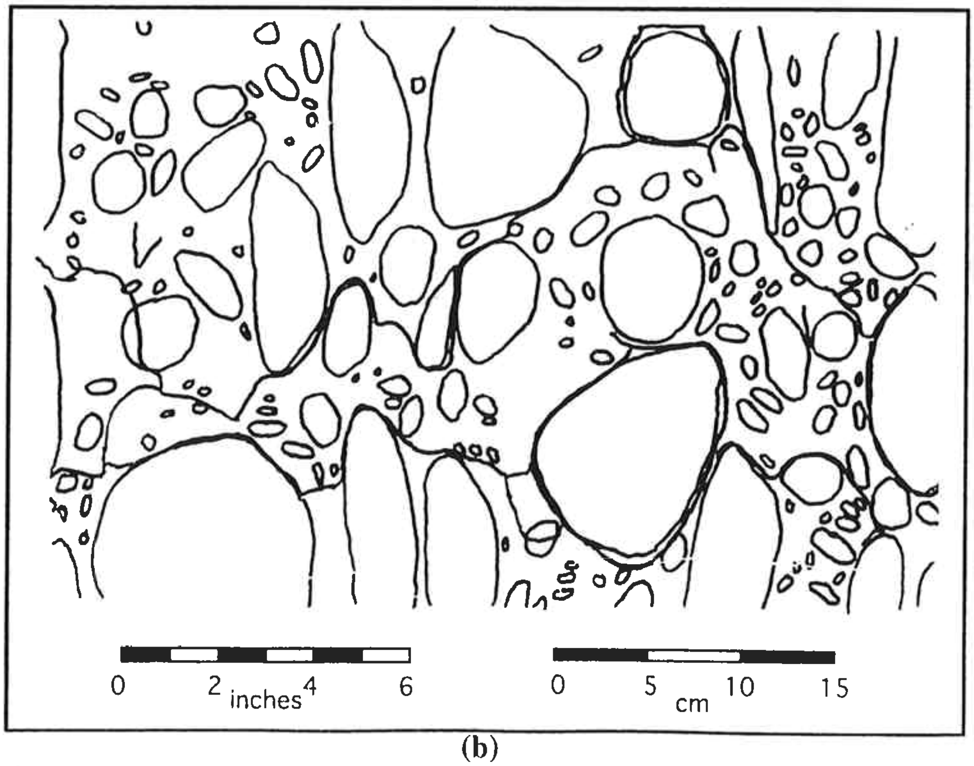

(b)

Figure D.52 **(a)** Photograph and **(b)** Tracing of Failed Specimen h-0-200

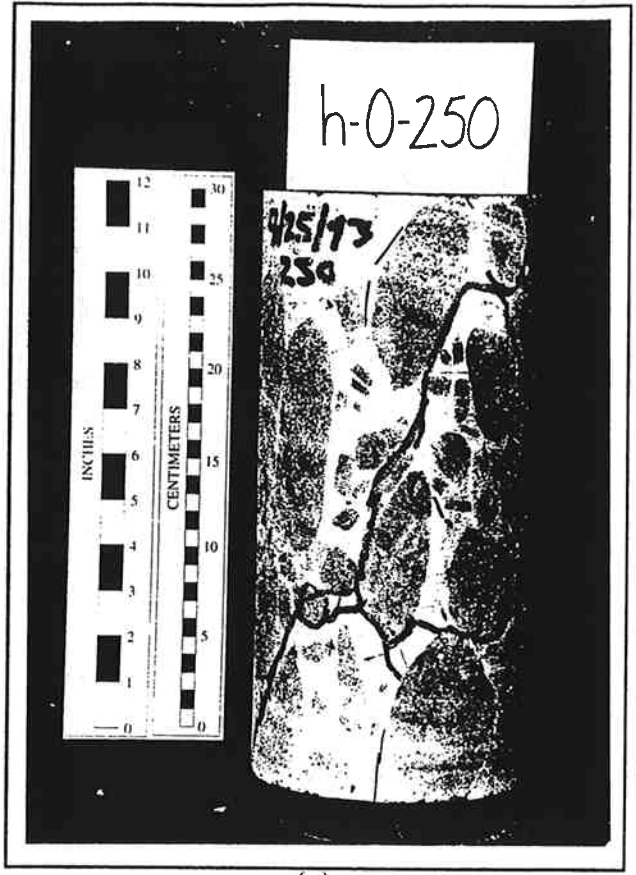

(a)

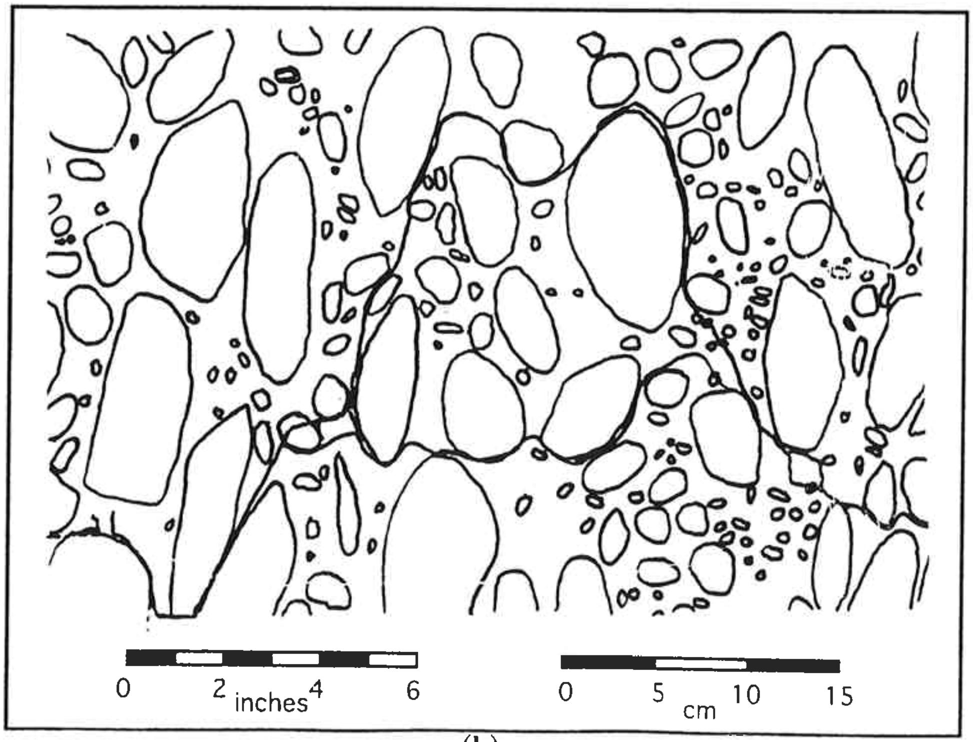

(b)

Figure D.53 (a) Photograph and **(b)** Tracing of Failed Specimen h-0-250

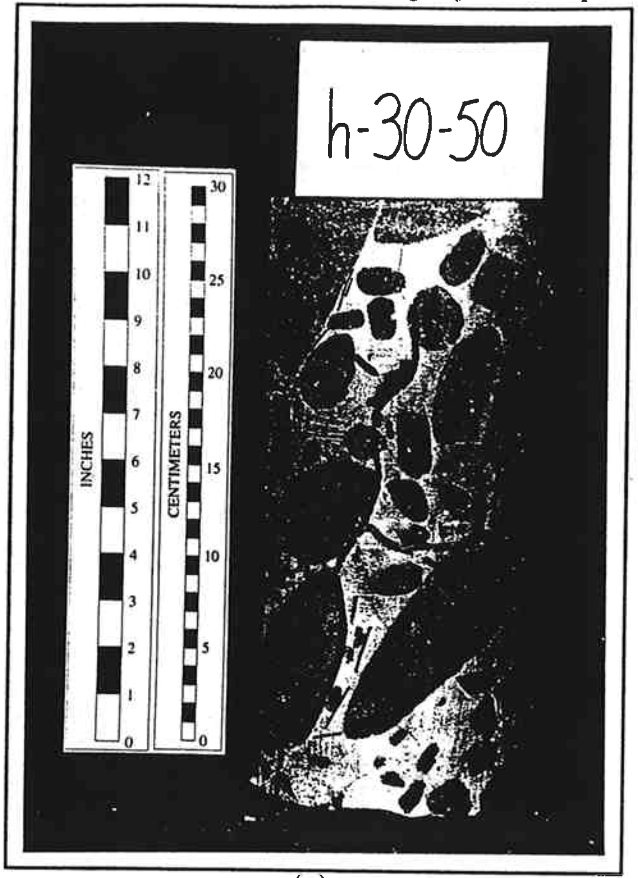

(a)

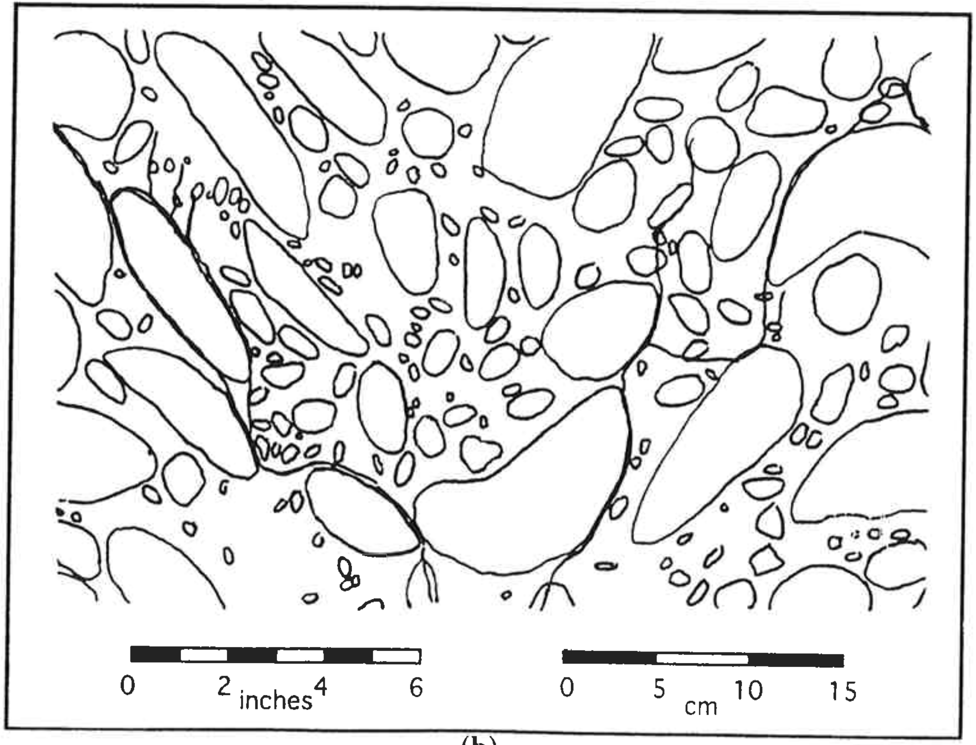

(b)

Figure D.54 **(a)** Photograph and **(b)** Tracing of Failed Specimen h-30-50

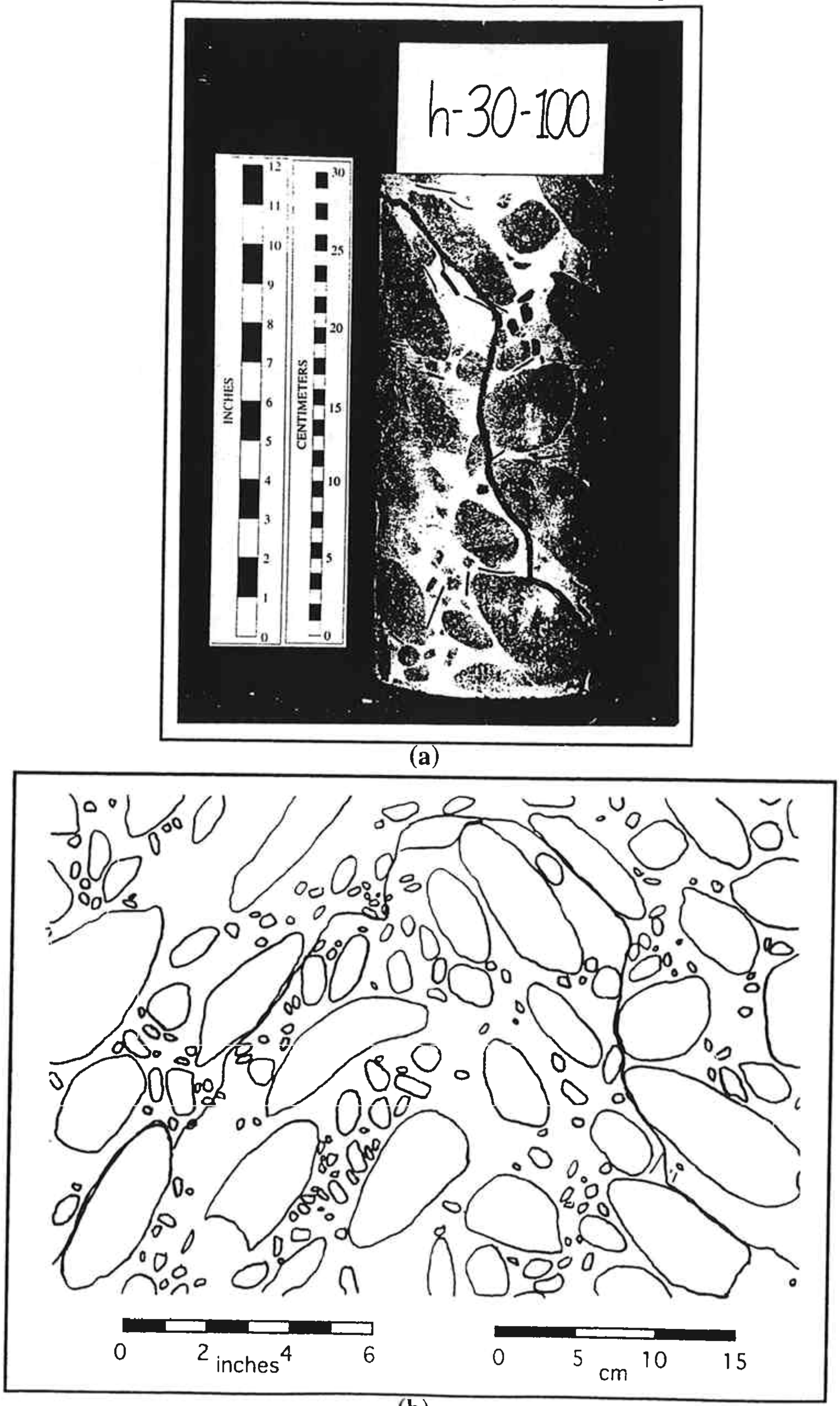

(a)

(b)

Figure D.55 (a) Photograph and **(b)** Tracing of Failed Specimen h-30-100

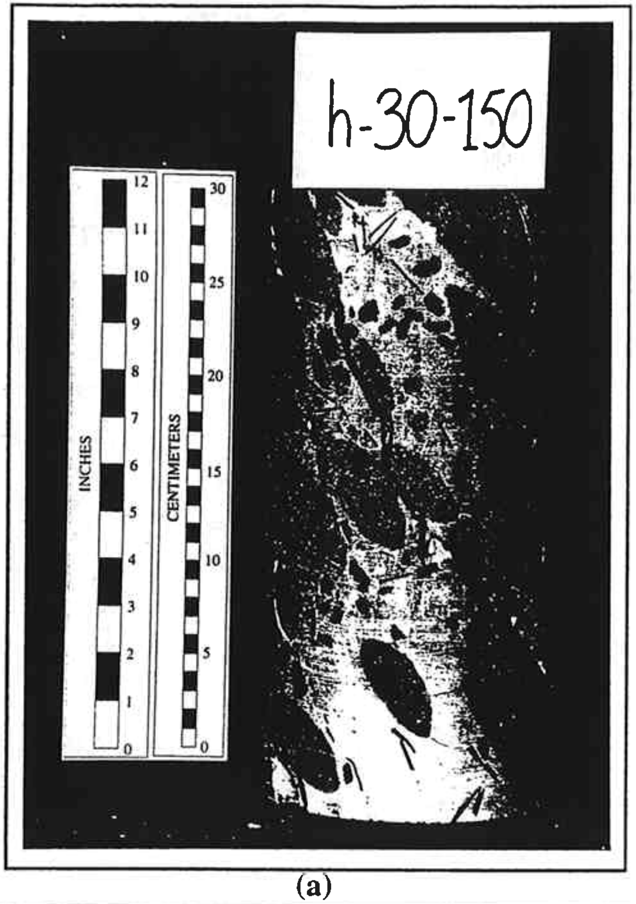

(a)

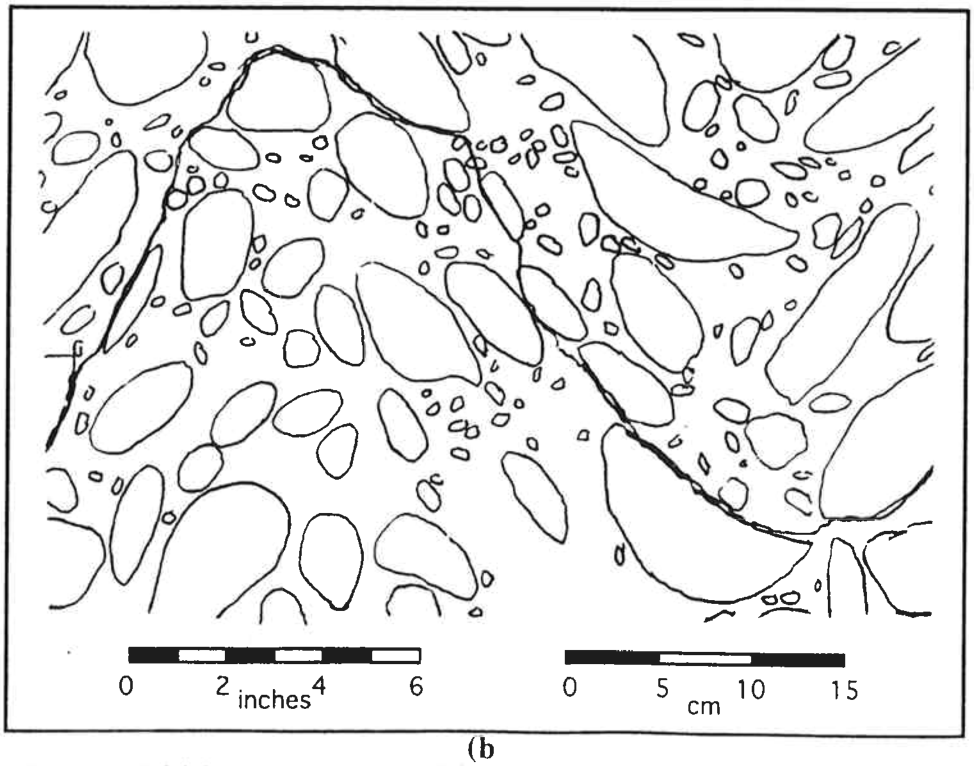

(b

Figure D.56 (a) Photograph and **(b)** Tracing of Failed Specimen h-30-150

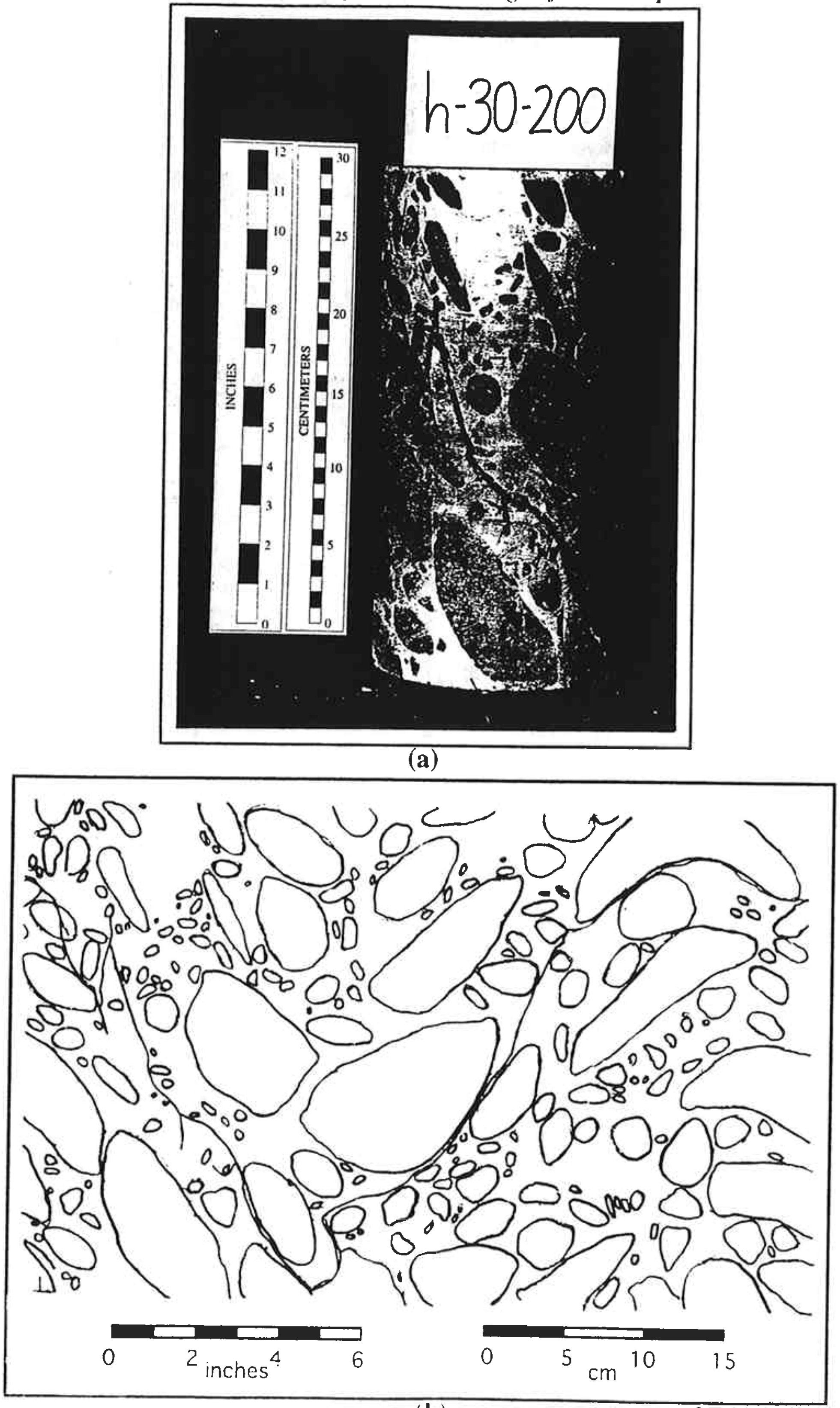

(b) courtesy of Ed Medley

Figure D.57 (**a**) Photograph and (**b**) Tracing of Failed Specimen h-30-200

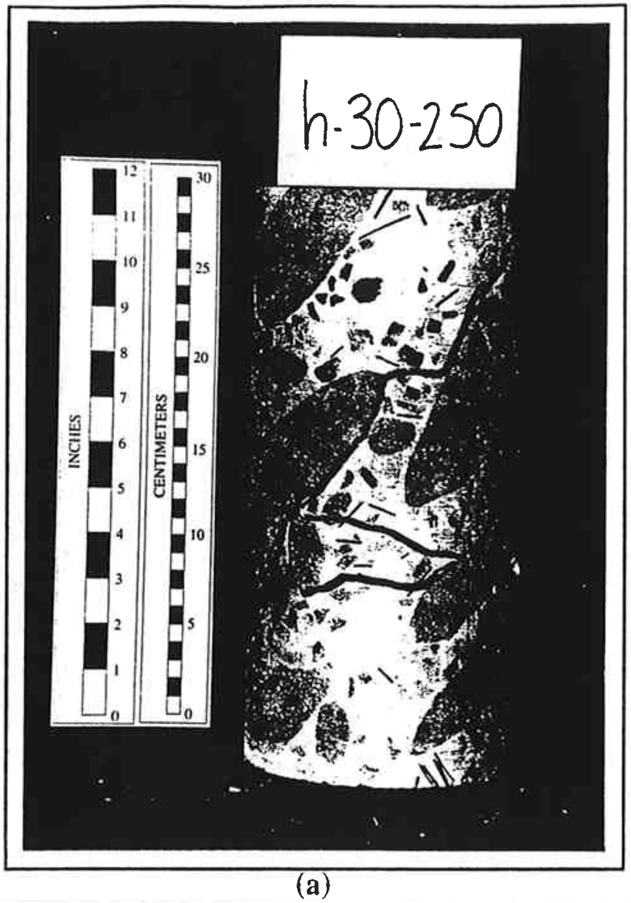

(a)

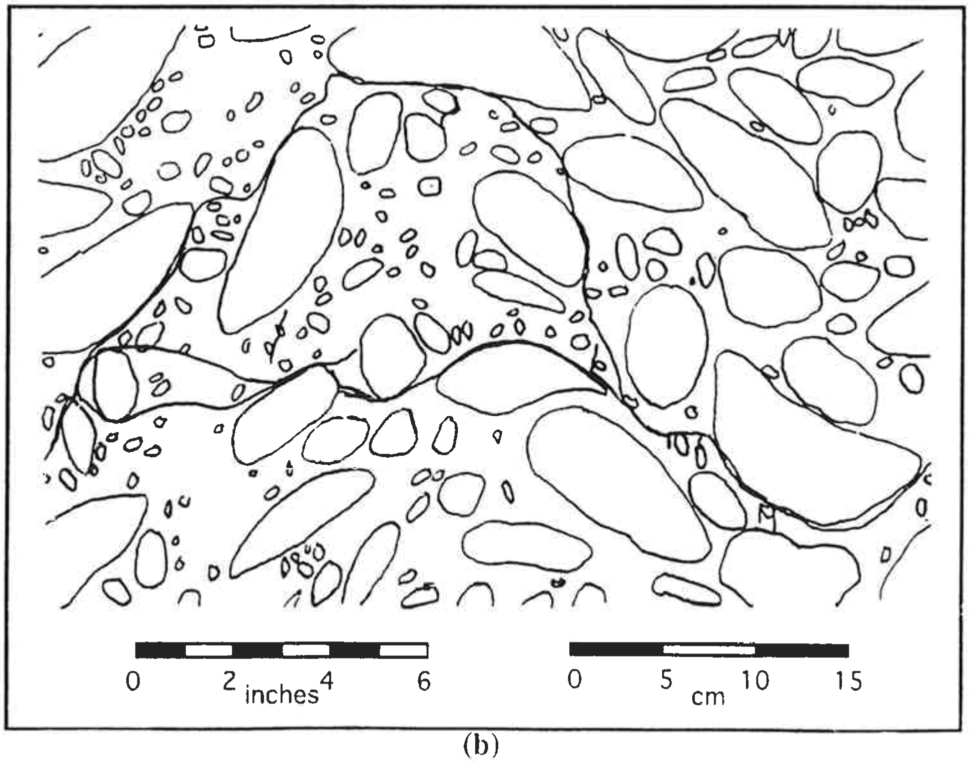

(b)

Figure D.58 (**a**) Photograph and (**b**) Tracing of Failed Specimen h-30-250

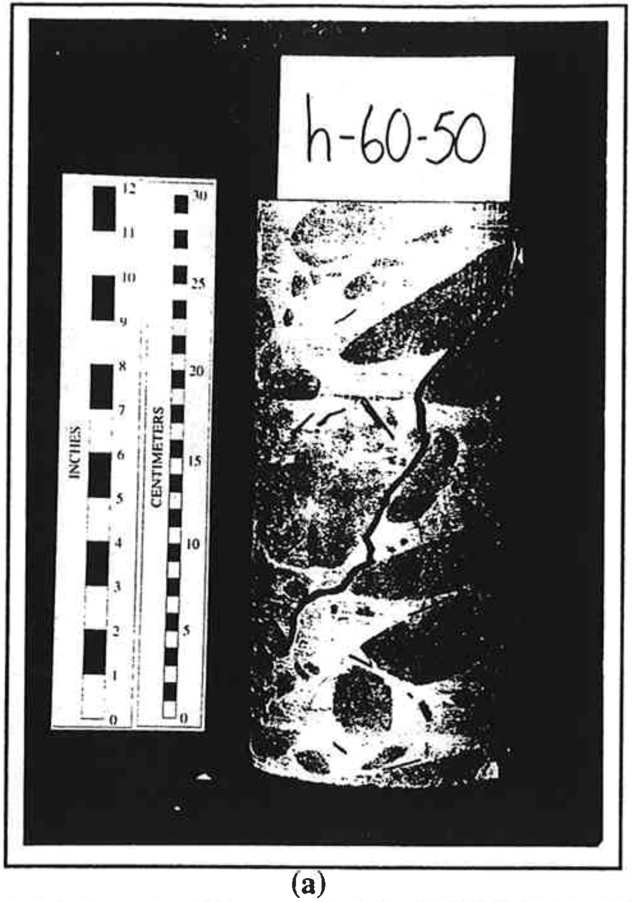

(a)

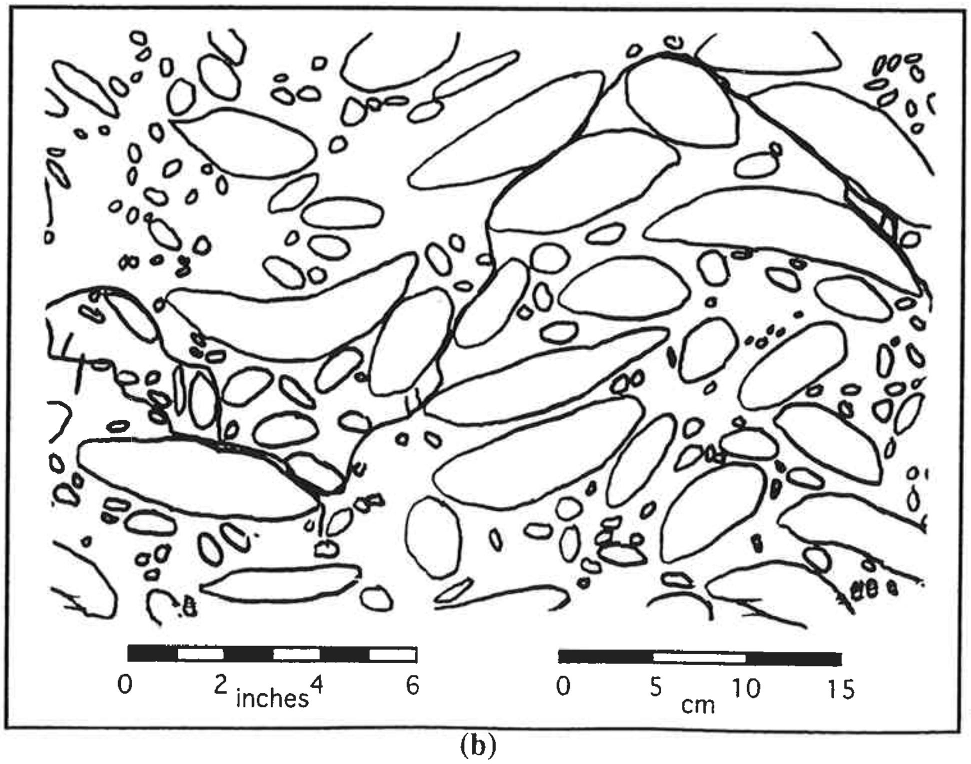

(b)

Figure D.59 **(a)** Photograph and **(b)** Tracing of Failed Specimen h-60-50

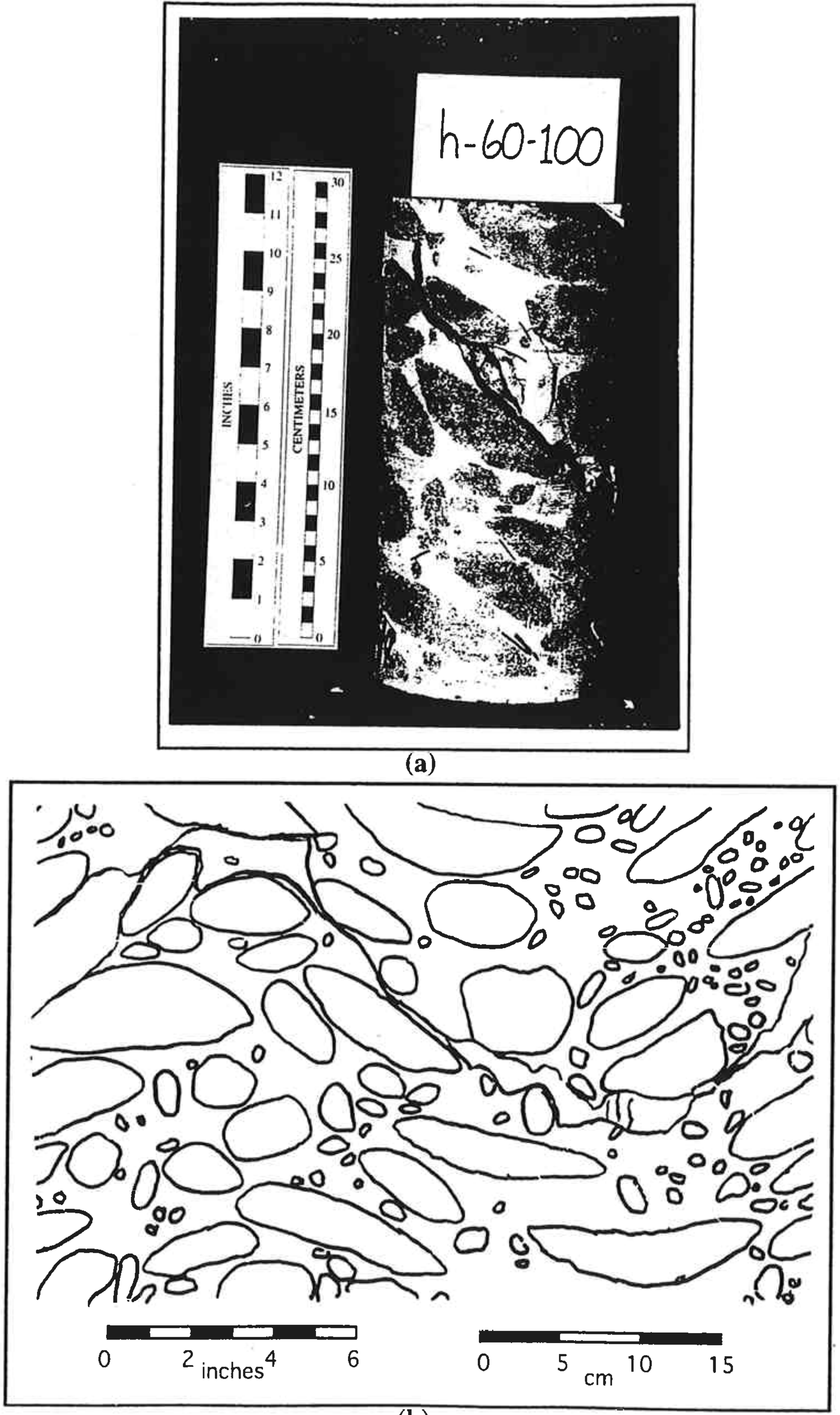

(a)

(b)

Figure D.60 **(a)** Photograph and **(b)** Tracing of Failed Specimen h-60-100

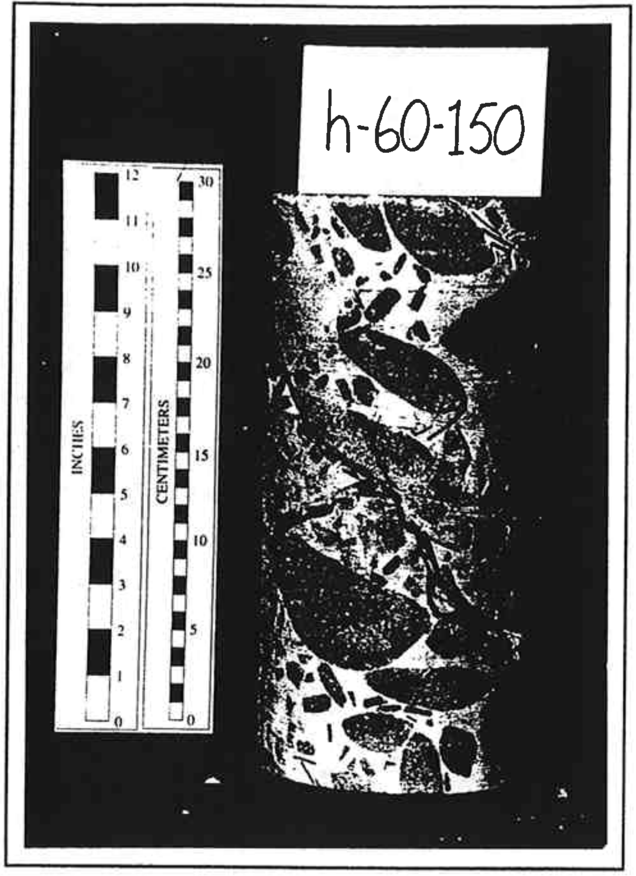

NOT POSSIBLE TO TRACE h-60-150

Figure D.61 Photograph of Failed Specimen h-60-150

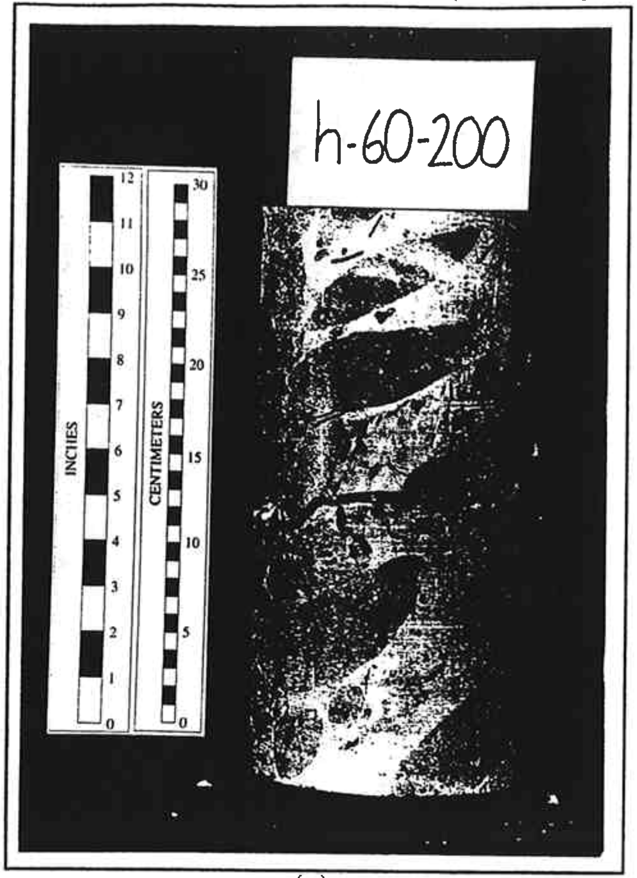

(a)

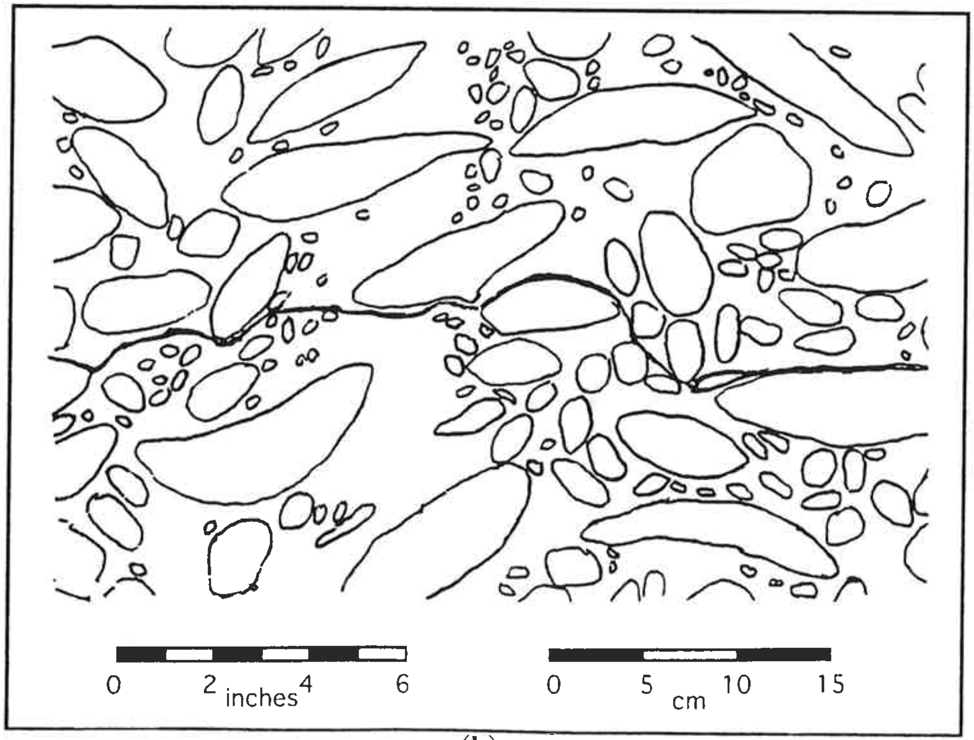

(b)

Figure D.62 (**a**) Photograph and (**b**) Tracing of Failed Specimen h-60-200

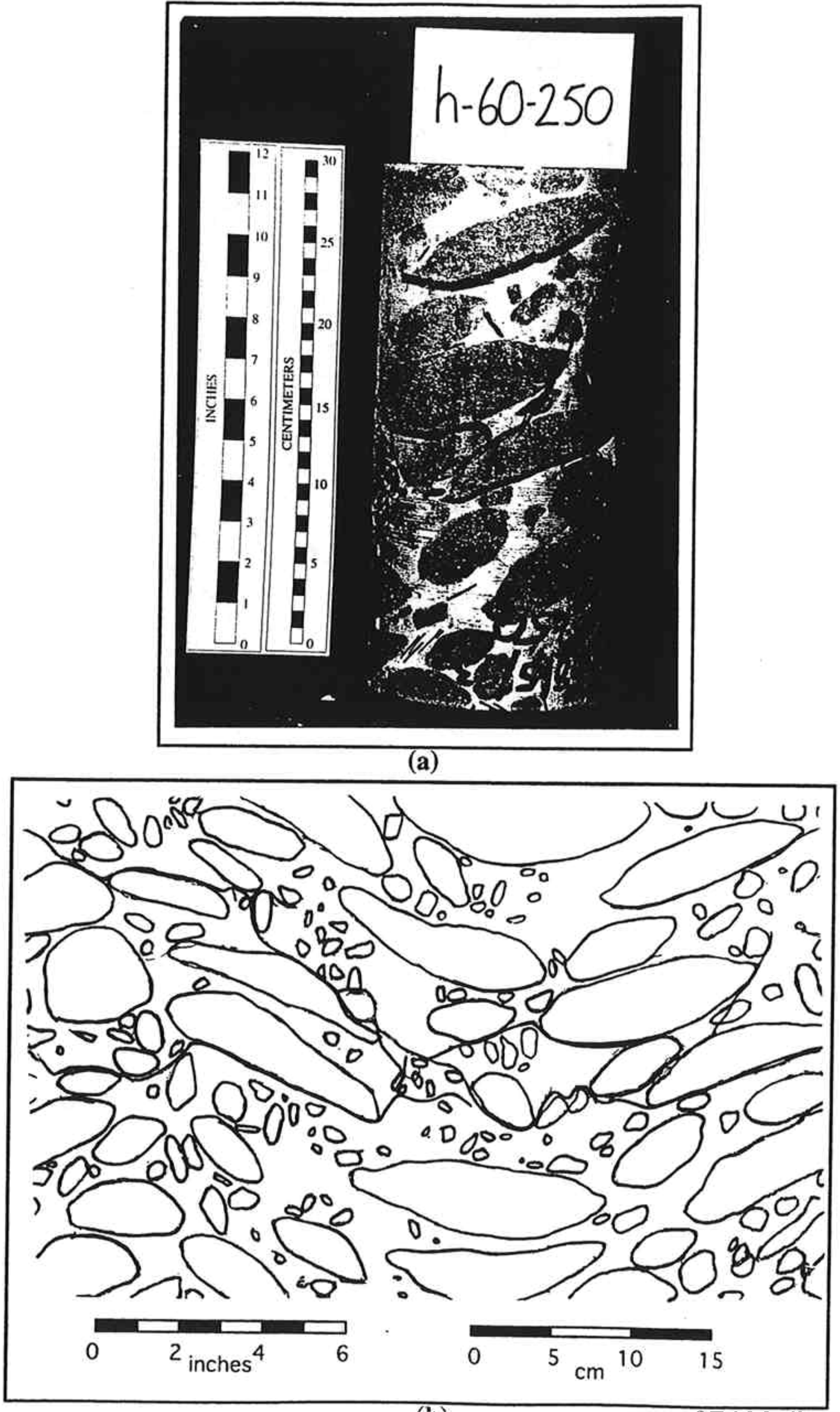

(a)

(b) courtesy of Ed Medley

Figure D.63 (a) Photograph and **(b)** Tracing of Failed Specimen h-60-250

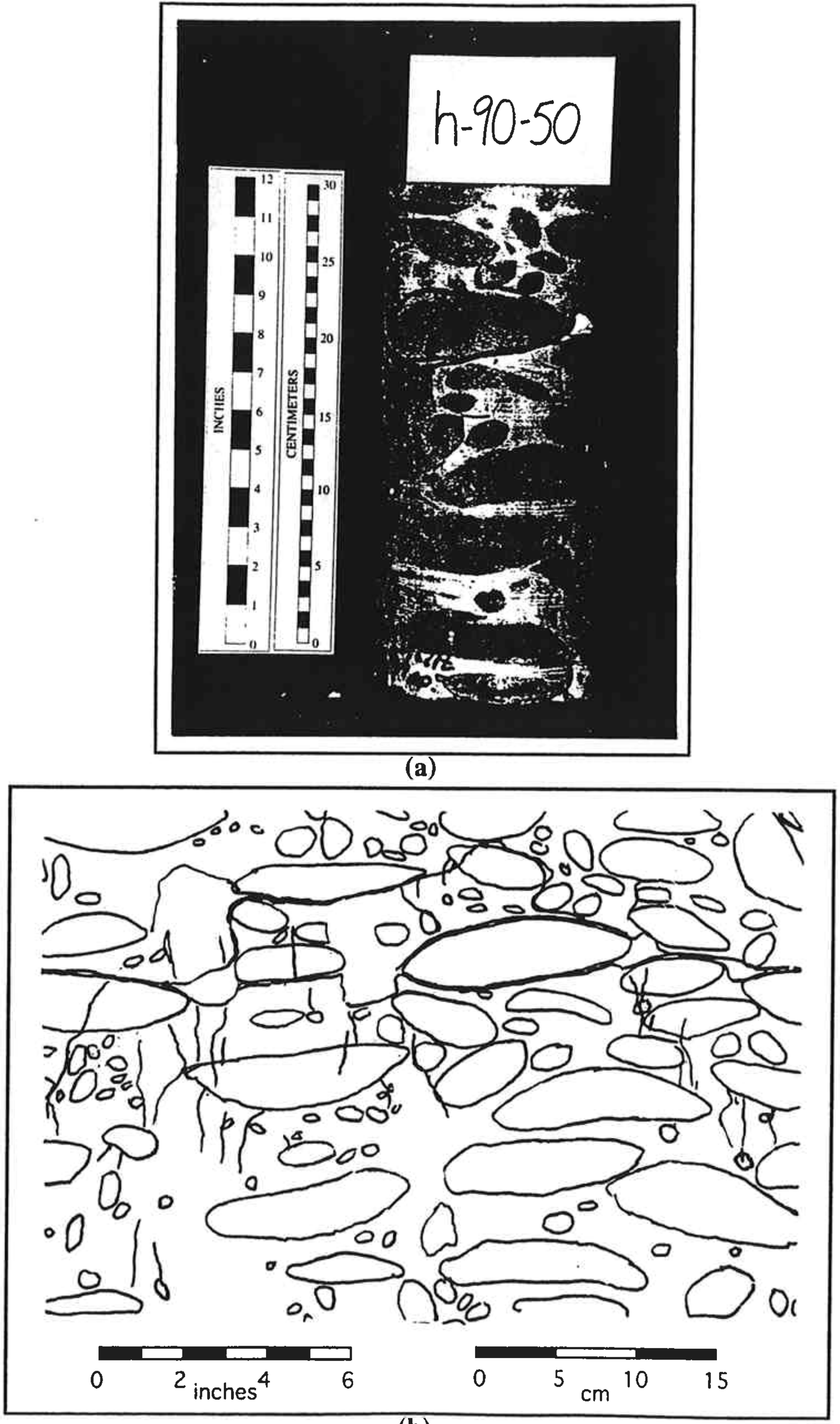

(a)

(b)

Figure D.64 (a) Photograph and **(b)** Tracing of Failed Specimen h-90-50

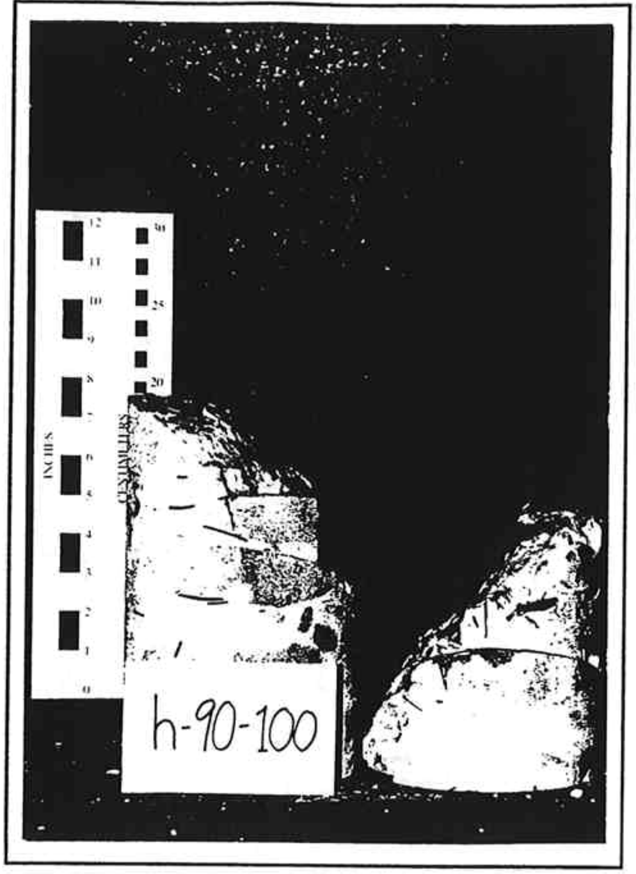

NOT POSSIBLE TO TRACE h-90-100

Figure D.65 Photograph of Failed Specimen h-90-100

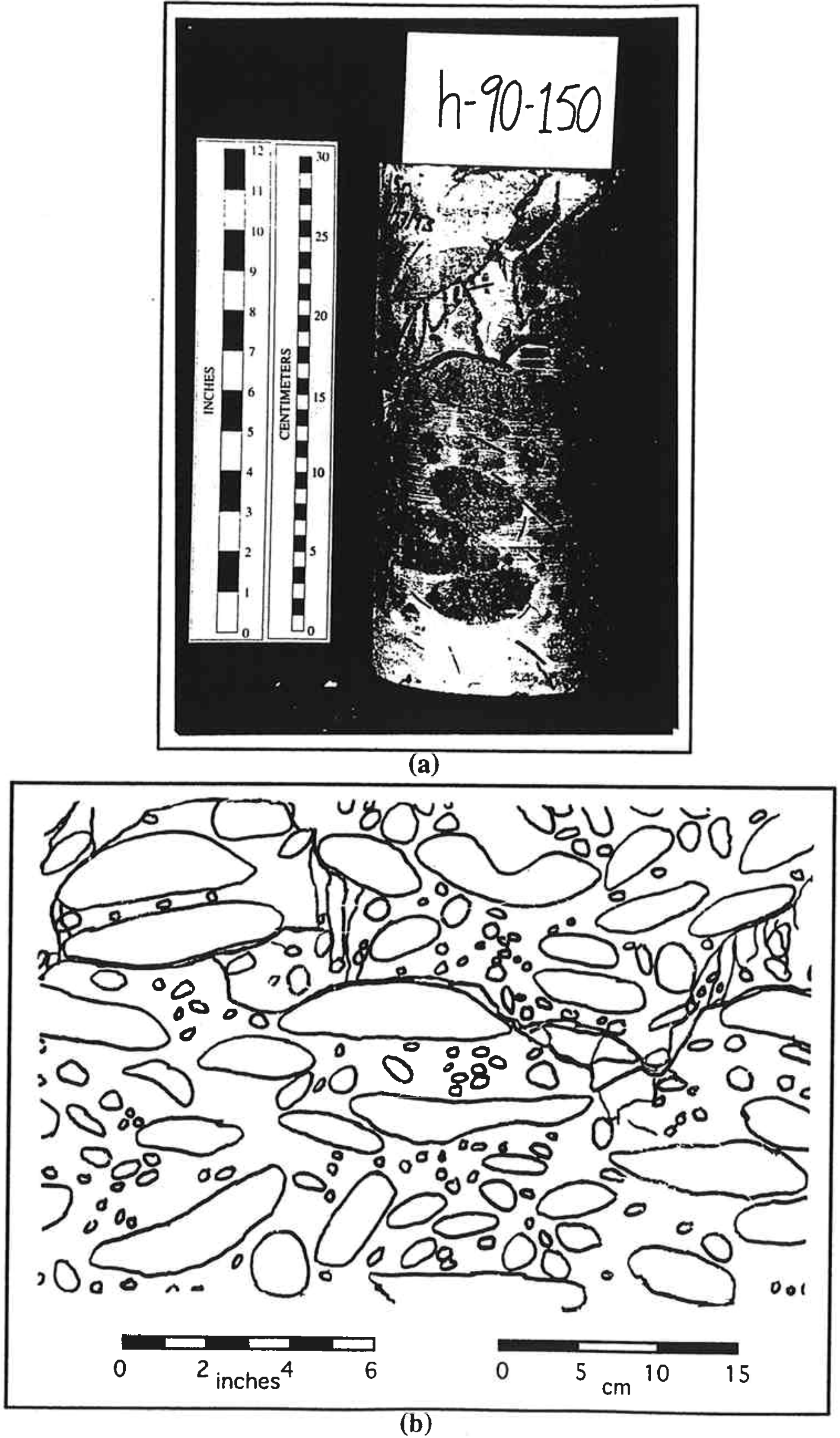

(a)

(b)

Figure D.66 (a) Photograph and **(b)** Tracing of Failed Specimen h-90-150

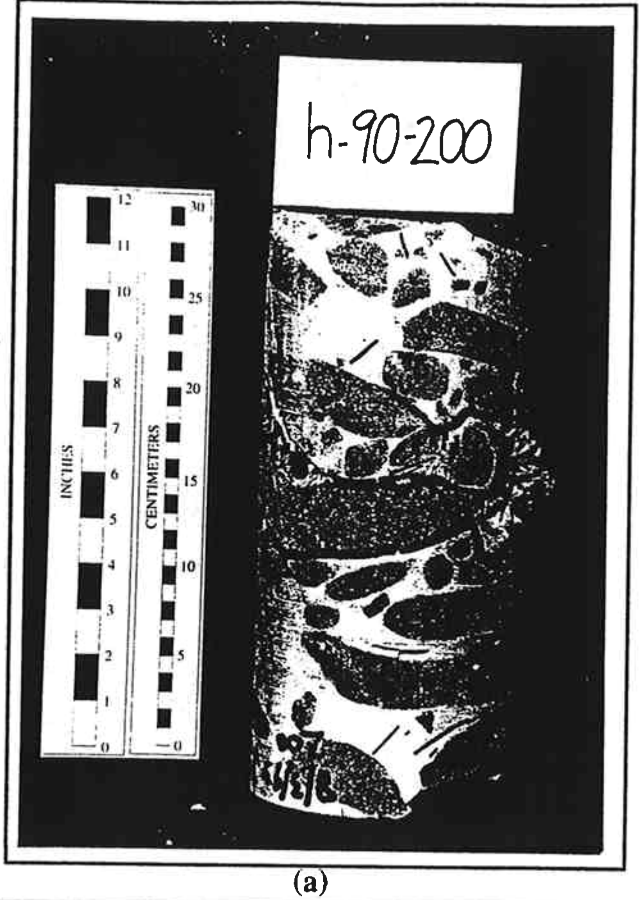

(a)

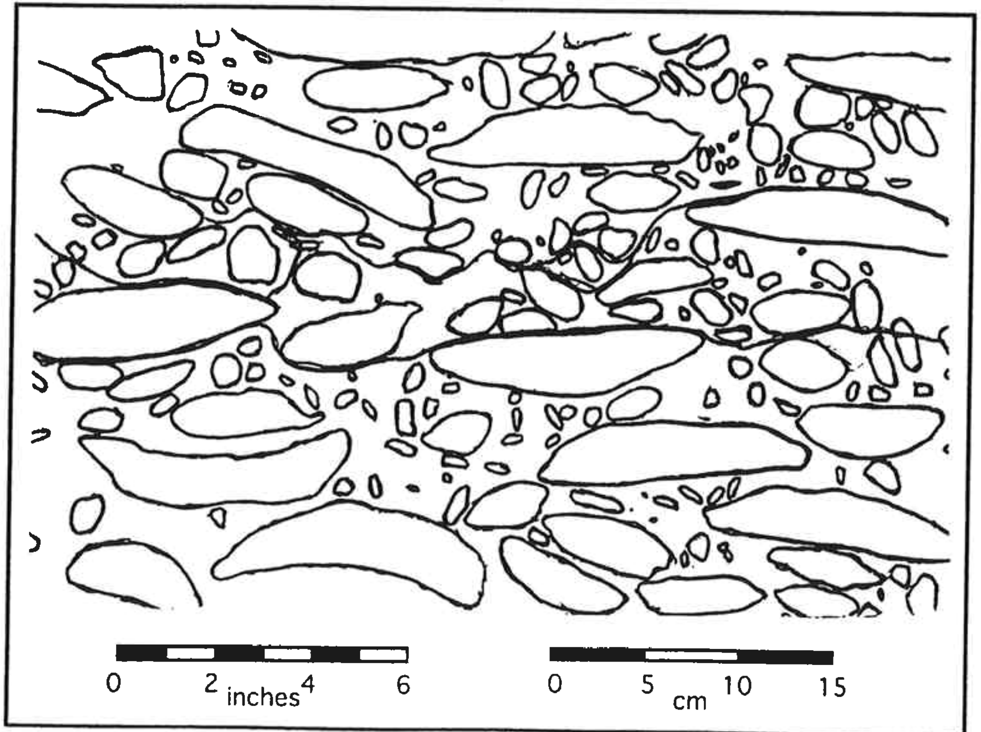

(b) courtesy of Ed Medley

Figure D.67 **(a)** Photograph and **(b)** Tracing of Failed Specimen h-90-200

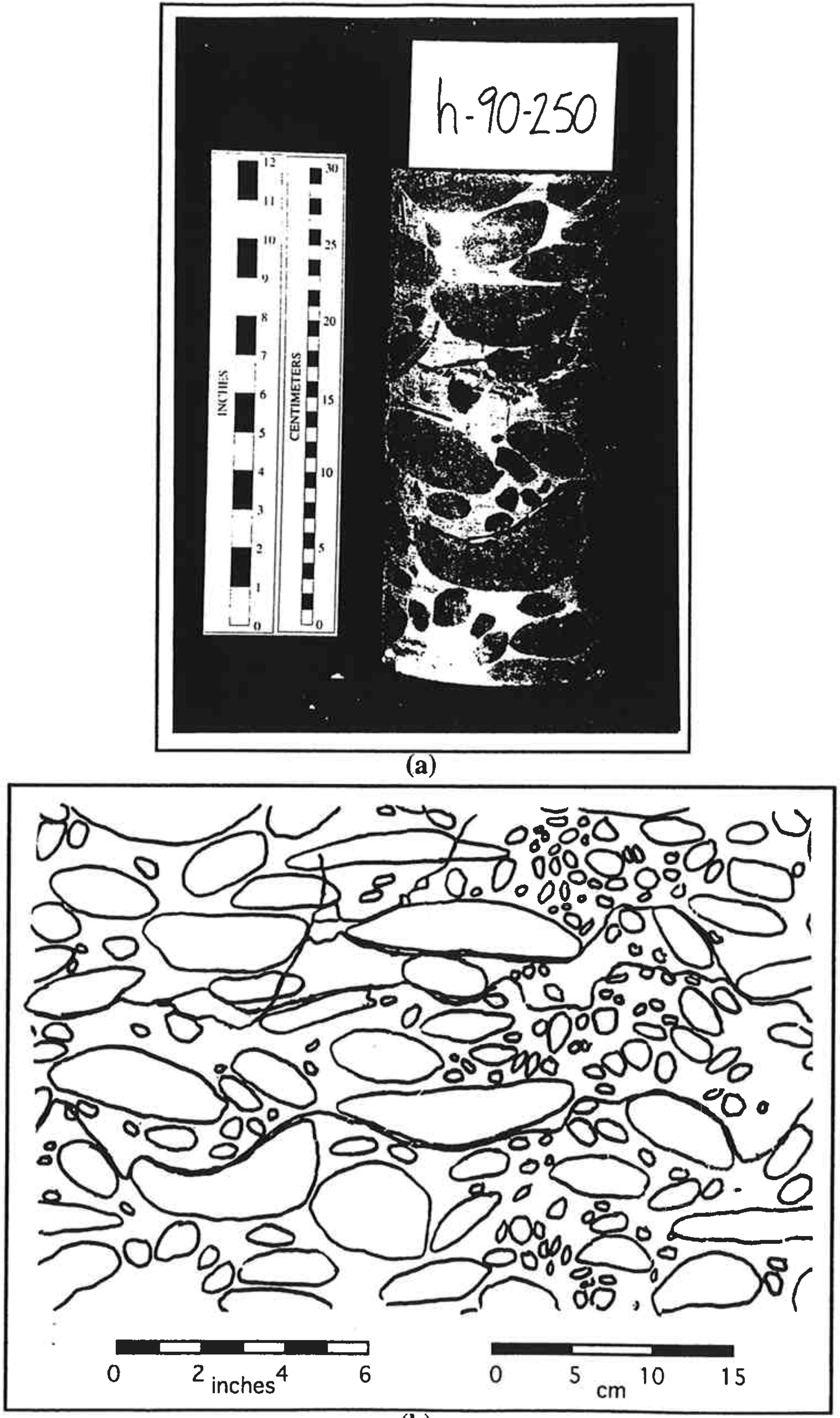

(a)

(b)

Figure D.68 (a) Photograph and **(b)** Tracing of Failed Specimen h-90-250

APPENDIX E

Interface Strength Measurements

This appendix contains the triaxial test results used to determine the shear strength (cohesion and angle of internal friction) of the block-matrix contacts and wax "shears".

Block-Matrix Contacts

Three cylindrical specimens with throughgoing block-matrix contacts were tested in triaxial compression. The confining stress ($(\sigma_3)_{fail}$) and axial stress ($(\sigma_1)_{fail}$) at failure and angle of the contact relative to the axial loading direction (ψ) are given in Table E.1. Figure E.1 illustrates the geometry of a test specimen and identifies the angle ψ.

Table E.1 Strength Data for Block-Matrix Contacts

Specimen #	$(\sigma_3)_{fail}$ (psi)	$(\sigma_1)_{fail}$ (psi)	ψ (°)
1	50	689	30°
2	150	1076	36°
3	250	1368	36°

These results are shown as Mohr circles in Figure E.2. The stresses along the contact at failure are found by the simple construction shown in Figure E.2. A line at an angle ψ from vertical is drawn from the furthest point to the left on the Mohr circle. The point at which the line crosses the circle gives the stresses on the contact at failure. A line fit to through the three resulting points gives the cohesion (c) and angle of internal friction (ϕ_j) along the block-matrix contact.

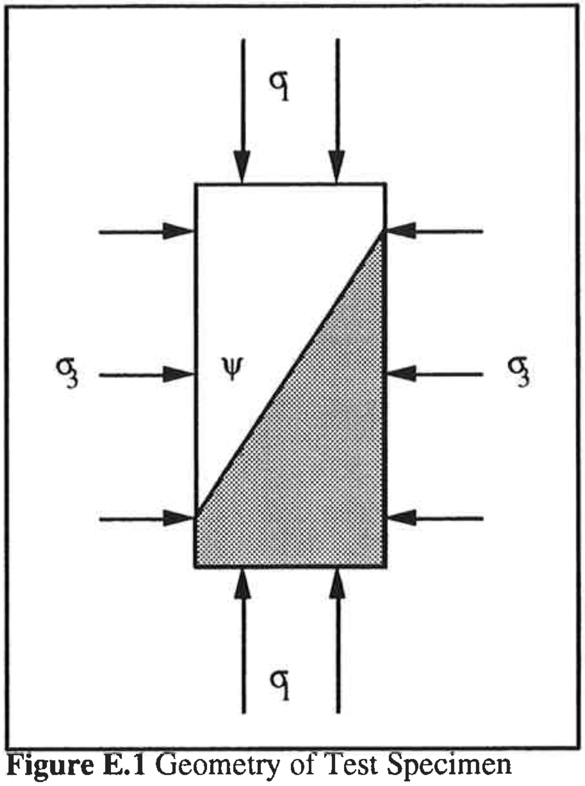

Figure E.1 Geometry of Test Specimen

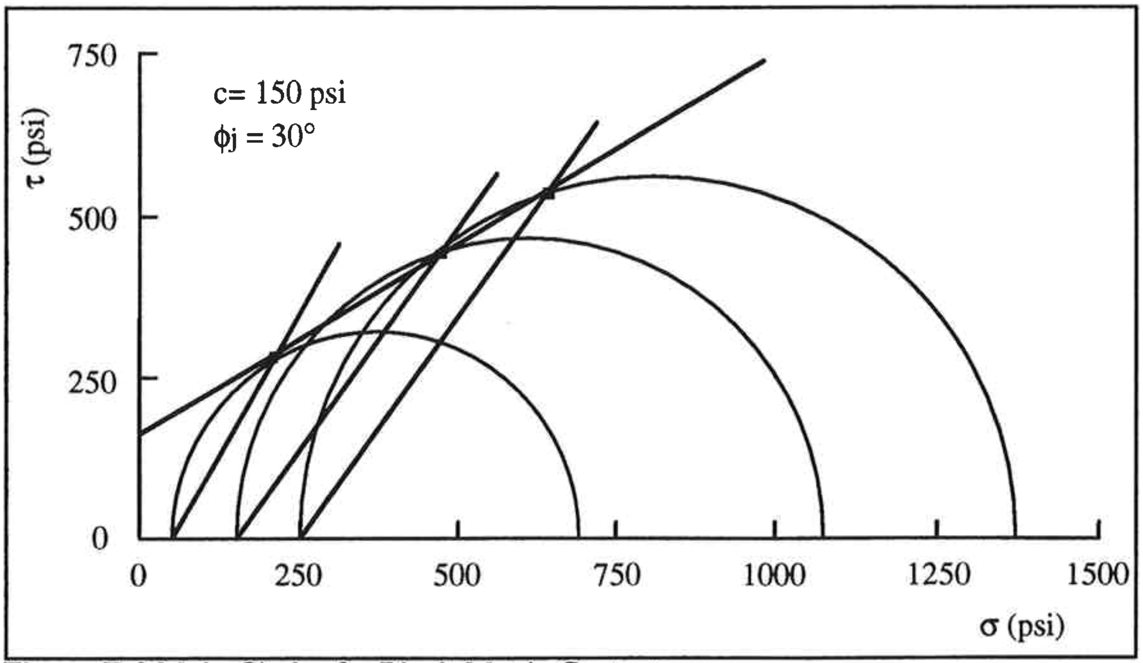

Figure E.2 Mohr Circles for Block-Matrix Contacts

Wax "Shears"

Three cylindrical specimens with throughgoing wax "shears" were tested in triaxial compression. The results of these tests are given in Table E.2.

Table E.2 Strength Data for Wax "Shears"

Specimen #	$(\sigma_3)_{fail}$ (psi)	$(\sigma_1)_{fail}$ (psi)	ψ (°)
1	50	220	60°
2	150	389	59°
3	250	522	55°

The same methodology was used to determine the cohesion and angle of internal friction for the block-matrix contacts is used with these data in Figure E.3 to determine the strength parameters for the wax "shears".

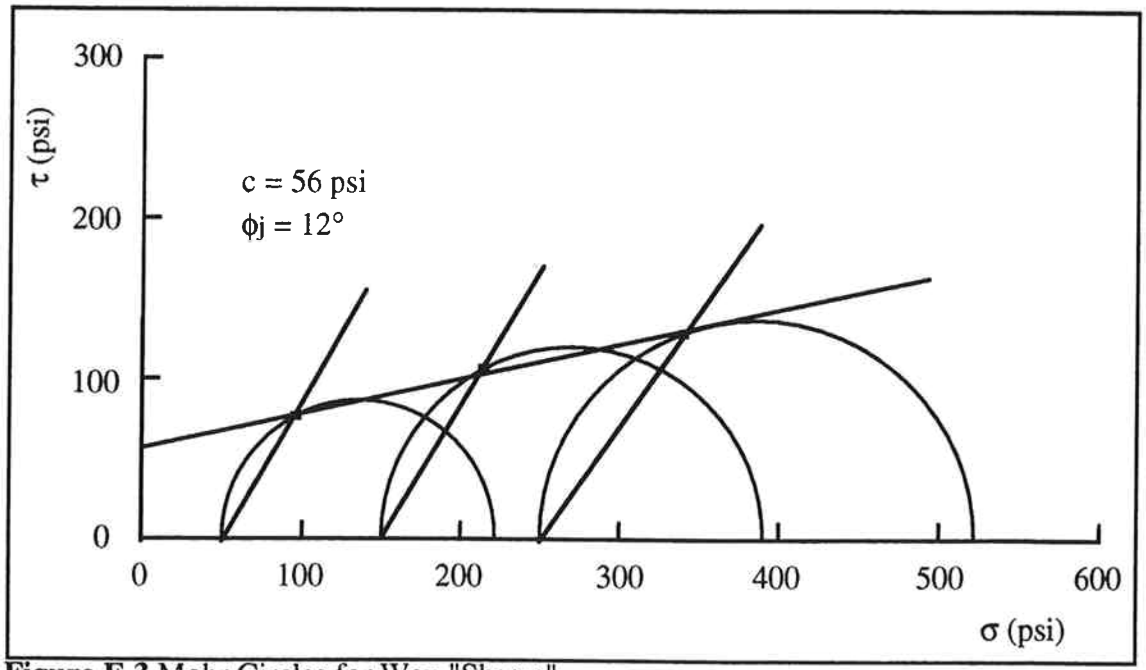

Figure E.3 Mohr Circles for Wax "Shears"

Appendix F Scott Dam Specimen Data

APPENDIX F

Scott Dam Specimen Data

Determination of Volumetric Block Proportion

1. Dry Specimen and Dry Block Weights

Initial weights of the dry specimens were taken and then the specimens were soaked. This soaking softened the matrix material sufficiently to allow the specimens to be disaggregated and the blocks separated. Any rock fragment larger than the No. 4 sieve size was considered to be block material. The group of blocks from each specimen was then dried and weighed.

Table F.1 Scott Dam Specimen and Block Weights

Specimen	Specimen Weight (g)	Block Weight (g)
82-1@125.9'	3411	2533
82-8@39.1'	3704	1632
82-8@113.0'	3913	2839
82-8@114.0'	3823	1465
82-9@45.4'	4364	1736
82-9@51.5'	4299	1118
82-9@53.0'	4262	592

2. Block and Matrix Dry Densities

Blocks:

Seven groups of blocks (one group from each specimen) were weighed dry. They were then prepared to approximately saturated surface dry condition (SSD). The blocks were then placed in a graduated container filled partially with water. Because the blocks were SSD, the amount of water displaced by each group was equal to their volume. With the dry weight and volume the dry density could determined.

The following block densities were calculated by this method.

Specimen 82-1@125.9': 163 pcf
Specimen 82-8@39.1': 171 pcf
Specimen 82-8@113.0': 160 pcf
Specimen 82-8@114.0': 160 pcf
Specimen 82-9@45.4': 166 pcf
Specimen 82-9@51.5': 169 pcf
Specimen 82-9@53.0': 161 pcf

Matrix:

Dry density determinations for the failed specimens were made by Harding-Lawson Associates after they completed their triaxial compression tests. Only two of the seven specimens considered here (82-9@45.4' and @53.0') were tested in triaxial compression without plaster caps. They were therefore the only ones that had their post test densities measured without plaster caps. Hence, the values of dry density determined for these two specimens were the only accurate values for the melange. Using the dry densities of these two specimens, the dry densities of the blocks in the specimens and the specimen and block weights given above, the dry densities of the matrix (sheared shale) could be determined. This was accomplished as follows:

1. the dry specimen weight was divided by the specimen dry density to give the specimen volume
2. the dry weight of blocks was divided by the dry density of blocks to give the block volume
3. the volume of blocks was subtracted from the specimen volume to give the matrix volume
4. the dry weight of blocks was subtracted from the dry specimen weight to give the dry matrix weight
5. the dry weight of the matrix was divided by the matrix volume to give the density

Using this method the density of the sheared shale matrix in specimen 82-9@45.4' was estimated to be 144 pcf, and the density of the sheared shale matrix in specimen 82-9@53.0' was estimated to be 145 pcf.

3. Volumetric Proportions

A matrix (sheared shale) dry density of 145 pcf was assumed, and the dry density of the blocks for each specimen as reported above was used in order to calculate the volumetric block proportion of each specimen. The volumetric block proportion was calculated by

1. dividing the weight of blocks in each specimen by the appropriate block density to get the block volume

2. dividing the weight of matrix in each specimen by the estimated matrix density (145 pcf) to get the matrix volume
3. dividing the block volume by the sum of the block and matrix volume to get the volumetric block proportion.

Table F.2 Volumetric Block Proportions of Scott Dam Specimens

Specimen	Volumetric Block Proportion
82-1@125.9'	72%
82-8@39.1'	40%
82-8@113.0'	71%
82-8@114.0'	36%
82-9@45.4'	37%
82-9@51.5'	23%
82-9@53.0	13%

Calculation of Effective Stress Angle of Internal Friction (ϕ')

Assuming the cohesion to be zero, the effective stress angle of internal friction for a specimen can be calculated given the values of effective axial stress (σ_1') and effective confining stress (σ_3') at failure (i.e. when $(\sigma_1'/\sigma_3')_{max}$). It is known that

$$\phi' = \arcsin\left(\frac{m-1}{m+1}\right) \tag{F.1}$$

where m is the slope of the slope of the line through the strength values in a plot of σ_1' versus σ_3'. In this case the only two plotted points are (0,0), because the cohesion is assumed to be zero, and $((\sigma_3')_{fail},(\sigma_1')_{fail})$. The slope (m) of the line drawn through these two points is simply $(\sigma_1'/\sigma_3')_{max}$, therefore

$$\phi' = \arcsin\left(\frac{(\sigma_1'/\sigma_3')_{max} - 1}{(\sigma_1'/\sigma_3')_{max} + 1}\right). \tag{F.2}$$

The following table presents the values of σ_1' and σ_3' at failure and the effective stress angle of internal friction for each specimen.

Table F.3 $(\sigma_1')_{fail}$ and $(\sigma_3')_{fail}$ and ϕ' for Scott Dam Specimens

Specimen	$(\sigma_1')_{fail}$ (psf)	$(\sigma_3')_{fail}$ (psf)	ϕ'
82-1@125.9'	3320	1090	30.4°
82-8@39.1'	2260	330	48.2°
82-8@113.0'	19310	2000	54.3°
82-8@114.0'	18490	4000	40.1°
82-9@45.4'	2430	890	27.6°
82-9@51.5'	3810	1170	32.0°
82-9@53.0'	7550	2680	28.4°